Università degli Studi di Ferrara

DOTTORATO DI RICERCA IN SCIENZE CHIMICHE

CICLO XXVI

COORDINATORE Prof. Carlo Alberto Bignozzi

SUPRAMOLECULAR SYSTEMS FOR ARTIFICIAL PHOTOSYNTHESIS

Settore Scientifico Disciplinare CHIM/03

Dottorando
Dott. Natali Mirco

(firma)

Tutore
Prof. Scandola Franco

(firma)

Anni 2011/2013

Abstract

Artificial photosynthesis, *i.e.*, conversion of solar energy into fuels, represents one of the most promising research fields which could potentially provide clean and renewable sources of energy for a sustainable development of the future generations. Among several possibilities, water splitting into molecular hydrogen and oxygen is one of the most challenging and appealing reaction schemes. Taking inspiration from nature several functional units are required to this aim: (i) an antenna system, responsible for light harvesting, (ii) a charge separating system, where the absorbed energy is converted into an electrochemical potential (electron/hole pair), and (iii) appropriate catalyst units, capable of stepwise storing the photogenerated electrons and holes in order to drive multi-electron transfer processes at low activation energy.

In the present thesis several points regarding both the photoinduced oxidation and reduction of water as well as charge separation are studied. In more detail, three different classes of water oxidation catalysts are examined, namely tetrametallic polyoxometalate, tetracobalt cubanes, and single-site cobalt salophen complexes, within light-activated catalytic cycles involving tris(bipyridine) ruthenium and persulfate as photosensitizer and sacrificial electron acceptor, respectively. Particular attention is paid to the evaluation of the interactions between the catalyst and the sensitizer and to the kinetics of both photochemical and thermal electron transfer steps. Concerning water reduction, the following systems are investigated: a self-assembling reductant/sensitizer/catalyst triad based on an aluminum pyridylporphyrin central unit, a cobaloxime catalyst, and an ascorbate electron donor, a cationic cobalt porphyrin catalyst in the presence of tris(bipyridine) ruthenium as sensitizer and ascorbic acid as electron donor, and a PAMAM dendrimer decorated with ruthenium polypyridine dyes at the periphery and inside of which platinum nanoparticles have been grown. Beside the optimization of the photocatalytic performance, detailed insights into the photoinduced hydrogen evolving mechanism are carefully provided. Finally, a triad system for photo-induced charge separation, based on a naphthalene bisimide electron acceptor, a zinc porphyrin electron donor, and a ferrocene secondary electron donor, connected *via* 1,2,3-triazole bridges, is also described. Detailed photophysical investigation of the system will show an unusual behavior with respect to photoinduced electron transfer.

Results obtained from a side-project in the field of molecular electronics will be also discussed, where photoinduced electron transfer processes are used to different aims.

Abstract *(italiano)*

La fotosintesi artificiale, intesa come conversione dell'energia solare in combustibili, rappresenta uno dei settori di ricerca più promettenti al fine di garantire risorse energetiche pulite e rinnovabili per uno sviluppo sostenibile delle generazioni future. Tra diverse possibilità, la scissione dell'acqua in idrogeno ed ossigeno costituisce uno degli schemi di reazione più impegnativi ma allo stesso tempo attraenti. Prendendo ispirazione dai sistemi naturali, diverse unità funzionali sono necessarie a questo scopo: (i) un sistema antenna, responsabile dell'assorbimento della luce, (ii) un sistema per la separazione di carica, dove l'energia assorbita è convertita in un potenziale elettrochimico (coppia elettrone/buca) ed (iii) appropriate unità catalizzatrici in grado di accumulare gradualmente gli elettroni e le buche fotogenerati al fine di realizzare processi multielettronici con basse energie di attivazione.

La presente tesi descrive diversi approcci sia verso l'ossidazione che la riduzione fotoindotte dell'acqua, nonché verso sistemi per la separazione di carica. Più in dettaglio, sono esaminate tre classi di catalizzatori per l'ossidazione dell'acqua, quali complessi tetrametallici con leganti poliossometallati, cubani di cobalto e complessi *single-site* di cobalto con leganti salophen, all'interno di cicli fotocatalitici in presenza di rutenio tris(bipiridile) come sensibilizzatore e persolfato come accettore sacrificale di elettroni. Particolare attenzione è riversata nello studio delle interazioni sensibilizzatore/catalizzatore e delle cinetiche dei processi di trasferimento elettronico. Nell'ambito della riduzione dell'acqua, sono indagati i seguenti sistemi: una triade autoassemblante riducente/ sensibilizzatore/catalizzatore costituita da un cromoforo centrale quale un alluminio piridilporfirina, una cobalossima come catalizzatore e ascorbato come donatore sacrificale, una porfirina cationica di cobalto come catalizzatore in presenza di rutenio tris(bipiridile) come sensibilizzatore e acido ascorbico come donatore elettronico, infine un dendrimero tipo PAMAM decorato con cromofori polipiridinici di rutenio alla periferia e al cui interno sono state cresciute nanoparticelle di platino. Oltre all'ottimizzazione delle performance fotocatalitiche, particolare attenzione è riversata nell'indagine del meccanismo di produzione di idrogeno. Infine, viene descritta una triade per separazione di carica costituita da unità naftalene diimmide (accettore), porfirina di zinco (donatore) e ferrocene (donatore secondario) connesse da ponti di tipo 1,2,3-triazolo. Lo studio fotofisico del sistema mostrerà un comportamento insolito per quanto concerne il trasferimento elettronico fotoindotto.

Verranno inoltre discussi risultati di un progetto laterale nell'ambito dell'elettronica molecolare, dove processi di trasferimento elettronico sono impiegati per scopi differenti.

Dedicated to Federica and Alessandro...

Table of Contents

Chapter 1

Introduction

1.1 Current energy situation

In 2007, worldwide energy consumption was 4.58×10^{20} J with an average rate of 16.2 TW.[1,2] Due to the population and economic growth, in particular in the developing country, this global energy need has been also estimated to increase sensitively in the next years and roughly doubling by 2050 and tripling by 2100.[3] By now, about 80% of the overall energy[4] (Figure 1.1) arises from combustion of fossil fuels with oil, coal, and natural gas playing in the order the major role. However, two main issues are emerging which mankind has to deal with in the next years.

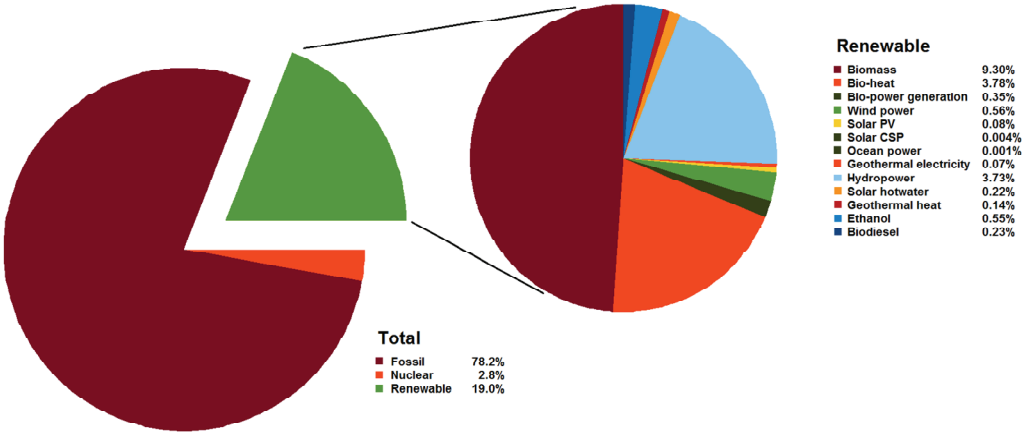

Fig. 1.1. Total world energy consumption by source (values referred to 2011).

First, fossil fuels are non-renewable energy sources, as the rate of their consumption strongly exceeds that for formation, since petroleum, coal, and natural gas deposits are derived from processes requiring a geologic time scale measured in millions of years. This means that, assuming a constant production rate, fossil fuel reserves will be depleted in 35, 107, and 37 years for oil, coal, and gas respectively,[5] and therefore coal will be the only fossil fuel available in the 22nd century. Second, combustion of fossil fuels introduces huge amount of carbon dioxide in the atmosphere. Preanthropogenic CO_2 levels[6] were swinging between 210-300 ppm, largely due to very small variations in Earth's orbit changing the amount of solar energy our planet received, and only in the last 50 years this level has raised importantly up to 380 ppm.[3] This strong increase of carbon dioxide levels in the atmosphere is responsible for very important issues like global warming and climate change. The enhancement of the greenhouse effect by the anthropogenic activities brought about an increase in the Earth's average temperature of 1°C in the 20th century and up to 3°C in the last decades.[7] Although these variations may be considered small, on a global scale this is not the case. In fact, effects

of the increase of the carbon dioxide levels in the planet can be clearly observed in terms of sea level rise (about 17 cm in the last century),[8] ocean warming (about 0.2°C from 1969),[9] shrinking of ice sheets in particular with the declining of Arctic sea ice,[10] glacier retreat, and enhancement of extreme events such as record high/low temperatures, intense rainfalls, tornadoes, etc.

As a matter of fact, the heavy impact of the use of fossil fuels on Earth's health forces global changes to be undertaken. Nowadays, however, only about the 20% of the overall energy supply comes from sources different from fossil fuels. Among the alternatives, nuclear energy (representing the 2.8%, Figure 1.1) seems not to be the most straightforward solution, since, albeit free from carbon dioxide emissions, suffers for several drawbacks such as safety of the reactors and disposal for nuclear wastes.[11]

On the contrary, renewables represent the most challenging way for producing clean energy. Among several possibilities, wind[12] and hydrogeneration are important way to generate electricity with a quite simple technology and relatively low costs. In the last decades particular attention has also been focused on other energy sources by exploiting geothermal energy, ocean and lakes temperature gradients, or ocean tides and currents.[13] Despite their potential zero impact on the environment, however, the use of these technologies for the production of electricity strongly relies on the sites where such natural effects can be observed. Therefore the very high degree of dishomogeneity in the distribution of these natural events seems to limit the development of such technologies in a large scale.

A substantial amount of energy (ca. 10%) is obtained from biomass, requiring very large areas of farming land and big amount of water. In the industrial countries, biomass is employed to directly produce heat and electricity, or to obtain liquid fuels, such as ethanol (from sugar cane or corn) and biodiesel.[11]

1.2 Solar energy

An energy flux at a rate of 172,500 TW strikes the Earth continuously: it is the sunlight. About one half of this power is reflected by the atmosphere while the remaining part passes through this layer and arrives to the Earth's surface, with 65,000 TW and 15,600 TW reaching the hydrosphere and lands, respectively.[14,15] According to this numbers, the overall consumption of energy by the mankind in one year could be in principle balanced by the amount of energy reaching the planet in 1 hour.[16] As such, solar energy has a very great

potential as a clean, abundant, and economical energy source. For a practical employment, however, it must be converted into useful forms.

Moreover, the Sun is an energy source which is quite homogeneously distributed on the entire living planet, meaning that all the people in the world could in principle take advantage equally from the development of solar energy conversion technologies with a strong contribution towards the depletion of the barrier between poor and rich nations.[11] The use of sunlight for the efficient production of energy is the goal of a very huge number of scientists all over the world. Lots of efforts have been done towards this direction and nowadays several technologies are actually available to this aim.

One simple possibility is given by the solar thermal conversion, where solar energy is collected, usually concentrated by means of mirrors or reflectors, for heating fluids that are then used for warming up purposes. Moreover, solar thermal conversion is often either coupled to steam production for engines yielding electricity or applied for thermochemical processes such as methane reforming or metal oxide reduction.[11]

A way to exploit solar energy for the production of electricity is that represented by photovoltaic cells and devices. The most common system is a p-n junction made of silicon in which electron/hole pairs are generated by absorption of light corresponding to the semiconductor energy band gap and an electric current is formed as electron and holes are swept in different directions by the built-in electric field of the depletion region of the p-n junction. Due to the relative high cost of silicon-based technology and adopting similar basic physical principles, dye-sensitized solar cells (DSSCs),[17] based on the sensitization of nanostructured wide band gap semiconductors such as n-type TiO_2, SnO_2, ZnO, etc.[18,19] or p-type NiO,[20] and polymer-based organic solar cells[21,22] have emerged sensitively as cheaper alternatives. All of these photovoltaic devices, however, suffer for photon-to-current efficiency limits (< 10-15%) mainly related to heating or electron-hole recombination processes; therefore, in order to overcome these intrinsic restrictions, tandem configurations are frequently employed.

One of the major limitations in the use of sunlight for generating clean energy, however, is related to the intermittency of this source which prevents the possibility of a continuous harvesting process. This evidence clearly establishes the need for the development of storage methods.

Nature has solved the same problem by means of photosynthesis:[23] green plants evolved mechanisms by which absorption of sunlight triggers the conversion of water and carbon dioxide into oxygen and reduced carbon fuels. Visible light coming from the Sun is absorbed by antennas and reaction center pigments initiating a series of energy and electron transfer

processes, with formation of separated reducing and oxidizing equivalents, followed by oxidation of water to dioxygen, accomplished by the oxygen evolving complex (OEC),[24] and reduction of a nicotinamide dinucleotide phosphate cofactor used to drive the conversion of carbon dioxide into carbohydrates.

1.3 Natural photosynthesis

Green plants and other organisms (such as algae and cyanobacteria) developed systems by which light absorption is followed by a series of energy and electron transfer reactions triggering the synthesis of high-energy content molecules.

In plant cells, this function is accomplished by two reaction centers, called photosystem I (PS I) and photosystems II (PS II) which are located in the chloroplast thylakoid membrane and work in parallel. Light is absorbed efficiently by antenna systems, mainly made of pigments like chlorophyll and carotenoids, which rapidly (few ps) transfer the excitation energy to the special pairs of both PS I and PS II. At this stage a series of electron transfer processes occurs which is ultimately responsible for water oxidation and carbon dioxide reduction. The whole situation is schematized, in a very simplified manner, in Figure 1.2.

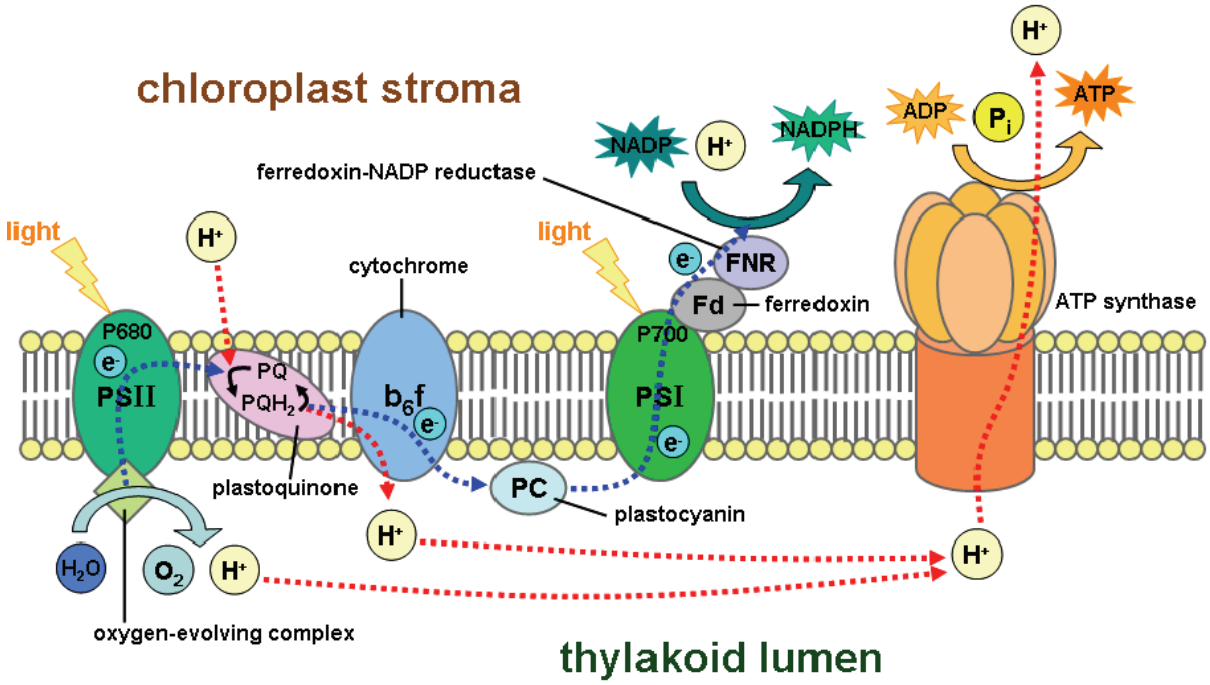

Fig. 1.2. Schematic structure of the thylakoid membrane of green plant chloroplast and related processes occurring after light absorption by the antenna pigments and the special pair. Legend: electron flow, dashed blue line; proton flow, dashed red line.

Excitation of the special pair P680 in PS II (see electron transfer cascade in Figure 1.3a)[25] is followed by electron transfer to a bacteriopheophetyn (ca. 3 ps) with the participation of an intermediary bacteriochlorophyll. Subsequently, from this unit the electron is transferred in ca. 300 ps to a tightly bound quinone (Q_A) and then to a loosely bound quinone (Q_B). Charge separation occurs with unitary efficiency, as charge recombination processes are largely prevented by both energetic (driving forces in the Marcus inverted region)[26] and distance factors. Electrons from the quinone are then transferred at the other side of the membrane to a cytochrome *b* and afterwards to a plastocyanin. Importantly, reduction of the quinone Q_B is a two-electron-two-proton process involving formation of a QH_2 species (quinol). Protons are thus extracted by the quinone from the chloroplast stroma after reduction by Q_A, the QH_2 species undergoes diffusion within the thylakoid membrane and then revers protons in the thylakoid lumen after electron transfer to cytochrome *b*. This contributes to the formation of a proton gradient across the thylakoid membrane which is fundamental for the production of ATP by the ATP-synthase (Figure 1.2).

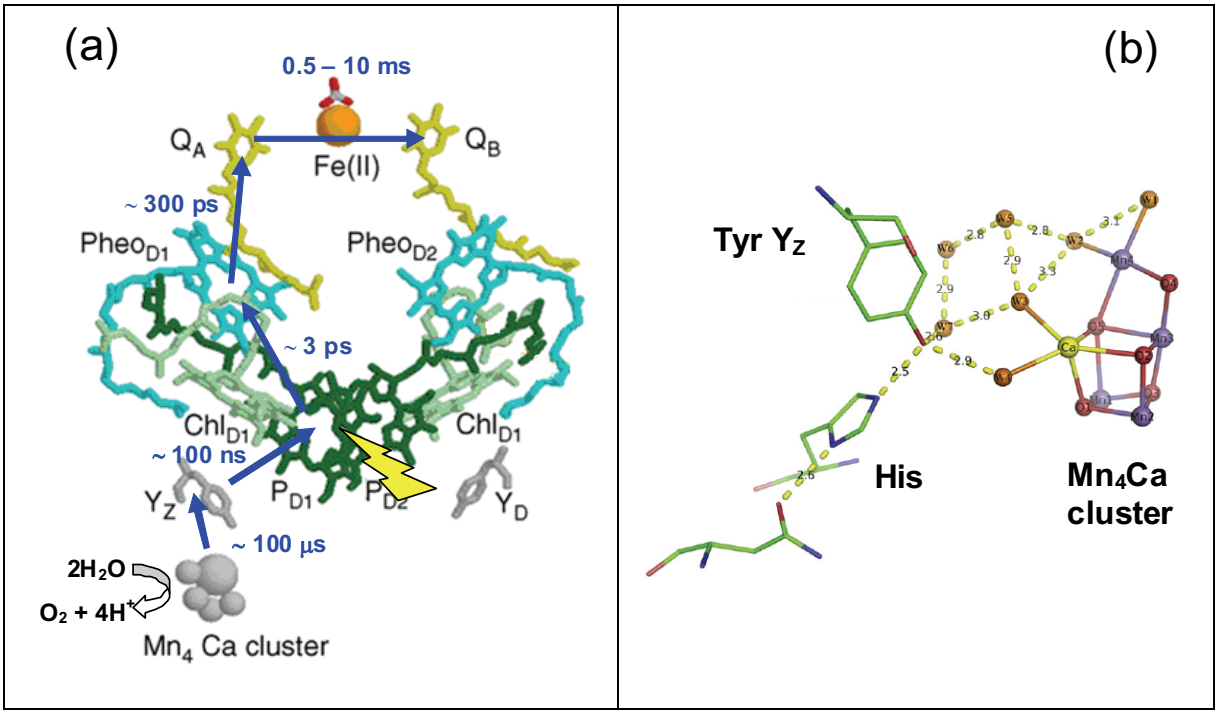

Fig. 1.3. (a) Photoinduced electron transfer cascade in PS II with related kinetic parameters, (b) detailed structure of the Mn_4Ca oxygen evolving complex.

At the other side, the photogenerated $P680^+$ is a very strong oxidant and extracts electrons from two water molecules by means of the Mn_4Ca oxygen evolving complex (Figure 1.3b).[24] This latter is based on a distorted cubane structure including three Mn, one Ca, and four

bridging oxygen atoms with an additional isolated fourth Mn center. Key unit is a tyrosine residue, Y_Z, participating to a hydrogen-bond network linking the Mn_4Ca OEC and acting as a relay for electron abstraction. Indeed, when Y_Z is oxidized, a proton moves in this hydrogen bond to the histidine, making the process thermodynamically allowed and leaving the oxidized tyrosine as a neutral radical (proton-coupled electron transfer). The stepwise oxidation of the OEC by the tyrosine radical is described by the Kok cycle (Figure 1.4).[27]

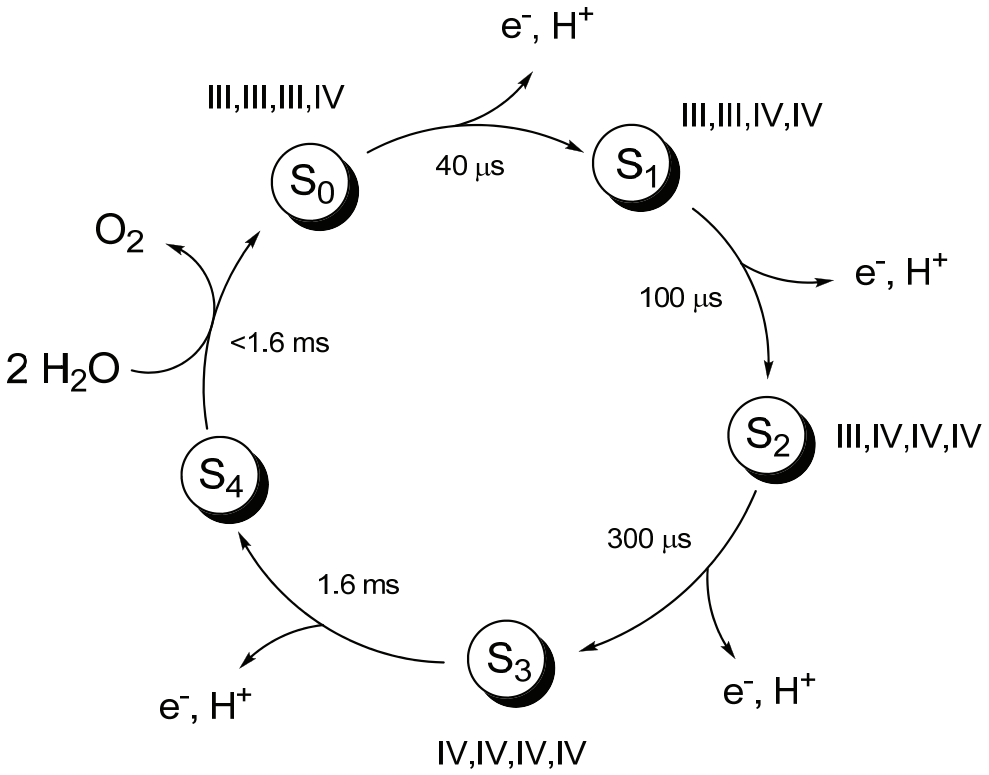

Fig. 1.4. Schematic representation of the Kok cycle for water oxidation by Mn_4Ca OEC[27] with kinetic parameters and formal oxidation states of the manganese atoms.

Excitation of the special pair P700 in PS I is followed by a cascade of electron transfer processes to a ferredoxin complex *via* the intermediary participation of a chlorophyll, a quinone and three 4Fe-4S clusters. The positive charge left on the P700 is neutralized by the transfer of an electron from the reduced plastocyanin (*vide supra*). Finally, the FNR ("ferredoxin-$NADP^+$ reductase") enzyme transfers the electron from the reduced ferredoxin to the $NADP^+$ cofactor to form NADPH. NADPH and ATP are then used in the Calvin cycle for converting carbon dioxide into reduced carbon fuels, *i.e.*, carbohydrates.

The whole series of electron transfer processes can be summarized in Figure 1.5 with the so-called Z-scheme.

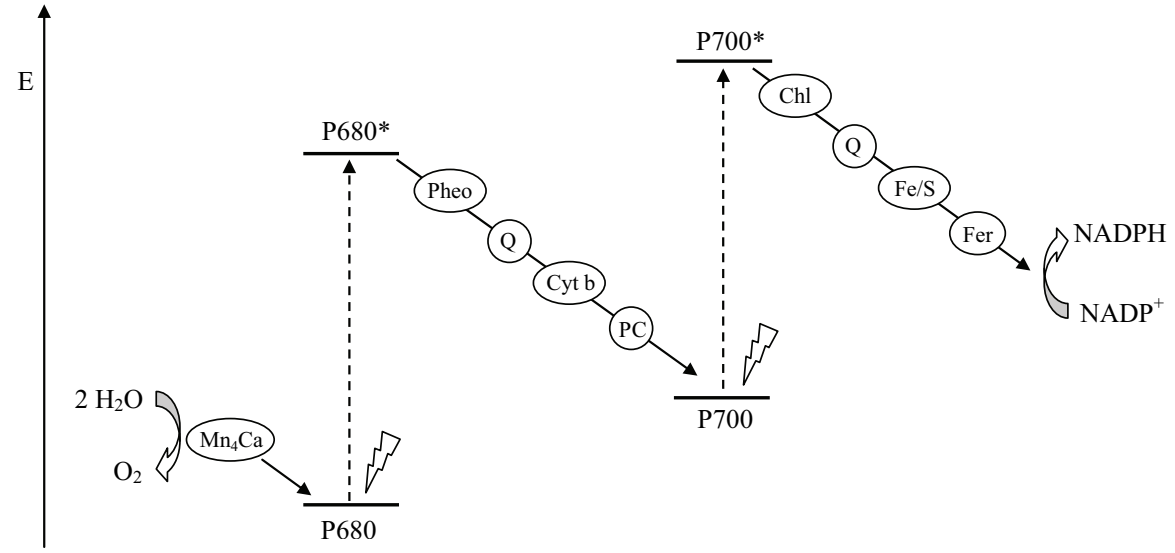

Fig. 1.5. Schematic representation of the Z-scheme of natural photosynthesis highlighting light-induced processes (dashed line) and electron transfer ones (solid line).

1.4 Artificial photosynthesis

The progressive understanding of the mechanism by which plants use sunlight for the conversion of water and carbon dioxide into carbohydrates has brought to the development of the concept of "artificial photosynthesis", namely conversion of solar energy into fuels.

In a biomimetic approach, a general scheme of an artificial photosynthetic device (Figure 1.5) should envision a light-harvesting antenna system, a photosensitized charge separation unit, and catalysts for the conversion of the substrates into products.

The antenna system is the functional unit responsible for light absorption. This unit should be ideally conceived with a large variety of chromophores to maximize absorption from the UV to the IR. The energy absorbed by the light-harvesting system is then efficiently funneled to a photosensitizer in a series of vectorial energy transfer processes which can occur through different mechanisms such as (i) FRET (Förster Resonance Energy Transfer)[28] between two different weakly coupled chromophores, (ii) Dexter-type energy transfer[29] involving an electron exchange process also possible between two molecules with forbidden optical transitions, and (iii) delocalized exciton migration between excitonically-coupled chromophores.[30] Several examples have been reported in the literature involving either covalent or self-assembling approaches for the construction of light-harvesting antenna systems.[31]

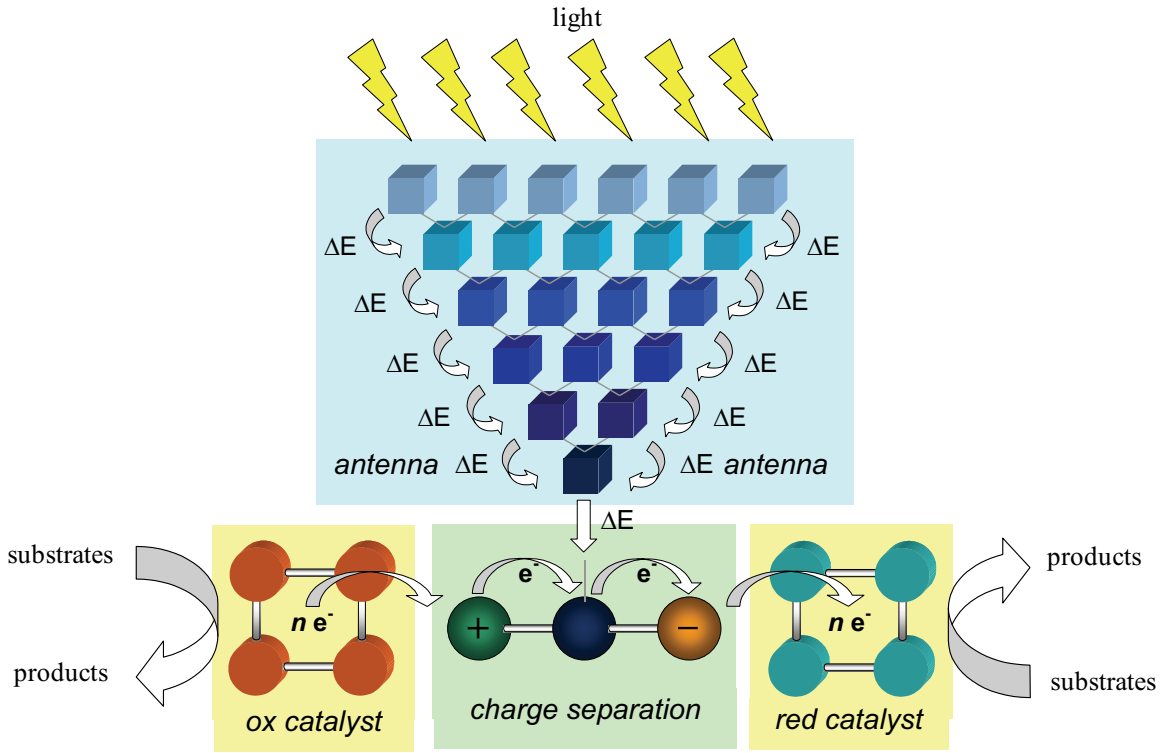

Fig. 1.6. General scheme of a system for artificial photosynthesis.

The charge separating unit is responsible for the conversion of the absorbed solar energy into an electrochemical potential required for triggering the redox reactions on the substrates. The minimum basis for charge separation is a dyad in which a donor and an acceptor are connected through a bridge. Excitation of the photosensitizing donor unit (eq 1) is followed by electron transfer to the acceptor (eq 2) yielding a charge separated state which then undergoes recombination to the ground state (eq 3).

$$P\text{-}A + h\nu \rightarrow {}^{*}P\text{-}A \qquad (1)$$

$${}^{*}P\text{-}A \rightarrow P^{+}\text{-}A^{-} \qquad (2)$$

$$P^{+}\text{-}A^{-} \rightarrow P\text{-}A \qquad (3)$$

The short distance between the photogenerated electron/hole pair in a dyad determines the relative short lifetime of the charge separated state. Therefore, in order to increase the lifetime, the introduction of additional units such as secondary electron donor/acceptor is needed. For instance, in the case of a D-P-A triad system (Figure 1.6), after the first electron transfer process (eqs 4,5) a secondary electron transfer occurs (eq 6) in competition with charge recombination, yielding the long-range charge separated state which, given the longer distance between the photogenerated electron and hole, recombines to the ground state (eq 7) with a slower rate by comparison with the P-A dyad (eq 3).

$$D\text{-}P\text{-}A + h\nu \rightarrow D\text{-}{}^{*}P\text{-}A \quad (4)$$

$$D\text{-}{}^{*}P\text{-}A \rightarrow D\text{-}P^{+}\text{-}A^{-} \quad (5)$$

$$D\text{-}P^{+}\text{-}A^{-} \rightarrow D^{+}\text{-}P\text{-}A^{-} \quad (6)$$

$$D^{+}\text{-}P\text{-}A^{-} \rightarrow D\text{-}P\text{-}A \quad (7)$$

According to the classical Marcus theory of electron transfer,[26] several parameters of the system may affect the charge separation efficiency and the lifetime of the charge separated state. Huge amount of literature is present describing charge separation molecular devices and evaluating structure-behavior relationships.[32]

Once charge separation has occurred, photogenerated electrons and holes must be accumulated by appropriate catalyst units capable of driving multi-electron redox processes at low activation energy. One of the most challenging artificial photosynthetic reaction scheme is represented by water splitting (eq 8), which paves the way for a solar hydrogen generation. According to this scheme hydrogen is produced as a clean fuel in a clean and zero emission process.

$$2\,H_2O \rightarrow 2\,H_2 + O_2 \quad (8)$$

Water splitting is an up-hill reaction with a thermodynamic requirement (driving force) of $\Delta G° = +474$ kJ/mol. The standard electrochemical potential (298 K, pH = 0) for the water splitting reaction can be estimated from this value as $\Delta E° = -1.23$ V. Although this thermodynamic hurdle could be in principle overcome by exploiting reductants/oxidants with appropriate redox potentials, its kinetic limitations represent the strongest drawbacks. This can be easily understood considering the water splitting reaction (eq 8) "split" into its two half-reactions (eqs 9,10).

$$2\,H_2O \rightarrow O_2 + 4\,H^{+} + 4\,e^{-} \quad (9)$$

$$4\,H^{+} + 4\,e^{-} \rightarrow 2\,H_2 \quad (10)$$

As a matter of fact, both water reduction (hydrogen evolving reaction, HER) and water oxidation (oxygen evolving reaction, OER) are multi-electronic processes. Therefore an efficient photochemical water splitting device must provide not only the required thermodynamic boost for the water splitting reaction, but must also be equipped with catalyst units capable of stepwise storing the redox equivalent in order to tackle the kinetic limitations

of the process. Several approaches have been attempted for the construction of molecular catalysts for both water oxidation and reduction.

As far as water oxidation is concerned, taking inspiration from the natural OEC tetrametallic molecular complexes based on either rare metals (Ru, Ir) or earth-abundant elements (Mn, Co) have been extensively studied.[33] They can indeed store the oxidizing equivalents on different centers, at reasonably similar oxidation potentials, before effecting water oxidation. In the last years, however, several attempts have also been done for the design of lower nuclearity water oxidation catalysts with particular emphasis on single-site metal complexes based on metals with several accessible oxidation states such as iron,[34] copper,[35] ruthenium,[36,37] iridium,[38] and cobalt.[39]

On the other hand, approaches towards hydrogen production have mainly involved the preparation of (i) synthetic hydrogenase molecular mimics of the [Fe,Fe], [Ni,Fe], or [Fe]-only hydrogenase natural enzymes,[40] (ii) cobaloximes, cobalt diimine, and other cobalt complexes,[41] (iii) nichel complexes based on phosphine[42] or thiolate[43] ligands and (iv) also molybdenum,[44] platinum,[45] palladium,[46] or rhodium[47] polypyridine complexes.

1.5 Scope of the thesis

The activity of photosynthetic organisms in nature strongly relies on their supramolecular architectures, in which the organization of molecules plays a crucial role in determining the efficiency of photochemical processes such as light-harvesting and charge separation. Taking inspiration from nature, supramolecular chemistry[48] gives the possibility to self-organize molecules into complex structures by exploiting different molecular interactions which may vary from weak intermolecular forces (electrostatic or hydrogen bonding) to strong ones (covalent bonding), provided that the degree of electronic coupling between the molecular component remains small with respect to relevant energy parameters of the component. To this respect, the supramolecular approach currently represents the ideal way to assemble molecular components for the construction of artificial photosynthetic devices.[49]

In this thesis different functional units of an artificial photosynthetic scheme are described such as charge separation, water oxidation and reduction, and particular attention is paid to the mechanistic investigation of the photoinduced processes with the use of spectroscopic techniques.

Chapter 2 will give a short description of the instrumental techniques employed for the study and characterization of the systems. Chapter 3, Chapter 4, and Chapter 5 will deal with water oxidation catalysis with particular emphasis on the electron transfer dynamics involved

within the photocatalytic processes, while Chapter 6, Chapter 7, and Chapter 8 will face up the other side of water splitting, namely proton reduction to molecular hydrogen, and Chapter 9 will describe a charge separating triad system. Finally, Chapter 10 will discuss on a side-project related to fluorescence-based photoswitching memories for application in optoelectronic devices, where similar basic concepts and experimental techniques have been applied.

Chapter 2

Experimental Methods

2.1 Stationary absorption/emission techniques

UV-Vis absorption spectra were recorded on a *Jasco V-570 UV/Vis/NIR* spectrophotometer, employing a W/I_2 and a H_2/D_2 lamps for the NIR/Vis and the UV irradiation, respectively. Standard quartz cuvettes with 0.2 cm or 1.0 cm optical path were used. The measurement consists in the detection of the amount of light intensity absorbed by a sample solution for comparison with a blank (solvent) at wavelengths between the NIR (maximum value 2500 nm) to the UV (minimum value 200 nm). The result is a plot of the absorbance (or optical density, OD) *vs.* wavelength, where the absorbance A is described by eq 11,12.

$$A = \log\frac{1}{T} \tag{11}$$

$$T = \frac{I}{I_0} \tag{12}$$

In eq 11,12, T is the transmittance, I and I_0 are the light intensities transmitted by the sample and the reference (blank), respectively. For optical diluted solutions the absorbance A can be correlated to the concentration of the absorbing species through the Lambert-Beer law (eq 13), where ε is the molar extinction coefficient, l is the optical path, and c is the concentration.

$$A = \varepsilon\, l\, c \tag{13}$$

Photoluminescence and excitation spectra were taken on a *Horiba-Jobin Yvon Fluoromax-2* spectrofluorimeter, equipped with a monochromatized Xe arc-lamp and a *Hamamatsu R3896* photomultiplier tube as excitation source and detector, respectively. Standard quartz cuvettes with 1.0 cm optical path were employed. Cut-off filters have been frequently used either after the excitation monochromator or before the emission one in order to remove higher-order diffraction phenomena which may affect the obtained spectra.[50] A photoluminescence measurement consists in the detection of the intensity of the emitted light by a sample at different wavelengths (in general in the UV/visible range) upon excitation at a fixed wavelength. The emission intensity is strongly dependent on the experimental conditions (excitation wavelength, absorbance of the emitter at that wavelength, integration time, slits of both excitation and emission monochromators), therefore care has to be taken in

order to compare emission spectra. Conversely, an excitation spectrum is measured by fixing the emission wavelength and measuring the intensity at that wavelength upon excitation at different wavelengths. Importantly, an excitation measurement is meaningful only after correction of the output considering the different intensities of the excitation source at every wavelengths and in the case of optical diluted solutions, since, only in these conditions, the amount of absorbed photons is proportional to the number of emitted ones. The result is a spectral profile resembling the absorption spectrum of the emitting species.

2.2 Time-resolved absorption/emission techniques

In order to unveil the complex mechanisms behind photochemical processes, time-resolved absorption/emission techniques are extremely useful. These techniques can be roughly distinguished on the basis of the type of detection (emission or transient absorption) or the investigated time domain, even though the technical and physical concepts behind these powerful equipments can be completely different.

As regarding transient absorption techniques, spectra and kinetics were measured in differential mode: the output is usually expressed as ΔOD (eq 14) where A^* is the absorbance of the transient species and A_0 is that of the ground state.

$$\Delta OD\ (\lambda, t) = A^* - A_0 \qquad (14)$$

By combining eq 14 with the Lambert-Beer law in eq 13, it is thus possible to calculate the concentration Δc of the photogenerated transient species (eq 15), provided that the molar extinction coefficient is known.

$$\Delta OD = \Delta\varepsilon\, l\, \Delta c \qquad (15)$$

More importantly, in this case the parameter l, correlating ΔOD and Δc, is not strictly the optical path of the cell, but rather the real fraction of the solution in the cell which is pumped by the excitation source and analyzed by the light probe. As such it could be better seen as an instrumental correction parameter which has to be known in order to perform the correlation reported in eq 15.

2.2.1 Time-correlated single photon counting (TC-SPC)

Time-correlated single photon counting is a time-resolved emission technique which is employed for the measurements of the lifetimes of emitting excited states. The basic principle of this instrument lies in the possibility of detecting single emitted photons and measure the delay time between excitation and emission.

Experiments were recorded using a TC-SPC apparatus (*PicoQuant Picoharp 300*) equipped with subnanosecond LED sources (280, 380, 460, and 600 nm, 500-700 ps pulsewidth) powered by a *PicoQuant PDL 800-B* variable (2.5-40 MHz) pulsed power supply (a schematic representation is reported in Figure 2.1). Detection is performed by a photomultiplier (*Hamamatsu PMA 185*) equipped with a monochromator. The decays were processed by an integrated Time-to-Digital Converter (TDC) and analyzed by means of *PicoQuant FluoFit* Global Fluorescence Decay Analysis Software.

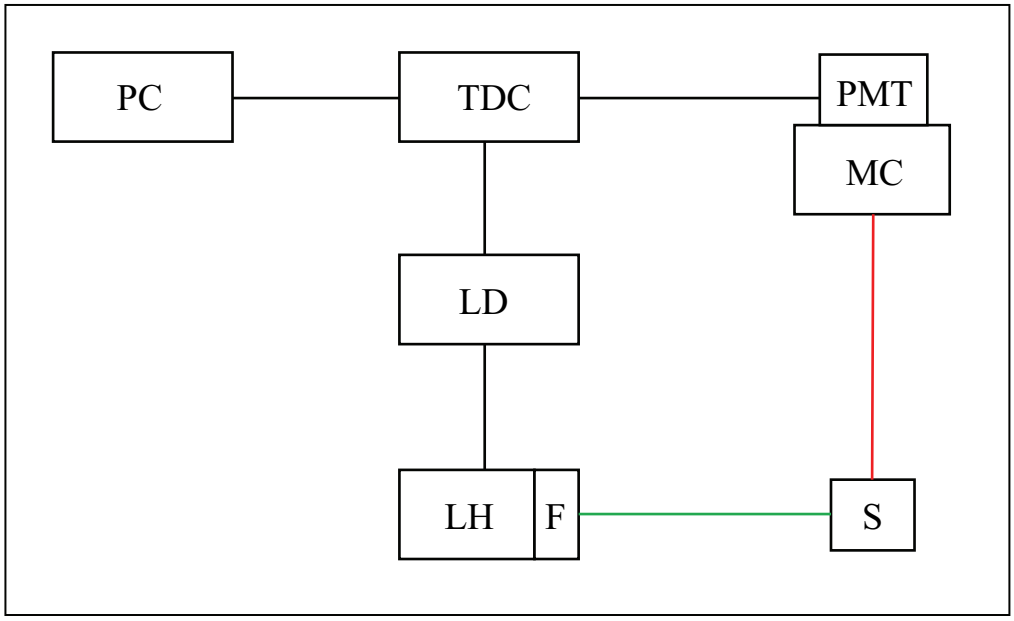

Fig. 2.1. General scheme of a TC-SPC apparatus: green line, excitation beam, red line, emission light, LH, laser head; F, filter; S, sample; MC, monochromator; PMT, photomultiplier tube; TDC, time-to-digital converter; LD, laser driver; PC, personal computer.

The time window of the experiment is dependent on the repetition rate and can arrive up to μs, while the time resolution is strictly dependent on the pulsewidth value and is ca. 250 ps.
In a typical experiment the excitation pulse produces a *start* signal, while the first photon emitted by the sample which is detected by the PMT yields the *stop* signal. The delay time between start/stop signals is measured. This experiment is repeated a certain number of times at a defined repetition rate until a sufficient number of counts is acquired to define an

histogram of the decay probability. It is demonstrated that the decay probability histogram matches the decay of the emission of the excited state involved in the analysis.

It is important to figure out that beside the emission from the sample there is a probability that photons of the excitation source are scattered by the sample solution and hit the detector, thus contributing to the probability histogram. The result is a convolution of the emission of the sample with the time profile of the laser source. From a practice viewpoint, when emission lifetimes are so short as to be comparable with the time profile of the excitation source (in general few ns) it is important to record, beside the experiment with the sample, the so-called IRF (instrumental response factor), by repeating the experiment in the presence of a scatterer. Under this condition, the interpretation of the probability histogram is only possible after deconvolution and subsequent exponential fitting.

2.2.2 Ultrafast spectroscopy (UFS)

Ultrafast spectroscopy is a time-resolved transient absorption technique with the possibility of investigating photophysical processes with a time resolution of hundreds of fs. With the instrument described in the following part the time resolution is ca. 300 fs and the time window between 0-2000 ps.

The spectrometer,[51] schematized in Figure 2.2, employs the *Spectra-Physics Hurricane* system as the laser source. This system is based on a seed laser (*Mai Tai*, diode pumped mode-locked Ti:sapphire pulsed laser), a pump laser (*Evolution*, diode-pumped Q-switched Nd:YLF laser), a stretcher, a Ti:sapphire regenerative amplifier, and a compressor.

The output of the system consists of pulses of 800 nm, with a full-width at half-maximum (FWHM) of 100 fs at a repetition rate of 1 kHz. The *Hurricane* output is first split (50%) in two beams. One of these (pump) is converted into useful excitation wavelengths by coupling it into a second-harmonic generator (for 400-nm excitation), or triple-harmonic generator (for 266-nm excitation), or into an optical parametric amplifier (*Spectra-Physics OPA 800*, for tunable wavelengths in the region 320-700 nm). The other one (probe) is first passed twice through a computer-controlled delay track line (*Physik Instrumente M-415 DG*), and then focused on a sapphire plate (*Crystal System, Inc.*, HEMLUX grade) to generate a white light continuum (effective useful range, 450-750 nm). The pump beam is passed through an optical chopper (*Scitec Instruments, 320C*) and focused on the sample cell, which is a 2-mm optical path quartz cell with the inner solution kept under continuous stirring to prevent sample degradation. The white light continuum probe beam is collimated and focused into the sample cell, superimposed to the pump beam.

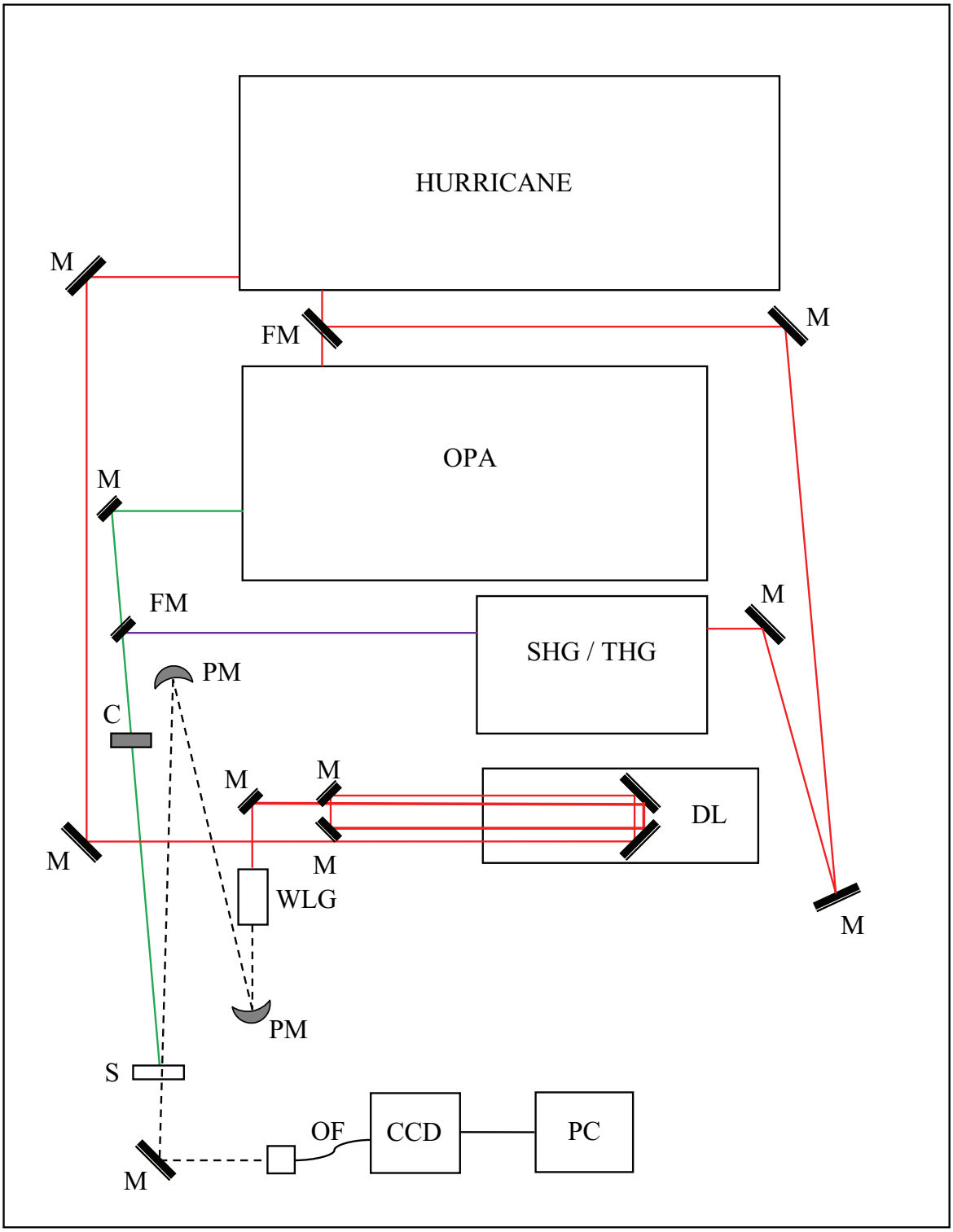

Fig. 2.2. Schematic layout of the UFS setup: red line, 800-nm beam; green line, pump light obtained by OPA; violet line, 400-nm pump obtained by SHG; black dashed line, white light continuum; OPA, optical parametric amplifier; SHG, second harmonic generator; THG, triple harmonic generator; DL, delay line; M, mirror; FM, flipping mirror; PM, parabolic mirror; WLG, white light generator; C, chopper; S, sample; OF, optical fiber; CCD, charge-coupled device spectrograph; PC, personal computer.

After passing through the sample cell, the white continuum is focused into a 100 μm optical fiber connected to a charge-coupled device (CCD) spectrograph (*Ocean Optics, PC 2000*). Typically, time-resolved absorption spectra are acquired averaging over 4000 excitation pulses at any delay time. The delay line, the CCD spectrograph, and the chopper are computer-controlled by a LabVIEW (National Instruments) software routine developed by *Ultrafast Systems, LLC*. These routines allow automatic spectral acquisition at any selected delay-line settings. Kinetic traces at chosen wavelengths can be extracted from the accumulated transient absorption data.

2.2.3 Nanosecond Laser Flash Photolysis

Nanosecond Laser Flash Photolysis is a spectroscopic technique used for time-resolved emission and absorption measurements in a time window from 6-8 ns up to ms.

Transient measurements were performed with a custom laser spectrometer (a schematic representation is given in Figure 2.3) comprised of a *Continuum Surelite II Nd:YAG* laser (1064 nm, FWHM = 6-8 ns) equipped with frequency doubled (532 nm), tripled (355 nm), or quadrupled (266 nm) options, an *Applied Photophysics* Xe light source including a mod. 720 150 W lamp housing, a mod. 620 power controlled lamp supply, and a mod. 03-102 arc lamp pulser. Laser excitation is provided at 90° with respect to the white light probe beam. This latter is controlled by means of an *Oriel 71445* shutter, which opens only for ca. 100 ms during the measurements, thus preventing continuous irradiation of the sample. Light transmitted (transient absorption measurements) or emitted (time-resolved emission measurements) by the sample is focused onto the entrance slit of a 300 mm focal length *Acton SpectraPro 2300i* triple grating, flat field, double exit monochromator equipped with a photomultiplier tube detector (*Hamamatsu R3896*), used for kinetic studies at fixed wavelength, and a *Princeton Instruments PIMAX II* gated intensified CCD camera, used for spectral detection at fixed time-delays, employing a *RB Gen II* intensifier, a *ST133* controller and a *PTG* pulser. Signal from the photomultiplier is processed by means of a *LeCroy 9360* (600 MHz, 5 Gs/s). The switch between the two types of detection is obtained by means of a mirror comprised in the monochromator unit. Excitation source, lamp and shutter are computer-controlled by a LabVIEW (National Instruments) software routine (courtesy from Dr. Roberto Argazzi, ISOF-CNR, c/o Department of Chemical and Pharmaceutical Sciences of the University of Ferrara).

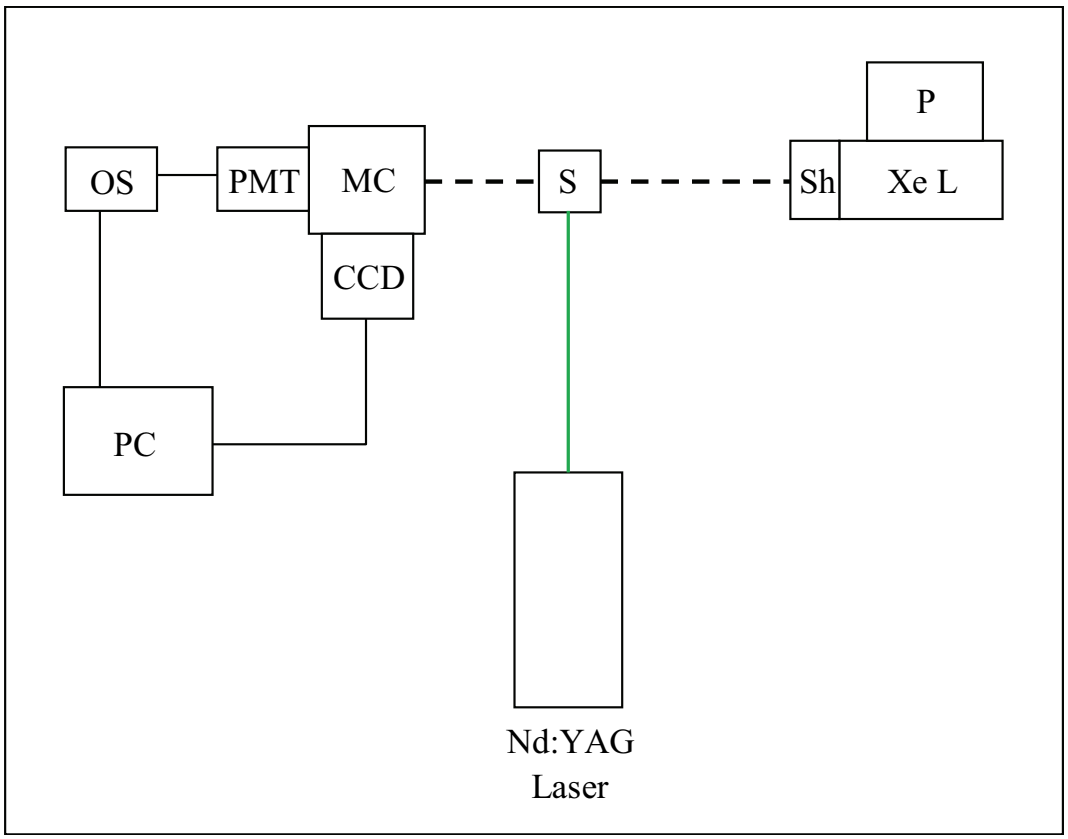

Fig. 2.3. Schematic layout of the Nanosecond Laser Flash Photolysis setup: green line, excitation beam; black dashed line, white light probe beam; Xe L, xenon arc lamp; P, Xe lamp pulser; Sh, shutter; S, sample; MC, monochromator, PMT, photomultiplier tube; CCD, CCD camera; OS, oscilloscope; PC, personal computer.

2.3 Electrochemical techniques

In order to obtain experimental information on the redox properties of the investigated systems, electrochemical techniques such as cyclic voltammetry (CV) and differential pulse voltammetry (DPV) have been used.

Electrochemical techniques are based on the possibility of studying electron transfer reactions between an electrode and a molecule in solution. By applying an external voltage it is possible to tune the virtual Fermi level of the electrode (a metal or more generally a conductor) thus allowing a "communication" with the electronic levels of the molecule in solution. This "communication" consists of a chemical reaction of the molecules in solution undergoing either oxidation (anodic process) or reduction (cathodic process) which is detected as a current. Considering a general reduction reaction (eq 16) occurring at the interface between the electrode and the solution, in order to measure a current it is necessary that A_{ox} reaches the electrode and accepts electrons from it.

$$A_{ox} + n\,e^- \rightarrow A_{red} \qquad (16)$$

Therefore the electron transfer process at the interface is controlled by two kinetic factors: (i) the rate of diffusion (v_d) of A_{ox} to the electrode/solution interface and (ii) the rate of electron exchange (v_e) between the electrode and A_{ox}. For simple electron transfer reactions, the situation $v_e >> v_d$ is often encountered, therefore the observed current is only dependent on the diffusion process of the analyte to the electrode.

Electrochemical measurements were carried out with a PC-interfaced *Eco Chemie Autolab/Pgstat 30* Potentiostat. A conventional three-electrode cell assembly was adopted: a saturated calomel electrode (SCE *Amel*) and a platinum electrode, both separated from the test solution by a frit, were used as reference and counter electrodes, respectively; a glassy carbon (GC) electrode was used as the working electrode. In a typical experiment argon-purged solutions of the sample (10^{-3}-10^{-4} M) in the presence of a supporting electrolyte (typically 0.1 M) were analyzed. In several cases a small amount of ferrocene was also added to the solution as internal standard to which redox potentials were referred.

In both techniques (CV and DPV) a voltage E is applied between the working electrode and the counter electrode (measured with respect to the reference electrode) and varied as a function of time t. A current i is measured at each potential value: the result is a voltammogram which is a plot of the current i *vs.* potential E.

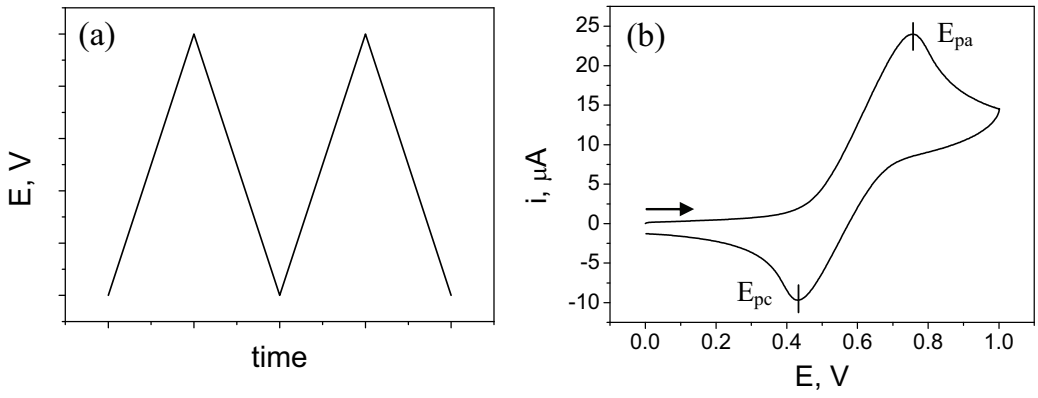

Fig. 2.4. Cyclic voltammetry (CV): (a) variation of the potential E as a function of time t (two cycles) and (b) example of a voltammogram obtained by CV.

In cyclic voltammetry (CV) the voltage E is varied linearly with time t between two potential values (Figure 2.4a), the scan rate is preset at the beginning of the experiment. In Figure 2.4b a typical voltammogram is reported representing the plot of the current i *vs.* the

applied potential E, in which two main features can be distinguished. Upon anodic scan (*i.e.*, from negative to positive potentials) a positive wave is observed, ascribable to the oxidation of the analyte at the electrode/solution interface, featuring an anodic peak potential E_{pa}. Upon reversed scan (cathodic scan) a negative wave with a cathodic peak potential E_{pc} is detected, due to the reduction reaction. Important information on the thermodynamic properties of the investigated system can be obtained by cyclic voltammetry. In fact, if the redox process is reversible the cathodic and anodic peak potentials should follow the relationship reported in eq 17 (true for monoeletronic processes, $n = 1$ in eq 16).

$$E_{pa} - E_{pc} = 0.059 \text{ V} \tag{17}$$

When these conditions are matched, according to eq 18 it is possible to calculate, with reasonably good approximation, the formal redox potential $E°$ of the redox couple in analysis.

$$E° \approx E_{1/2} = ½ (E_{pa} + E_{pc}) \tag{18}$$

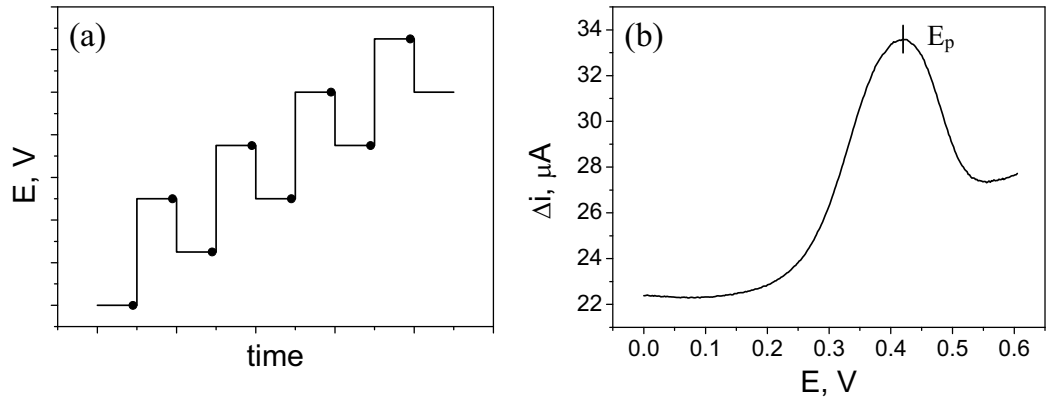

Fig. 2.5. Differential pulse voltammetry (DPV): (a) variation of the potential E as a function of time t (black dots, sampling time) and (b) example of a voltammogram obtained by DPV.

As regarding differential pulse voltammetry (DPV), potential pulses with fixed pulsewidth are superimposed to a linear sweep potential scan (Figure 2.5a). The current values before and after the pulses (see black dots in Figure 2.5a) are taken and their difference is plotted versus the potential yielding the voltammogramm (Figure 2.5b), a wave featuring a peak potential E_p. Reversible processes display symmetric peaks in DPV and from the E_p value the formal redox potential can also be calculated according to eq 19 (true for monoeletronic processes, $n = 1$ in eq 16), where ΔE is the potential pulsewidth.

$$E^\circ \approx E_{1/2} = E_p + \tfrac{1}{2}\,\Delta E \qquad (19)$$

While the reversibility of a process can be better discerned by means of CV, the very great advantage in the use of DPV is that it permits, comparing to CV, a better resolution of redox processes occurring at similar potentials.

2.4 Spectroelectrochemical techniques

Spectroelectrochemistry is a powerful technique combining stationary UV-Vis absorption spectroscopy and electrochemistry. This is employed quite commonly to obtain the absorption spectra of oxidized or reduced species of compounds displaying reversible redox behavior. These oxidized/reduced species are generated *in situ* upon application of an electrochemical potential directly in a spectrophotometric cell.

The spectroelectrochemistry measurements were carried out on a *Jasco V-570 UV/Vis/NIR* spectrophotometer. For this purpose, sample solutions in the presence of a supporting electrolyte were transferred into a thin-layer OTTLE (Optical Transparent Thin Layer Electrochemical) cell with an optical path of 0.1 cm, with a platinum mini-grid as the working electrode, a platinum wire as the counter electrode and a silver wire as a quasi-reference electrode. Electrodes are connected to an *Amel 552* potentiostat.

2.5 Photolysis apparatus and gas detection

The hydrogen evolving activity of the investigated systems upon continuous visible irradiation was studied employing a photolysis apparatus interfaced with a gas chromatograph (GC) for the detection and the quantification of the amount of hydrogen produced. The instrumental setup is schematized in Figure 2.6.

The hydrogen evolution experiments were carried out upon continuous irradiation with a 175 W xenon *CERMAX* arc-lamp, a cut-off filter at 400 nm was put between the lamp and the reactor in order to remove the UV component of the xenon emission. The reactor (see a picture in Figure 2.7) is a 10 mm pathlength Pyrex glass cuvette containing the solution (typically 5 mL) with head space obtained from a round-bottom flask.

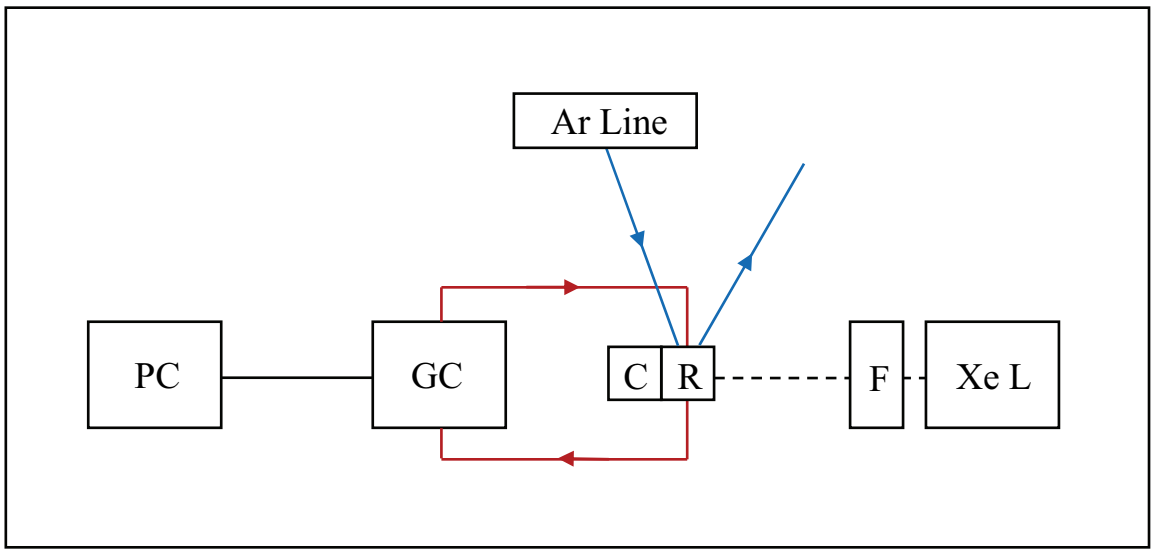

Fig. 2.6. Schematic layout of the photolysis and gas detection setup: black dashed line, white light; blue line, Ar flow for the purging procedure; red line, gas inlet and vent; Xe L, xenon arc lamp; F, cut-off filter; R, reactor; C, cooling system; GC, gas chromatograph; PC, personal computer.

The measuring cell is sealed during the photoreaction: the head to which cell is attached has indeed four ports, closed with Swagelok® connections, two of them are part of a closed loop involving GC gas inlet and sample vent in order to analyze head space content without an appreciable gas consumption, and the other two are for the degassing procedure (input and output). In order to avoid warming effects due to the IR component of the xenon emission the reactor is thermostated at 15°C during the whole photolysis.

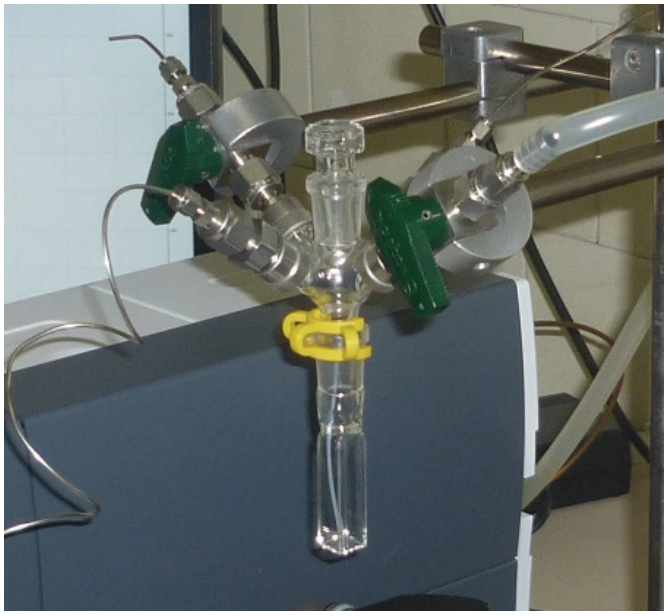

Fig. 2.7. Picture of the reactor where photolysis experiments were conducted.

The gas phase of the reaction vessel was analyzed on an *Agilent Technologies* 490 microGC equipped with a 5 Å molecular sieve column (10 m), a thermal conductivity detector, and using Ar as carrier gas (kept at a pressure of 550 kPa at the injector level). In a typical experiment 5 mL from the headspace of the reactor are sampled by the internal GC vacuum pump (flow rate 30 mL/min) and used to fill a built-in 10 μL loop. At this stage 200 nL are then injected in the column maintained at 60°C for separation and detection of gases. The unused gas sample is then reintroduced in the reactor in order to minimize its consumption along the whole photolysis. The sampling process and the data analysis are provided by a computer-controlled *Agilent EZChrom Elite* software routine.

The amount of hydrogen was quantified through the external calibration method. This procedure was performed, prior to analysis, through a galvanostatic (typically 1 mA) electrolysis of a 0.1 M H_2SO_4 solution in an analogous cell (same volume) equipped with two Pt wires sealed in the glass at the bottom of the cell. A 100% faradaic efficiency was assumed leading to a linear correlation between the amount of H_2 evolved at the cathode and the electrolysis time.

Chapter 3

Tetrametallic Polyoxometalate Water Oxidation Catalysts

This chapter is the result of a collaboration with the group of Prof. Marcella Bonchio at the Department of Chemical Sciences of the University of Padova. Parts of this chapter are published in the literature.[33,52,53]

3.1 Introduction

Oxidation of water to molecular oxygen is a key step common to most artificial photosynthetic reaction schemes.[3,54] It is a very complex process, involving the four-electron oxidation of two water molecules, the formation of a new oxygen-oxygen bond, and the release of four protons. As such, water oxidation is considered to be the real kinetic bottleneck towards artificial photosynthesis.[55] In recent years, substantial progress has been made in the development of catalysts for oxygen evolution. Current research is strongly involved in the study of heterogeneous systems such as colloidal metal oxides[56,57,58,59,60] and electrodeposited films.[61]

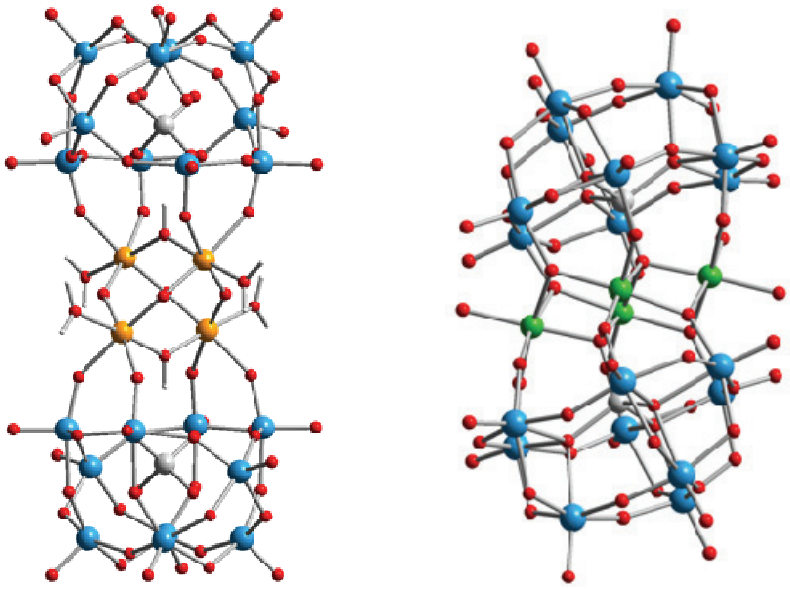

Fig. 3.1. Molecular water oxidation catalysts studied in this chapter: **Ru4POM** (left), **Co4POM** (right); atom legend: light blue, tungsten; red, oxygen; white, hydrogen; orange, ruthenium; green, cobalt; grey, silicon (left) or phosphor (right).

Molecular water oxidation catalysts,[33-39,62] have also found a considerable appeal, in particular because their redox and kinetic properties are, in principle, easily tunable by

molecular design with a wide choice of redox active metal centers and set of ligands. However, one of the mandatory requirements that an artificial device for water splitting has to match is the long-term durability of all its components. This opens a serious issue, since many of the molecular catalysts proposed to date fail to resist under the harsh oxidizing conditions needed to perform water oxidation. Self-oxidation of the organic ligand set is indeed one of the major causes of catalyst degradation and consequent loss of catalytic activity.

A number of tetra-metallic molecular catalysts, bearing structural affinity to the oxygen evolving center (OEC) of photosystem II,[24] have recently been reported.[63,64,65,66,67] By virtue of their robustness when exposed to the harsh conditions of oxygen evolution catalysis, all-inorganic polyoxometalates (POMs) embedding a multi-redox tetrametallic core are receiving great attention. Two of such systems, $[Ru_4(\mu\text{-}O)_4(\mu\text{-}OH)_2(H_2O)_4(\gamma\text{-}SiW_{10}O_{36})_2]^{10-}$ (**Ru4POM**, Figure 3.1, left)[63,64] and $[Co_4(H_2O)_2(\alpha\text{-}PW_9O_{34})_2]^{10-}$ (**Co4POM**, Figure 3.1, right),[66,68] have been synthesized and used in homogeneous water oxidation with strong chemical oxidants (dark cycles)[63a,64a,66a] or in photocatalytic cycles employing sacrificial electron acceptors.[64b,66b,69]

In a standard homogeneous photocatalytic cycle (Figure 3.2), a strong oxidant (P^+) is irreversibly generated by reaction of an excited photosensitizer (P) and a sacrificial electron acceptor (S) that decomposes upon reduction. The photocatalytic mechanism leading to water oxidation is generally assumed to involve four sequential hole-transfer steps from the photochemically oxidized sensitizer to the catalyst, which then evolves to a series of high valent intermediates, capable of water oxidation.

In oxygen evolution studies reported to date, relevant practical parameters, such as chemical and quantum yields, turnover numbers (TON) and frequencies (TOF), have been determined to evaluate the overall system performance. Very rarely, however, time-resolved techniques have been applied to the detection of elementary processes and transient intermediates.[59b,70] Time-resolved techniques can provide kinetic information of great importance for the optimization of oxygen-evolving sacrificial cycles and, in perspective, of photochemical water splitting systems. In principle, the rates of hole transfer from the oxidized sensitizer (S^+) to the catalyst along its evolution pathway (C, C^+, …C^{4+}) can be measured by appropriate laser flash photolysis experiments. In sacrificial cycles, as represented in Figure 3.2, the oxidized sensitizer is irreversibly produced so that, in principle, very fast hole transfer is not a strict requirement. In practice, however, the sensitizers, in their oxidized form, are often unstable under the reaction conditions used,[59a,71] and fast hole scavenging is pivotal to minimize their decomposition (usually the main limiting factor in terms of turnover performance). On the other hand, fast hole-transfer rates will become

absolutely crucial in regenerative systems where the catalyst must be able to scavenge the hole on the photogenerated oxidant in competition with charge recombination.

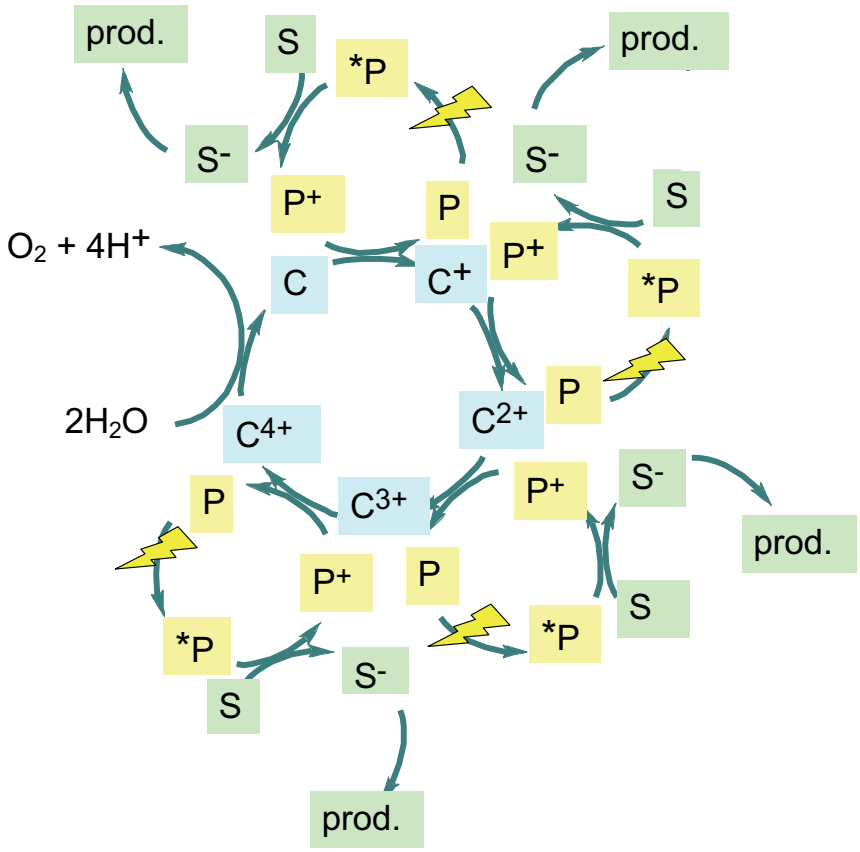

Fig. 3.2. Sequential electron transfer mechanism for oxygen evolution in a sacrificial cycle involving a photosensitizer (P), a sacrificial electron acceptor (S) and a tetrametallic catalyst (C).

In this chapter time-resolved techniques have been applied in systems involving **Ru4POM** and **Co4POM** as molecular catalysts, $Ru(bpy)_3^{2+}$ (bpy = 2,2'-bipyridine) as photosensitizer, and persulfate ($S_2O_8^{2-}$) as sacrificial electron acceptor in order to get information on the interactions between the catalysts and the sensitizer in solution, important for the optimization of the photocatalytic conditions, and to study the electron transfer processes from the photogenerated oxidant to the catalyst. While in the case of **Ru4POM** time-resolved techniques permit a thorough investigation of the light-induced and thermal processes (and their kinetics) within the sacrificial photocatalytic cycles described above, in the case of **Co4POM** these types of experiments will shine light on the actual behavior of this compound in homogeneous light-driven water oxidation.

3.2 Experimental section

3.2.1 Synthesis

The synthesis of the tetraruthenium polyoxotungstate **Ru4POM** was performed by Dr. Andrea Sartorel (Department of Chemical Sciences, University of Padova) following literature procedures.[63a] 262 mg (0.36 mmol) of $K_4Ru_2OCl_{10}$ were dissolved in 30 mL of deionized water; 1 g (0.34 mmol) of $K_8\gamma$-$SiW_{10}O_{36}\cdot 12H_2O$, was then added. The dark-brown solution was kept at 70°C for 1 h, then allowed to cool at room temperature and filtered. Excess of CsCl (4.4 g) was added to precipitate **Ru4POM** as cesium salt. This latter was transformed into the sodium salt by ion-exchange chromatography; the crude sodium salt is then purified by exclusion dimensional chromatography; total yield = 80%. The synthesis of the tetracobalt polyoxotungstate **Co4POM** was performed by Dr. Serena Berardi (Department of Chemical Sciences, University of Padova) following literature procedures.[66a] 35.6 g of $Na_2WO_4\cdot 2H_2O$ (108 mmol), 3.22 g of $Na_2HPO_4\cdot 7H_2O$ (12 mmol) and 6.98 g of $Co(NO_3)_2\cdot 6H_2O$ (24 mmol) were added to 100 mL of water. The pH was adjusted to 7.8, with the solution still being turbid, and then refluxed for two hours. After reflux, NaCl was added to achieve 3 M concentration. Crystals were collected after few hours. Thermogravimetric analysis evidences 24 water molecules of hydration.

3.2.2 Apparatus and procedures

Reagents were used as received. Ultrapure milli-Q water and related buffer solutions were used. See Chapter 2 for any details regarding the spectroscopic apparatus employed for the characterization of the systems.

3.3 Tetraruthenium polyoxotungstate catalyst (Ru4POM)

3.3.1 Background on Ru4POM

The X-ray characterization[63a] of **Ru4POM** (Figure 3.1, left) established the adamantane-like structural motif of the ruthenium-oxo core, that poses analogies with the natural OEC,

with four redox active transition metals, connected through μ-oxo or μ-hydroxo bridges, while maintaining available coordination sites.

Electrochemical characterization of **Ru4POM** in aqueous acidic solution shows several equally spaced (ca. 0.2 V) redox processes in the −0.5 / 1.0 V *vs.* SCE range.[63] **Ru4POM**, which as a sodium salt has the tetraruthenium core in a (IV,IV,IV,IV) state, is found to be present as a paramagnetic species in aerated conditions both at acidic and at neutral pH.[63] According to the electrochemical assignments, this paramagnetic species can be likely identified as the (V,IV,IV,IV) single-oxidized state of the tetraruthenium core.

The activity of **Ru4POM** as water oxidation catalyst was evident from simple cyclic voltammetry experiments, where the catalytic wave due to water oxidation appears at low overpotentials (η = 0.35 V), over a broad pH range (ca. 1 to 7).[63a,64b] Outstanding water oxidation activity was also shown under dark conditions in the presence of chemical oxidants such as Ce(IV) or $Ru(bpy)_3^{3+}$, at pH 0.6 and 7, respectively, where **Ru4POM** was found to catalyze oxygen evolution from water with multiple turnover numbers (up to 500) and notable turnover frequencies (up to 0.60 s^{-1}).[63a,64b] Together with a thorough spectroscopic characterization (UV-vis and rRaman)[63b] of some relevant intermediates, these results allowed to elucidate some key features of the catalytic mechanism of **Ru4POM**.

Interestingly, highly efficient oxygen evolving anodes were developed by supporting **Ru4POM** onto a conductive bed of either multi-walled carbon nanotubes[72,73,74] or graphene[75,76] with the resulting hybrid material being drop-casted onto indium tin oxide plates. Efficient functionalization was achieved by exploiting electrostatic interactions between polyanionic **Ru4POM** and cationic pendant arms anchored onto the carbonaceous material.

Ru4POM exhibits outstanding catalytic performance also in light-driven water oxidation, in the presence of a $Ru(bpy)_3^{2+}$ photosensitizer and a sacrificial electron acceptor such as persulfate anion. At neutral pH (7.2, phosphate buffer) and under visible light illumination (420 - 550 nm) dioxygen is rapidly formed, accompanied by stoichiometric persulfate consumption, achieving TON up to 350 with a quantum yield of 0.045.[64b] A strong improvement in terms of quantum efficiency of the process (Φ = 0.3, corresponding to an overall efficiency of 60%) was then obtained by using a tetranuclear dendritic photosensitizer $Ru\{(\mu\text{-dpp})Ru(bpy)_2\}_3^{8+}$ instead of $Ru(bpy)_3^{2+}$.[69a]

As a final remark, by still exploiting electrostatic interactions, **Ru4POM** was also supported on sensitized semiconductor surface based on TiO_2 and a ruthenium(II) sensitizer in a photoelectrochemical cell configuration.[70,77] Fast hole-transfer processes from the

photogenerated oxidant (obtained after electron injection in the conduction band of the titania) to the teteraruthenium catalyst were observed by means of laser techniques.[70] Upon continuous visible irradiation, however, very low photocurrents (ca. 15 μA/cm^2) corresponding to internal quantum efficiency of 0.2% were measured.[77]

The tremendous efforts in the use of **Ru4POM** as water oxidation catalyst, in particular in light-activated experiments, stimulated this study, with the aim of investigating in more detail photoinduced and thermal processes (and their kinetics) within the **Ru4POM**/$Ru(bpy)_3^{2+}$/ $S_2O_8^{2-}$ system.

3.3.2 Results and discussion

Given the high negative charge (10−), **Ru4POM** is expected to be involved in ionic associations (ion-pairs) with the dicationic $Ru(bpy)_3^{2+}$ when both compounds are introduced in water. As a matter of fact, in an aqueous solution containing 50 μM $Ru(bpy)_3^{2+}$ and 50 μM **Ru4POM**, the emission of the sensitizer is completely quenched.

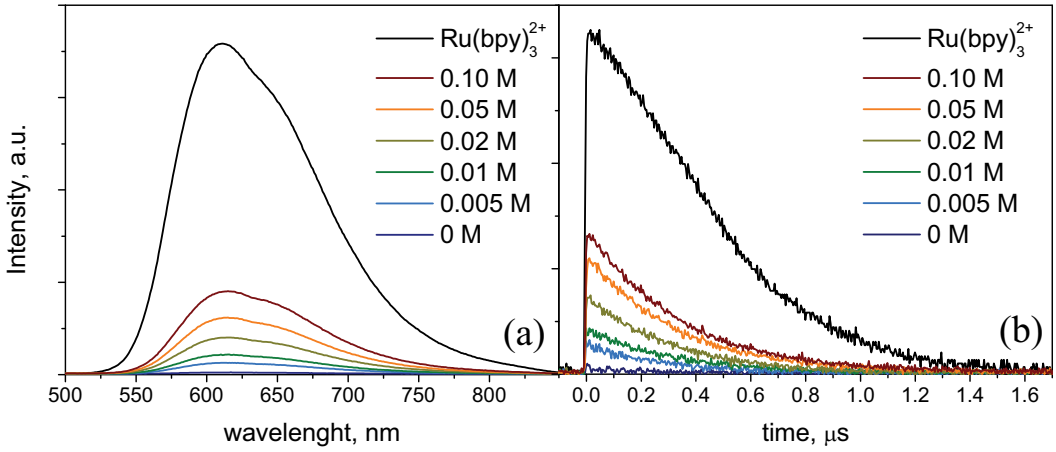

Fig. 3.3. De-quenching" of the $Ru(bpy)_3^{2+}$ emission upon addition of Na_2SO_4 to an aqueous solution containing 50 μM $Ru(bpy)_3^{2+}$ and 50 μM **Ru4POM**. Results of stationary (a, excitation at 450 nm) and time-resolved experiments (b, excitation at 355 nm). Data corrected for the inner filter effect of **Ru4POM** at the excitation wavelength.[63b] The black curves refer to 50 μM $Ru(bpy)_3^{2+}$ (neither catalyst nor salt added).

The quenching process takes place within sensitizer-catalyst ion-paired species, as demonstrated by the "de-quenching" effect of ionic strength: the $Ru(bpy)_3^{2+}$ emission builds up when Na_2SO_4 is added to the solution (Figure 3.3a). The constant lifetime of the growing emission (ca. 400 ns), coincident with that of free $Ru(bpy)_3^{2+}$ in aerated water solution (Figure

3.3b) demonstrates the static nature of the quenching process. As to the nature of the ion-paired species, the presence in solution of **Ru4POM**, $Ru(bpy)_3^{2+}$, and their counterions (Na^+ and Cl^-, respectively) likely leads to a complex distribution of variously ion-paired species. Fluorescence titration of $Ru(bpy)_3^{2+}$ with **Ru4POM** (Figure 3.4) and conductometric titration of **Ru4POM** with $Ru(bpy)_3^{2+}$ (Figure 3.5) can be used to monitor this type of aggregation in aqueous solutions. Both measurements indicate the formation of aggregates with an average [**Ru4POM**]:[$Ru(bpy)_3^{2+}$] ratio close to 1:4.

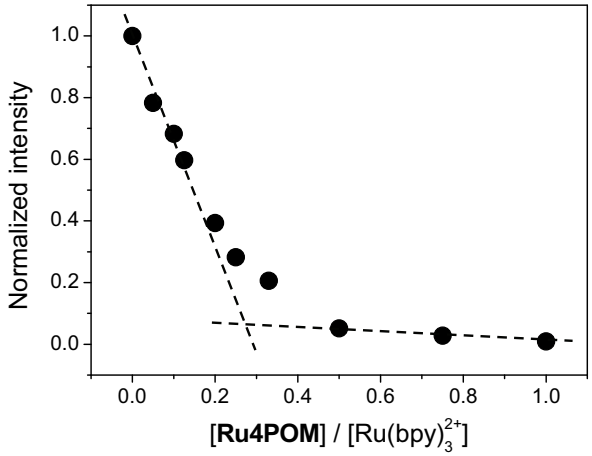

Fig. 3.4. Fluorimetric titration (excitation at 450 nm) of 50 μM $Ru(bpy)_3^{2+}$ with **Ru4POM** in water.

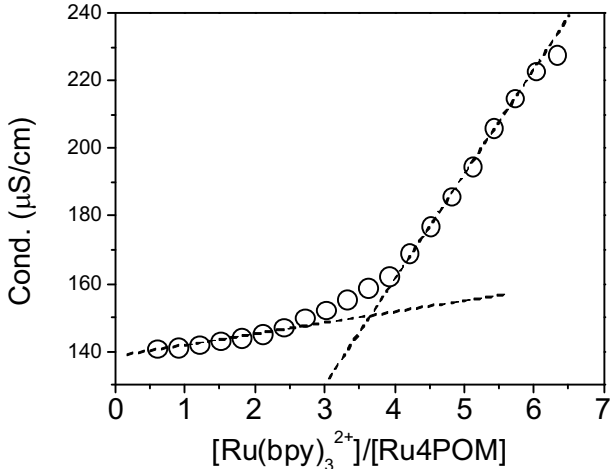

Fig. 3.5. Conductometric titration of 50 μM **Ru4POM** with $Ru(bpy)_3^{2+}$ in water.

The quenching process taking place within sensitizer/catalyst ion pairs can be conveniently monitored by ultrafast spectroscopy (Figure 3.6). The initial spectrum, with bleaching of the ground-state MLCT band at 450 nm and weak, broad, positive absorption at $\lambda > 530$ nm, is the typical spectrum of the $Ru(bpy)_3^{2+}$ MLCT excited state.[78] The subsequent spectral changes

are clearly biphasic. In the first few picoseconds, the positive absorption disappears while the bleach remains almost constant (Figure 3.6a). Then, the bleach disappears completely, decaying smoothly to the baseline (Figure 3.6b). The time constant of the first process is ca. 2 ps; the second decay has a complex kinetic, requiring at least two time constants (ca. 15 and 150 ps) for a reasonable fit.

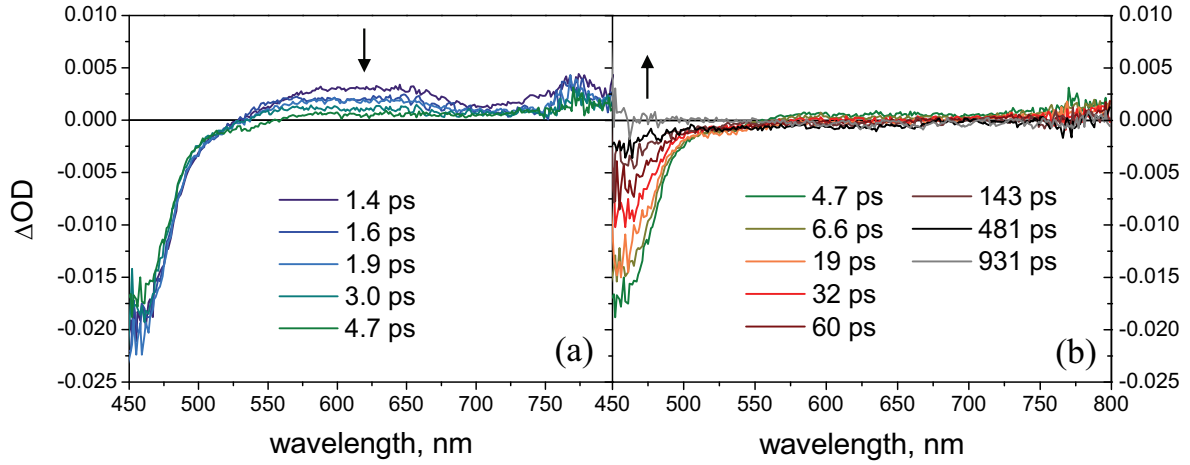

Fig. 3.6. Ultrafast spectroscopy (excitation at 400 nm) of an aqueous solution containing 0.2 mM $Ru(bpy)_3^{2+}$ and 0.2 mM **Ru4POM**; (a) 1.4-4.7 ps and (b) 4.7-931 ps.

As regarding the mechanism, the spectral changes are compatible with a fast oxidative quenching of the triplet MLCT excited state by the catalyst, with formation of the oxidized sensitizer, featuring MLCT bleach and no additional absorption in the visible, and reduction of the **Ru4POM** catalyst, followed by charge recombination. The tetrametallic core has indeed several reduction steps[79] which can be accessible to make oxidative quenching thermodynamically feasible.

The formation of ion pairs between $Ru(bpy)_3^{2+}$ and **Ru4POM**, with ultrafast quenching of the sensitizer excited state, is relevant to the use of these units in sacrificial cycles, which require an efficient reaction of the excited sensitizer with the sacrificial acceptor. In fact, complications inherent to ion-pair formation clearly show up (see below) in laser flash photolysis experiments intended to measure rates of hole transfer between the oxidized sensitizer and the catalyst. In these experiments, a given concentration of oxidized sensitizer is generated "instantaneously" (*i.e.*, within 10 ns) by photoreaction of the sensitizer with the sacrificial acceptor, and its re-reduction by the catalyst can be monitored in time over a relatively wide window (0-100 ms). In the experiment illustrated in Figure 3.7, aqueous solutions containing 50 μM $Ru(bpy)_3^{2+}$, 5 mM $Na_2S_2O_8$, and 80 mM phosphate buffer at pH 7 are excited with 8-ns pulses of 355-nm light, and the disappearance of $Ru(bpy)_3^{3+}$ is

monitored as a function of the concentration of **Ru4POM** (varied in the range 0-50 μM). The evident qualitative result is that $Ru(bpy)_3^{3+}$ (as monitored by the bleach at 450 nm) is reduced back to $Ru(bpy)_3^{2+}$ with kinetics dependent on the catalyst concentration. The bimolecular hole-transfer rate constant k can be easily calculated from the decays at high catalyst concentrations (≥ 25 μM, traces shown in Figure 3.7b and omitted for clarity in Figure 3.7a) where the kinetics of recovery becomes pseudo-first order. In these kinetic conditions ([**Ru4POM**] >> $[Ru(bpy)_3^{3+}]$) the rate of the process can be written as in eq 20. The pseudo-first order rate constant k_{obs} can be then calculated from the bleach recovery at 450 nm (where ΔOD is proportional to $[Ru(bpy)_3^{3+}]$, eq 15) according to eq 21, whose value can be divided by the concentration of **Ru4POM** thus obtaining k (eq 22).

$$v = k\,[Ru(bpy)_3^{3+}][\mathbf{Ru4POM}] = k_{obs}\,[Ru(bpy)_3^{3+}] \qquad (20)$$

$$[Ru(bpy)_3^{3+}] = [Ru(bpy)_3^{3+}]_0 \exp(-k_{obs}\,t) \qquad (21)$$

$$k_{obs} = k\,[\mathbf{Ru4POM}] \qquad (22)$$

The high value obtained (k = 3.6 ± 0.1 × 10^9 $M^{-1}s^{-1}$) confirms that the molecular catalyst **Ru4POM** is superior, in this respect, to some of the best colloidal catalysts, such as, *e.g.*, IrO_x (for which values of the order of 10^6 $M^{-1}s^{-1}$ have been measured).[59] All the kinetic experiments have been shown to give identical results using freshly prepared (experiment performed within 1 min after dissolution) or aged (up to 3 h) **Ru4POM** solutions.

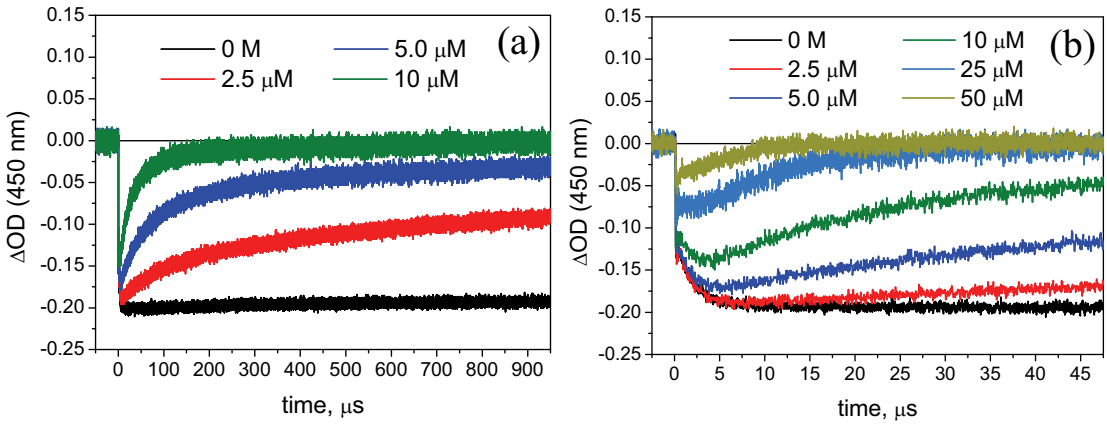

Fig. 3.7. Flash photolysis of aqueous solutions containing 50 μM $Ru(bpy)_3^{2+}$, 5 mM $Na_2S_2O_4$, 80 mM phosphate buffer (pH 7), and variable concentrations of **Ru4POM** (0-50 μM). Excitation with 8-ns pulses of 355-nm light. (a) Full time scale (0-1 ms); (b) details of the early time scale (0-47 μs).

Some intriguing aspects are revealed by the laser flash photolysis results, however, when the early time scale of the experiment is zoomed on (Figure 3.7b). In the absence of **Ru4POM**, the formation of $Ru(bpy)_3^{3+}$, clearly exhibits a prompt and delayed component of almost equal amplitude, the former corresponding to the primary photoreaction between the excited $Ru(bpy)_3^{2+}$ and $S_2O_4^{2-}$ (occurring within the laser flash, *i.e.*, few ns) and the latter to the secondary dark reaction[80] between the oxidizing SO_4^{-} radical anion and $Ru(bpy)_3^{2+}$ (estimated bimolecular rate constant $k = 1.1 \times 10^{10}$ $M^{-1}s^{-1}$). The addition of the catalyst, besides speeding up the disappearance of $Ru(bpy)_3^{3+}$ in the long time scale (Figure 3.7a), has also pronounced effects on its formation (Figure 3.7b). In particular, as the concentration of **Ru4POM** is increased (i) the amount of $Ru(bpy)_3^{3+}$ formed promptly undergoes a strong decrease and (ii) the secondary process becomes less and less efficient (and practically disappears for 50 μM **Ru4POM**). The reason for the first effect lies in the above described ion pairing phenomenon, which, although less pronounced than in pure water, is still effective in concentrated aqueous buffer solution: only the fraction of sensitizer which is not ion-paired with (and thus quenched by) **Ru4POM** can react with the persulfate yielding the $Ru(bpy)_3^{3+}$ oxidant. This conclusion can also be checked quantitatively considering the amount of free sensitizer detectable by emission spectroscopy at the different **Ru4POM** concentration used in the laser flash photolysis experiments (Figure 3.8a) by comparison with the efficiency of the quenching by persulfate (Figure 3.8b).

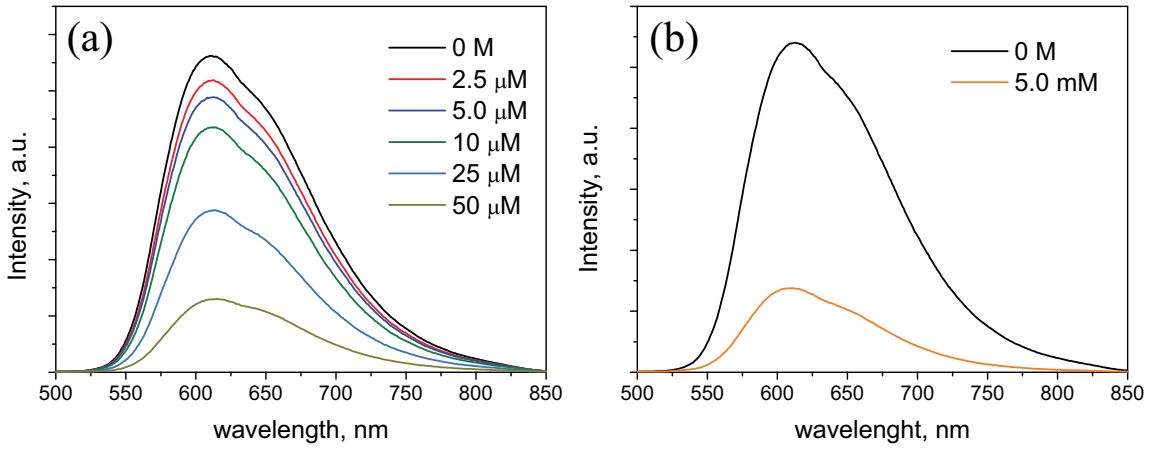

Fig. 3.8. Photoluminescence spectra (excitation at 450 nm) of aqueous solutions containing (a) 50 μM $Ru(bpy)_3^{2+}$, 80 mM phosphate buffer (pH 7), and variable concentrations of **Ru4POM** (0-50 μM, inner filter correction applied) and (b) 50 μM $Ru(bpy)_3^{2+}$, 80 mM phosphate buffer (pH 7) and 0-5 mM $Na_2S_2O_8$.

The reason for the second observation is that, when the **Ru4POM** concentration increases, the strongly oxidizing SO_4^{-} radical reacts directly with the catalyst instead of with $Ru(bpy)_3^{2+}$. This effect, while diminishing the amount of photogenerated $Ru(bpy)_3^{3+}$, is not detrimental from the photocatalytic viewpoint, as it consists of a direct oxidation of the **Ru4POM** catalyst. The rate of the electron transfer from the SO_4^{-} radical to the catalyst can be estimated to be ca. five times higher than the rate of the electron transfer to the photosensitizer (*i.e.*, ca. 5×10^{10} $M^{-1}s^{-1}$), considering that an apparent 50% competition between the two pathways takes place when the **Ru4POM** concentration is 10 μM (Figure 3.7b).

The complex set of processes is summarized in Figure 3.9.

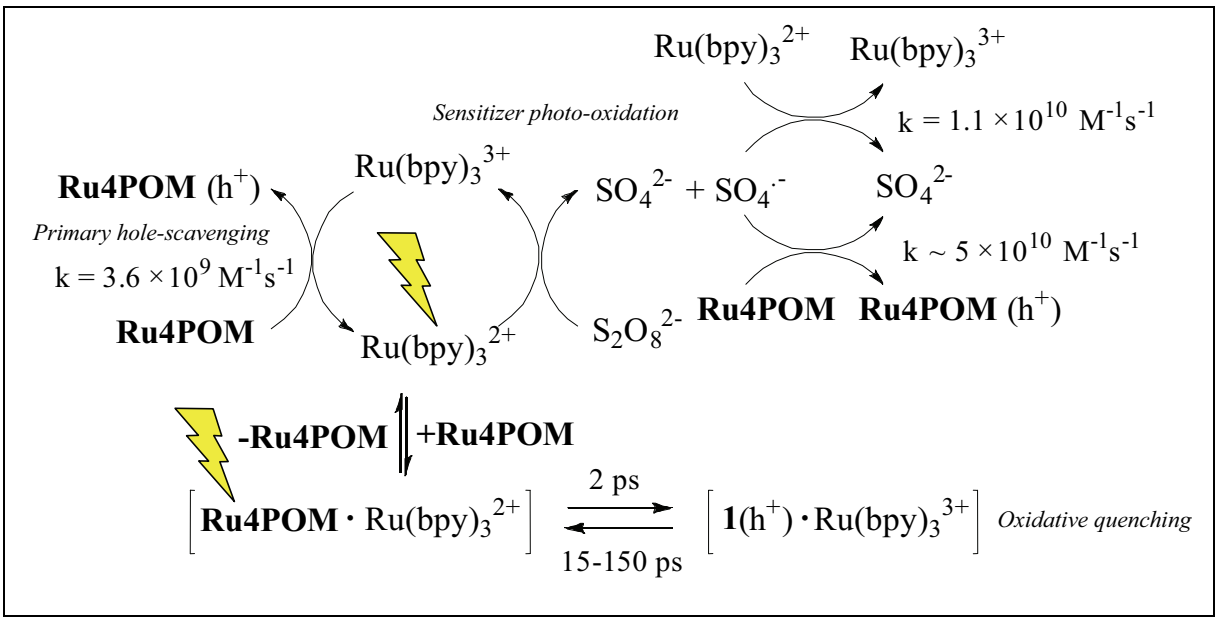

Fig. 3.9. Summary of the light-induced and thermal processes with related kinetics occurring in the **Ru4POM**/$Ru(bpy)_3^{2+}$/$S_2O_8^{2-}$ system.

Interesting observations can be made when the data in Figure 3.7a are considered from a quantitative viewpoint. The concentration of photogenerated $Ru(bpy)_3^{3+}$ (calculated according to eq 15 considering a $\Delta\varepsilon$ = 13,000 $M^{-1}cm^{-1}$ at 450 for such a species and an instrumental correction parameter of 0.74, obtained with the saturation technique) is in the range of 14-20 μM depending on the catalyst concentration (due to ion-pairing phenomena). This means that 2.5 μM and 5.0 μM **Ru4POM** are able to reduce 10 and 14 μM $Ru(bpy)_3^{3+}$, respectively. This clearly means that in the time window of the laser flash photolysis experiment a single catalyst molecule undergoes several (ca. 4) consecutive hole-transfer steps which amounts to

say that in these conditions the whole 4-h^+ charging sequence of the catalyst (Figure 3.2) takes place in about one millisecond.

By further pushing up the initial concentration of $Ru(bpy)_3^{3+}$ (using 0.1 mM $Ru(bpy)_3^{2+}$ solution and increasing laser power, Figure 3.10a) or by lowering the concentration of **Ru4POM** (Figure 3.10b), it is possible to enter a catalytic domain. It can be indeed observed that the amount of recovered $Ru(bpy)_3^{2+}$ far exceeds the value of 4, which means that not only the whole charging sequence, but also the discharge of the C^{4+} catalyst by water oxidation takes place efficiently within a time window of 40 ms. For instance, 2.5 μM **Ru4POM** reduces ca. 44 μM $Ru(bpy)_3^{3+}$, meaning that ca. 18 holes are transferred per catalyst molecule. It is therefore possible to estimate turnover numbers (TON) for oxygen evolution after 40 ms, assuming a unitary yield of oxygen formation, as defined in eq 23.

$$TON = \frac{1}{4}\frac{\Delta[Ru(bpy)_3^{3+}]}{[\mathbf{Ru4POM}]} \qquad (23)$$

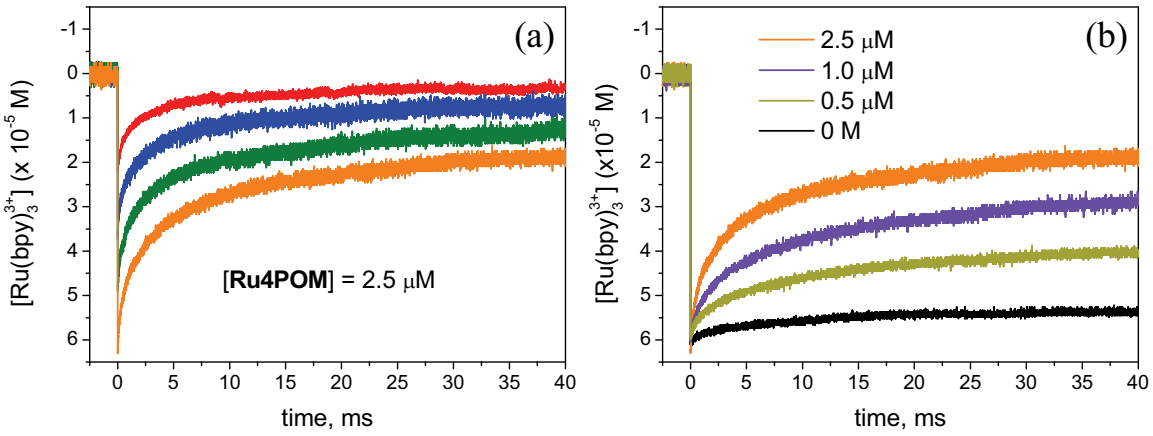

Fig. 3.10. Reduction of photogenerated $Ru(bpy)_3^{3+}$ (from bleach recovery at 450 nm) by **Ru4POM**. (a) [**Ru4POM**] = 2.5 μM, initial concentration of $Ru(bpy)_3^{3+}$ varied in the range 22-63 μM with increasing laser power, (b) initial $[Ru(bpy)_3^{3+}]$ = 63 μM, [**Ru4POM**] varied in the range 2.5-0.5 μM (black trace: control experiment at initial $[Ru(bpy)_3^{3+}]$ = 63 μM in the absence of **Ru4POM**).

The results can be summarized as follows: [**Ru4POM**] = 2.5 μM, TON (40 ms) = 4.4; [**Ru4POM**] = 1.0 μM, TON (40 ms) = 8.6; [**Ru4POM**] = 0.5 μM, TON (40 ms) = 11.2. These numbers translate into very high values of average turnover frequency for oxygen formation, as defined in eq 24.

$$TOF_{av} = \frac{1}{4}\frac{\Delta[Ru(bpy)_3^{3+}]}{\Delta t\ [\mathbf{Ru4POM}]} \quad (24)$$

For instance, with [**Ru4POM**] = 0.5 μM, the TON obtained over 40 ms corresponds to the rather spectacular TOF_{av} value of 280 s^{-1}. This value should be taken with caution, since a unitary yield of oxygen formation was assumed and turnover frequencies depend heavily on the type of experiment (*e.g.*, use of chemical oxidant or photogenerated one and, in the latter case, generation by laser flash or continuous irradiation) and, for each type of experiment, on various experimental parameters (oxidant and catalyst concentrations, light intensity).

3.4 Tetracobalt polyoxotungstate catalyst (Co4POM)

3.4.1 Background on Co4POM

The X-ray structure of **Co4POM** has been known since the early 1970's.[68] It displays a belt of four Co(II) metal ions sandwiched between two lacunary $PW_9O_{34}^{9-}$ Keggin ligands and with two water molecules coordinated at the external cobalt centers.

In 2010, Hill and co-workers[66a] described the activity of **Co4POM** as a water oxidation catalyst, emphasizing its advantages of an all-inorganic system based on earth abundant metal. The catalyst was shown to give high performance in: (i) electrochemical experiments with large catalytic currents at low overpotential (E = 1.1 V *vs.* Ag/AgCl, pH 8),[66a] (ii) dark chemical oxidation with $Ru(bpy)_3^{3+}$ as oxidant where O_2 evolution from water at pH 8 was observed featuring 60% yield, 75 turnovers, and TOF = 5 s^{-1},[66a] and (iii) standard photocatalytic cycles (see Figure 3.2) using persulfate as a sacrificial electron acceptor and $Ru(bpy)_3^{2+}$ as a photosensitizer with TON up to 220, limited solely by depletion of the sacrificial electron acceptor.[66b] Several lines of experimental evidence were presented that **Co4POM** is a stable molecular water oxidation catalyst under turnover conditions and does not form either aqueous cobalt ions or cobalt hydroxide/oxide.[66a]

A strong caveat concerning the nature of the real water oxidation catalyst with this class of tetracobalt polyoxometalate ions was advanced more recently by Stracke and Finke.[81] The remarks were based on a detailed study of the behavior of **Co4POM** (sodium salt) as catalyst in electrochemical water oxidation at a glassy carbon electrode, in pH 8.0 sodium phosphate buffer. When a constant potential of 1.1 V *vs.* Ag/AgCl was applied to the cell, the oxidation

current increased rapidly and O_2 bubbles formed at the working electrode. Concomitant with the increase in current, however, a film of cobalt oxide (as identified by SEM and EDX) was deposited onto the glassy carbon electrode. The catalytic activity was maintained by the film even in the absence of **Co4POM**. Evidence for slow hydrolysis of **Co4POM** in pH 8.0 solution was obtained by complementary spectrophotometric and electrochemical techniques. The conclusion was that the active water oxidation catalyst was heterogeneous CoO_x formed, under the electrocatalytic conditions used, from Co(II) species released upon partial decomposition of **Co4POM**. From this viewpoint, **Co4POM** would be, rather than a molecular catalyst, a precursor of the active heterogeneous water oxidation catalyst.

While this evidence for the heterogeneous nature of the active catalyst is strong, it remained to be ascertained to what extent the cobalt oxide formation may be specific of the experimental electrocatalytic conditions used in that work,[81] with the decomposition of the polyoxometalate complex driven by anodic bias at the electrodic surface. In principle, therefore, the possibility cannot be excluded that **Co4POM** may behave as a genuine molecular water oxidation catalyst in different types of experiment, *e.g.*, with chemical oxidants such as $Ru(bpy)_3^{3+}$, either in dark[66a] or in photochemical experiments.[66b]

3.4.2 Results and discussion

In order to check whether **Co4POM** may behave as a competent water oxidation catalyst in homogeneous photocatalytic cycles involving $Ru(bpy)_3^{2+}$ as photosensitizer and persulfate as sacrificial electron acceptor, fast spectroscopic methods were used to follow the primary processes expected to initiate photocatalytic water oxidation, namely photogeneration of the oxidant and its consumption *via* primary hole-scavenging by the catalyst. As shown in the previous section, laser flash photolysis is a convenient technique to monitor this primary process.

Figure 3.11a shows the results obtained in the flash photolysis (excitation with 355-nm light, 8-ns pulses) of aqueous solutions containing 50 μM $Ru(bpy)_3^{2+}$, 5 mM $Na_2S_2O_4$, 80 mM phosphate buffer (pH 8). The black trace shows the constant bleach (*i.e.*, constant $Ru(bpy)_3^{3+}$ concentration) obtained in the absence of the catalyst. The other traces refer to solutions containing 50 μM **Co4POM** and measured at different time delays from **Co4POM** dissolution. All these solutions were prepared upon dilution of a 1 mM **Co4POM** mother solution in 80 mM phosphate buffer at pH 8, left aging in the dark. The presence of **Co4POM** is shown to lead to bleach recovery, *i.e.*, to disappearance of $Ru(bpy)_3^{3+}$ by hole scavenging.

The evident result, however, is that the hole-scavenging activity increases with aging time of the **Co4POM** solution.

Looking at the dependence of the amount of $Ru(bpy)_3^{3+}$ being reduced on the aging time (calculated according to eq 15, Figure 3.11b), it must actually be concluded that pristine **Co4POM** (*i.e.*, solution extrapolated at zero aging time) does hardly perform any hole scavenging from the oxidized sensitizer. Rather, some product forming in time from **Co4POM** is actually responsible for the observed reduction process. Moreover, the amount of $Ru(bpy)_3^{3+}$ being reduced in each experiment sets an upper limit to the concentration of the effective reductant present in solution, depending on whether the reduction is stoichiometric or catalytic. At 90 min aging time (Figure 3.11b) this value is ca. 10 μM, which, given the 50 μM nominal concentration, implies that a ≤ 20% decomposition of **Co4POM** takes place in 80 mM pH 8 phosphate buffer.

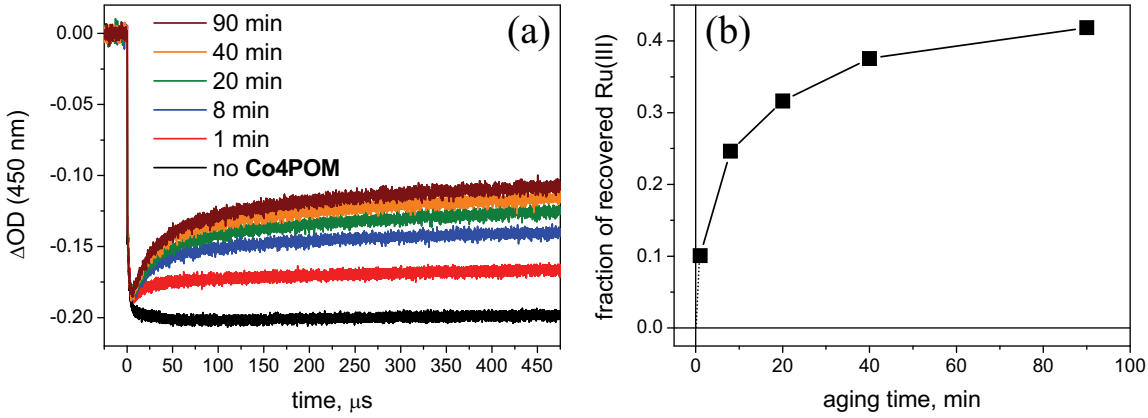

Fig. 3.11. (a) Hole scavenging kinetics measured using 50 μM solutions of **Co4POM** of various aging time. 1 min: solid catalyst dissolved in 80 mM phosphate buffer at pH 8 and measured immediately. 8-90 min: prepared from a 1 mM **Co4POM** mother solution in 80 mM phosphate buffer at pH 8 at various time intervals from dissolution; (b) amount of $Ru(bpy)_3^{3+}$ being reduced by 50 μM **Co4POM** after 450 μs as a function of the aging time of the solution used.

As to the nature of such an active product, free aqueous Co(II), an obvious candidate on the way to cobalt oxide formation, is ruled out by control experiments performed with $Co(NO_3)_2$, where no appreciable $Ru(bpy)_3^{3+}$ reduction takes place in this time scale, consistent with the intrinsic slowness of the Co(III)/Co(II) redox pair. Moreover dynamic light scattering (DLS) measurements on the probed solutions show the absence of appreciable amounts of colloidal oxide phases. Therefore, the most likely hypothesis is that of an earlier

decomposition product, possibly a partially dissociated cobalt polyoxometalate species of 2:1 Co:POM stoichiometry.[82]

The time-dependent reactivity of **Co4POM** with $Ru(bpy)_3^{3+}$ can be explained on thermodynamic grounds by cyclic voltammetry experiments (Figure 3.12). Immediately after its dissolution (ca. 1 minute), the cyclic voltammetry of **Co4POM** in 0.2 M phosphate buffer shows a small anodic wave at ca. 1.2 V *vs.* Ag/AgCl; in these conditions, the onset of a catalytic wave due to water oxidation is observed at higher voltage, corresponding to an overpotential higher than 0.7 V (Figure 3.12, red trace). The high potential of these events are then not compatible with that of $Ru(bpy)_3^{2+}/Ru(bpy)_3^{3+}$ (1.05 V *vs.* Ag/AgCl, Figure 3.12, green trace), therefore $Ru(bpy)_3^{3+}$ has not the thermodynamic power to oxidize **Co4POM**, neither to promote water oxidation catalyzed by **Co4POM**. Conversely, monitoring the cyclic voltammetry of **Co4POM** over time results in the onset of a catalytic wave due to water oxidation starting at 1.05 V (corresponding to an overpotential of ca. 0.5 V), increasing in intensity with aging time. This oxidation process is now thermodynamically accessible with $Ru(bpy)_3^{3+}$ as the oxidant, thus justifying the increase of the bleach recovery observed in laser flash photolysis experiments after prolonged aging of **Co4POM** (Figures 3.11).

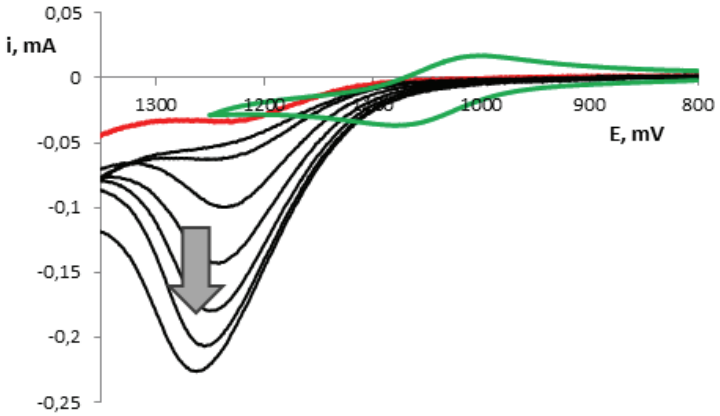

Fig. 3.12. Cyclic voltammetry of 2 mM **Co4POM** in 0.2 M phosphate buffer (pH 8) recorded at 1 (red trace), 4, 10, 20, 30, 40, 50 and 60 minutes after dissolution (black traces), and cyclic voltammetry of $Ru(bpy)_3^{2+}$ in the same media (green trace). Working electrode: glassy carbon; auxiliary electrode: platinum; reference electrode: Ag/AgCl.

Interestingly, the nature of the buffer plays an important role in the decomposition of **Co4POM**. In fact, both the recovery of the $Ru(bpy)_3^{2+}$ in flash photolysis experiments and the increase in intensity of the catalytic current are slowed down considerably if, instead of

phosphate buffer, the aging process takes place in borate buffer (Figure 3.13 and 3.14), indicating a slower decomposition of **Co4POM** in this medium.

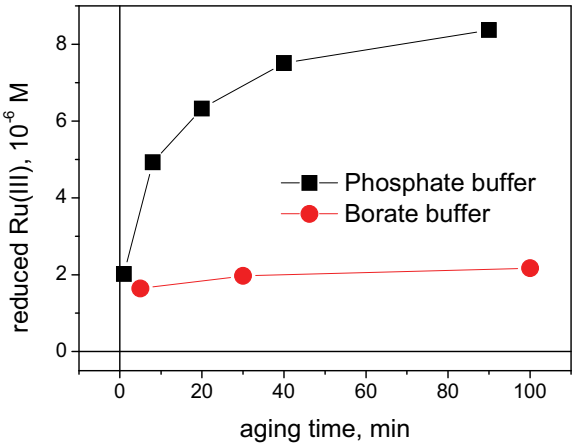

Fig. 3.13. Amount of $Ru(bpy)_3^{3+}$ being reduced by 50 μM **Co4POM** in laser flash photolysis after 450 μs as a function of the aging time of the solution used in 80 mM phosphate (black squares) and 80 mM borate (red dots) buffers (pH 8).

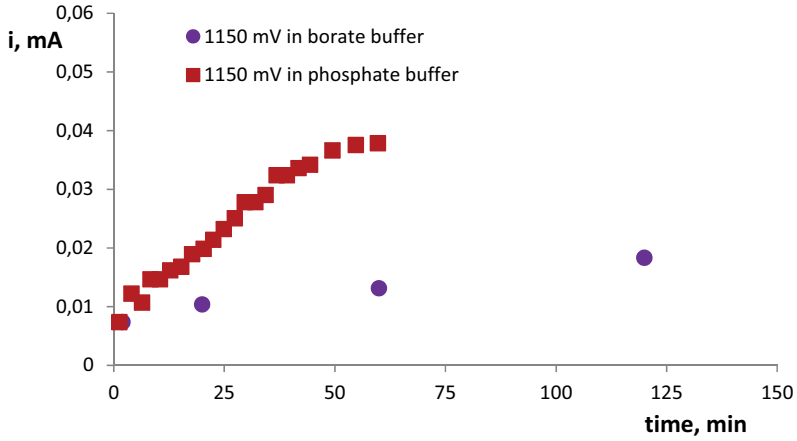

Fig. 3.14. Plot of the anodic current at 1150 mV *vs.* time observed in the CV of 2 mM **Co4POM** in 0.2 M phosphate (red squares) and borate (violet dots) buffers (pH 8).

The slower decomposition of **Co4POM** in borate buffer with the simultaneous observed low reactivity with the photogenerated $Ru(bpy)_3^{3+}$ oxidant seems to be in contrast with reports by Hill and coworkers[66b,c] where the best oxygen evolving activity of **Co4POM** was recorded in such an aqueous environment. It should be pointed out, however, that the laser flash photolysis experiments aim to study a simple primary process (reduction of $Ru(bpy)_3^{3+}$ by hole scavenging), whereas many other steps (photochemical and thermal) are involved in the

complex cycle for oxygen evolution. Thus, this apparent inconsistency might be related to the fact that in the photocatalytic cycle where persulfate is used as sacrificial electron acceptor, oxidative activation of the catalyst can also be promoted by the photogenerated strongly oxidizing SO_4^- radicals (see Section 3.3).[52,65a]

3.5 Conclusions

In this chapter it has been shown how time-resolved spectroscopy experiments are so powerful tools for investigating photoinduced and thermal steps involved in the complex cycle of water oxidation. Two well-known polyoxometalate catalysts, namely **Ru4POM** and **Co4POM**, have been studied and important informations have been acquired.

In the case of **Ru4POM**, complementary charge interactions in aqueous solution leads to an efficient static quenching of the $Ru(bpy)_3^{2+}$ excited state. It occurs by very fast (ca. 2 ps) electron transfer from the excited photosensitizer to the catalyst followed by fast (15-150 ps) charge recombination (reversible oxidative quenching mechanism). This process competes appreciably with the primary photoreaction of the excited sensitizer with the sacrificial oxidant, even in high ionic strength media. The $Ru(bpy)_3^{3+}$ generated by photoreaction of the excited sensitizer with the sacrificial oxidant undergoes bimolecular hole scavenging by **Ru4POM** at a remarkably high rate ($3.6 \pm 0.1 \times 10^9$ $M^{-1}s^{-1}$). Moreover, the kinetics of the subsequent steps can also be assumed to be relatively fast, as provided by the flash photolysis experiments, where a single molecule of **Ru4POM** is shown to undergo, in 40 ms, ca. 45 turnovers in $Ru(bpy)_3^{3+}$ reduction.

As regarding **Co4POM**, the final scenario elucidated by laser flash photolysis experiments is that **Co4POM** cannot be operative in catalytic cycles where $Ru(bpy)_3^{3+}$ is the chemical oxidant (either photogenerated or in dark reactions); its decomposition products, formed upon dissolution of **Co4POM** in phosphate buffer, are instead capable of quenching $Ru(bpy)_3^{3+}$ in a microsecond timescale. Therefore **Co4POM** acts as a precursor of an actual water oxidation catalyst, which most likely is an earlier decomposition product, such as partially dissociated cobalt polyoxometalate species.

Chapter 4

Cobalt Cubanes
Water Oxidation Catalysts

This chapter is the result of a collaboration with the group of Prof. Marcella Bonchio at the Department of Chemical Sciences of the University of Padova, and the group of Prof. Sebastiano Campagna at the Department of Chemical Sciences of the University of Messina. Parts of this chapter are published in the literature.[33,65a,c]

4.1 Introduction

As previously mentioned in Chapter 3, in the quest for artificial photosynthesis the discovery of efficient water oxidation catalysts represents the holy grail of scientists and several approaches have been attempted in order to prepare molecules and materials capable of performing this reaction.

A recent breakthrough in the field has been the electrocatalytic deposition of a cobalt-based film which occurs in the presence of inorganic phosphate (CoPi) and enables water oxidation at pH 7, and at moderate overpotential (280 mV).[61a,b] CoPi features self-assembly and self-healing properties, mimicking the natural systems, and its electrocatalytic potential was also recently exploited for the construction of solid state light-activated devices (the so-called "artificial leaf").[83]

In this chapter a new class of water oxidation catalysts will be introduced, namely tetracobalt cubanes (Figure 4.1), which stems from the interplay of carboxylate and pyridine ligands stabilizing a tetracobalt core.

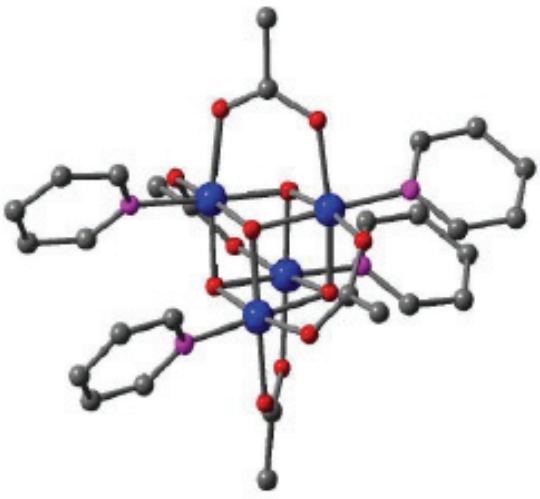

Fig. 4.1. Molecular water oxidation catalyst (**CoCub-H**) studied in this chapter; atom legend: blue, cobalt; red, oxygen; grey, carbon; pink, nitrogen; hydrogens have been omitted for clarity reasons.

The resulting complex deserves particular attention for several reasons: (i) it is stable in aqueous solution where it has been shown capable of catalyzing the oxidation of several aromatic molecules,[84] (ii) its tetranuclear oxo core mimics the natural oxygen-evolving complex of Photosystem II,[24] and (iii) it stands as the homogeneous analogue of the amorphous cobalt oxide/hydroxide film (CoPi) described by Nocera.[61,83] As such, it has been indeed used as molecular model for the understanding of the water oxidation mechanism by CoPi.[85,86]

In Section 4.3 a full study of the tetracobalt(III) cubane (**CoCub-H**) catalyst will be addressed in terms of electrochemical, spectroscopic, and photocatalytic characterization within the typical cycle involving $Ru(bpy)_3^{2+}$ as photosensitizer and persulfate as sacrificial electron acceptor. In the subsequent Section 4.4 a similar study will be applied on a whole class of tetracobalt(III) cubanes of the type shown in Figure 4.2 (**CoCub-X**) where suitable functionalizations of the *para* position of the pyridine ligands have been performed in order to tune the photocatalytic activity.

4.2 Experimental section

4.2.1 Synthesis

The synthesis of the **CoCub-H** was performed by Irene Bazzan and Dr. Serena Berardi (Department of Chemical Sciences, University of Padova) following literature procedures.[84] $Co(NO_3)_2 \cdot 6H_2O$ (2.90 g, 10 mmol) and $CH_3COONa \cdot 3H_2O$ (2.70 g, 20 mmol) were stirred in methanol (30 mL) and heated to refluxing temperature. Pyridine (800 μL, 10 mmol) was then added to the stirred reaction mixture, followed by a portion of 11.95 M hydrogen peroxide (4.47 mL, 50 mmol), added dropwise. The reaction mixture was stirred under refluxing condition for 4 h, then allowed to cool to room temperature. After reducing the volume of the mixture, the latter was introduced into a separating funnel and dichloromethane was then added. The pink aqueous phase was discarded, while the dark green organic phase was dried over anhydrous Na_2SO_4 and then filtered. After evaporation of the solvent, a dark green solid was obtained with 76% yield based on cobalt. ESI-MS, FT-IR, and H-NMR characterizations confirmed the obtained product.

The synthesis of the isostructural **CoCub-X** was performed by Irene Bazzan and Dr. Serena Berardi (Department of Chemical Sciences, University of Padova) following literature procedures.[84] The same experimental procedure as for **CoCub-H** was adopted by suitably

changing the pyridine used with the desired *para*-substituted one. ESI-MS, FT-IR, and H-NMR characterizations confirmed the obtained products. A series of cobalt cubanes (Figure 4.2) with the general formula $Co_4(\mu_3\text{-}O)_4(\mu\text{-}O_2CMe)_4(NC_5H_4X)_4$ was synthesised (with X = substituent in the *para* position). The substituents used include electron-donating groups such as methyl (Me), tert-butyl (*t*Bu), and methoxy (OMe), and electron-withdrawing groups such as bromide (Br), methylcarboxy (COOMe), and cyano (CN).

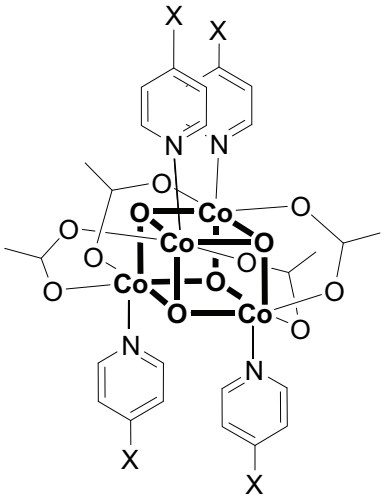

CoCub-Me	X = Me
CoCub-*t*Bu	X = *t*Bu
CoCub-OMe	X = OMe
CoCub-H	X = H
CoCub-Br	X = Br
CoCub-COOMe	X = COOMe
CoCub-CN	X = CN

Fig. 4.2. Isostructural tetracobalt cubanes **CoCub-X** (*para*-substituted at the pyridine moieties) studied in this chapter.

4.2.2 Apparatus and procedures

Reagents were used as received, spectroscopic grade acetonitrile, ultrapure milli-Q water and related buffers were used. See Chapter 2 for details on the electrochemistry and spectroscopic equipment.

Oxygen evolution studies were performed by Dr. Giuseppina La Ganga (Department of Chemical Sciences, University of Messina), by irradiation (λ > 400 nm) of 2 mL of a deoxygenated solution containing the $Ru(bpy)_3Cl_2$ sensitizer, the catalyst, and persulfate kept under continuous stirring in a cuvette closed with a perforable septum. Oxygen evolution was monitored in a second cuvette, containing deoxygenated solution (acetonitrile, 2.5 mL) of $Ru(bpy)_3Cl_2$, by taking a specific gas volume from the head of the first cuvette by using a gas-tight syringe and injecting it in the second cuvette, at various irradiation times. The quantitative oxygen determination was based on the oxygen-dependent emission lifetime of $Ru(bpy)_3Cl_2$, measured by a time-correlated single photon counting spectrometer.

Quantitative calibration of time-resolved spectral response as a function of oxygen was made before all experiments.

4.3 Tetracobalt(III) cubane CoCub-H

Electrochemical characterization by cyclic voltammetry of **CoCub-H** in phosphate buffer at pH 7 (Figure 4.3) shows the presence of an oxidation process at about 1.05 V *vs.* Ag/AgCl, which can be reasonably assigned to a one-electron oxidation leading to a formal $[3Co(III),Co(IV)]^{+}$ species. Notably, this anodic process is found to be shifted at more positive potentials in aqueous buffer with respect to acetonitrile, where a potential of 0.73 V *vs.* Ag/AgCl was reported.[84] The one-electron oxidation of **CoCub-H** is then followed by the catalytic discharge typical of water oxidation, similar to that of $Co(NO_3)_2$ a well-known, but unstable, water oxidation catalyst.[71,87] Such a result clearly indicates that **CoCub-H** can catalyze water oxidation. Considering the onset of the catalytic wave due to water oxidation (assumed as the potential at which the current intensity of the CV curve reaches 50 μA), an overpotential of ca. 0.55 V can be estimated in this conditions for the oxygen evolving reaction (OER).

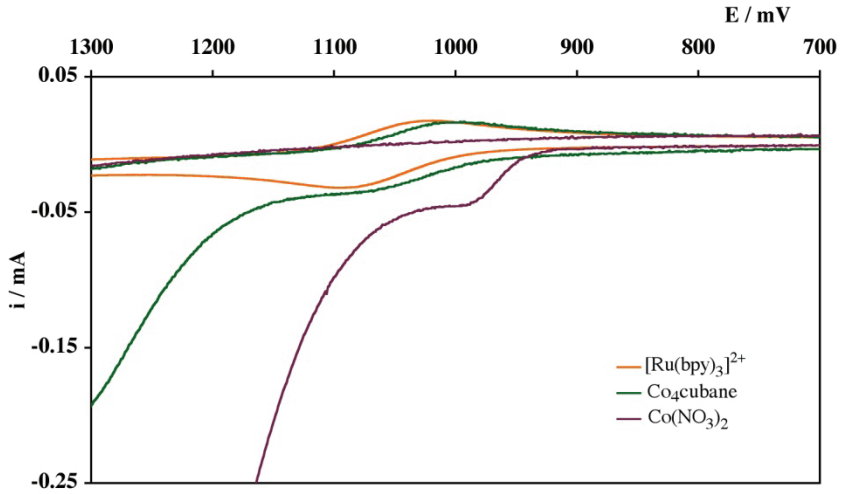

Fig. 4.3. Cyclic voltammograms of **CoCub-H** (2 mM), $Ru(bpy)_3^{2+}$ (2 mM) and $Co(NO_3)_2$ (2 mM) in phosphate buffer (0.2 M) at pH 7. Working electrode: glassy carbon; counter electrode: platinum; reference electrode: Ag/AgCl, scan rate, 100 mV/s.

The catalytic activity of **CoCub-H** was then tested in light-activated experiments involving $Ru(bpy)_3^{2+}$ and persulfate as photosensitizer and sacrificial electron acceptor, respectively. Oxygen production (Figure 4.4) was observed upon visible light irradiation of a 2 mL solution containing 18.7 μM **CoCub-H**, 1 mM $Ru(bpy)_3Cl_2$, and 5 mM $Na_2S_2O_8$ in 80 mM borate buffer at pH 8, achieving TON up to 40 after approximately 30-35 min of irradiation.

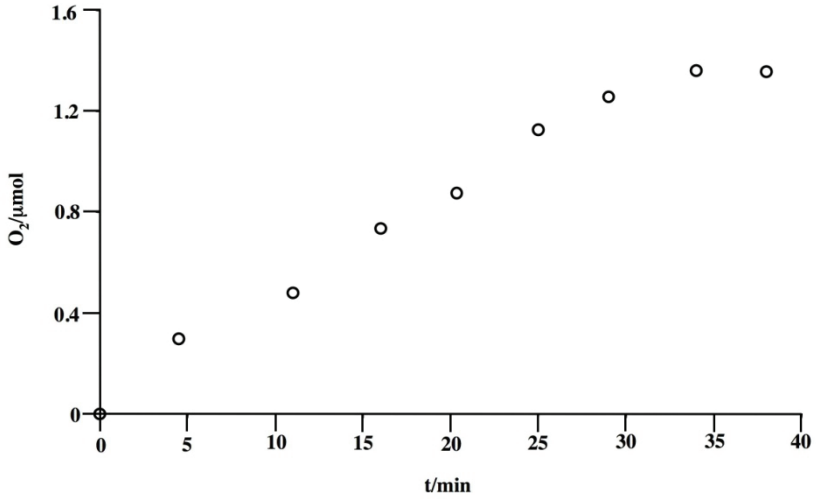

Fig. 4.4. Photocatalytic oxygen evolution as a function of time from a 2 mL solution of **CoCub-H** (18.7 μM) containing $Ru(bpy)_3^{2+}$ (1 mM) and $Na_2S_2O_8$ (5 mM), at pH 8 in borate buffer (80 mM $Na_2B_4O_7$, adjusted at pH 8 with HCl), upon visible light irradiation.

The chemical yield of the process can be estimated as 28%, by comparing the total amount of oxygen produced with the theoretical, maximum yield based on oxidant consumption. Comparison of absorption spectra before and after the photolysis suggests that the photocatalytic activity is limited by decomposition of the ruthenium(II) sensitizer, most likely involving nucleophilic attack to the photogenerated $Ru(bpy)_3^{3+}$ oxidant species.[59a,71] The photochemical quantum yield Φ of molecular oxygen evolution (calculated upon excitation at 450 nm) is 0.30 ± 0.03, which is one of the highest reported in the literature for molecular catalyst. A clear decrease in the photocatalytic activity of the system occurs on passing from pH 8 to pH 7 (40 mM phosphate buffer), when sensitizer and catalyst concentrations are kept constant at 1 mM and 18.7 μM, respectively. In these latter conditions, in fact, the photochemical quantum yield of oxygen production decreases to 0.10, while the chemical yield, referred to the available persulfate anions, is practically the same (30%). At first sight, reason for such a decreased photochemical quantum yield at pH 7 could be attributed to the potential *E* for water oxidation, which increases with decreasing pH. Moreover, at each pH value (7 and 8) quantum yields for oxygen evolution are found to be dependent on the amount

of catalyst present in the photoreaction mixture with values peaking at different **CoCub-H** concentration (Figure 4.5). The reason for such a behavior can be at least in part explained in terms of self-poisoning effects competing with the evolution of the catalyst to its high-valence states capable of oxidizing water to dioxygen.

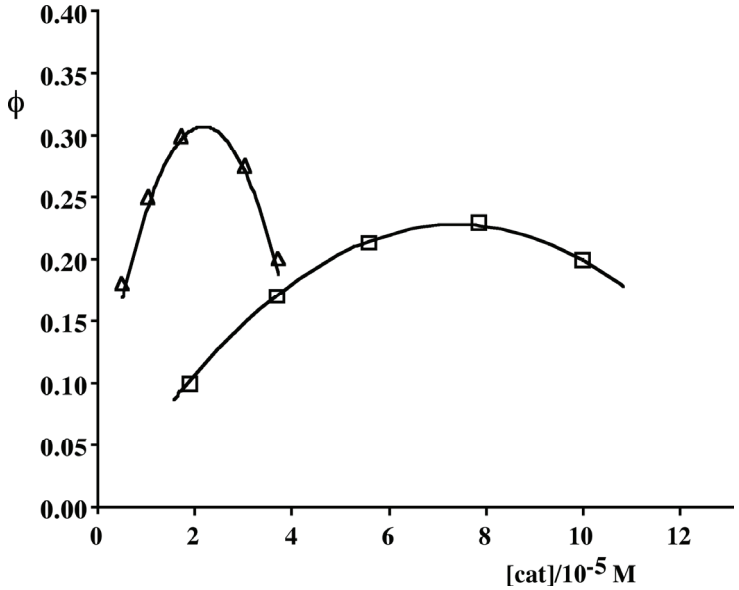

Fig. 4.5. Dependence of photochemical quantum yield for oxygen production on **CoCub-H** concentration. Experimental conditions: 1 mM $Ru(bpy)_3^{2+}$, 5 mM $Na_2S_2O_8$, 450-nm excitation. Triangles are data at pH 8 in borate buffer; squares are data at pH 7 in phosphate buffer.

In order to get experimental insight into the mechanistic aspects of the photocatalytic systems, investigation of the primary hole-transfer process from the photogenerated oxidant to **CoCub-H** was performed by means of laser flash photolysis experiments. In fact, $Ru(bpy)_3^{3+}$ is not stable in neutral or basic aqueous solution, mostly returning to the reduced species $Ru(bpy)_3^{2+}$ but also in part undergoing irreversibly decomposition,[71] thus fast hole-scavenging by the catalyst is important to prevent or at least minimize such a decomposition pathway.

Figure 4.6 shows the effect of added **CoCub-H** on the kinetics of disappearance of $Ru(bpy)_3^{3+}$, generated upon excitation of solutions containing $Ru(bpy)_3^{2+}$ in the presence of persulfate anions, at pH 7 in buffered phosphate solution (Figure 4.6a) and at pH 8 in borate buffer (Figure 4.6b). In a typical nanosecond laser flash photolysis experiment (355-nm excitation), the fast bleach of the metal-to-ligand charge-transfer (MLCT) absorption of $Ru(bpy)_3^{2+}$ at 450 nm corresponds to the formation of $Ru(bpy)_3^{3+}$ by oxidative irreversible quenching by persulfate. In the absence of the catalyst this bleach remains almost constant over the whole time-window of the experiment. The recovery of the bleach (due to regeneration of $Ru(bpy)_3^{2+}$) is observed when **CoCub-H** is introduced in solution and in

particular this recovery is accelerated on increasing the **CoCub-H** concentration. The pseudo-first order rate constants (obtained for [**CoCub-H**] >> $[Ru(bpy)_3]^{3+}$), calculated according to eqs 20-22, correspond to an average bimolecular rate constant of $(1.2 \pm 0.4) \times 10^7$ $M^{-1}s^{-1}$ and $(1.6 \pm 0.4) \times 10^7$ $M^{-1}s^{-1}$ for the processes at pH 7 and 8, respectively. These experiments indicate that (i) the rate constant of the hole scavenging does not change significantly between pH 7 and 8 and (ii) hole scavenging is always significantly faster than the slow decomposition of the oxidized photosensitizer (reported to be in the order of $10^{-3}/10^{-2}$ s^{-1}, not detectable in the time scale of the flash photolysis experiments).

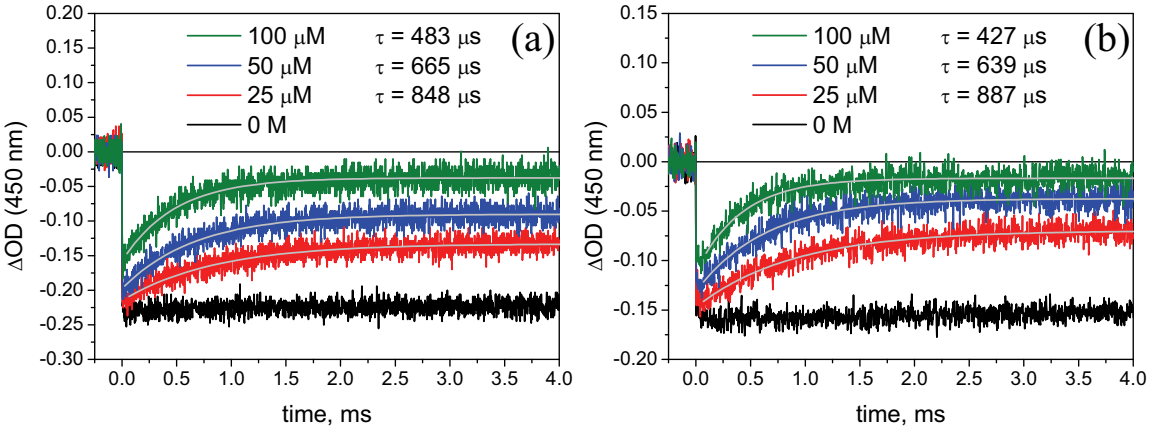

Fig. 4.6. Flash photolysis experiments: kinetics of bleach recovery as a function of catalyst concentration. Experimental conditions: 355-nm excitation; 50 μM $Ru(bpy)_3^{2+}$, 5 mM $Na_2S_2O_8$, 0-100 μM **CoCub-H**. (a) pH = 7 (40 mM phosphate buffer); (b) pH = 8 (80 mM borate buffer).

Additional information can be also obtained from the transient absorption experiments of Figure 4.6. The recovery of the bleach, while increasing both in rate and in magnitude with increasing catalyst concentration, does never reach completion. This could be related to the small driving force for the electron transfer process, as suggested by the redox data of Figure 4.3 (see above). In fact, since the reduction potential of the $Ru(bpy)_3^{3+}/Ru(bpy)_3^{2+}$ couple is very close to that of the **CoCub-H$^+$/CoCub-H** redox couple, the primary hole-transfer reaction could probably be better seen as an equilibrium process, rather than an irreversible redox reaction. This fact may affect sensitively the fate of the photogenerated $Ru(bpy)_3^{3+}$ oxidant, thus contributing importantly to its decomposition along the whole photolysis (the main reason responsible for the observed low chemical yield of the photocatalytic reaction).

Moreover, the transient absorption data give other interesting pieces of information. The initial bleach of the $Ru(bpy)_3^{2+}$ MLCT band at 450 nm, proportional to the amount of produced $Ru(bpy)_3^{3+}$, decreases with increasing **CoCub-H** concentration. Since **CoCub-H**

has no appreciable quenching effect on the $Ru(bpy)_3^{2+}$ excited state, and the amount of persulfate is constant in all the transient absorption experiments, the efficiency of the primary quenching step must be independent of the concentration of **CoCub-H**. The most likely explanation of the experimental results is that, similarly to what observed for the tetraruthenium polyoxometalate catalyst (Chapter 3, Section 3.3), in competition with the secondary oxidation of $Ru(bpy)_3^{2+}$ to $Ru(bpy)_3^{3+}$, the radical SO_4^{-} may also react directly with the catalyst. This hypothesis can be checked in Figure 4.7, where the first 20 μs of Figure 4.6a have been zoomed on. In fact, in the absence of the catalyst the secondary (radical) formation of $Ru(bpy)_3^{3+}$ is clearly detectable, whereas this reaction is progressively quenched when **CoCub-H** is introduced and its concentration increased.

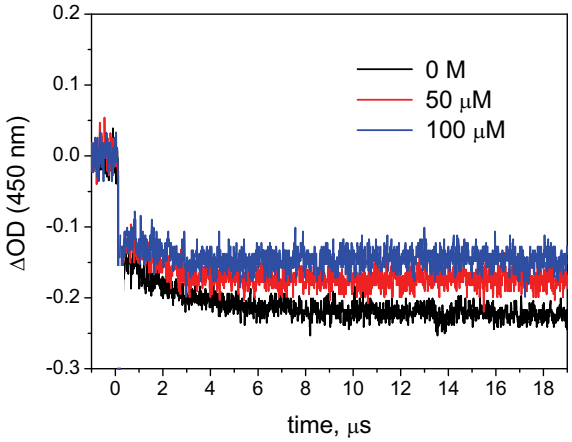

Fig. 4.7. Flash photolysis experiments: bleach formation and development in the early time scale. Same experimental conditions as in Figure 4.6a.

From a quantitative viewpoint, the secondary reaction is quenched by about one half when **CoCub-H** concentration is the same as that of $Ru(bpy)_3^{2+}$ (i.e, 50 μM), this seems to indicate that the rate constants of the hole transfer from the radical SO_4^{-} to $Ru(bpy)_3^{2+}$ and to the catalyst are comparable. According to this scenario and considering the poor driving force for the electron transfer processes involving **CoCub-H** and the photogenerated $Ru(bpy)_3^{3+}$ oxidant, the radical SO_4^{-} most likely plays a crucial role within the photocatalytic mechanism of the **CoCub-H**/$Ru(bpy)_3^{2+}$/$S_2O_8^{2-}$ system.

4.4 Substituted tetracobalt(III) cubane CoCub-X

The effect of ligand modification can be immediately observed when comparing the cyclic voltammetry of the **CoCub-X** series in acetonitrile (Figure 4.8). As a matter of fact the first one-electron oxidation process is found to fall at 0.73 V *vs.* Ag/AgCl for the unsubstituted **CoCub-H**,[84] while is seen to shift to less positive potentials in the presence of electron-donating *para*-substituted pyridines or to more positive potentials with electron-withdrawing ones.

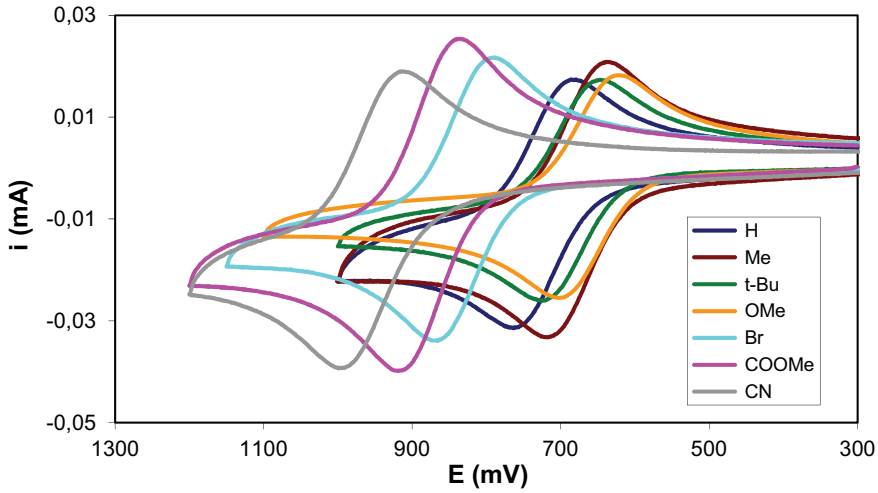

Fig. 4.8. Cyclic voltammograms of 2 mM **CoCub-X** in acetonitrile (0.1 M $TBAClO_4$). Working electrode, GC; counter electrode, Pt; reference electrode, Ag/AgCl.

The electrocatalytic water oxidation activity of **CoCub-X** was then tested in phosphate buffer at pH 7 by cyclic voltammetry. Under this experimental conditions, beside the one-electron oxidation of the tetracobalt core (shifted at more positive potential as described in the previous section), catalytic water discharge is observed starting at ca. 1.05 V *vs.* Ag/AgCl. This confirm that the whole **CoCub-X** series is capable of performing water oxidation with overpotentials for the oxygen evolving reaction, taken at a current value of 50 μA, varying in a narrow range (0.50-0.57 V, see Table 4.1), but with no apparent ordering as a function of the pyridine substituent.

The impact of ligand modification was then explored under light-activated conditions within the typical system involving $Ru(bpy)_3^{2+}$ and persulfate as photosensitizer and sacrificial electron acceptor, respectively. In this system, photocatalytic performance is triggered by sequential hole transfer events from the photogenerated $Ru(bpy)_3^{3+}$ oxidant to the catalyst. As abundantly described in Chapter 3 and in Section 4.3 of this chapter, the primary

hole-transfer event can be conveniently monitored by appropriate laser flash photolysis experiments, by flashing solutions containing $Ru(bpy)_3^{2+}$, persulfate, and different amounts of the catalyst and monitoring the evolution in time of the MLCT bleach at 450 nm due to reduction of the photogenerated $Ru(bpy)_3^{3+}$ oxidant by the catalyst. In the case of the isostructural **CoCub-X** catalysts, these experiments were conducted in a 50:50 CH_3CN:10 mM borate buffer (pH 8) solvent mixture.

Table 4.1. Water oxidation activity by isostructural **CoCub-X**.

X	η (V)[a]	$E_{1/2}$ (mV)[b]	k_X (10^8 $M^{-1}s^{-1}$)[c]	Φ (%)[d]
OMe	0.57	877	2.51	40[e]
Me	0.52	880	1.92	15
***t*Bu**	0.50	855	1.39	5
H	0.55	926	1.33	13
Br	0.53	990	0.60	16
COOMe	0.51	1040[f]	0.70	23
CN	0.51	1081[f]	0.14	13

[a] Overpotential for water discharge in 0.2 M phosphate buffer (pH 7) determined at an anodic current of 50 μA; [b] first one-electron oxidation half-wave potential measured by cyclic voltammetry in 50:50 CH_3CN/10 mM borate buffer (pH 8); [c] bimolecular rate constant for ET measured in 50:50 CH_3CN/10 mM borate buffer (pH 8); [d] quantum yield measured in 50:50 CH_3CN/10 mM borate buffer (pH 8) over the first 30 min of reaction; [e] observed with freshly prepared solutions; [f] measured in 50:50 CH_3CN/10 mM phosphate buffer (pH 7), not observed in 50:50 CH_3CN/10 mM borate buffer (pH 8) due to overlapping with catalytic water discharge.

As observed in the previous section for **CoCub-H**, in pure aqueous buffer (both at pH 7 and 8) primary hole-transfer rates were found between 1.2-1.6 × 10^7 $M^{-1}s^{-1}$ and the recovery of the bleach never reached completion at all catalyst concentrations. This was ascribed to the low thermodynamic driving force dictating the electron transfer process (see Section 4.3). The redox gap can be enhanced, however, in a 50:50 CH_3CN:10 mM borate buffer (pH 8) solvent mixture where the redox potentials, measured by cyclic voltammetry, become 1.20 V and 0.93 V for the $Ru(bpy)_3^{3+}/Ru(bpy)_3^{2+}$ and **CoCub-H$^+$/CoCub-H** couples, respectively.

As promptly observed by laser flash photolysis (Figure 4.9), this thermodynamic boost brings about an acceleration of the hole transfer process of about one order of magnitude with a measured bimolecular rate constant, calculated according to eqs 20-22, of 1.33 × 10^8 $M^{-1}s^{-1}$ for **CoCub-H**. At the same time the recovery of the bleach becomes complete for all the explored catalyst concentrations. This net improvement in the hole transfer kinetics may cause an important effect on the durability of the system by reducing the decomposition of the photosensitizer under continuous light irradiation, a major problem of this type of photocatalytic systems.

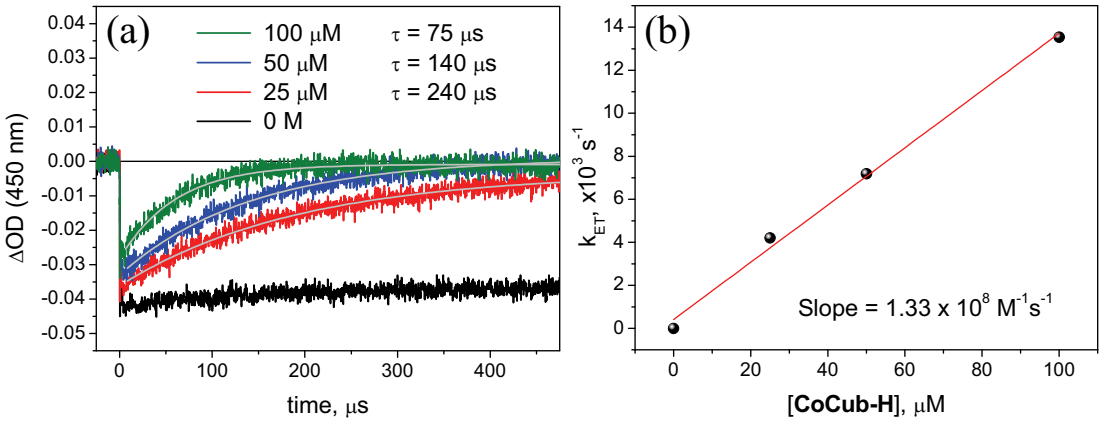

Fig. 4.9. (a) Flash photolysis experiments (355-nm excitation) obtained on 50:50 CH_3CN:10 mM borate buffer (pH 8) solutions containing 50 μM $Ru(bpy)_3^{2+}$, 5 mM $S_2O_8^{2-}$, and 0-100 μM **CoCub-H**. (b) Plot of the pseudo-first order rate *vs.* **CoCub-H** concentration for the calculation of the bimolecular rate constant.

In the mixed solvent, complete recovery of the $Ru(bpy)_3^{2+}$ absorption is obtained with all the isostructural **CoCub-X** complexes. Moreover, a remarkable ligand effect is observed on the hole transfer kinetics as a function of the pyridine substituent, with bimolecular rate constants in the range (0.14-2.51) × 10^8 M^{-1} s^{-1} (Table 4.1). A Hammett linear free energy relationship (LFER) is obtained by plotting $\log(k_X/k_H)$ versus the substituent σ constants (Figure 4.10). The Hammett analysis provides a negative slope value, ρ = −1.3, indicating that electron transfer from the catalyst to the oxidized sensitizer is favored by electron-rich pyridine ligands. The direct participation of the cobalt core is also confirmed by the parallel analysis of the **CoCub-X$^+$/CoCub-X** redox potentials in CH_3CN:10 mM borate buffer (pH 8) media (Table 4.1). Indeed, the $\log(k_X/k_H)$ values correlate with the redox potential gap ΔE = $E_{1/2}(Ru(bpy)_3^{3+/2+})$ − $E_{1/2}$(**CoCub-X$^{+/0}$**), see inset in Figure 4.10. This observation confirms that hole-transfer rate increases with increasing the sensitizer/catalyst ΔE, and therefore this process must occur in the normal region of the classical Marcus theory[26] being accelerated by a higher driving force.

The straightforward correlation of the hole transfer rates with the substituent σ constants, however, is not strictly observed considering *t*Bu and COOMe substituents (Figure 4.10). Indeed, while photoinduced electron transfer rates appear to be mainly controlled by the thermodynamic driving force along the whole series, other stereoelectronic effect may come into play as far as the *t*Bu and COOMe groups are concerned. In particular, while a difficult

explanation can be evision for the positive deviation of the COOMe substituent, in the case of *t*Bu the negative deviation can be easily attributed to steric hindrance effects.

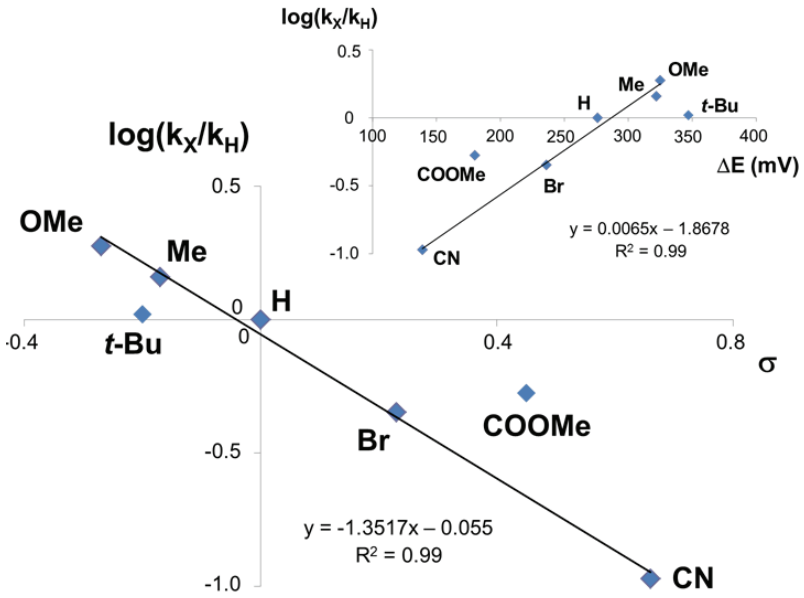

Fig. 4.10. Hammett linear free energy relationship (LFER) plot of hole transfer rate constants (Table 4.1) and (inset): plot of hole transfer rate constants *vs.* redox potential gap $\Delta E = E$ (Ru(bpy)$_3^{3+/2+}$) – E (**CoCub-X**$^{+/0}$).

The oxygenic activity of the **CoCub-X** series was investigated in the presence of an excess of the Ru(bpy)$_3^{2+}$/$S_2O_8^{2-}$ couple and under continuous irradiation. In a typical experiment, visible irradiation ($\lambda > 400$ nm) of **CoCub-X** (18 μM) in 50:50 acetonitrile:10 mM aqueous borate buffer (pH 8) containing 1 mM Ru(bpy)$_3^{2+}$ and 5 mM $S_2O_8^{2-}$ leads to continuous oxygen production with the time-evolution profiles reported in Figure 4.11. Under the conditions explored, the kinetics obey to a zero order law, up to 80% of persulfate consumption which maintains a stationary state of photogenerated Ru(bpy)$_3^{3+}$. Differently from what observed in pure aqueous buffer (Section 4.3), in the mixed solvent, oxygen evolution occurs until quantitative consumption of the sacrificial electron acceptor (100% chemical yield), corresponding to an overall turnover number (TON) of 140 for all the isostructural **CoCub-X** catalysts. Such major improvement of the photosynthetic performance can result from an improved stability of the Ru(bpy)$_3^{2+}$ photosensitizer, as can be checked from the comparison of the absorption spectra before and after the photolysis. This is very likely the consequence of the faster electron transfer processes involving the photogenerated Ru(bpy)$_3^{3+}$ oxidant and the **CoCub-X** catalysts achieved in the new solvent mixture with respect to the purely aqueous buffers. As regarding the quantum yields (Table 4.1), a record

value of 0.4 has been observed for **CoCub-OMe**, which is one of the highest reported in photoactivated water oxidation catalysis. Considering the limiting value of 0.5 for systems involving $Ru(bpy)_3^{2+}$ and persulfate as photosensitizer and sacrificial acceptor, respectively, it translates into an overall quantum efficiency of 80%.

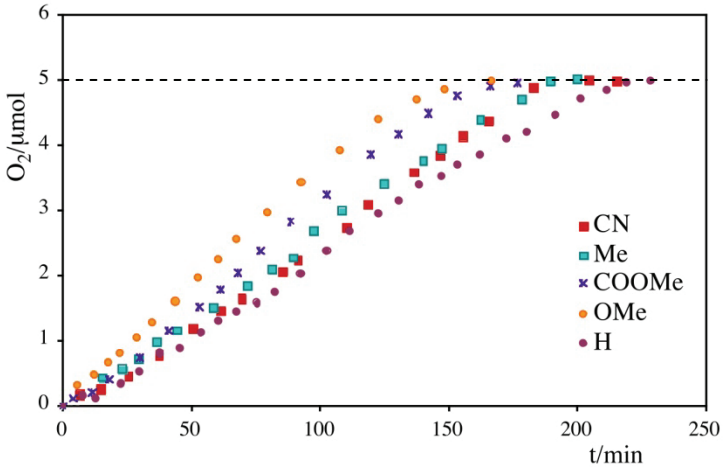

Fig. 4.11. Photoinduced oxygen evolution kinetics by **CoCub-X** (18 μM), $Ru(bpy)_3^{2+}$ (1 mM), $S_2O_8^{2-}$ (5 mM) in 2 mL 50:50 acetonitrile:10 mM borate buffer (pH 8), visible irradiation (λ > 400 nm) with a 50 W halogen lamp (kinetics of **CoCub-Br** and **CoCub-*t*Bu** have been omitted for clarity reasons).

The quantum yields, however, do not follow a straightforward correlation with the ligand electronic effects, in fact resulting in the following order (see Table 4.1): OMe > COOMe > Me ≈ H ≈ Br ≈ CN > *t*Bu. This observation can be likely explained considering that, while the primary hole-transfer process is favored by more electron-donating substituents, the subsequent steps towards oxygen formation (including the water nucleophilic attack) can be much more favored by electron-withdrawing ones. Therefore the result is a balance between these effects playing together within the overall complex water oxidation mechanism.

4.5 Conclusions

In this chapter a new class of water oxidation catalysts has been synthesized and studied, which (i) poses as molecular cobalt-based analogue of the oxygen evolving complex (OEC) of Photosystem II and (ii) represents the basic structural unit of the heterogeneous cobalt oxide/hydroxide water oxidation catalyst CoPi.[61,83]

It has been shown that the tetracobalt(III) cubane-shaped species **CoCub-H**, in combination with $Ru(bpy)_3^{2+}$ and persulfate as sensitizer and sacrificial acceptor, respectively,

is an efficient molecular catalyst for photo-driven water oxidation with visible light. The photochemical quantum yield of the process can reach the value of 0.30 in pure buffered water at pH 8. In these experimental conditions, however, this system undergoes rapid deactivation due to the observed decomposition of the sensitizer (ca. 30% chemical yield). The reason for this behavior have been ascribed to the hole transfer process from the photogenerated $Ru(bpy)_3^{3+}$ oxidant to the catalyst, which, although relatively fast (1.2-1.6 × 10^7 $M^{-1}s^{-1}$), is not complete, most likely due to the poor driving force.

An improvement of the system has been then attempted by suitably changing the solvent from pure buffered water to a mixture of 50:50 acetonitrile:10 mM borate buffer (pH 8) which causes an increase of the driving force for the hole transfer, as the oxidation potential of **CoCub-H** shifts to less positive values in acetonitrile. As a matter of fact, an acceleration of the hole-transfer rate of one order of magnitude with complete recovery of the bleach has been observed in these latter conditions. At the same time a series of tetracobalt cubanes **CoCub-X**, obtained by suitable functionalization at the *para* position of the pyridine ligands, has been characterized thoroughly. In these cases hole-transfer rates from the photogenerated $Ru(bpy)_3^{3+}$ to the catalyst follow a straightforward correlation with the substituent σ constants and redox potential gaps. Oxygen evolving activity is also dependent on the ligand electronic effect with the best result in terms of quantum yield obtained with the methoxy-substituted cubane **CoCub-OMe** (Φ = 0.4). Finally, for all the **CoCub-X** class, thanks to the change in solvent (from pure buffered water to the acetonitrile/buffer mixture), the photoreactions become quantitative (100% chemical yield) and negligible decomposition of the sensitizer is observed.

Chapter 5

A Single-Site Cobalt Salophen Water Oxidation Catalyst

This chapter is the result of a collaboration with the group of Prof. Marcella Bonchio at the Department of Chemical Sciences of the University of Padova. A part of this chapter is published in the literature.[88]

5.1 Introduction

Water oxidation to molecular oxygen represents the kinetic bottleneck towards water splitting for a solar hydrogen generation as a clean and renewable fuel. Several approaches have been attempted for the preparation of molecular water oxidation catalysts. In particular great efforts have been devoted to the preparation of multimetallic catalysts,[33] which could in principle distribute the oxidation equivalents necessary for water oxidation over several metal centers, thus lowering the energy barrier of the overall catalytic process. However, the design of multimetallic cores with oxygen evolving activity poses synthetic and stability hurdles.

Noteworthy, single site metal complexes have been recently taken into consideration to this aim, with the possibility of exploiting the fundamental coordination chemistry in order to modify and tune the oxygen evolving activity. Among this class of metal complexes used for the water oxidation purpose single site ruthenium catalysts play by far the main role in the field;[36,37] their well-defined and relatively robust structures have also enabled a detailed mechanistic account of the complicated water oxidation reaction. Of particular interest are also the earth-abundant cobalt complexes featuring polydentate organic ligands, such as corroles,[89] polypyridines,[90] and porphyrines,[91,92] which have been used under dark electrocatalytic conditions[89,90,91] and in few other cases in light-activated experiments.[92]

In a simplified manner, the mechanism for water oxidation by single-site cobalt catalysts, using the well-defined reactivity of single-site ruthenium ones[37,93] and other cobalt-based systems[90] as a guide, should foresee a series of proton-coupled electron transfer (PCET) processes (Figure 5.1). Starting from a Co(II) species with a coordinated water molecule, a first electron transfer process (with contemporary loss of a proton) involves the formation of a Co(III)-hydroxo species, which can be subsequently oxidized to a formal Co(IV)-oxo state. This last process is not “strictly” proton-coupled, as it is observed to require the presence of an intermediary base (*e.g.*, hydroxide or phosphate) in order to take place.[90] Water nucleophilic attack to the latter with simultaneous deprotonation is then followed by a third electron transfer with formation of a Co(III)-hydroperoxo species. Finally, after an additional proton-coupled electron-transfer process, water attack to a formal Co(IV)-peroxo species is

responsible for the release of an oxygen molecule. In several instances,[92] however, supported by a quadratic dependence of the oxygen evolution rate on catalyst concentration and by computational calculations a different mechanism, involving the cooperation of two catalytic centers (dashed lines in Figure 5.1), was also envisioned. Overall, according to this scenario it is easy to understand that the ligand set surrounding the catalytic cobalt center plays a crucial role in determining the redox potentials of all the electron transfer processes involved within the whole catalytic cycle.

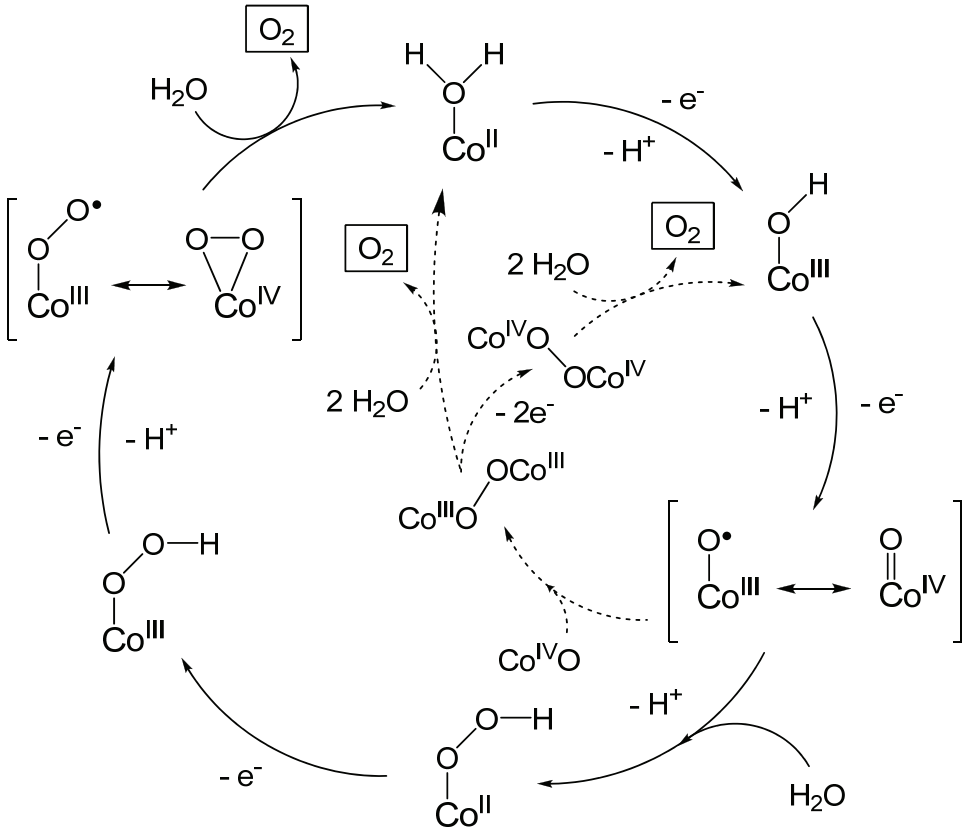

Fig. 5.1. Water oxidation catalytic mechanism by a single-site cobalt catalyst: unimolecular mechanism (solid lines) and bimolecular "cooperative" pathway (dashed lines).

In Section 5.3, a cobalt(II) complex, based on the well-known salophen ligand (**CoSlp**, Figure 5.2), will be presented as a water oxidation catalyst and its activity will be screened both in dark conditions and upon light irradiation within the $Ru(bpy)_3^{2+}/S_2O_8^{2-}$ sacrificial cycle. In Section 5.4, the very same catalyst will be ideally supported on the photosensitizer platform, thus obtaining a compartmental sensitizer-catalyst dyad for water oxidation.

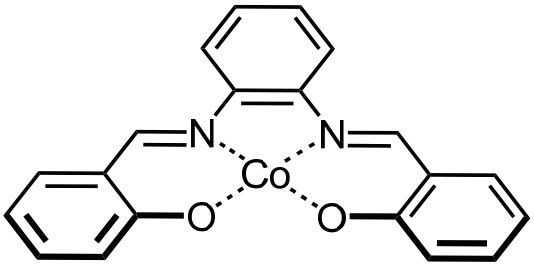

Fig. 5.2. Structural representation of the single-site **CoSlp** water oxidation catalyst.

5.2 Experimental section

5.2.1 Synthesis of CoSlp

The synthesis was performed by Erica Pizzolato (Department of Chemical Sciences, University of Padova) following literature procedures.[94,95] In a 100 mL round-bottom flask 1.00 g (9.25 mmol) of 1,2-benzenediamine was solved in 15 mL of ethanol by using vigorous magnetic stirring. To this solution, 1.97 mL (18.50 mmol) of salicyaldehyde was dropped. The mixture was refluxed by applying continuous MW irradiation (40 W, 78ºC) for 10 min and the crude was cooled to 0ºC observing the presence of a precipitate. This solid was filtered and washed with ethanol to obtain the desired **Slp** ligand as a microcrystalline yellowish orange solid (2.90 g, 84% yield). All characterization data was in agreement with literature.[94] In a 100 mL round-bottom flask 397 mg (1.256 mmol) of **Slp** were then dissolved in 30 mL of methanol. To this solution, 313 mg (1.260 mmol) of $Co(OAc)_2 \cdot 4\ H_2O$ were added and an immediate color change in the solution from pale orange to dark brown was observed. The mixture was stirred for 3 hours at room temperature, when diethyl ether (20 mL) was added to induce the formation of a precipitate; this latter was filtered and washed with diethyl ether and recrystallized from chloroform to obtain a brownish orange solid (75% yield). ESI-MS, FT-IR, and UV-Vis absorption spectrum were all in agreement with literature data[95] confirming the product.

5.2.2 Synthesis of RuCoSlp covalent dyad

The synthesis of dyad **RuCoSlp** (Figure 5.3) was performed by Dr. Alejandro Montellano Lòpez (Department of Chemical Sciences, University of Padova) adapting literature procedures.[96]

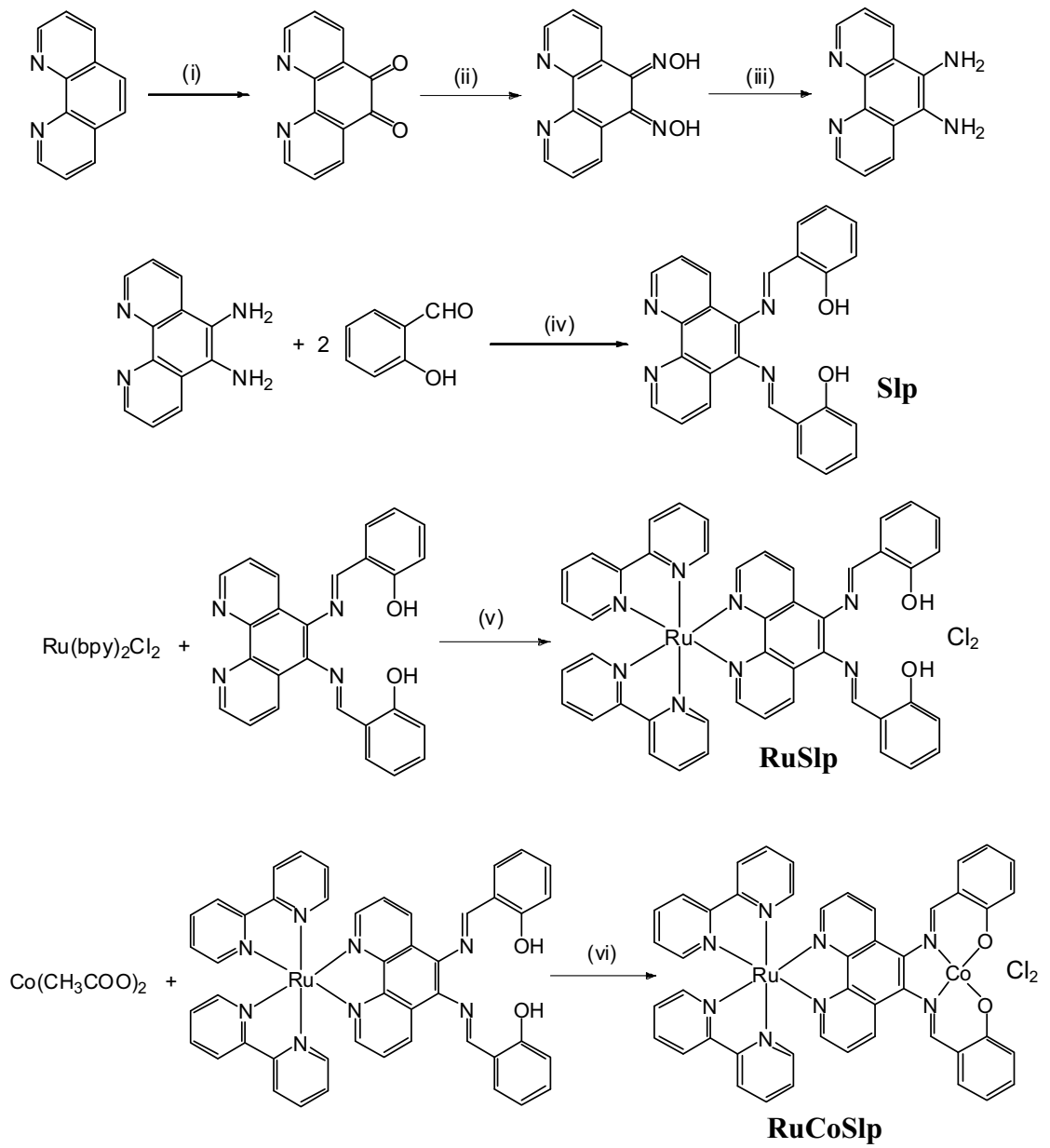

Fig. 5.3. Synthesis of **RuCoSlp**. (i) H_2SO_4/HNO_3, NaBr, 100°C, yield 35%; (ii) $NH_2OH{\cdot}HCl$, $BaCO_3$ in refluxing ethanol, yield 57%; (iii) 10% Pd/C, N_2H_4 in refluxing ethanol, yield 42%; (iv) triethylortoformate in refluxing ethanol, yield 42%; (v) triethylortoformate, $AgNO_3$ in refluxing ethanol, yield 66%; (vi) methanol, room temperature, yield 91%.

The key intermediate is the heteroditopic ligand *N,N'*-bis(salicylidene)-5,6-(1,10-phenantroline)diamine, **Slp**, prepared by a four-step synthesis starting from 1,10-phenantroline. These steps include: (i) oxidation of 1,10-phenantroline to 1,10-phenantroline-5,6-dione under reflux of H_2SO_4/HNO_3, (ii) reaction with hydroxylamine to yield the 1,10-phenantroline-5,6-dioxime, (iii) its reduction to 1,10-phenantroline-5,6-diamine with hydrazine, and (iv) condensation of 1,10-phenantroline-5,6-diamine with two equivalents of salicilaldehyde. The identity of all intermediates was confirmed by comparison of ESI-MS,

infrared and ^{1}H-NMR characterisation with literature.[96] Metallation of the phenantroline unit with Ru(II) was then achieved by reaction of **Slp** with *cis*-Ru(bpy)$_2$Cl$_2$, under refluxing methanol in the presence of triethylorthoformate; in the resulting complex, **RuSlp**, isolated in 66% yield, the Ru(II) center is coordinated to the heteroditopic ligand **Slp**, while maintaining the two bpy ligands in its coordination sphere, as confirmed by elemental analysis and by ^{1}H-NMR characterisation. The final step is metallation of the salophen cavity with Co(II), readily achieved under room temperature conditions by addition of cobalt acetate to a methanol solution of **RuSlp**, precipitating the product **RuCoSlp** in 91% yield by addition of diethyl ether. Elemental analysis and FT-IR confirmed the obtained product.

5.2.3 Apparatus and procedures

Reagents were used as received, spectroscopic grade acetonitrile, ultrapure milli-Q water and related buffer solutions were used. See Chapter 2 for details on the spectroscopic apparatus.

Photocatalytic water oxidation tests were conducted at the Department of Chemical Sciences of the University of Padova in a home-made glass reactor equipped with a steel cap, where a *FOXY-R-AF* probe was mounted and interfaced with a *Neofox Real-Time* software for data collection. Irradiation was performed with a monochromatic LED (7 mW power) emitting at 450 nm; the photon flux was 2.63×10^{-8} einstein/s.

X-band continuous-wave EPR spectra were recorded at the Department of Chemical Sciences of the University of Padova on a *Bruker ELEXSYS E580* spectrometer equipped with a *ER4102ST* cavity working at 9.38 GHz. Cryogenic temperatures were achieved using a liquid helium flow cryostat (*Oxford Instruments ESR-900*) driven by a temperature controller (*Oxford Instruments ITC503*).

5.3 Cobalt(II) Salophen

Electrochemical characterisation of **CoSlp** by cyclic voltammetry in aqueous phosphate buffer at pH 7.1 shows the onset of an intense anodic wave starting at ca. 0.90 V *vs.* Ag/AgCl reaching a current peak of 250 μA (current density of 3.5 mA cm^{-2}) at 1.35 V (Figure 5.4a). This intense wave can be attributed to catalytic water oxidation, as a cathodic wave at −0.23 V, due to reduction of dioxygen formed at the working electrode, is only observed when an

anodic scan is performed before the cathodic one. A very low operating overpotential, $\eta = 0.3$ V (calculated at 0.7 mA cm^{-2} current density) is measured in these conditions, which outperforms previously reported cobalt OECs, with overpotentials in the range 0.5-0.6 V. In electrochemical experiments involving molecular cobalt complexes care has to be taken in order to dissect whether the observed electrocatalytic activity arises from homogeneous molecular species or heterogeneous cobalt oxide phases generated under application of an anodic bias.[81] However, it can be observed that the **CoSlp** cyclic voltammetry is markedly different with respect to that of the "ligand-free" cobalt aquo complex, known to evolve to electrodeposited oxide phases. Moreover an increase of the normalized current (current divided by the square root of the scan rate) at low scan rates confirms the presence of a rate determining chemical step preceding electron transfer (Figure 5.4b).[90]

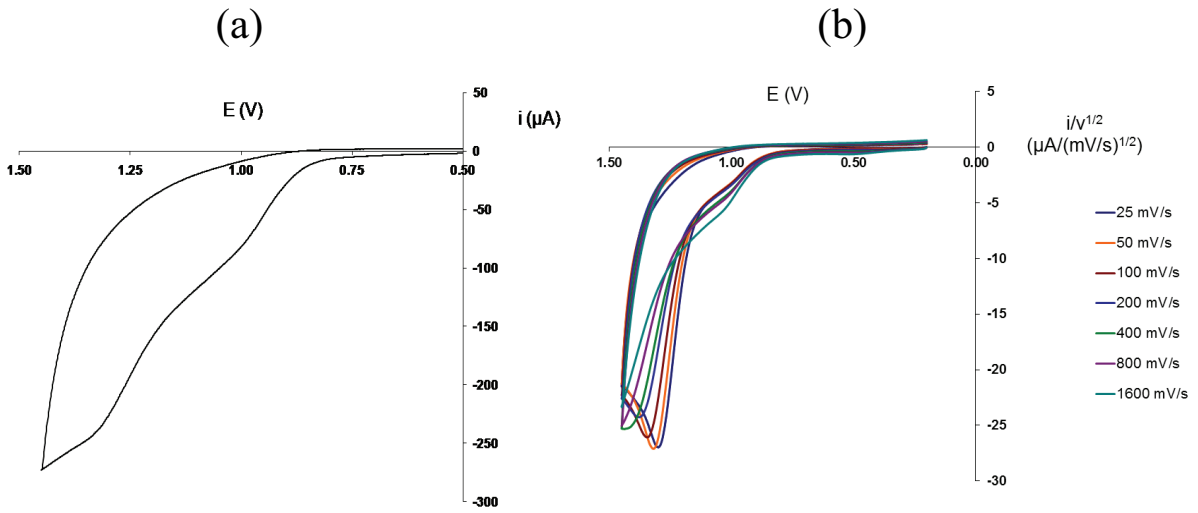

Fig. 5.4. (a) CV scan of a 0.5 mM **CoSlp** solution in 0.2 M phosphate buffer (pH 7.1); (b) CV scan of a 0.4 mM **CoSlp** solution in 0.2 M phosphate buffer (pH 7.1) at different scan rates.

Water oxidation activity of **CoSlp** was then studied in light-activated experiments involving $Ru(bpy)_3^{2+}$ and persulfate as photosensitizer and sacrificial electron acceptor, respectively. As a matter of fact, oxygen evolution was observed upon illumination of a 20 mM phosphate buffered aqueous solution (pH 7) containing **CoSlp** (15-125 μM), 1 mM $Ru(bpy)_3^{2+}$ and 5 mM $S_2O_8^{2-}$ (Figure 5.5). An initial lag-time is observed in all the kinetic traces, which can be reasonably assigned to the accumulation of a steady-state concentration of the catalytic intermediates capable of water oxidation. Oxygen evolving kinetics, in terms of rate and maximum turnover number (Table 5.1), display a strong dependence on catalyst concentration showing a saturation-inhibition behavior for [**CoSlp**] > 100 μM. The oxygen production levels off after ca. 2 hours due to $Ru(bpy)_3^{2+}$ degradation, as revealed by the

partial bleaching of the MLCT band at 450 nm. In this timeframe, **CoSlp** operates for up to 17 turnovers. The quantum yield (Φ) for oxygen evolution was found to be in the range 0.048-0.079, corresponding to overall quantum efficiencies of photon-to-oxygen conversion between 9.6-15.8%. Quantum yields were also found to follow a bell-shaped profile depending on **CoSlp** concentration, situation that was also previously observed for the tetracobalt cubane catalysts (see Chapter 4). In a similar manner, this behavior can be likely explained in terms of competitive unproductive routes emphasizing at high catalyst concentrations, most likely involving quenching of $Ru(bpy)_3^{2+}$ excited state by **CoSlp** and its intermediates along the catalytic cycle.

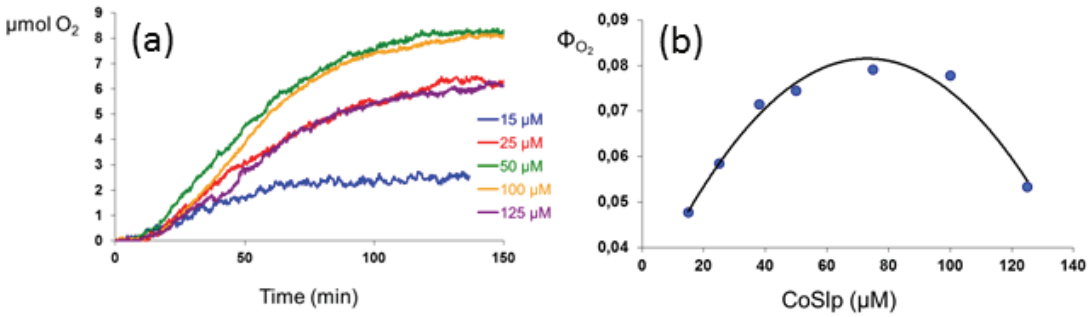

Fig. 5.5 (a) Kinetics of oxygen evolution upon continuous irradiation with 450-nm LED in 20 mM phosphate buffer solutions (pH 7) containing 15-125 μM **CoSlp**, 1 mM $Ru(bpy)_3^{2+}$, 5 mM $S_2O_8^{2-}$; (b) dependence of quantum yield on catalyst concentration.

Table 5.1. Water oxidation activity by **CoSlp**. [a]

CoSlp, μM	TON	TOF [b], s^{-1}	Φ (%) [b]
15	12	$5.58 \cdot 10^{-3}$	0.048
25	17	$4.10 \cdot 10^{-3}$	0.058
37.5	15	$3.30 \cdot 10^{-3}$	0.071
50	11	$2.61 \cdot 10^{-3}$	0.074
75	8	$1.86 \cdot 10^{-3}$	0.079
100	8	$1.36 \cdot 10^{-3}$	0.077
125	6	$0.75 \cdot 10^{-3}$	0.053

[a] Obtained upon continuous irradiation with 450-nm LED (2.63×10^{-8} einstein/s); [b] calculated in the linear part of the kinetic between 10 and 20 min of irradiation.

In order to get an insight into the electron transfer processes occurring upon light excitation, time-resolved techniques have been applied to the **CoSlp**/$Ru(bpy)_3^{2+}$/$S_2O_8^{2-}$ system. In particular, the primary hole transfer event can be conveniently monitored with laser flash photolysis, by flashing solution containing $Ru(bpy)_3^{2+}$, persulfate, and different

concentration of **CoSlp** and looking at the time evolution of the MLCT bleach at 450 nm due to reduction of the photogenerated $Ru(bpy)_3^{3+}$ oxidant by the catalyst. As shown in Figure 5.6, the rate of the recovery of the transient bleach at 450 nm depends on **CoSlp** concentration, and under pseudo-first order kinetic conditions (eqs 20-22), a bimolecular rate constant of 1.12×10^8 $M^{-1}s^{-1}$ is obtained for the first electron transfer event, likely involving the formation of a Co(III) intermediate. Interestingly, from the same laser flash photolysis experiments (Figure 5.6a) it can be observed that the secondary thermal reaction of $Ru(bpy)_3^{2+}$ with the SO_4^{-} radical (which should roughly double the amount of $Ru(bpy)_3^{3+}$ oxidant produced) becomes less efficient in the presence of **CoSlp** and again with increasing its concentration. This means that, similarly to what observed for the tetrametallic catalyst investigated with the same technique (see Chapter 3 and Chapter 4), the SO_4^{-} radical may directly oxidize the **CoSlp** catalyst instead of $Ru(bpy)_3^{2+}$.

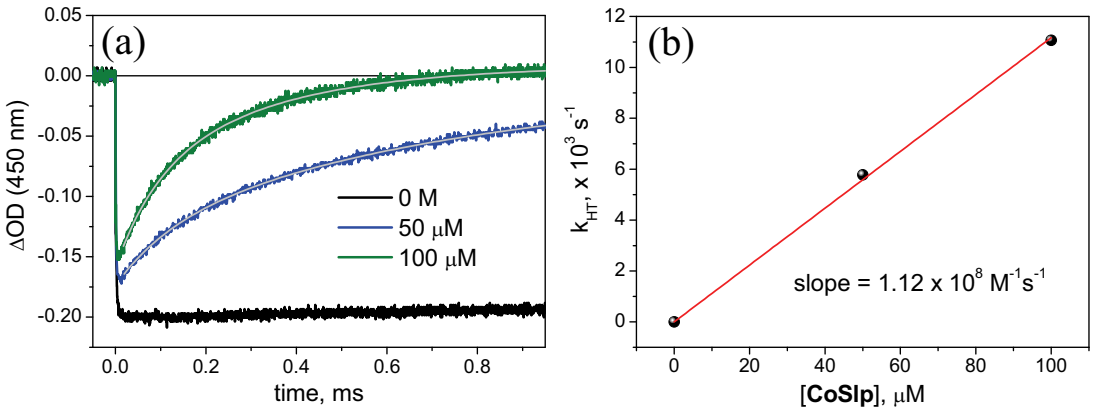

Fig. 5.6. (a) Flash photolysis experiments (355-nm excitation) obtained on 20 mM phosphate buffer (pH 7) solutions containing 50 μM $Ru(bpy)_3^{2+}$, 5 mM $S_2O_8^{2-}$, and 0-100 μM **CoSlp**. (b) Plot of the pseudo-first order rate *vs.* **CoSlp** concentration for the calculation of the bimolecular rate constant.

Additional mechanistic information can also be obtained when the concentration of photogenerated $Ru(bpy)_3^{3+}$ oxidant is increased (by working with 0.1 mM $Ru(bpy)_3^{2+}$ and increasing the excitation power, see Chapter 3) with respect to the **CoSlp** one (Figure 5.7). In fact, examination of the process with sub-stoichiometric catalyst solutions shows that each **CoSlp** is capable of performing hole-scavenging from up to ca. two $Ru(bpy)_3^{3+}$ within a time window of 40 ms. This situation suggests that, according to the catalytic scheme in Figure 5.1, the formation of a formal Co(IV) derivative by two consecutive one-electron oxidation of **CoSlp** by $Ru(bpy)_3^{3+}$ takes place in a ms time scale, whereas the subsequent processes occur in a much longer time scale.

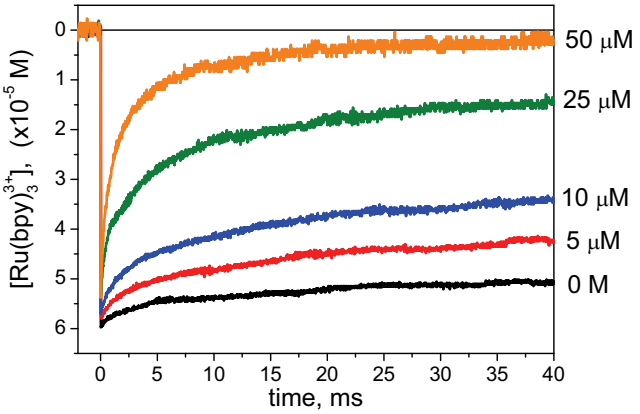

Fig. 5.7. (a) Flash photolysis experiments (355-nm excitation) obtained on 20 mM phosphate buffer (pH 7) solutions containing 0.1 mM $Ru(bpy)_3^{2+}$, 5 mM $S_2O_8^{2-}$, and 0-50 μM **CoSlp**.

As a final remark two complementary tests were conducted in order to prove the stability of the **CoSlp** catalyst under turnover conditions. First, dynamic light scattering (DLS) analysis of the reaction mixtures yields no evidence of any dispersion, suggesting the absence of Co-oxide colloids. Second, the reaction mixture was proved by EPR spectroscopy. When frozen in a CH_2Cl_2:CH_3OH 9:1 matrix, **CoSlp** shows an orthorombic EPR spectrum at 10 K with $g_1 = 7.90$, $g_2 = 1.90$ and $g_3 = 1.85$, where the signal due to the highest g component shows an eight-line cobalt-hyperfine splitting (A_1= 1100 MHz, Figure 5.8a).

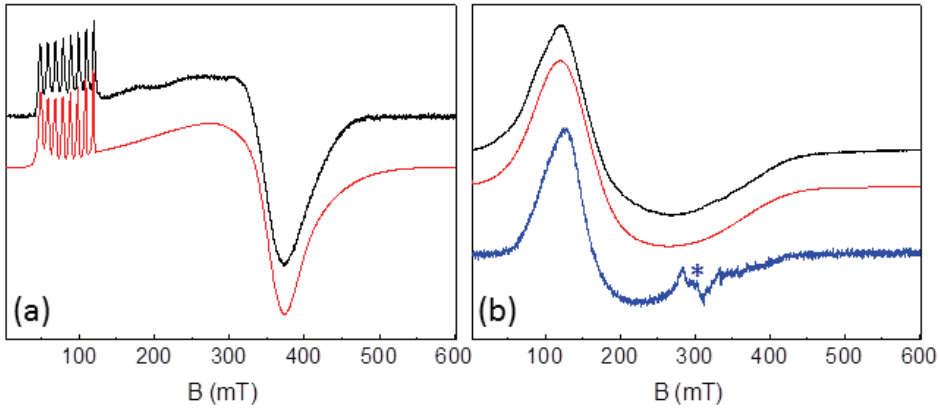

Fig. 5.8. X-band CW-EPR experimental spectra at 10 K and corresponding simulations (in red) of **CoSlp**: (a) 1 mM in CH_2Cl_2:CH_3OH 9:1; (b) black trace: 1 mM in CH_3CN:phosphate buffer (20 mM, pH 7) 1:1; blue trace: 0.5 mM in CH_3CN:phosphate buffer (20 mM, pH 7) 1:1 containing 1 mM $Ru(bpy)_3^{2+}$ and 5 mM $S_2O_8^{2-}$ after 1 h illumination. * = cavity artifact.

According to spectral simulation this is consistent with a S = 3/2 species, as expected for a d^7 high spin configuration of the Co(II) ion.[97] In aqueous phase (CH_3CN:phosphate buffer 1:1), the EPR spectrum is characterized by the presence of a featureless and nearly axial

signal with g values of $g_1 = 4.95$, $g_2 = 3.75$ and $g_3 = 2.05$ (black trace in Figure 5.8b), which is still assigned to an S = 3/2 Co(II) species.[98] The occurrence of a high-spin Co(II) signal is likely due to strong axial interactions and/or distortions of the planar structure of the complex in both media.[98] Under photocatalytic conditions, the EPR spectrum obtained for **CoSlp**, does not undergo major changes even after prolonged illumination in the presence of $Ru(bpy)_3^{2+}$ and $S_2O_8^{2-}$ (blue trace in Figure 5.7b). No signals of free Co(II) ions or Co(III) oxides are detectable, thus confirming the resting form of **CoSlp** and its stability under the operating conditions.

5.4 Ru(II) polypyridine - Cobalt(II) Salophen dyad

5.4.1 Electrochemical characterization

Electrochemical characterization by cyclic voltammetry of dyad **RuCoSlp** and its cobalt free analogue **RuSlp** was initially performed in acetonitrile solution (Table 5.2). Under cathodic scan, **RuSlp** shows three reversible reduction waves at −1.34, −1.54, and −1.89 V *vs.* Ag/AgCl. These are consistent with subsequent one-electron reductions at the phenantroline and bipyridine ligands.[96] The first two reduction events are observed also for **RuCoSlp**, at almost unaffected potentials; moreover, an irreversible process is observed at −0.94 V, and ascribed to the reduction of Co(II) to Co(I) coordinated by a salophen ligand.[99] Under anodic scan, two irreversible processes are observed for **RuSlp** at 0.70 and 1.23 V, compatible with oxidation of the salophen moiety, likely involving the phenol groups. A third, reversible event at 1.33 V is observed, which can be attributed to the Ru(III)/Ru(II) couple. In the case of **RuCoSlp**, only the reversible wave due to Ru(III)/Ru(II) couple is observed at 1.32 V, since the hydroxo groups of the salophen moiety are involved in the coordination of the cobalt center and therefore protected from oxidation.

Table 5.2. Electrochemistry of **RuSlp** and **RuCoSlp**.[a]

	E (V) *vs.* Ag/AgCl						
RuCoSlp		−1.54	−1.34	−0.94[b]			1.32
RuSlp	−1.89	−1.54	−1.34		0.70[c]	1.23[c]	1.33

[a] Obtained by cyclic voltammetry in acetonitrile (0.1 M $TBAClO_4$) on a 0.5 mM solution; working electrode, glassy carbon; counter electrode, Pt wire; reference, Ag/AgCl; [b] cathodic peak for irreversible process; [c] anodic peak for irreversible process.

5.4.2 Photophysical characterization in acetonitrile

Absorption spectra of both compounds **RuSlp** and **RuCoSlp** (compared to that of model $Ru(bpy)_3^{2+}$ in Figure 5.9) display the typical metal-to-ligand charge-transfer (MLCT) band of ruthenium(II) polypyridine complexes centered at 460 nm. This absorption bands are more broadened with respect to the MLCT transition in the $Ru(bpy)_3^{2+}$ model, likely because of partial CT character on the salophen moiety. In the case of **RuCoSlp**, a second broad absorption between 350-450 nm superimposes which may be attributed to cobalt-based transitions.[88] Finally, ligand-centered (LC) transitions in the 250-350 nm region can also be discerned ascribable to the 2,2'-bipyridine (maximum at 288 nm) and to the phenantroline-based (maxima at 334 and 348 nm) units.[100] Upon excitation at 466 nm (isosbestic point) the emissions of **RuSlp** and **RuCoSlp** are both completely quenched with respect to model $Ru(bpy)_3^{2+}$ (> 95% quenching).

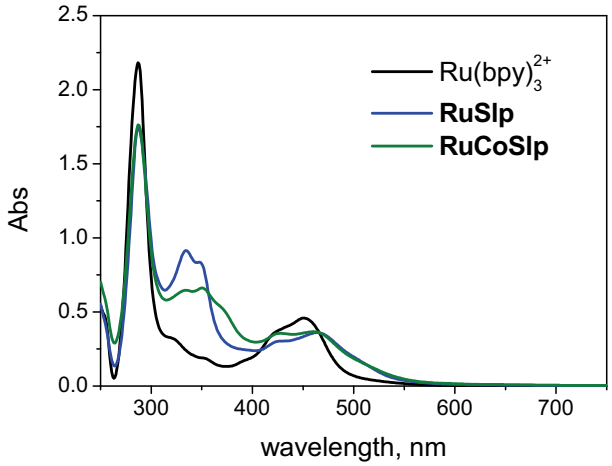

Fig. 5.9. Absorption spectra of **RuSlp** and **RuCoSlp** in acetonitrile compared to model $Ru(bpy)_3^{2+}$.

In order to get information on the mechanism responsible for the observed quenching, ultrafast spectroscopy (UFS) experiments were performed on both **RuSlp** and **RuCoSlp** compounds. Concerning compound **RuSlp**, the initial transient spectrum (1 ps time delay, Figure 5.10a) obtained upon 400-nm excitation displays an MLCT bleach and a broad absorption at longer wavelength with a relative maximum at 530 nm, which can be reasonably assigned to the triplet excited state, promptly formed by ultrafast intersystem crossing from the singlet excited state. The subsequent spectral changes are clearly biphasic. In the time window between 1-244 ps (Figure 5.10a) the MLCT bleach practically disappears, while the positive absorption increases in intensity with a shift of the maximum from 530 nm to 510

nm; the time constant for this first process is ca. 45 ps (Figure 5.11). Then, this new transient starts decaying to the baseline in the time interval between 244-1890 ps (Figure 5.10b). The time resolution of the experiment (2000 ps) does not allow any reliable detection of the kinetic parameter for this second process.

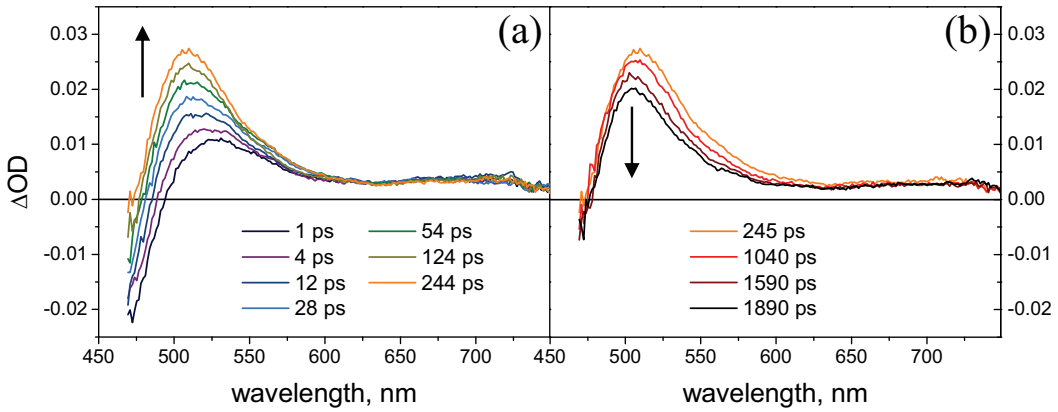

Fig. 5.10. Transient absorption spectra obtained by ultrafast spectroscopy (400-nm excitation) between (a) 1-244 ps and (b) 245-1890 ps on **RuSlp** in acetonitrile.

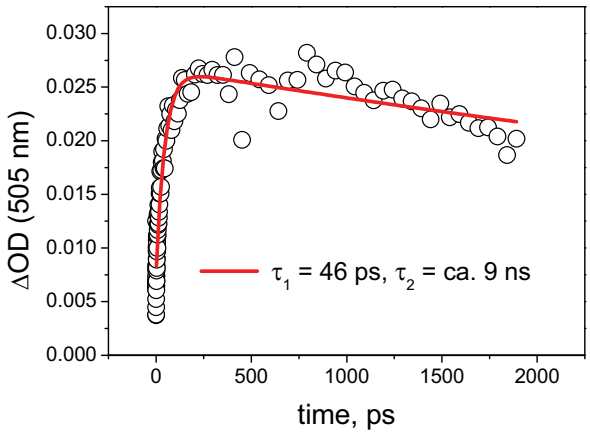

Fig. 5.11. Kinetic analysis at 505 nm with related bi-exponential fitting obtained by ultrafast spectroscopy (400-nm excitation) on **RuSlp** in acetonitrile.

However, the same transient spectrum (Figure 5.12a) can be revealed also by laser flash photolysis with a time profile (Figure 5.12b) following that of the excitation source (6-8 ns). This means that the transient produced in the first hundred ps, as observed by UFS, decays to the ground state with a time constant of about 6-8 ns.

Concerning the mechanism, from the electrochemical data shown before only reductive quenching of the MLCT excited state is thermodynamically allowed (with a driving force of ca. −0.2 eV, without electrostatic correction applied), featuring reduction of the bipyridyl

ligand of the complex and oxidation of the aromatic hydroxo groups of the salophen moiety. As a matter of fact, formation of a positive absorption with a maximum at 510 nm is a fingerprint[101] of the reduction of ruthenium polypyridine complexes. This electron-transfer process is likely proton-coupled, assisted by intramolecular hydrogen bonding within the Schiff base moiety of the ligand.[102]

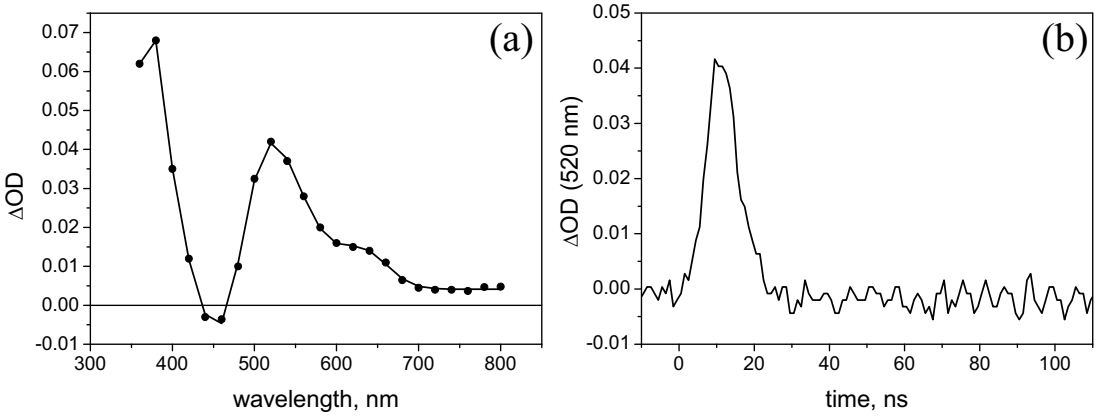

Fig. 5.12. (a) Transient absorption spectrum obtained by laser flash photolysis (355-nm excitation) at 10 ns time-delay on **RuSlp** in acetonitrile; (b) kinetic profile of the transient recorded at 520 nm.

As regarding dyad **RuCoSlp**, the insertion of the cobalt center within the salophen cavity has a remarkable impact on the photophysical processes (Figure 5.13). Similarly to **RuSlp**, the prompt transient spectrum obtained by UFS corresponds to the triplet MLCT excited state.

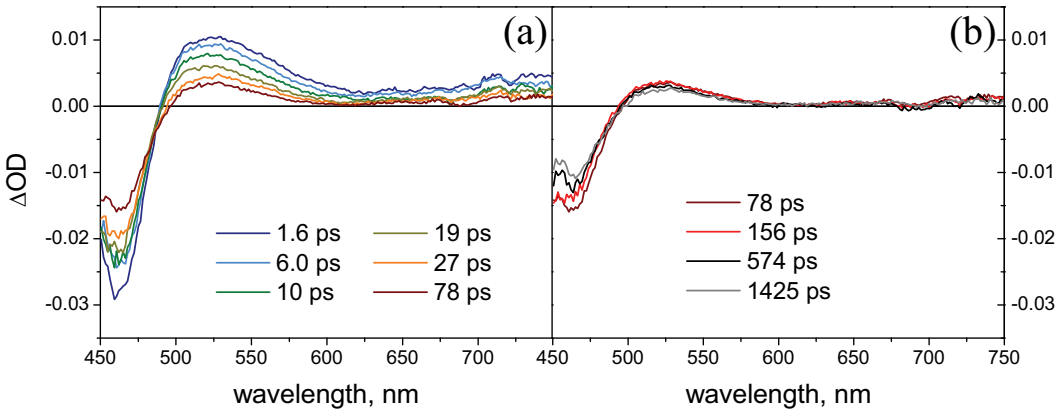

Fig. 5.13. Transient absorption spectra obtained by ultrafast spectroscopy (400-nm excitation) between (a) 1.6-78 ps and (b) 78-1425 ps on **RuCoSlp** in acetonitrile.

In this case (Figure 5.13a), however, the positive absorption at 530 nm decays rapidly with a time constant of 15 ps (Figure 5.14a). In this process (isosbestic point at 485 nm and ΔOD = −0.005), a long-lived transient is formed, characterized by little positive absorption and

substantial bleach left at 470 nm. This transient decays (Figure 5.13b) with recovery of the 470-nm bleach in a much longer time scale (estimated lifetime ca. 6 ns, Figure 5.14b). Overall, these spectral changes are compatible with fast oxidative quenching of the MLCT excited state by the cobalt center, followed by slow charge recombination.

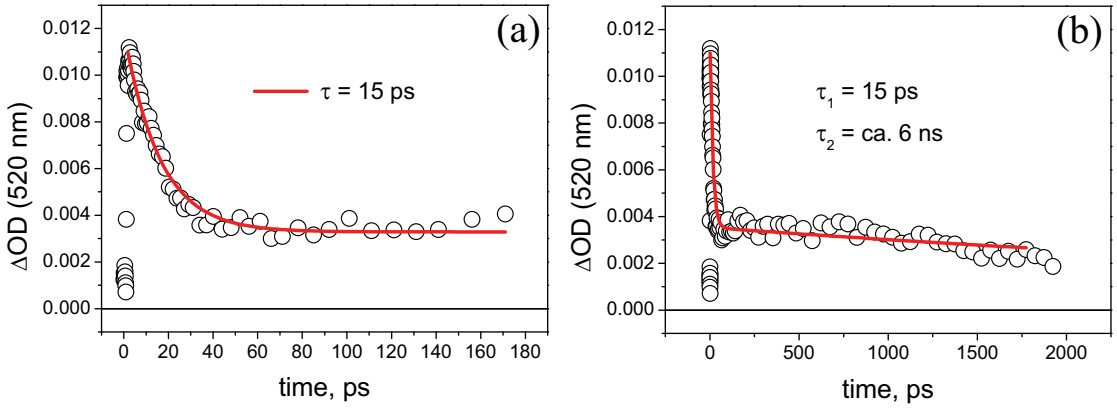

Fig. 5.14. Kinetic analysis at 520 nm obtained by ultrafast spectroscopy (400-nm excitation) on **RuCoSlp** in acetonitrile: (a) 0-180 ps and (b) 0-2000 ps.

5.4.3 Photophysical characterization in aqueous buffer and water oxidation.

The photophysical properties of both **RuSlp** and **RuCoSlp** change dramatically in aqueous phosphate buffer at pH 7, where partial recovery of the typical emission of Ru(II) polypyridine species is observed for both compounds (Figure 5.15). Moreover, the static nature of the quenching, as observed from the time-resolved decay of the MLCT emission measured by comparison with model $Ru(bpy)_3^{2+}$ (Figure 5.15b), strongly suggests that the aqueous environment introduces new chemical equilibria affecting the photoinduced dynamics. In particular, in the case of **RuSlp**, partial protonation of the salophenic ligand may take place in phosphate buffer at pH 7, thus preventing the proton-coupled electron transfer mechanism of the reductive quenching. This can be also checked considering that a similar recovery in emission is observed in acetonitrile upon addition of $HClO_4$.

Concerning **RuCoSlp**, the lack of quenching by the cobalt center seems to be hardly attributable to a simple solvent effect. A possible explanation could be the presence of more complex equilibria in aqueous environment, possibly involving (i) coordination of axial ligands to the cobalt[103] which may affect its electrochemical redox potentials, thereby making oxidative quenching thermodynamically unfavorable, or, more likely, (ii) partial leaching of cobalt from the salophenic cavity.

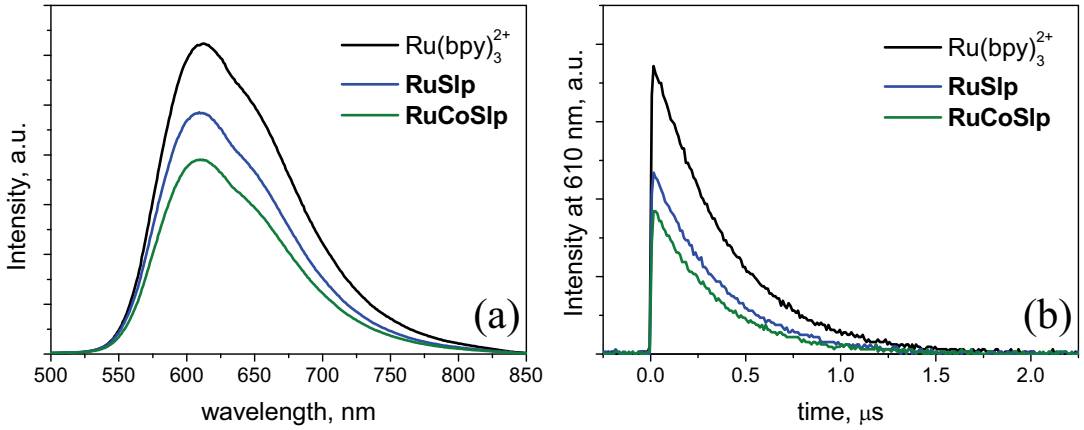

Fig. 5.15. (a) Steady-state photoluminescence spectra and (b) time-resolved emission profile at 610 nm of $Ru(bpy)_3^{2+}$, **RuSlp**, and **RuCoSlp** in 20 mM phosphate buffer (pH 7).

Light-activated water oxidation experiments were conducted in solution, in the presence of 5 mM sodium persulfate ($Na_2S_2O_8$) as the sacrificial electron acceptor and 1 mM $Ru(bpy)_3^{2+}$ as photosensitizer. In Figure 5.16, kinetics of O_2 evolution with 20 and 40 μM of **RuCoSlp** are reported (blue and red traces, respectively). In these two runs, 3.50 and 4.55 μmol of O_2 are produced after 3 hours; these correspond to a total turnover number per cobalt center of 11.7 and 7.6, respectively. The maximum O_2 production rates (measured in the linear range of the kinetic profile, between 5 and 10 minutes after irradiation) are 0.80 and 0.96 × 10^{-4} μmol s^{-1}, corresponding to turnover frequencies of 2.67 and 1.61 × 10^{-3} s^{-1}, respectively. The quantum yield (Φ) of the process for the reaction where [**RuCoSlp**] = 40 μM, defined as the ratio between the rate of O_2 produced and the photon flux absorbed by the system, is 0.037. Since the maximum value of the quantum yield in sacrificial cycles using sodium persulfate is 0.5, this value corresponds to overall 7.4% quantum efficiency of the system. As expected, the cobalt free system **RuSlp** is inactive under the same reaction conditions (black trace in Figure 5.16). In order to check if the catalytic activity could be partially ascribed to Co(II) ions leaching from **RuCoSlp** (hypothesis (ii) presented above), oxygen evolution tests were run also with $Co(NO_3)_2$ as the catalyst, at the same metal concentrations (light blue and pink traces in Figure 5.16).

Oxygen evolution occurs in the presence of either **RuCoSlp** or Co(II) ions as catalyst, with similar kinetic profiles in the concentration range 20-40 μM (Figure 5.16). Therefore, the presence of dissociation equilibria generating Co(II) aquo-ions from **RuCoSlp** cannot be ruled out by kinetic evidence. This equilibria hypothesis can justify the partial emission recovery observed when **RuCoSlp** is dissolved in aqueous solution as compared to the

quenched system in acetonitrile. The emission properties can thus be ascribed to ligand **RuSlp**, generated from **RuCoSlp** upon partial leaching of Co(II) center (Figure 5.15). Therefore, under the conditions explored, oxygen evolving catalysis is likely due to both **RuCoSlp** and aquo Co(II) ions in 20:80 ratio as possibly estimated by the emission intensity in Figure 5.15.

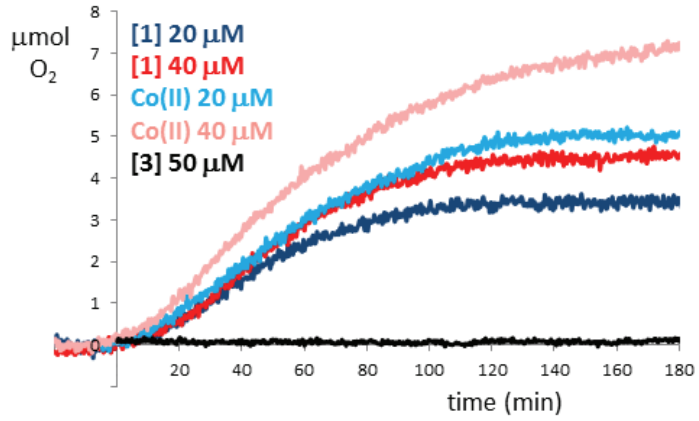

Fig. 5.16. Kinetics of oxygen evolution upon continuous 450-nm irradiation from 15 mL water solutions containing 20 mM phosphate buffer (pH 7), 5 mM $Na_2S_2O_8$, 1 mM $Ru(bpy)_3^{2+}$, and 20 µM **RuCoSlp** (blue trace), or 40 µM **RuCoSlp** (red trace), or 20 µM $Co(NO_3)_2$ (light blue trace), or 40 µM $Co(NO_3)_2$ (pink trace), or 50 µM **RuSlp** with (black trace).

Consistent with this hypothesis, albeit close to the detection limit, similar scattering intensities were observed in both cases by dynamic light scattering run on the spent reaction mixtures, likely due to cobalt oxide particles formed from Co(II) during catalysis,[104] which suggest that partial leaching of Co(II) ions from **RuCoSlp** does occur.

In photocatalytic cycles of this kind (see previous chapters) the primary photochemical process, *i.e.*, oxidative quenching of the sensitizer MLCT excited state by $S_2O_8^{2-}$, with generation of a Ru(III) species, must be followed by hole transfer to the catalyst. As determined by emission measurements on **RuCoSlp**, **RuSlp**, and $Ru(bpy)_3^{2+}$, the emission observed in phosphate buffer (Figure 5.15) is quenched comparably (> 90%) by persulfate in the three cases. Laser flash photolysis experiments have then been performed to probe the photoinduced generation of Ru(III) by excitation of **RuCoSlp** and **RuSlp** (50 µM) with $Na_2S_2O_8$ in 20 mM phosphate buffer at pH 7 (Figure 5.17). With compound **RuSlp**, after a few nanoseconds very little amounts of Ru(III) are detected (Figure 5.17b), ca. 5% of what expected from comparative experiments carried out with an isoabsorning solution at the excitation wavelength of $Ru(bpy)_3^{2+}$ (Figure 5.17a). This result is very likely ascribable to fast (sub-ns) intramolecular hole scavenging by the phenolic group, similarly to what observed in

acetonitrile solution at the excited state level (Figure 5.10). The fact that a similar, very small amount of Ru(III) is obtained with dyad **RuCoSlp** (Figure 5.17c) is fully consistent with the hypothesis of extensive dissociation of **RuCoSlp** into **RuSlp**.

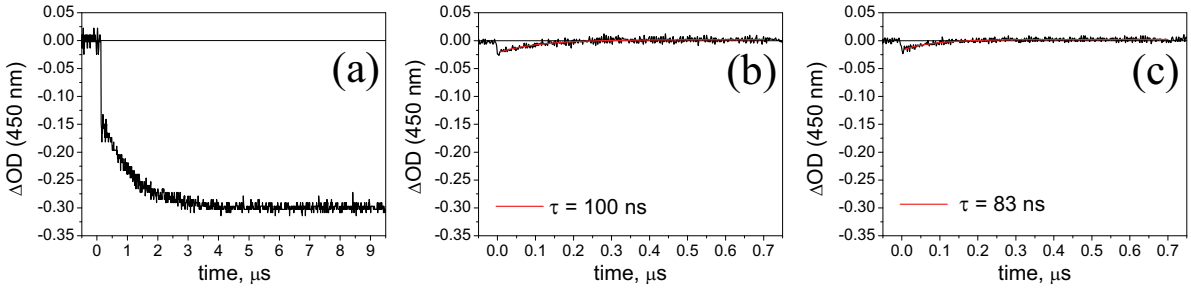

Fig. 5.17. Kinetics of MLCT bleach recovery (recorded at 450 nm) obtained by laser flash photolysis (355-nm excitation) on optically matched water solutions (at the excitation wavelength) containing 20 mM phosphate buffer (pH 7), 5 mM $S_2O_8^{2-}$, and (a) $Ru(bpy)_3^{2+}$, (b) **RuSlp**, and (c) **RuCoSlp**.

5.5 Conclusions

In this chapter a single-site cobalt(II) salophen (**CoSlp**) water oxidation catalyst has been described. Oxygen evolution has been observed upon continuous light irradiation in the presence of $Ru(bpy)_3^{2+}$ and persulfate as photosensitizer and sacrificial electron acceptor, respectively, with maximum turnover numbers (TON) and quantum yields dependent on catalyst concentration. Several complementary techniques have confirmed the integrity and stability of **CoSlp** in aqueous buffer along the whole photolysis. Time-resolved absorption spectroscopy experiments showed that **CoSlp** is capable of scavenging the hole from the photogenerated oxidant at a remarkable rate (1.12×10^8 $M^{-1}s^{-1}$ for the first electron transfer process) and undergoing two subsequent electron-transfer steps in a time-window of 40 ms.

Integration of **CoSlp** into a molecular dyad **RuCoSlp** has then been attempted in order to make hole-transfer steps as intramolecular processes. Complete electrochemical and photophysical characterization of dyad **RuCoSlp** and its non-complexated analogue **RuSlp** in acetonitrile has been performed showing photoinduced electron transfer processes occurring in the ps time-scale upon excitation of the ruthenium(II) moiety in both systems. Concerning the photosynthetic performance, water oxidation activity is retained by the **RuCoSlp** dyad with quantum efficiency up to 7.4% in the presence of external $Ru(bpy)_3^{2+}$. However, photophysical characterization in aqueous buffer seems to suggest partial instability of the latter with possible cobalt(II) ions leaching which may act as the real water oxidation catalyst.

The source of this instability can be very likely attributed to the steric hindrance between the protons in 4 and 4' positions of the phenantroline moiety and the protons of the imine groups, which is expected to cause a slight distortion of the salophenic ligand.[96a] This situation may actually affect the stability of the cobalt(II) coordination by comparison with what happens in the model complex **CoSlp** (Figure 5.2).

Chapter 6

Self-Assembling Reductant-Sensitizer-Catalyst Triad for Hydrogen Production

This chapter is the result of a collaboration with Dr. Elisabetta Iengo (Department of Chemical and Pharmaceutical Sciences, University of Trieste). Parts of this chapter can be found in the literature.[105,106]

6.1 Introduction

In the quest for solar energy conversion by photochemical water splitting, beside the oxygen evolving reaction (OER) representing the kinetic bottleneck of the overall process, the hydrogen evolving reaction (HER) plays a crucial role in the field as well. Thus large effort has been devoted worldwide for the synthesis and preparation of molecular catalysts capable of performing this reaction by employing several metal centers and different coordination chemistry.[40-47,107,108,109]

Among cobalt-based catalysts,[107,108] cobaloximes (Figure 6.1) have emerged importantly in the last decades. As a matter of fact, their ability to act as hydrogen evolving catalysts has been well documented in electrochemical experiments[110] as well as in homogeneous light-activated experiments in the presence of sacrificial electron donors and involving either noble-metal containing[111,112,113,114,115] or noble-metal-free photosensitizers.[116,117]

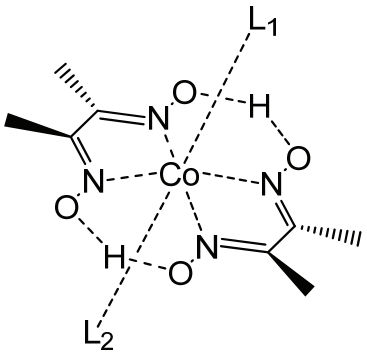

Fig. 6.1. General molecular structure of a cobaloxime.

Concerning the catalytic mechanism,[118] several pathways are actually available towards hydrogen generation (Figure 6.2) depending on the experimental conditions. The key step is the formation of a Co(III)-hydride intermediate by reduction and protonation of a Co(II) species, which can then evolve hydrogen either by protonation (*heterolythic route*) or by disproportionation (*homolythic route*) depending mainly on the proton donor used (for electrocatalytic experiments) or the pH (in photochemical ones). In some instances, however,

if both the acidic strength of the proton source is not high enough (electrocatalysis) or the pH low enough (photocatalysis) to protonate the Co(III)-H intermediate and the steady-concentration of reducing agent is too big with respect to that of the Co(III)-H intermediate (both electro- and photocatalysis), an additional reduction may take place, yielding a Co(II)-H species, which then can evolve hydrogen similarly by either a *heterolythic* or a *homolythic* pathway.

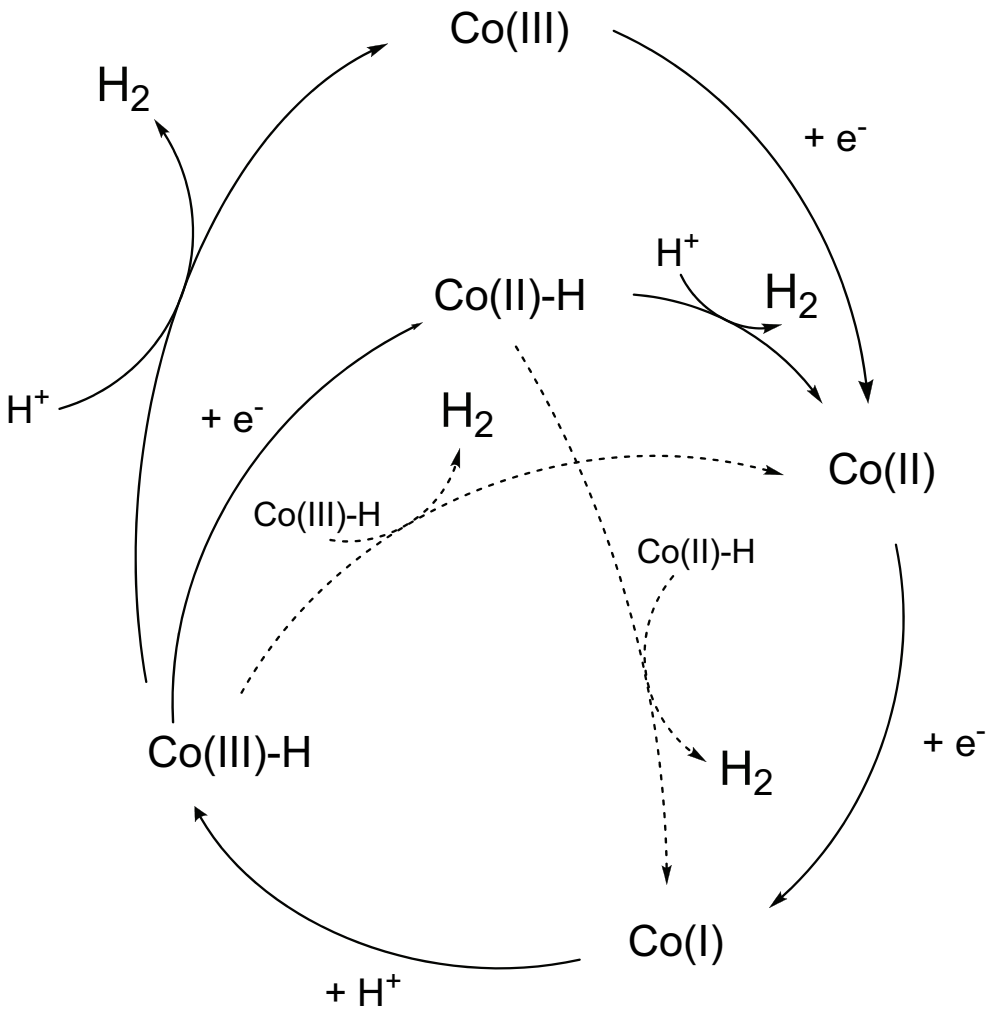

Fig. 6.2. Catalytic mechanism for hydrogen generation by cobaloxime. Solid lines, heterolythic mechanism; dashed lines, homolythic mechanism.

Various types of synthetic strategies have been also applied to suitably assemble cobaloximes into functional supramolecular systems. For instance, supramolecular dyads, by coupling the cobaloxime catalyst unit to metal complexes[119,120] or organic sensitizers, such as porphyrins/corroles,[121,122] perylenebisimides,[123] and boron-dipyrromethenes (BODIPYs),[124] have been indeed prepared and studied.

Aluminum(III) pyridylporphyrins are interesting molecular components for the construction of functional supramolecular arrays.[125,126] What makes them particularly attractive is their bifunctional nature, *i.e.*, the simultaneous presence of a Lewis acid (the aluminum center) and a Lewis basic (the *meso*-pyridyl group) function. The aluminum center can axially bind a variety of ligands, with particular affinity for oxygen-based functionalities, while the pyridyl function can coordinate to a large variety of transition metals. By using the acid and basic functionalities and exploiting selective coordination, aluminum pyridylporphyrins can be used to tackle the non-trivial problem of obtaining intrinsically asymmetric three-component supramolecular systems by self-assembling. The aluminum(III) porphyrin platform has been recently employed to self-assemble a triad for photoinduced charge separation.[126] In that case, the Lewis acid and basic functions were used to bind, an electron acceptor (a carboxyl derivative of naphthalene bisimide) and an electron donor unit (a ruthenium porphyrin), respectively. Selective coordination (of carboxyl to Al and of pyridyl to Ru) ensured exclusive formation of the required triad by simple mixing of the molecular components. Stepwise photoinduced charge separation was verified by ultrafast spectroscopic techniques.

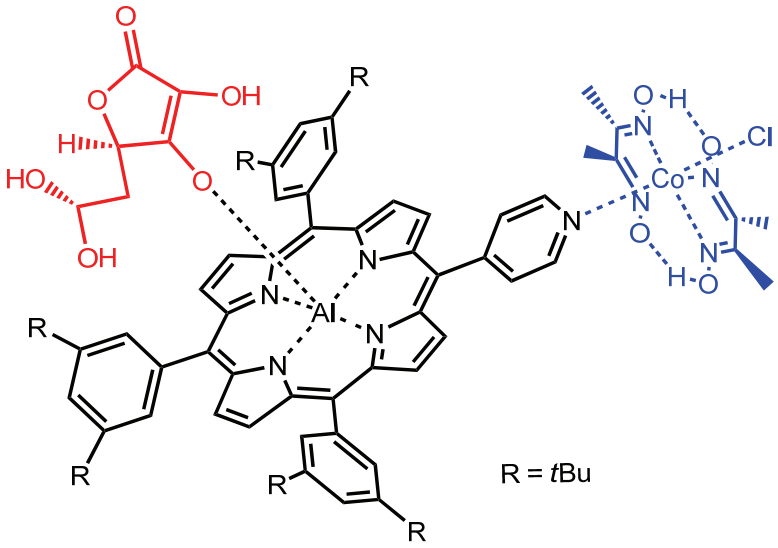

Fig. 6.3. Schematic representation of the target self-assembling triad for photoinduced hydrogen production.

In this chapter the aluminum(III) pyridylporphyrin platform will be exploited to obtain a noble-metal-free reductant/sensitizer/catalyst triad system for photoinduced hydrogen generation by self-assembling. A hydrogen evolving catalyst can be bound *via* the *meso*-pyridyl group, while axial coordination at the aluminum center can be used to reversibly tether a variety of sacrificial oxygen-based electron donors.

In Section 6.3 the self-assembling of a triad (Figure 6.3) involving a cobaloxime catalyst and an ascorbate sacrificial donor will be studied, and hydrogen evolving experiments will be performed to check the photocatalytic activity. Time-resolved spectroscopic technique will be also employed to get an insight into the photocatalytic mechanism.

In Section 6.4 a series of porphyrin-cobaloxime dyads will be investigated in detail from a photophysical viewpoint in order to clarify some key mechanistic issues.

6.2 Experimental section

6.2.1 Synthesis of the component of the self-assembling triad

The synthesis of **AlP(OH)** was performed by Dr. Elisabetta Iengo at the Department of Chemical and Pharmaceutical Sciences of the University of Trieste following literature procedures.[125,126] **AlP(OH).** 5-(4'pyridyl)-10,15,20-(3,5-di-*tert*-butyl)-triphenylporphyrin (**P**) was synthesized and purified according to literature methods.[127] 300 mg of **P** (2.82 mmol) were then dissolved in 100 mL of dry toluene and 0.2 mL of trimethylaluminum (2.0 M in toluene, 5.6 mmol) were added under N_2 atmosphere. The solution was stirred at room temperature, under N_2 atmosphere, for 4 hr, at which time 5 mL of H_2O were added and stirring was continued overnight. The toluene was removed and the violet solid thus formed was redissolved in CH_2Cl_2. The solution was filtered dried over Na_2SO_4 and passed over a column of alumina to give 265 mg of product (85%). ^{1}H NMR (pyridine-d_5), δ_H: 9.28 (6H, m, β_4+ β_3+β_2), 9.12 (4H, m, β_1+ py_{Ha}), 8.2 (6H, br d, oH+oH'), 8.15 (2H, d, py_{Hb}), 7.84 (3H, d, br, pH+pH'), 1.54 (s, *t*Bu), 1.52 (s, *t*Bu).

Co(dmgH)(H_2O). $Co(dmgH)_2Cl(H_2O)$ was synthesized by slightly adapting a literature procedure.[128] 1.10 g of $CoCl_2 \cdot 6H_2O$ (5 mmol) and 1.18 g of $dmgH_2$ (dimethylglioxime, 11 mmol) were dissolved in 50 mL of 95% ethanol, and heated at 70°C. 5 mL of a 1 M NaOH solution (5 mmol) were then added to the whole mixture and the solution was stirred for 1 hr at 70°C. After cooling at room temperature, a stream of air was blown through the solution for 30 min. The solution was filtered to remove side-reaction products and concentrated to allow precipitation. The so obtained brown crystals were collected by filtration on a Büchner funnel and washed with 5 mL water and then with 10 mL diethyl ether. The solid was then dried at room temperature to yield 590 mg of product (35%). ^{1}H NMR (acetonitrile-d_3), δ_H: 18.40 (2H, br s, OHO), 2.45 (12H, s, CH_3).

Co(dmgH)(EtPy). $Co(dmgH)_2Cl$(4-ethylpyridine), used as molecular model of the cobaloxime unit in several instances, was synthesized according to literature procedures.[128]

6.2.2 Synthesis of porphyrin-cobaloxime dyads and model compounds

The synthesis of monopyridyl- (molecular precursors) and tetraphenyl- (molecular models) porphyrins was performed by Dr. Elisabetta Iengo at the Department of Chemical and Pharmaceutical Sciences of the University of Trieste.

Molecular precursors.

5-(4'-pyridyl)-10,15,20-triphenylporphyrin. 5-(4'-pyridyl)-10,15,20-triphenylporphyrin was synthesized and purified according to literature methods.[127]

[5-(4'-pyridyl)-10,15,20-triphenylporphyrinato] zinc(II). A concentrated CH_2Cl_2 solution of 5-(4'-pyridyl)-10,15,20-triphenylporphyrin was treated overnight with an 8-fold molar excess of $Zn(CH_3COO)_2$ dissolved in the minimum amount of MeOH. The solution was dried in vacuo and the obtained solid dissolved in CH_2Cl_2. The product was precipitated by addition of *n*-hexane, removed by filtration, washed thoroughly with cold methanol and diethyl ether and vacuumdried (Yield > 85%). ^{1}H NMR ($CDCl_3$), δ_H: 8.90 (2H, d, β_4), 8.85 (2H, d, β_3), 8.55 (2H, d, β_2), 8.20 (2H, d, oH'), 8.10 (4H, d, oH), 7.75 (3H, m, mH'+pH'), 7.68 (6H, m, mH+pH), 7.45 (2H, d, β_1), 6.25 (2H, br s, py_{Hb}), 3.45 (2H, br s, py_{Ha}).

[5-(4'-pyridyl)-10,15,20-(3,5-di-*tert*-butyl)-triphenylporphyrinato-hydroxo] aluminum(III).[125,126] See above **AlP(OH)**.

Molecular dyads.

P-Co. For {5-(4'-pyridyl)-10,15,20-triphenylporphyrin}chloro bis(dimethylglyoximate) cobalt(III), 49.2 mg (0.08 mmol) of 5-(4'-pyridyl)-10,15,20-triphenylporphyrin were dissolved in 400 mL of a 1/5 CH_3CN/CH_2Cl_2 mixture and 101.2 mg (0.32 mmol) of $Co(dmgH)_2Cl(H_2O)$ were added to the solution under continuous stirring. The reaction mixture was left stirring for 1 hr at room temperature, and then concentrated to allow precipitation; the violet solid was collected by filtration on a Büchner funnel and washed with 10 mL diethyl ether to yield 55.2 mg of **P-Co** (73%). ^{1}H NMR (CD_2Cl_2), δ_H: 18.65 (2H, br s, OHO), 8.93 (6H, m, py_{Ha}+ β_3+ β_4), 8.70 (2H, d, β_2), 8.66 (2H, d, β_1), 8.24 (6H, m, oH+oH'), 8.16 (2H, d, py_{Hb}), 7.84 (9H, m, mH+mH'/pH+pH'), 2.60 (12H, s, CH_3), -2.85 (2H, s, NH).

ZnP-Co. For {[5-(4'-pyridyl)-10,15,20-triphenylporphyrinato] zinc(II)} chloro bis(dimethylglyoximate) cobalt(III), 22.3 mg (0.03 mmol) of [5-(4'-pyridyl)-10,15,20-triphenylporphyrinato] zinc(II) were dissolved in 190 mL 1/5 CH_3CN/CH_2Cl_2 mixture and 41.5 mg (0.12 mmol) of $Co(dmgH)_2Cl(H_2O)$ were added to the solution under continuous stirring. The reaction mixture was left stirring for 1 hr at room temperature, and then concentrated to allow precipitation. The violet solid was collected by filtration on a Büchner funnel and washed with 10 mL diethyl ether to yield 23.4 mg of **ZnP-Co** (71%). ^{1}H NMR (CD_2Cl_2), δ_H: 18.65 (2H, br s, OHO), 9.00 (6H, m, β_2+ β_3+ β_4), 8.78 (2H, d, β_1), 8.63 (2H, d, py_{Ha}), 8.23 (6H, m, oH+oH'), 8.16 (2H, d, py_{Hb}), 7.82 (9H, m, mH+mH'/pH+pH'), 2.60 (12H, s, CH_3).

AlP-Co. For {[5-(4'-pyridyl)-10,15,20-(3,5-di-*tert*-butyl)-triphenylporphyrinato-hydroxo] aluminum(III)}chloro bis(dimethylglyoximate) cobalt(III), 30 mg (0.03 mmol) of [5-(4'-pyridyl)-10,15,20-(3,5-di-*tert*-butyl)-triphenylporphyrinato-hydroxo] aluminum(III) were dissolved in 190 mL 1/5 CH_3CN/CH_2Cl_2 mixture and 41.1 mg (0.12 mmol) of $Co(dmgH)_2Cl(H_2O)$ were added to the solution under continuous stirring. The reaction mixture was left stirring for 1 hr at room temperature, and was then concentrated to allow precipitation. The violet solid was collected by filtration on a Büchner funnel and washed with 10 mL diethyl ether to yield 21.7 mg of **AlP-Co** (55%). ^{1}H NMR (CD_2Cl_2), δ_H: 18.4 (2H, br s, OHO), 9.00 (8H, m, β_2+ β_3+ β_4+ py_{Ha}), 8.69 (2H, d, β_1), 8.10 (8H, m, oH+oH'+py_{Hb}), 7.78 (3H, m, pH+pH'), 2.45 (12H, s, CH_3), 1.65 (m, *t*Bu).

Molecular models

P (5,10,15,20-tetraphenylporphyrin), **ZnP** ([5,10,15,20-tetraphenylporphyrinato] zinc(II)), and **AlP** (5,10,15,20-(3,5-di-*tert*-butyl)-tetraphenylporphyrinato-hydroxo} aluminum(III)) were prepared with the same experimental procedures reported for the monopyridyl porphyrin analogues (see above).

6.2.3 Apparatus and procedures

Ascorbic acid was purchased from Sigma Aldrich and used as received, all other reagents were used as received. Solvents of spectroscopic grade were used. See Chapter 2 for details on the electrochemical, spectroscopic, and photolysis apparatus. A *Nonius Kappa CCD* diffractometer was employed for obtaining the X-ray structure of **P-Co**, using a graphite monochromated Mo Kα radiation (λ = 0.7107 Å).

6.3 Self-assembling reductant/sensitizer/catalyst triad

The molecular components (Figure 6.4) used for the assembling of the reductant/photosensitizer/catalyst (R-P-C) target triad system are: (i) an aluminum monopyridyl porphyrin bearing an axial hydroxo group, (5-(4'-pyridyl)-10,15,20-(3,5-di-*tert*-butyl)-triphenylporphyrinato-hydroxo)aluminum(III)), (**AlP(OH)**); (ii) a cobaloxime with a chloride and a labile water ligand in the axial positions, chloro(aquo)bis(dimethylglioximate) cobalt(III), (**Co(dmgH)(H$_2$O)**); (iii) ascorbic acid (**AscH**).

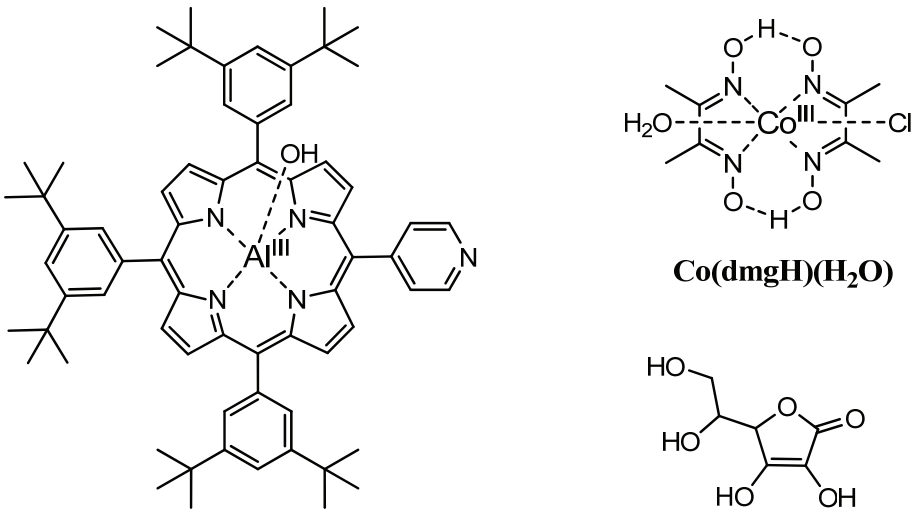

Fig. 6.4. Molecular components used in this study.

6.3.1 Photophysics and electrochemistry of molecular components

The absorption spectrum of **AlP(OH)** in tetrahydrofuran (Figure 6.5a, black trace) is typical of metallo porphyrins, with Soret band at 425 nm and Q-bands at 521, 559, and 600 nm; a weak additional absorption band at ca. 620 nm is also observed, arising from self-association through formation of aluminum-pyridyl bonds.[126] Both **Co(dmgH)(H$_2$O)** and **AscH** have negligible absorption at $\lambda > 400$ nm. The fluorescence of **AlP(OH)** (615, 663 nm, black trace in Figure 6.5b) has a lifetime of 6.4 ns in THF. Relevant electrochemical data on these molecular components, as well as on their assemblies, are given in Table 6.1.

Table 6.1. Electrochemical data for molecular units and dyads.[a]

	Oxidation (V)			Reduction (V)			
AlP(OH)	1.22[b]	0.96[b]				−1.22[b]	−1.59[b]
Co(dmgH) [c]				−0.68[d]	−1.22[d]		
AlP(OH)-Co(dmgH)	1.21[b]	1.02[b]		−0.63[d]	−1.13[d]	−1.23[b]	−1.66[b]
Asc-AlP	1.38[b]	1.12[b]	0.61[e,f]			−1.20[b]	

[a] Obtained by differential pulse voltammetry (DPV) in THF at 298 K, 0.1 M TBA(PF_6) as supporting electrolyte, SCE as reference electrode, ferrocene (0.56 V *vs.* SCE)[129] as internal standard, 50 mV pulse width; [b] process attributed to the porphyrin unit; [c] for solubility reasons, $Co(dmgH)_2Cl(EtPy)$ was used as a model instead of the aquo complex; [d] process attributed to the cobaloxime unit; [e] process attributed to ascorbate; [f] irreversible process.

6.3.2 Self-assembling on the aluminum porphyrin platform

The assembling of the triad system can be appropriately characterized in THF, a solvent that provides the best balance between the solubility of the three molecular units, by separately studying the formation of the two component dyads. The association between the aluminum porphyrin and the cobaloxime (eq 25), taking place by coordination of the *meso*-pyridyl group of the porphyrin to the cobalt center with displacement of the labile water ligand can be followed by conventional stationary techniques (Figure 6.5).

$$\textbf{AlP(OH)} + \textbf{Co(dmgH)(H}_2\textbf{O)} \rightleftharpoons \textbf{AlP(OH)-Co(dmgH)} + H_2O \qquad (25)$$

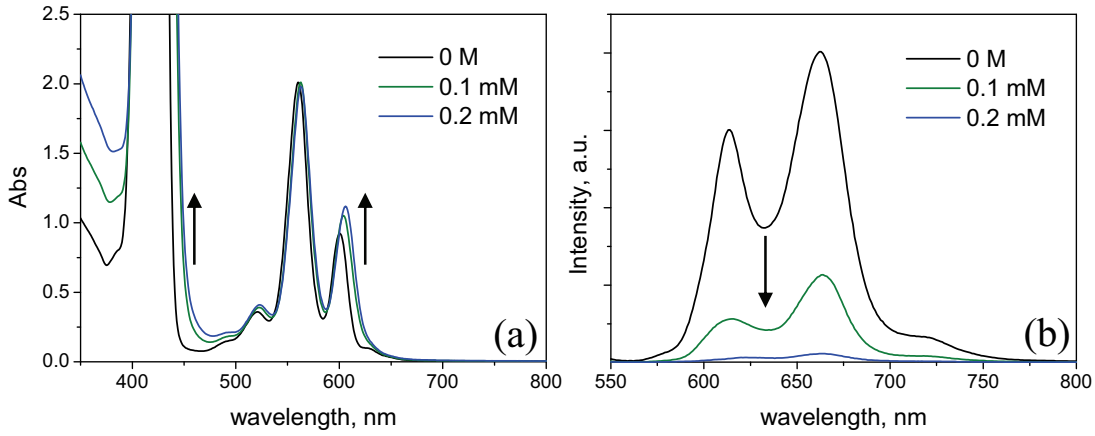

Fig. 6.5. (a) Absorption spectra and (b) emission spectra of 0.1 mM **AlP(OH)** in THF in the presence of 0-0.2 mM **Co(dmgH)(H$_2$O)**.

In fact, complexation of the cobaloxime catalyst with the aluminum porphyrin is followed by a 5-nm red shift of the porphyrin Soret- and Q-bands (Figure 6.5a) and by the quenching of the fluorescence (Figure 6.5b). From the spectrofluorimetric titration (Figure 6.6), the association equilibrium in 0.1 mM THF solution is seen to require ca. × 2 molar excess of **Co(dmgH)(H$_2$O)** in order to obtain complete formation of the dyad.

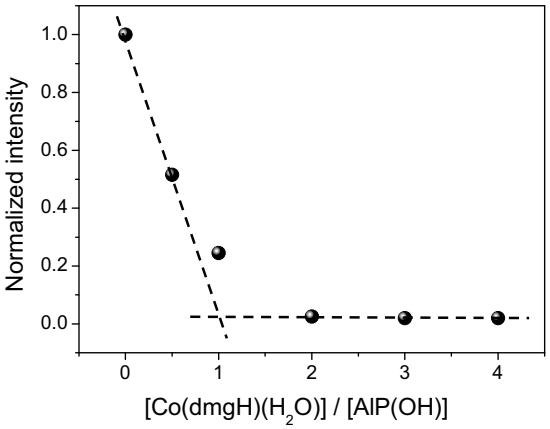

Fig. 6.6. Spectrofluorimetric titration of a 0.1 mM **AlP(OH)** solution in THF with **Co(dmgH)(H$_2$O)**.

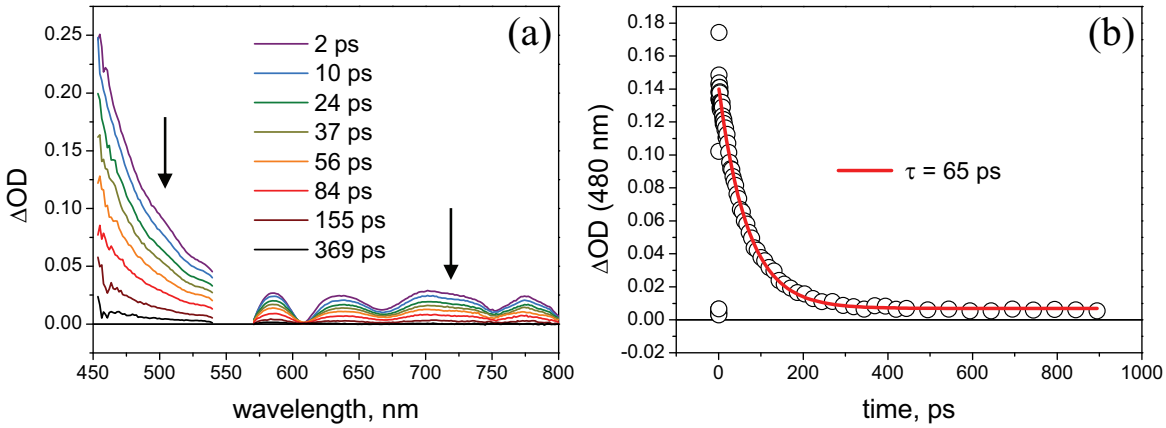

Fig. 6.7. (a) Transient absorption spectra obtained by ultrafast spectroscopy (excitation at 550 nm) in THF with 0.1 mM **AlP(OH)** and 0.3 mM **Co(dmgH)(H$_2$O)**; (b) kinetic analysis at 480 nm.

The fluorescence quenching in the associated dyad takes place in a time scale shorter than the time resolution of the time-correlated single photon counting technique, *i.e.* < 250 ps.

Time-resolved femtosecond spectroscopy (Figure 6.7) shows a clean decay of the absorption of the aluminum porphyrin excited singlet state to the ground state, with a time constant of 65 ps, which, according to the electrochemical potentials of Table 6.1, can be reasonably assigned to a photoinduced electron transfer (estimated $\Delta G° = -0.4$ eV, without electrostatic correction applied)[130] from the aluminum porphyrin excited state ($E^{0\text{-}0} = 2.04$ eV)

to the cobaloxime (oxidative quenching), followed by a faster charge recombination (see Section 6.4 for a more detailed account).

In the same way, association of the aluminum porphyrin with the ascorbic acid sacrificial electron donor (eq 26) can be followed by both conventional absorption and emission techniques. As a matter of fact, addition of ascorbic acid to a THF solution containing **AlP(OH)** brings about a red-shift of the absorption porphyrin bands (Figure 6.8a) and the quenching of the fluorescence (Figure 6.8b).

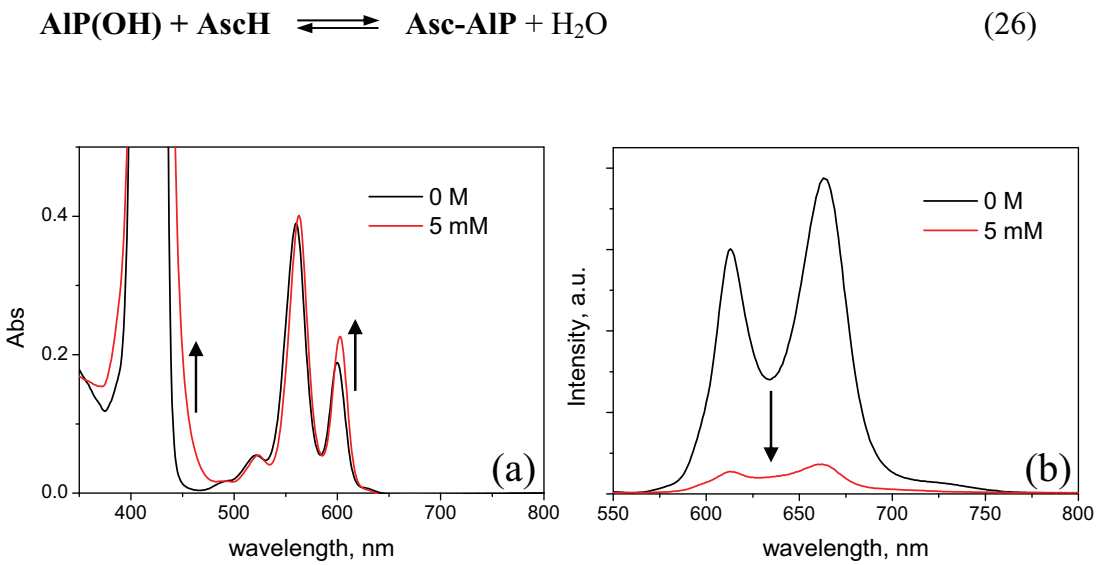

Fig. 6.8. (a) Absorption spectra and (b) emission spectra of 10^{-4} M **AlP(OH)** in THF in the presence of 0-5 mM **AscH**.

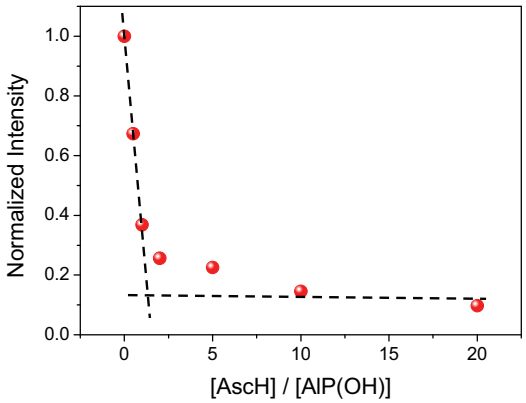

Fig. 6.9. Spectrofluorimetric titration of a 0.1 mM **AlP(OH)** solution in THF with **AscH**.

As it can be checked from the spectrofluorimetric titration in Figure 6.9, the association in 0.1 mM THF solution is efficient, with ca. 70% dyad formed with stoichiometric amounts and practically complete formation with 10-fold excess of ascorbic acid. The quenching in the

associated dyad very likely takes place by reductive photoinduced electron transfer (estimated $\Delta G° = -0.2$ eV from the electrochemical data in Table 6.1, without electrostatic correction applied)[130] involving reduction of the porphyrin and oxidation of the ascorbate donor. The process in the dyad takes place in a time scale shorter than the time resolution of the time-correlated single photon counting technique, *i.e.* < 250 ps. Time-resolved ultrafast spectroscopy (Figure 6.10) shows a clean decay of the absorption of the aluminum porphyrin excited singlet state to the ground state (bi-exponential, with time constants of 5 ps, 60%, and 26 ps, 40%), without apparent accumulation of significant amounts of transient intermediate products.

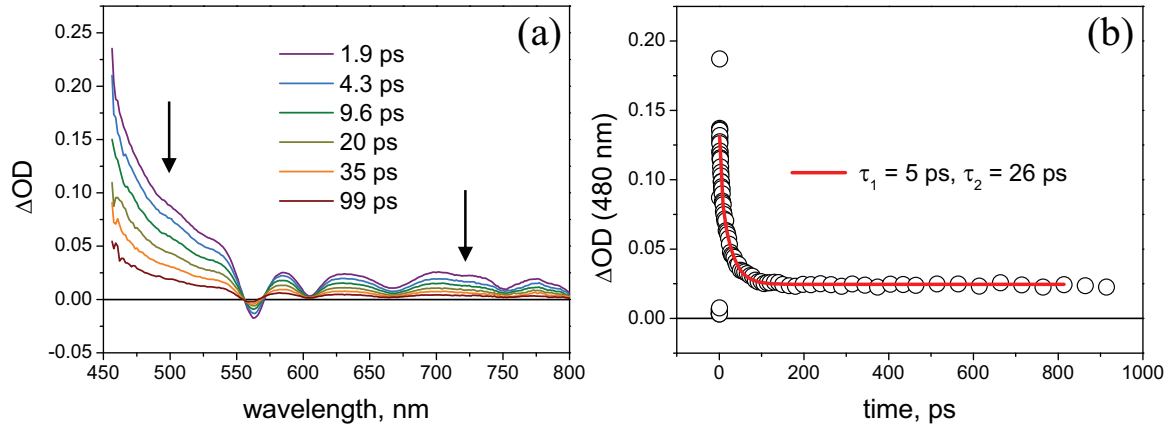

Fig. 6.10. (a) Transient absorption spectra obtained by ultrafast spectroscopy (excitation at 550 nm) in THF in the presence of 0.1 mM **AlP(OH)** and 10 mM **AscH**; (b) kinetic analysis at 480 nm.

This implies that the reductive electron transfer is largely reversible, in the sense that photoinduced charge separation is followed by ultrafast charge recombination to reform the ground state. This reversible behavior is quite unexpected since ascorbic acid is known from the electrochemistry to show an irreversible oxidation in both aqueous media[131] and THF (Table 6.1). Upon continuous visible irradiation, however, **Asc-AlP** dyad undergoes some irreversible changes as monitored by spectrophotometric technique (Figure 6.11): the spectral variations, with development of a characteristic band at 630 nm, indicate the formation of chlorin[78,132] likely originating, upon further reduction or disproportionation and protonation, from the metal porphyrin radical anion.[133] The quantum yield of chlorin formation in THF is estimated in ca. 10^{-2}, a figure fully compatible with the failure to observe irreversibility by time-resolved spectroscopy.

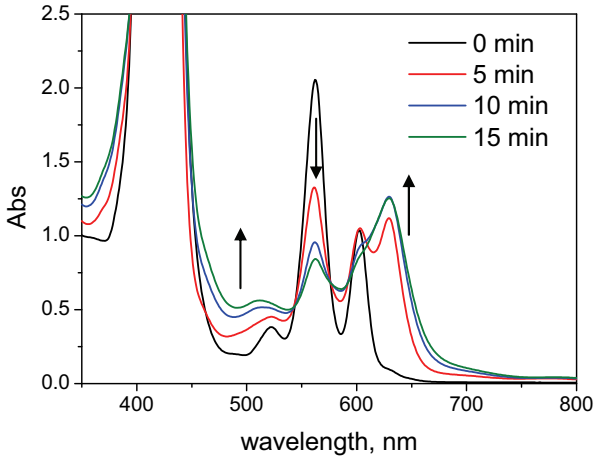

Fig. 6.11. Time-dependent absorption spectra obtained upon continuous visible irradiation of a THF solution containing 0.1 mM **AlP(OH)** and 10 mM **AscH.**

The results obtained on the two dyads suggest complete formation of the **Asc-AlP-Co(dmgH)** triad in a THF solution containing 0.1 mM **AlP(OH)**, ≥ 1 mM **AscH,** and ≥ 0.2 mM **Co(dmgH)(H$_2$O)**. In the triad, as well as in the component dyads, the aluminum porphyrin fluorescence is completely quenched.

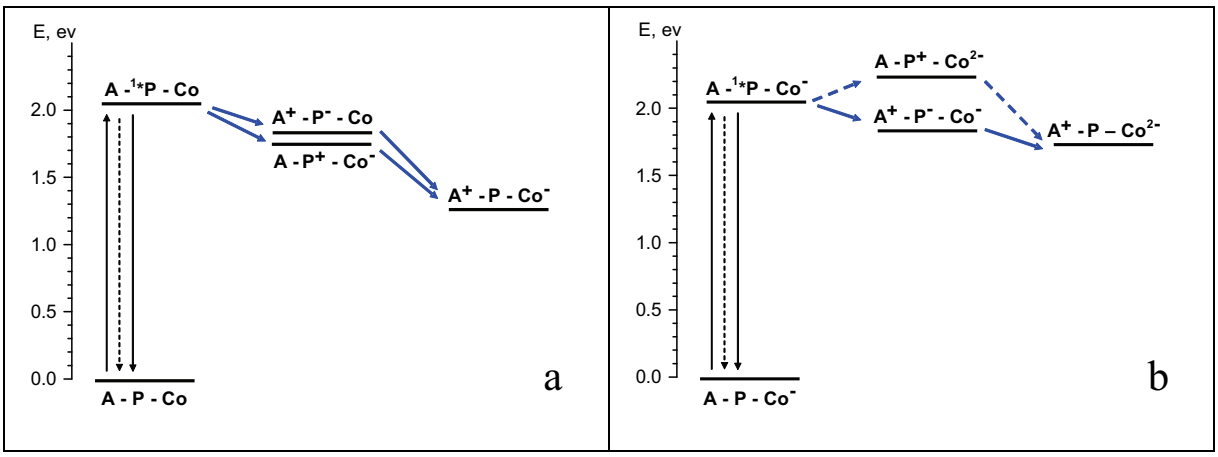

Fig. 6.12. Energy levels (without electrostatic correction applied) and elementary electron transfer steps potentially involved in the (a) **Asc-AlP-Co(dmgH)** triad and (b) **Asc-AlP-Co(dmgH)**$^-$ triad with a reduced cobaloxime. For space reasons: A = **Asc**, P = **AlP**, Co = **Co(dmgH)**.

As far as hydrogen evolution by the self-assembling **Asc-AlP-Co(dmgH)** triad is concerned, two-electron reduction steps of the cobaloxime catalyst are required (Figure 6.2). According to the observed quenching and the electrochemical data (Table 6.1) the first electron transfer process may occur by both oxidative and reductive quenching of the aluminum porphyrin sensitizer (see energy level diagram in Figure 6.12a). As regarding the second electron transfer process in a formal **Asc-AlP-Co(dmgH)**$^-$ triad with a reduced

cobaloxime (see energy level diagram in Figure 6.12b), it is seen that, at least by one of the two pathways, namely reductive quenching by ascorbate, the second reduction step of the cobaloxime unit is thermodynamically allowed.

6.3.3 Hydrogen evolution experiments

The hydrogen evolution experiments were performed by irradiating Ar-purged solutions (5 mL) with a 175 W Xe arc-lamp and a cut-off filter at 400 nm, and by monitoring hydrogen evolution by gas chromatography. In neat THF (Figure 6.13), some hydrogen was detected upon visible irradiation of a solution containing **AlP(OH)** 0.1 mM, **Co(dmgH)(H$_2$O)** 0.3 mM, **AscH** 10 mM.

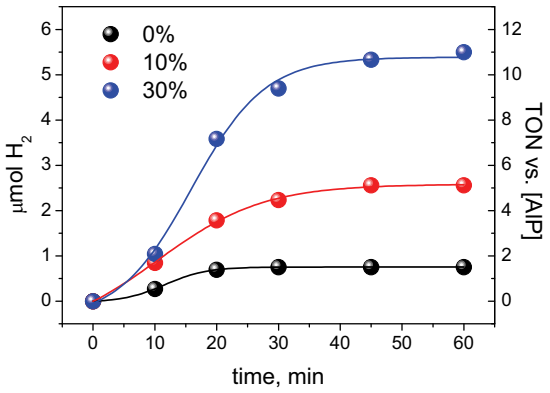

Fig. 6.13. Effect of water content on photocatalytic hydrogen evolution in THF (0.1 mM **AlP(OH)**, 0.3 mM **Co(dmgH)(H$_2$O)**, 10 mM **AscH**).

It was produced, however in small, non-catalytic amounts (0.75 µmol, corresponding to turnover number values of 0.5 relative to **Co(dmgH)(H$_2$O)** and 1.5 relative to **AlP(OH)**, quantum yield, ca. 4×10^{-4}). An improvement in hydrogen production was then obtained upon addition of water to the organic solvent (Figure 6.13). Therefore, optimization of the system was performed in water/organic solvent mixtures containing 0.1 mM **AlP(OH)**, by checking the effects on hydrogen evolution of systematic changes in (i) nature of the organic solvent, (ii) fractional amount of water, (iii) pH of the irradiated solution, (iv) concentration of ascorbic acid, (v) concentration of cobaloxime catalyst, (vi) concentration of added dimethylglyoxime ligand. Among various water/organic solvent mixtures tested, those containing acetone were found to give the best results in terms of both quantum yield (slope) and maximum chemical yield (long time asymptotic behavior) (Figure 6.14a). In water/acetone solvent mixtures, the hydrogen evolving performance first improves with

increasing water content up to 30%, but then decreases upon further addition of water (Figure 6.14b). Therefore, the remaining experiments were carried out in 30/70 water/acetone.

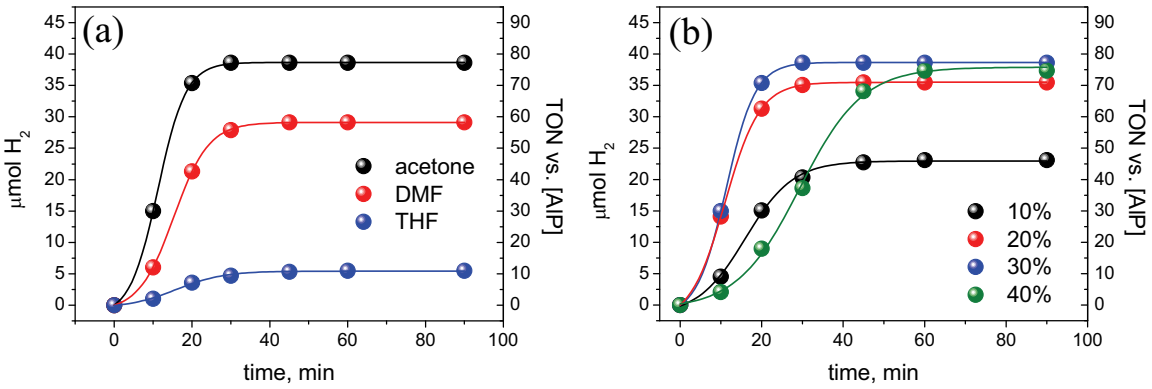

Fig. 6.14. (a) Effect of the type of solvent on photocatalytic hydrogen evolution (0.1 mM **AlP(OH)**, 0.3 mM **Co(dmgH)(H$_2$O)**, 10 mM **AscH**, 30/70 water/organic solvent); (b) effect of the water content on photocatalytic hydrogen evolution in water/acetone mixture (0.1 mM **AlP(OH)**, 0.3 mM **Co(dmgH)(H$_2$O)**, 10 mM **AscH**).

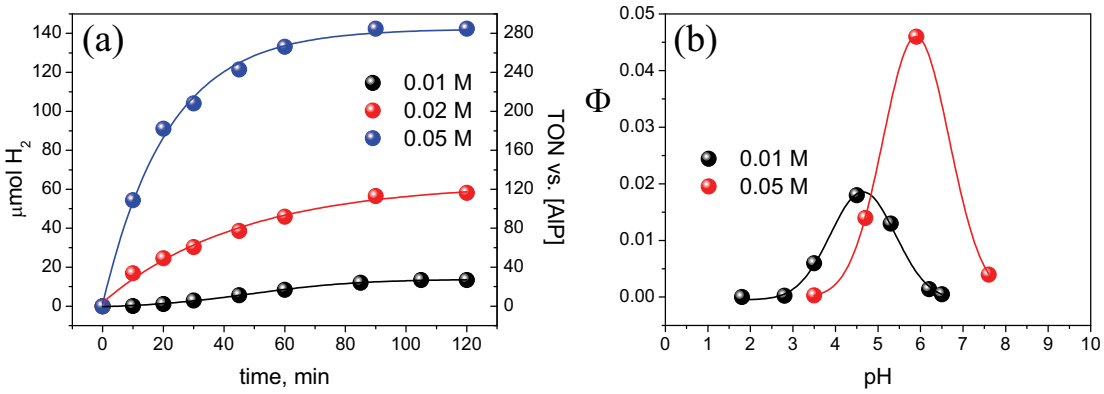

Fig. 6.15. (a) Effect of **AscH** concentration on photocatalytic hydrogen evolution at pH 6 (0.1 mM **AlP(OH)**, 0.3 mM **Co(dmgH)(H$_2$O)**, 30/70 water/acetone); (b) combined effect of pH and **AscH** concentration (0.1 mM **AlP(OH)**, 0.3 mM **Co(dmgH)(H$_2$O)**, 30/70 water/acetone).

The effects of the concentration of sacrificial reductant and pH are intertwined as, *e.g.*, increasing the concentration of ascorbic acid from 10 mM to 50 mM brings a change in measured pH from 4.5 to 3.5. The effects can be disentangled controlling the pH upon addition of appropriate amounts of NaOH or $HClO_4$. At pH 6, an increase in the concentration of ascorbic acid from 10 mM to 50 mM brings about a steady increase in both quantum yield and maximum chemical yield of hydrogen evolution (Figure 6.15a). The effect of pH is more complex, however, with quantum yields of hydrogen production peaking at different pH

values depending on the ascorbic acid concentration (Figure 6.15b). The best hydrogen evolving conditions are obtained working at pH 6 with 50 mM ascorbic acid.

The effect of the concentration of **Co(dmgH)(H$_2$O)** catalyst was then explored both at natural pH (4.5) with 10 mM **AscH** and at pH 6 with 50 mM **AscH** (Figure 6.16). It is seen that a considerable gain in performance can be achieved by increasing the catalyst concentration from 0.1 mM (stoichiometric with the **AlP(OH)** sensitizer) up to a threefold excess (no further gain observed upon further increase).

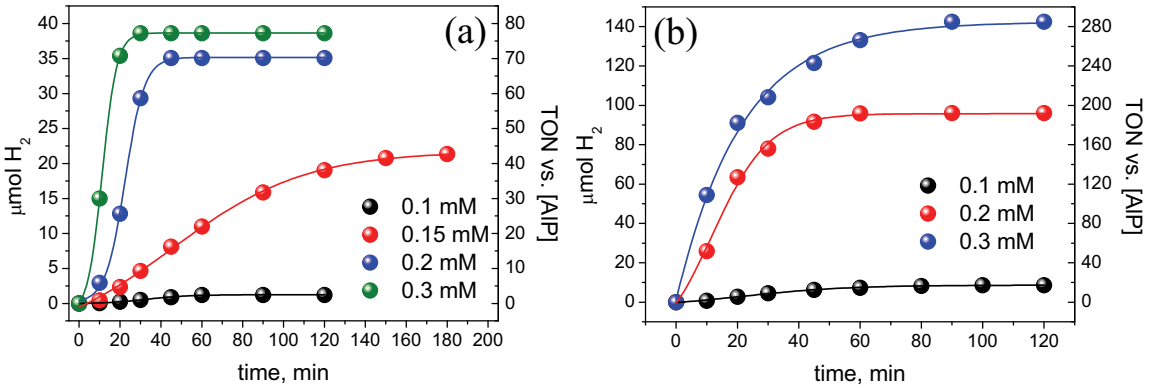

Fig. 6.16. (a) Effect of **Co(dmgH)(H$_2$O)** concentration on photocatalytic hydrogen evolution (0.1 mM **AlP(OH)**, 10 mM **AscH**, 30/70 water/acetone, natural pH); (b) effect of **Co(dmgH)(H$_2$O)** concentration on photocatalytic hydrogen evolution (0.1 mM **AlP(OH)**, 50 mM **AscH**, 30/70 water/acetone, pH 6).

Finally, as already observed in related work with cobaloxime catalysts,[116] the addition of free dimethylglyoxime ligand (**dmgH$_2$**) brings about a further increase in maximum chemical yield of hydrogen evolution (Figure 6.17).

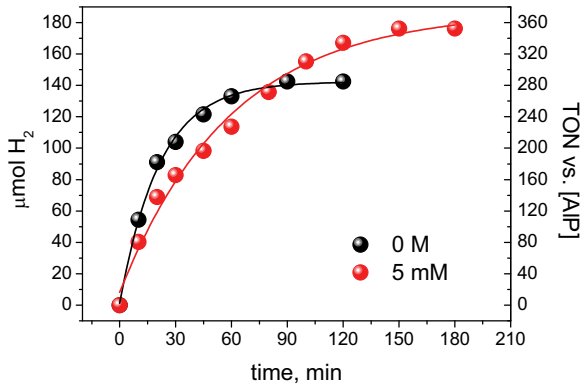

Fig. 6.17. Effect of added external **dmgH$_2$** on photocatalytic hydrogen evolution (0.1 mM **AlP(OH)**, 50 mM **AscH**, 0.3 mM **Co(dmgH)(H$_2$O)**, 30/70 water/acetone, pH 7).

According to these experiments, overall the best hydrogen evolving conditions can be summarized as follows: **AlP** 0.1 mM, **Co(dmgH)(H$_2$O)** 0.3 mM, **AscH** 50 mM, pH 6, **dmgH$_2$** 5 mM. In these optimized conditions, the quantum yield of hydrogen evolution (defined as the moles of hydrogen divided by the moles of absorbed photons) is 0.046 which, given the two-photons two-electron nature of the process, corresponds to an overall quantum efficiency of 9.2%. The TON values, referred to the possible limiting components, are 352 relative to **AlP(OH)** and 117 relative to **Co(dmgH)(H$_2$O)**. The corresponding turnover frequency (TOF) values are 10.8 min^{-1} and 3.6 min^{-1}, respectively.

6.3.4 Photocatalytic mechanism

The first point to be emphasized is that in THF, where the association equilibria between the three molecular components have been studied and the electrochemical data defining the thermodynamics of the system have been obtained, practically no photocatalytic activity is observed (Figure 6.13). This is obviously the consequence of the fast charge recombination and largely reversible behavior observed by ultrafast spectroscopy in this solvent. When the solvent is changed to water/organic solvent mixtures, efficient photocatalytic hydrogen evolution is observed (Figures 6.13 and 6.14). In such solvents, however, the association equilibria are clearly very different from THF. For instance, in 30/70 water/acetone pH 6 solution containing 0.1 mM **AlP(OH)** and 50 mM **AscH** the porphyrin fluorescence is only quenched to an extent of 38% (Figure 6.18), indicating that the axial bond is hydrolyzed in these conditions, with the porphyrin being just partially coordinated by ascorbate. A 57% quenching is observed, on the other hand, when 0.3 mM **Co(dmgH)(H$_2$O)** is added to such a solution, implying that in these conditions coordination of the cobaloxime to the pyridyl porphyrin takes place only partially. This is likely determined by the excess ascorbate ligand competing efficiently with the pyridyl porphyrin for cobalt coordination. In summary, under conditions of photocatalytic hydrogen evolution, catalyst and sacrificial donor are only partially coordinated to the aluminum porphyrin chromophore, which is largely (ca. 43%) present in solution as a free species.

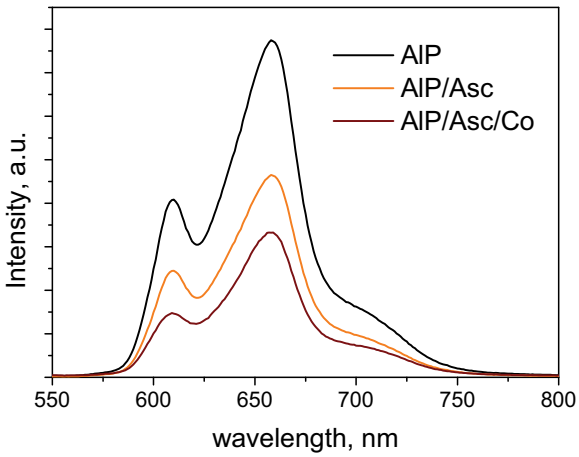

Fig. 6.18. Photoluminescence spectra (excitation at 500 nm) of 30/70 water/acetone pH 6 solutions containing: 0.1 mM **AlP(OH)** (black trace); 0.1 mM **AlP(OH)**, 50 mM **AscH** (orange trace); and 0.1 mM **AlP(OH)**, 50 mM **AscH**, 0.3 mM **Co(dmgH)(H$_2$O)** (brown trace).

The fate of the associated fraction of aluminum porphyrin chromophore upon excitation can be monitored by ultrafast spectroscopy. It is clearly seen that, both in the **AlP(OH)/AscH** (Figure 6.19a) and **AlP(OH)/AscH/Co(dmgH)(H$_2$O)** systems (Figure 6.19b), a fraction of the initially formed excited singlet state (roughly corresponding to the fluorescence-quenched fraction under the same conditions) decays completely in a time scale of tens of picosecond, while the remaining part is appreciably constant in the whole time window of the experiment (2 ns). By comparison with what observed in THF (Figures 6.7 and 6.10), the fast decay of the singlet excited state can be easily assigned to rapidly reversible electron transfer quenching taking place in the associated fraction of the aluminum porphyrin chromophore.

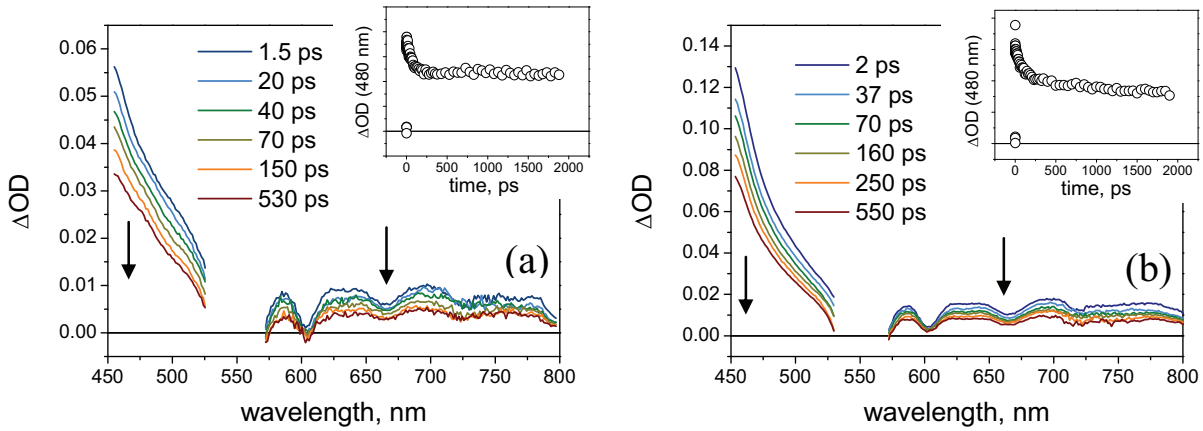

Fig. 6.19. Transient absorption spectra obtained by ultrafast spectroscopy (excitation at 550 nm) in 30/70 water/acetone pH 6 solutions containing (a) 0.1 mM **AlP(OH)**, 50 mM **AscH**, and (b) 0.1 mM **AlP(OH)**, 50 mM **AscH**, 0.3 mM **Co(dmgH)(H$_2$O)**; (insets) kinetic analysis at 480 nm.

The fate of the long-lived fraction of excited states, corresponding to the free chromophore, can be investigated by nanosecond laser flash photolysis. In the **AlP(OH)/AscH** system (Figure 6.20), the initial spectrum (100-ns time delay) can be attributed to the aluminum porphyrin triplet state,[126] populated in few nanoseconds by intersystem crossing from the singlet. The evolution of the spectral changes is clearly biphasic: in the earlier period (0.1-5 μs, Figure 6.20a), a new spectrum with sharp maximum at 720 nm develops, characteristic of the radical anion of metal tetraphenylporphyrins.[134]

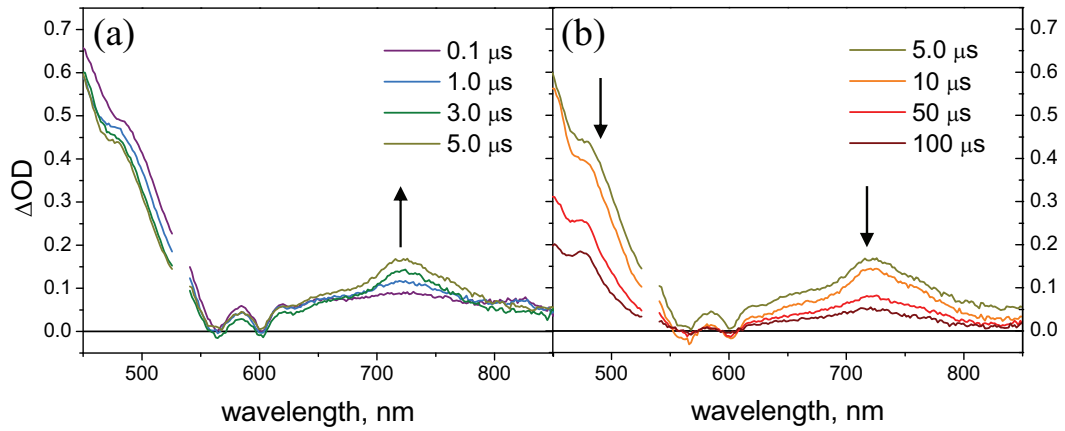

Fig. 6.20. Transient absorption spectra obtained by laser flash photolysis (excitation at 532 nm) in 30/70 water/acetone pH 6 solutions containing 0.1 mM **AlP(OH)** and 50 mM **AscH** at (a) 0.1-5.0 μs and (b) 5-100 μs time-delays.

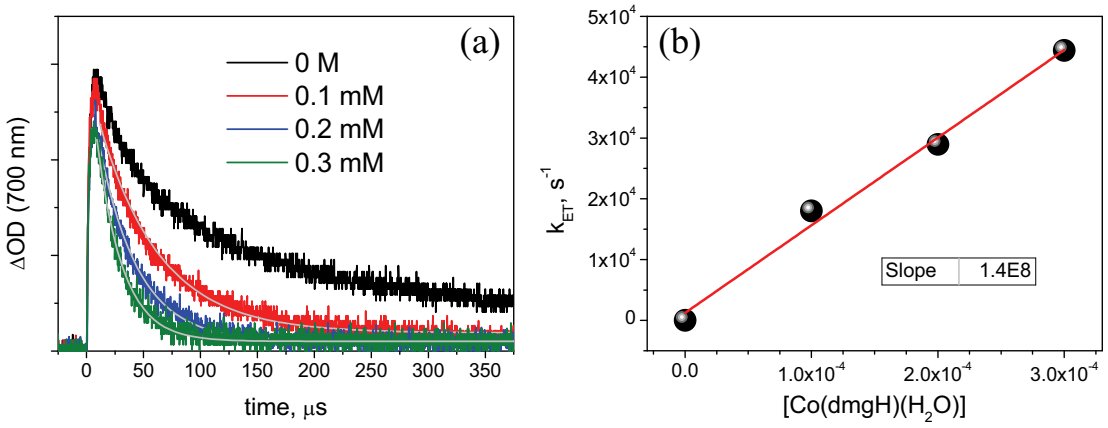

Fig. 6.21. (a) Single-wavelength kinetics (700 nm) obtained by laser flash photolysis (excitation at 532 nm) on a 30/70 water/acetone solution containing 0.1 mM **AlP(OH)** 0-0.3 mM **Co(dmgH)(H$_2$O)**, and 50 mM **AscH** at pH 6; (b) plot of rate constant (obtained by monoexponential fitting on the kinetic traces) *vs.* cobaloxime concentration for the calculation of the bimolecular rate constant.

This transient then decays (Figure 6.20b) to the baseline with a complex kinetics (Figure 6.21a, black trace). This experiment provides clear evidence that the free aluminum porphyrin reacts upon excitation with the ascorbate donor bimolecularly at the triplet level, giving rise to the reduced form of the sensitizer, which then undergoes very slow recombination with the oxidized ascorbate in a ms time-scale.

The reaction of the aluminum porphyrin radical anion with the catalyst can then be monitored by laser flash photolysis in the **AlP(OH)/AscH/Co(dmgH)(H_2O)** system. The transient spectral changes are indeed qualitatively similar to those obtained for the **AlP(OH)/AscH** system, since the reduced form of the cobaloxime displays very weak absorption in the visible (negligible at $\lambda > 500$ nm)[135] by comparison with the transient porphyrin radical anion. However, a faster decay of the long-lived aluminum porphyrin radical anion spectrum is observed, due to the electron transfer to the cobaloxime catalyst. As expected, the decay rate shows an appreciably first-order dependence on the **Co(dmgH)(H_2O)** concentration (Figure 6.21), the bimolecular rate constant k can be thus calculated according to eq 27-29 (true under pseudo-first order kinetic conditions) where the concentration of the aluminum porphyrin radical anion (**AlP**$^-$) is followed by the absorption at 700 nm (Figure 6.21a).

$$v = k\,[\mathbf{AlP^-}][\mathbf{Co(dmgH)(H_2O)}] = k_{obs}\,[\mathbf{AlP^-}] \qquad (27)$$

$$[\mathbf{AlP^-}] = [\mathbf{AlP^-}]_0 \exp -(k_{obs}\,t) \qquad (28)$$

$$k_{obs} = k\,[\mathbf{Co(dmgH)(H_2O)}] \qquad (29)$$

Neglecting the competition with charge recombination with the oxidized ascorbate (which should in principle affect the k_{obs} values) taking place in a much longer time-scale, the bimolecular rate constant is 1.4×10^8 $M^{-1}s^{-1}$.

The main mechanistic conclusions from these experiments can be summarized as schematized in Figure 6.22. (i) Contrary to what initially envisioned, association of the catalyst and sacrificial donor with the sensitizer is not useful towards photocatalytic hydrogen evolution. In fact, it turns out to be detrimental, to the extent to which the associated species are rapidly quenched by largely reversible electron transfer. (ii) The photocatalytic hydrogen evolution comes from bimolecular reaction of the triplet state of the free sensitizer with the sacrificial donor. This primary photoreaction produces the reduced photosensitizer, which reacts further bimolecularly with the catalyst, triggering the photocatalytic hydrogen

production. An additional confirmation of the bimolecular nature of the reaction with the catalyst arises from the observation that comparable hydrogen yields are obtained if, instead of **Co(dmgH)(H$_2$O)**, a coordinatively saturated analogue such as **Co(dmgH)(EtPy)** (EtPy = 4-ethylpyridine) is used as cobaloxime component of the reaction mixture.

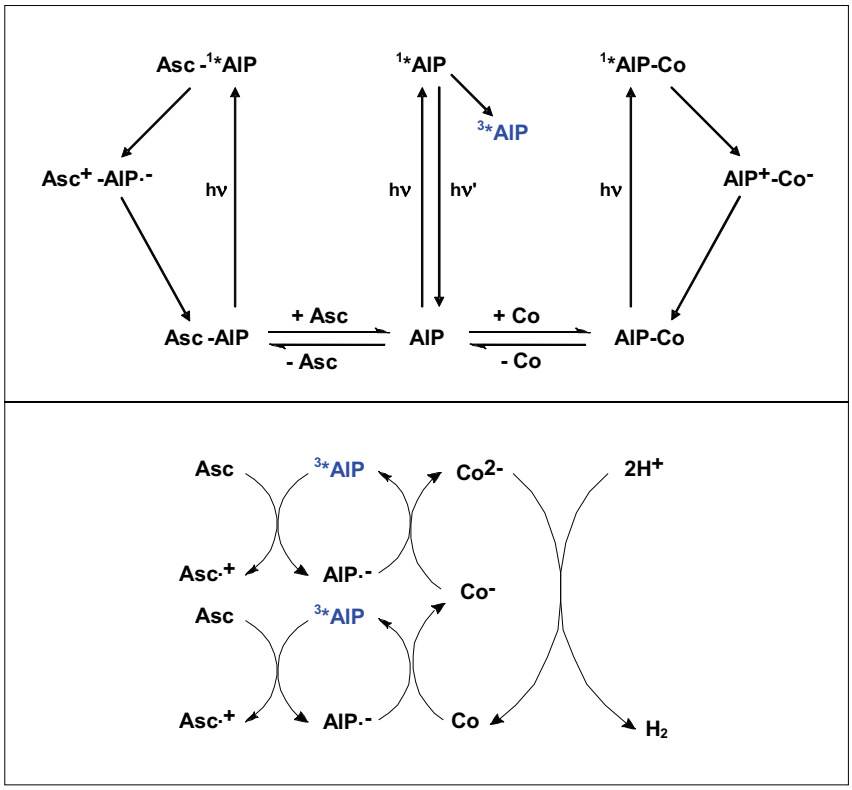

Fig. 6.22. Schematic representation of the mechanism leading to cobaloxime reduction and hydrogen generation. Abbreviations: Asc, ascorbate; AlP, aluminum porphyrin; Co, cobaloxime.

An interesting comparison is that between the hydrogen evolution experiments carried out at pH 6 and at natural pH (3.5 with 50 mM **AscH** and 4.5 with 10 mM **AscH**). It should be remarked that at low pH a much more efficient quenching of the aluminum porphyrin fluorescence takes place (*e.g.*, ≥ 95% for a solution containing 0.1 mM **AlP(OH)**, 0.3 mM **Co(dmgH)(H$_2$O)**, and 10-50 mM **AscH**). Efficient coordination of cobaloxime is the main responsible for the observed quenching, as shown by a comparison between the behavior of the two **AlP(OH)**/**Co(dmgH)(H$_2$O)** and **AlP(OH)**/**AscH** subsystems (Figure 6.23). In fact, at these pH (3.5 and 4.5 with 50 mM and 10 mM **AscH**, respectively) ascorbic acid is supposed to be largely present in its protonated form thus preventing competition with the pyridyl porphyrin to coordination of the cobalt. In these conditions, with strong quenching by coordinated cobaloxime, a low triplet yield and thus a low photocatalytic activity should be expected.

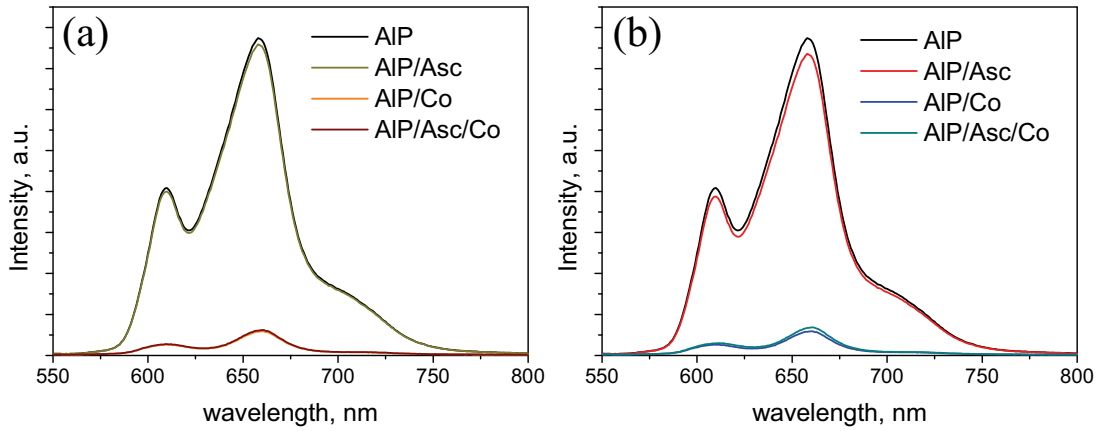

Fig. 6.23. Emission spectra (excitation at 500 nm) of 30/70 water/acetone (natural pH) solutions containing: (a) 0.1 mM **AlP(OH)** (black trace); 0.1 mM **AlP(OH)**, 10 mM **AscH** (yellow trace); 0.1 mM **AlP(OH)**, 0.3 mM **Co(dmgH)(H$_2$O)** (orange trace); 0.1 mM **AlP(OH)**, 10 mM **AscH**, 0.3 mM **Co(dmgH)(H$_2$O)** (brown trace). (b) 0.1 mM **AlP(OH)** (black trace); 0.1 mM **AlP(OH)**, 50 mM **AscH** (red trace); 0.1 mM **AlP(OH)**, 0.3 mM **Co(dmgH)(H$_2$O)** (blue trace); 0.1 mM **AlP(OH)**, 50 mM **AscH**, 0.3 mM **Co(dmgH)(H$_2$O)** (green trace).

In fact, at natural pH good hydrogen production efficiency is nevertheless observed (see above), although with a prominent induction period. A key to this issue is the behavior of the aluminum porphyrin fluorescence in the early time lag of the irradiation experiments at pH 4.5 (Figure 6.24). The fluorescence, initially completely quenched, rises rapidly upon irradiation, reaching in few minutes the level of emission characteristic of a two-component mixture of **AlP(OH)** and **AscH**. The likely explanation is that, in the initial stage of the irradiation, a photochemical detachment of the cobaloxime quenching unit from the aluminum pyridyl porphyrin takes place. In the absorption spectrum, a blue shift (ca. 5 nm) of the porphyrin Soret and Q-bands, symmetric to the red shift observed upon complexation in THF, is also detected along the photolysis, confirming this hypothesis. The photochemical detachment of the cobaloxime is likely to take place after oxidative quenching of the sensitizer singlet state in competition with charge recombination, as Co(II) centers are generally known to be substitutionally labile.[136]

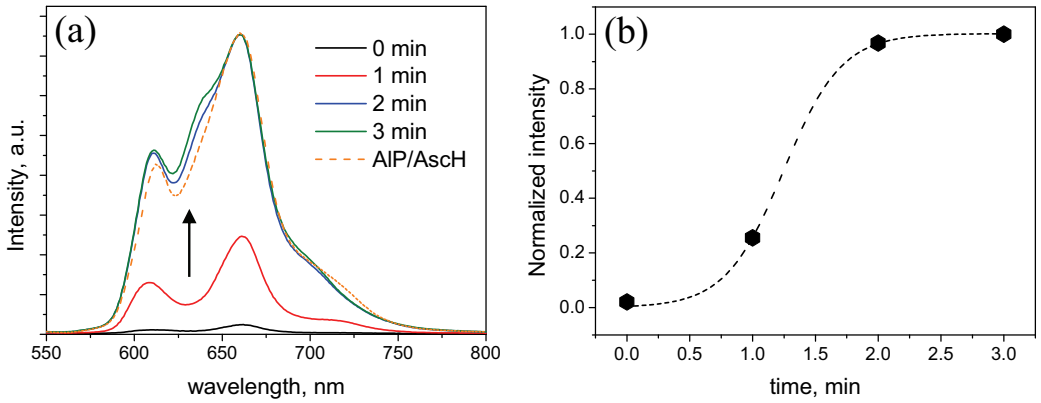

Fig. 6.24. (a) Time-dependent emission spectra obtained upon continuous irradiation of a 30/70 water/acetone (natural pH) solution containing 0.1 mM **AlP(OH)**, 10 mM **AscH**, 0.3 mM **Co(dmgH)(H_2O)** compared with a solution lacking the cobaloxime (dashed orange line); (b) plot of the normalized intensity *vs.* time.

In the hydrogen evolution experiments carried out under these conditions (Figures 6.14 and 6.16a), an induction period is clearly present. Part of this induction period (according to the quenching data of Figure 6.24) can be accounted for by the photochemical detachment of the cobaloxime quenching unit and part is as expected since an appreciable fraction of reduced cobaloxime must accumulate at stationary state before a constant hydrogen formation rate is established. It can be noticed that the induction period in hydrogen formation is apparently absent, or much less pronounced, at higher pH (Figures 6.15, 6.16b, and 6.17). Two reasons can account for this observation: (i) as discussed before, the higher concentration of ascorbate chemically removes the quenching cobaloxime from the aluminum porphyrin, thus largely suppressing that part of the induction period related to the need for photochemical release of this unit; (ii) the overall much higher rate is expected to compress any induction period to a time scale shorter than that of the actual measurements.[116]

As far as the hydrogen evolution experiments are concerned, according to the mechanism of Figure 6.22, the effects played by the cobaloxime and ascorbic acid concentrations can be rationalized as follows. The effect of the cobaloxime concentration on the hydrogen production rates and yields can be easily related to the efficiency of its bimolecular reaction with the porphyrin radical anion. This reaction competes with evolution of the latter to permanent reduction products, such as chlorins. Therefore, fast electron scavenging is expected to be crucial to minimize photosensitizer degradation. As a matter of fact, in all the experiments an inverse relationship has been observed between the extent of chlorin product formation and the efficiency of hydrogen evolution (Figure 6.25).

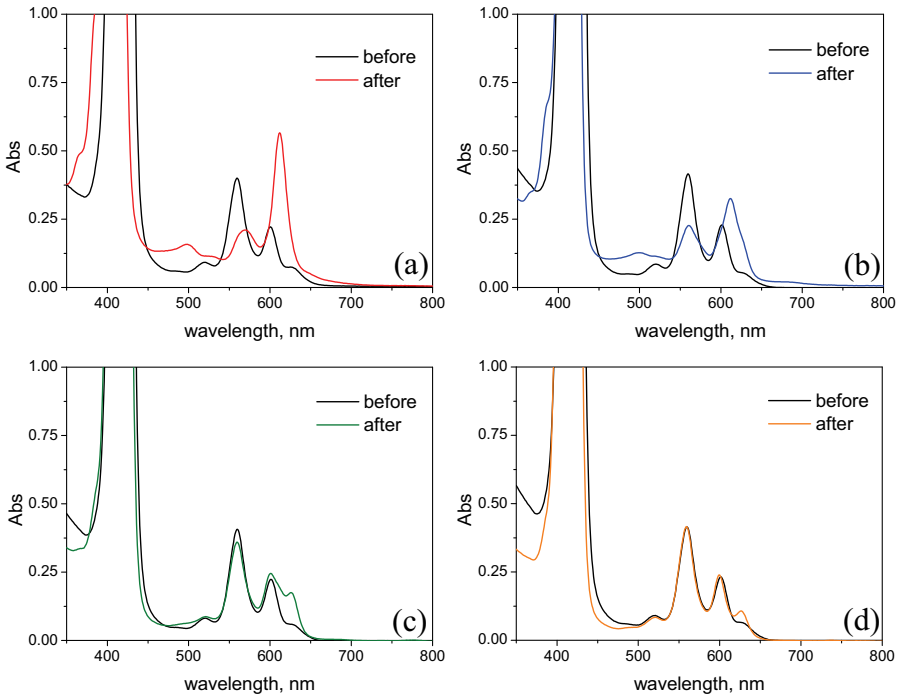

Fig. 6.25. Comparison of absorption spectra before/after irradiation of experiments reported in Figure 6.16a; experimental conditions: 30/70 water/acetone (natural pH), 0.1 mM **AlP(OH)**, 10 mM **AscH**, and (a) 0.1 mM **Co(dmgH)(H$_2$O)**, (b) 0.15 mM **Co(dmgH)(H$_2$O)**, (c) 0.2 mM **Co(dmgH)(H$_2$O)**, and (d) 0.3 mM **Co(dmgH)(H$_2$O)**.

In terms of kinetics, the dependence of the initial rate of hydrogen production, calculated from the slope of the linear part of the kinetics for [**Co(dmgH)(H$_2$O)**] ≥ 0.2 mM (Figure 6.16), on cobaloxime concentration is appreciably a first-order one (Figure 6.26).

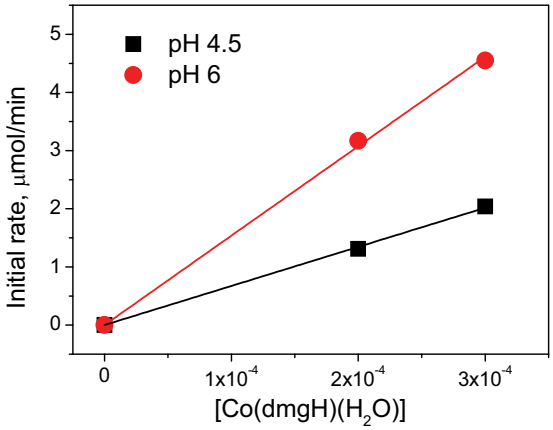

Figure 6.26. Plot of initial rate of hydrogen production *vs.* catalyst concentration obtained from kinetics of 30/70 water/acetone solutions containing 0.1 mM **AlP(OH)**, 0-0.3 mM **Co(dmgH)(H$_2$O)**, at 10 mM **AscH**, pH 4.5 (red dots, see Figure 6.16a) and at 50 mM **AscH**, pH 6 (black squares, see Figure 6.16b).

As in similar cases,[116a,119b] this could be taken as an indication that, among the hydrogen evolution mechanisms available to the two-electron reduced form of the cobaloxime (Figure 6.2),[118] a heterolytic pathway, involving protonation of the cobalt hydride complex, is prevailing here.

The effect of increasing ascorbic acid concentration on the hydrogen production rates (Figure 6.15a) can be mainly attributed to two effects: the above-mentioned decrease in singlet quenching by cobaloxime, with consequent increased triplet formation yield, and the increasing efficiency of the bimolecular reaction of ascorbate with the aluminum porphyrin triplet. The bell-shaped effects of pH (Figure 6.15b) are likely the result of at least two factors playing in opposite directions as the pH is increased: the above-mentioned positive effects of increasing ascorbate concentration and the decreasing thermodynamic driving force for water reduction. An interesting observation is that in several experiments (*e.g.*, with 10 mM ascorbic acid, Figures 6.15 and 6.16a) the total amount of hydrogen evolved equals the total amount of ascorbic acid present in solution. This means that, although reductive quenching of the aluminum porphyrin by ascorbate is a one-electron transfer process, each sacrificial donor molecule eventually undergoes two-electron oxidation to dehydroascorbic acid. This most likely occurs by disproportionation[137,138] of the ascorbate radical formed as primary product.

As far as the TON limiting reactions are concerned, as discussed above, formation of permanent reduction products of the sensitizer (chlorins) is certainly one of the main factors. Another one is clearly the consumption of the catalyst, presumably by hydrogenation of the dimethylglyoximate ligands.[114,116] The improvement in performance obtained upon addition of free dimethylglyoxime (Figure 6.17) is consistent with this notion.

6.4 Primary photochemical process of porphyrin-cobaloxime dyads

Supramolecular dyads involving a photosensitizer and a hydrogen evolving catalyst have been a subject of considerable research.[139] The aim of these approaches is mainly dictated by the idea that intramolecular electron transfer processes should be faster and more efficient thus improving the overall photocatalytic mechanism.

Among these sensitizer/catalyst dyads, those involving a porphyrin sensitizer and a cobaloxime catalyst have received particular attention (see Section 6.1),[105,121,122] in particular with regard to the noble-metal free character of these assemblies. In all these cases, once the porphyrin-cobaloxime dyad was formed, quenching of the porphyrin fluorescence was observed. A photoinduced electron transfer from the excited singlet state of the chromophore

to the cobaloxime catalyst was postulated as the process responsible for the observed quenching. However, detailed evidence for the nature of such photochemical event was not shown. In this section, a spectroscopic study of three porphyrin-cobaloxime dyads (Figure 6.27) has been addressed in order to clarify this issue.

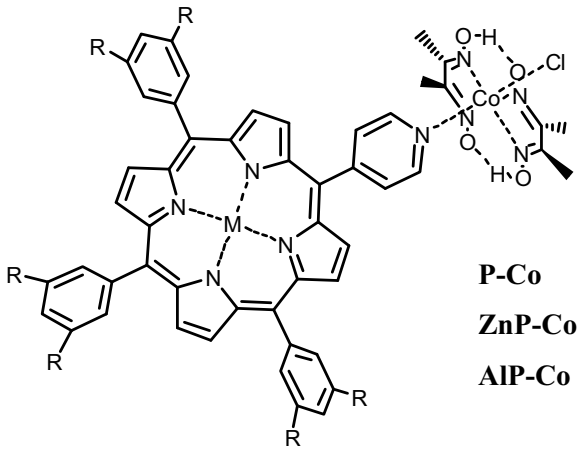

P-Co M = 2H, R = H

ZnP-Co M = Zn, R = H

AlP-Co M = Al-OH, R = *t*Bu

Fig. 6.27. Structural representation of the porphyrin-cobaloxime dyads studied in this section.

6.4.1 Results and discussion

The X-ray molecular structure of the free-base porphyrin-cobaloxime dyad **P-Co** (Figure 6.28) was obtained by X-ray diffraction of suitable crystals collected by slow vapour diffusion of cyclohexane into a concentrated chloroform solution. Some relevant diffraction parameters are summarized in Table 6.2.

Table 6.2. Crystal data and structural refinement for **P-Co**.[a]

Empirical formula	$C_{51}H_{43}ClCoN_9O_4 \cdot CHCl_3$	
Crystal system	Monoclinic	
Space group	$P2_1/c$	
Unit cell dimensions	a = 20.2161(3) Å	$\alpha = 90°$
	b = 12.5775(2) Å	$\beta = 99.3737(6)°$
	c = 20.8200(4) Å	$\gamma = 90°$
Volume	5223.2(2) Å^3	
Z	4	

[a] Data were collected on a *Nonius Kappa CCD* diffractometer using graphite monochromated Mo Kα radiation (λ = 0.7107 Å) at 295 K.

A related structure was reported by Marzilli and coworkers[140] for an adduct with four methylcobaloxime units bound to a tetrapyridylporphyrin. The bond lengths and angles are very similar in the two structures, except for the Co-N (pyridyl) bond being shorter here (1.976 Å) than there (2.055, 2.079 Å), reflecting the different trans effect of the axial groups, chloride and methyl, respectively, present in the two types of cobaloxime.

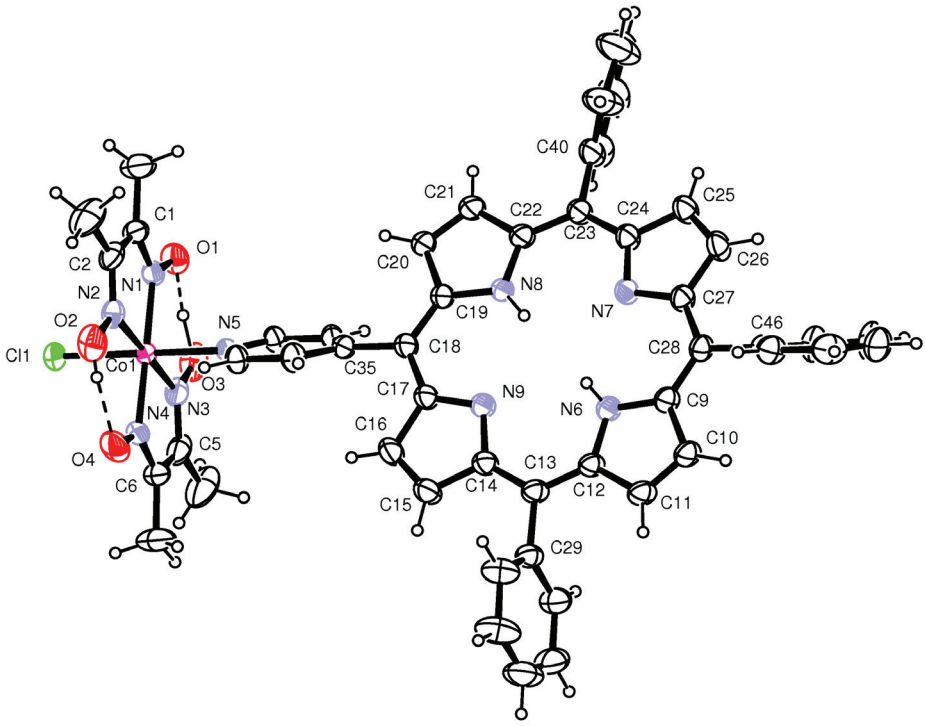

Fig. 6.28. ORTEP diagram of dyad **P-Co**. Thermal ellipsoids are drawn at the 30% probability level.

The absorption spectra of dyads **P-Co**, **ZnP-Co**, and **AlP-Co** in tetrahydrofuran (Figure 6.29) display the typical spectral features of porphyrin chromophores: Soret and Q-bands at 416, 513, 549, 590, and 646 nm for **P-Co**, at 425, 558, and 600 nm for **ZnP-Co**, at 420, 562, and 604 nm for **AlP-Co**. All of these spectral patterns appear about 5-nm red-shifted with respect to those of the reference tetraphenyl porphyrins (**P**, **ZnP**, and **AlP**). The Co(III) cobaloxime complex displays very weak absorption in the visible ascribable to ligand-field transitions (from the absorption spectrum of the $Co(dmgH)_2Cl(EtPy)$ model shoulders at ca. 500 nm, ε = 200 $M^{-1}cm^{-1}$ and ca. 600 nm ε = 60 $M^{-1}cm^{-1}$ can be discerned), thus its contribution to the spectra of the dyads mainly arises to ligand-centered (LC) transition in the 350-400 nm region involving the conjugated bis(dimethylglioximate) macrocycle. Aside from the spectral red-shift observed upon complexation, no additional transitions are observed, in agreement with the supramolecular nature of the assemblies.

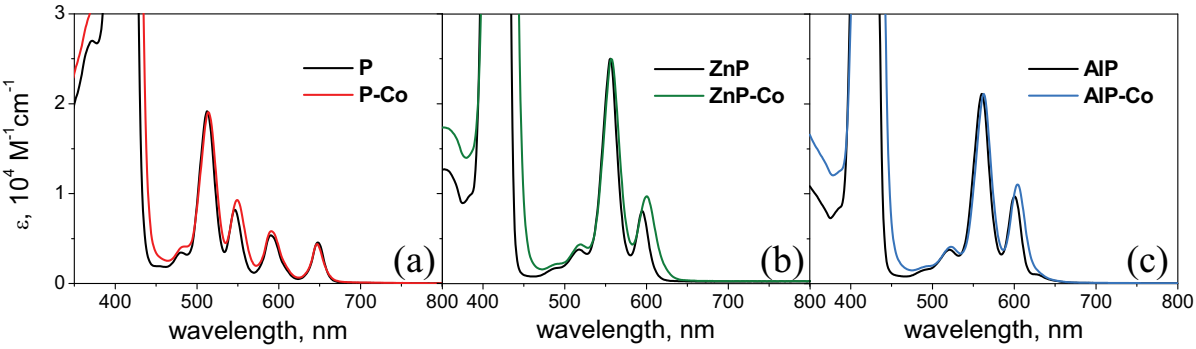

Fig. 6.29. Comparison of absorption spectra in THF between dyads and related reference tetraphenyl model: (a) **P-Co** and **P**, (b) **ZnP-Co** and **ZnP**, and (c) **AlP-Co** and **AlP**.

Fluorescence spectra of dyads **P-Co**, **ZnP-Co**, and **AlP-Co** in THF (ca. 10 μM), as compared to those of the reference porphyrin models **P**, **ZnP**, and **AlP** respectively (optically matched at the excitation wavelength, Figure 6.30), show that the excited singlet state of the porphyrin is always strongly quenched by the bound cobaloxime, with values I/I_0 of 0.15 for **P-Co** and 0.12 for both **ZnP-Co** and **AlP-Co**. The residual emission (12-15%) observed in these experiments is largely due to free pyridyl porphyrin not coordinated to the cobaloxime unit, as it can be checked from the fluorescence lifetime measurements in dyads **P-Co**, **ZnP-Co**, and **AlP-Co** by comparison with the parent porphyrin models **P**, **ZnP**, and **AlP**. In **P**, a lifetime of 10.8 ns is measured by time-correlated single photon counting technique (emission at 650 nm, excitation at 600 nm), whilst for **P-Co** a biexponential decay is recorded with lifetimes of 0.3 and 12 ns, accounting for 89% and 11%, respectively, of the overall fluorescence intensity.

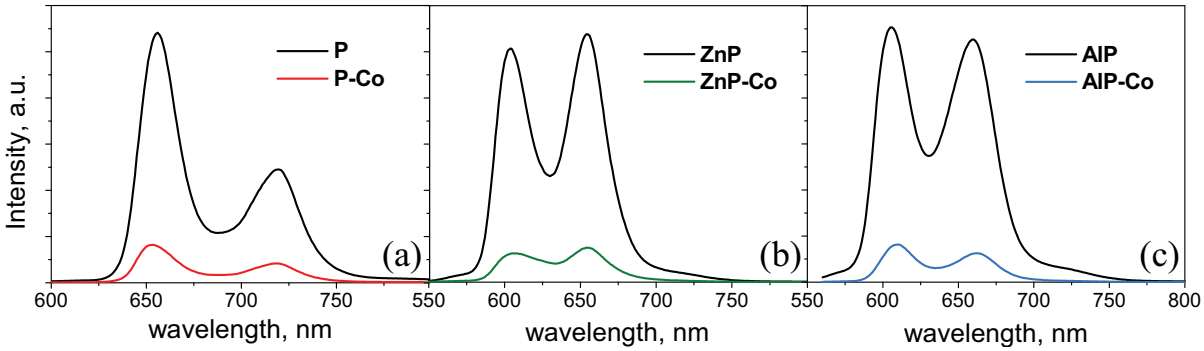

Fig. 6.30. Comparison of emission spectra in THF of optically matched solutions at the excitation wavelength of dyads and related reference tetraphenyl model: (a) **P-Co** and **P** (excitation at 530 nm), (b) **ZnP-Co** and **ZnP** (excitation at 530 nm), and (c) **AlP-Co** and **AlP** (excitation at 550 nm).

In the case of **ZnP** and **AlP** (emission at 610 nm, excitation at 600 nm), lifetimes of 1.9 and 6.4 ns are observed respectively, whereas in dyads **ZnP-Co** and **AlP-Co** most of the emission decays in a timescale shorter than instrumental resolution (< 0.25 ns) and a minor part (ca. 10% by comparison with models **ZnP** and **AlP**) is observed to decay with unquenched lifetimes of 1.9 and 6.5 ns, respectively. This suggests that, in the dilute (ca. 10 μM) solutions used for the emission measurements, the residual fluorescence observed in the dyads arises from partial dissociation of the quenching cobaloxime from the chromophore. As a matter of fact, an increase in the fluorescence quenching is detected upon addition of free $Co(dmgH)_2Cl(H_2O)$.

As far as the quenching mechanisms is concerned, three possibilities should be in principle considered: (i) enhanced intersystem crossing in the porphyrin by the cobalt center (heavy-atom effect);[140] (ii) electronic energy transfer to the Co(III) complex;[114c] (iii) oxidative quenching by photoinduced electron transfer (as supposed in Section 6.3).[105,121]

Heavy-atom effects are well documented in a variety of porphyrin systems.[141] In particular, this effect played by the central metal is already evident in the three model porphyrins of this study, with fluorescence lifetime decreasing (*i.e.*, intersystem crossing rate increasing) in the **P**, **AlP**, **ZnP** series. Obviously, a heavy-atom effect of the peripheral cobalt center in the dyads should be more pronounced for the free-base system **P-Co** than for the metal-containing ones.

Energy transfer to the Co(III) complex can be considered as a possible quenching mechanism since Co(III) complexes with this ligand set are likely to have low-energy d-d states potentially accessible from the porphyrin singlet excited state (as stated before, weak ligand field transitions can be discerned in the absorption spectrum of $Co(dmgH)_2Cl(EtPy)$ model).

Finally, considering a photoinduced electron transfer mechanism, information on its energetic feasibility can be obtained from cyclic voltammetry meaurements (Table 6.3) with particular attention to the first oxidation (porphyrin-localized) and reduction potentials (cobaloxime-localized) of the dyads, which are relevant to estimate the energy of the charge-separated state and therefore the driving force for the electron transfer process. It should be pointed out that, while the differences in the oxidation potential reflect the chemical differences between the porphyrin units of the three dyads, the scatter in the figures for first reduction of the cobaloxime unit is likely due to the strongly irreversible electrochemical behavior of this process. Therefore, an average value of −0.75 (± 0.04) V is assumed for the cathodic peak potential of the three dyads.

Table 6.3. Electrochemical data of models **P**, **ZnP**, **AlP** and dyads **P-Co**, **ZnP-Co**, **AlP-Co**.[a]

	Oxidation (V)		Reduction (V)		
P	1.37[b]	1.17[b]	− 0.75[c,d]	− 1.11[b,c,d,e]	
ZnP	1.32[b]	1.04[b]	− 0.71[c,d]	− 1.17[c,d]	− 1.39[b]
AlP	1.21[b]	1.02[b]	− 0.79[c,d]	− 1.13[c,f]	− 1.23[b,f]
P-Co	1.42[b]	1.19[b]			− 1.13[b]
ZnP-Co	1.31[b]	0.97[b]			− 1.45[b]
AlP-Co	1.22[b]	0.96[b]			− 1.22[b]

[a] Obtained by cyclic voltammetry (CV) in THF at 298 K, 0.1 M TBA(PF_6) as supporting electrolyte, SCE as reference electrode, ferrocene (0.56 V vs SCE)[129] as internal standard, scan rate 100 mV/s. [b] Attributed to the porphyrin unit. [c] Attributed to the cobaloxime unit. [d] Cathodic peak potential. [e] From peak intensity, two overlapping waves. [f] Half-wave potential obtained by differential pulse voltammetry (see Table 6.1).

The driving force for the photoinduced electron transfer involving oxidation of the porphyrin and reduction of the cobaloxime can be thus estimated by means of a Rehm-Weller type calculation (eq 30)[130] where E (D^+/D) and E (A/A^-) are the oxidation and reduction potentials of the donor (porphyrin) and the acceptor (cobaloxime) respectively, $E^{0\text{-}0}$ is the $S_0 \rightarrow S_1$ spectroscopic transition of the chromophore, and the third term is the electrostatic correction where Z_X is the electric charge of donor ($X = D$), acceptor ($X = A$), oxidized donor ($X = D^+$), or reduced acceptor ($X = A^-$), and d is the donor-acceptor distance.

$$\Delta G^{o}_{ET} = e\,[E(D^+/D) - E(A/A^-)] - E^{0-0} + [Z_{D^+}Z_{A^-} - Z_D Z_A]\frac{e^2}{4\pi\varepsilon_0\varepsilon_S d} \qquad (30)$$

Considering the first oxidation and reduction potentials as previously mentioned, the excited state energy of the porphyrins, calculated from the wavelength at the intersection of the normalized absorption/emission spectra (1.91 eV for **P-Co**, 2.07 eV for **ZnP-Co**, and 2.04 eV for **AlP-Co**), the electrostatic correction to the electron transfer state energy (0.20 eV, estimated assuming a center-to-center distance of 9.5 Å between the chromophore and the cobaloxime unit, as obtained from the X-ray molecular structure data, and a dielectric constant of 7.6 for THF) the driving force for the photoinduced electron transfer process can be obtained. These estimates yield ΔG° values of −0.19 eV, −0.48 eV, and −0.47 eV for **P-Co**, **ZnP-Co**, and **AlP-Co** respectively, indicating that the photoinduced electron transfer is always thermodynamically allowed, with a larger driving force for the two metallo-porphyrin containing dyads with respect to the free-base analogue.

To get experimental insight into the quenching mechanism, ultrafast spectroscopy experiments were carried out on dyads **P-Co**, **ZnP-Co**, **AlP-Co** (Figure 6.31) as well as on models **P**, **ZnP**, **AlP** (Figure 6.32).

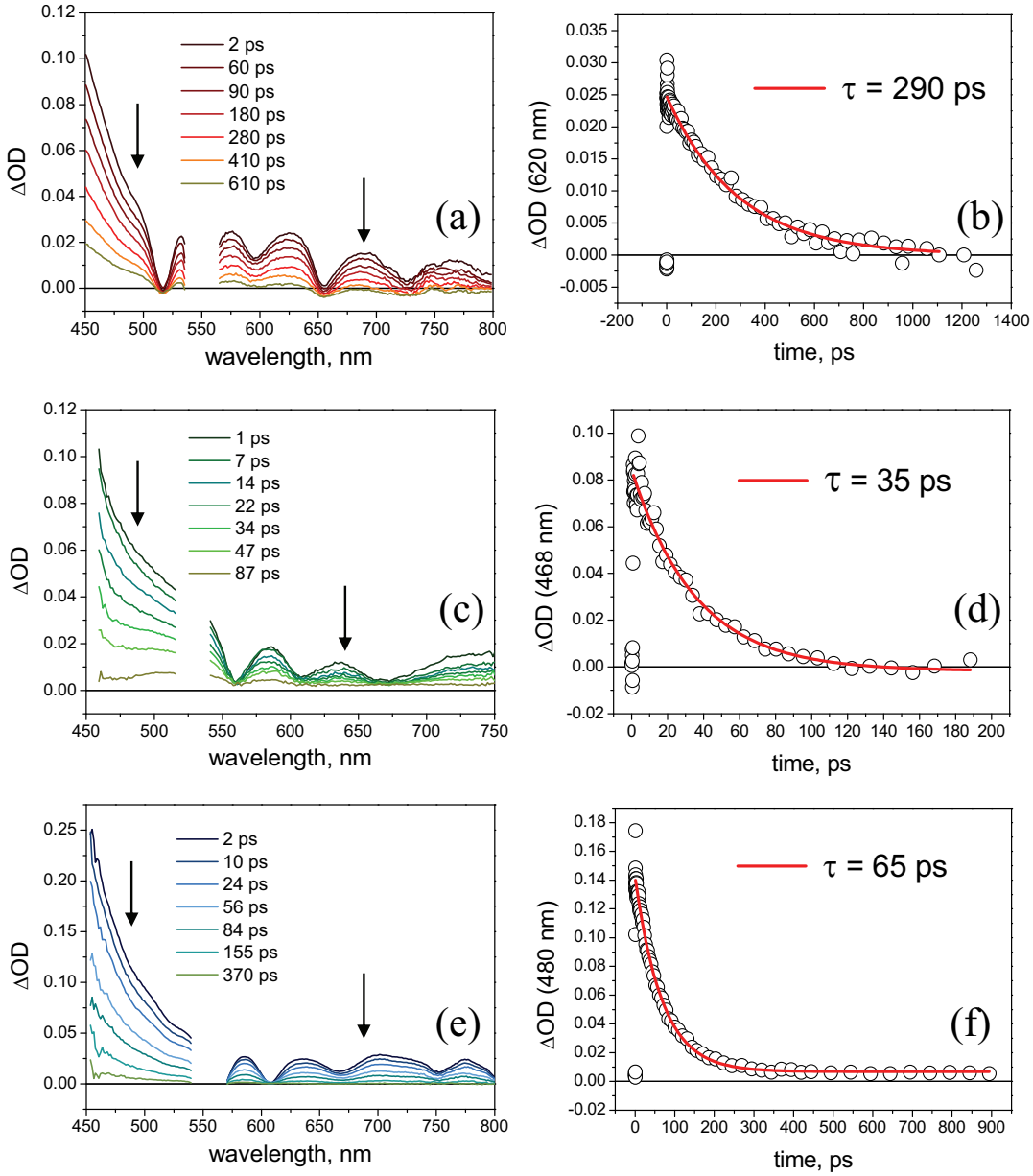

Fig. 6.31. Ultrafast spectroscopy in THF: **P-Co** (a) transient absorption spectra (excitation at 550 nm) and (b) kinetic analysis at 620 nm; **ZnP-Co** (c) transient absorption spectra (excitation at 530 nm) and (d) kinetic analysis at 468 nm; **AlP-Co** (e) transient absorption spectra (excitation at 550 nm) and (f) kinetic analysis at 480 nm.

Supramolecular adducts between monopyridyl porphyrins and metal complexes are usually known[126] to be stable in non-coordinating solvent for concentration ≥ 50 μM. Thus, the concentration of **P-Co**, **ZnP-Co**, and **AlP-Co** in the probed solutions was kept ≥ 0.1 mM in

order to minimize eventual dissociation of the cobaloxime, partially observed in the fluorescence experiments where the concentration was about one order of magnitude lower.

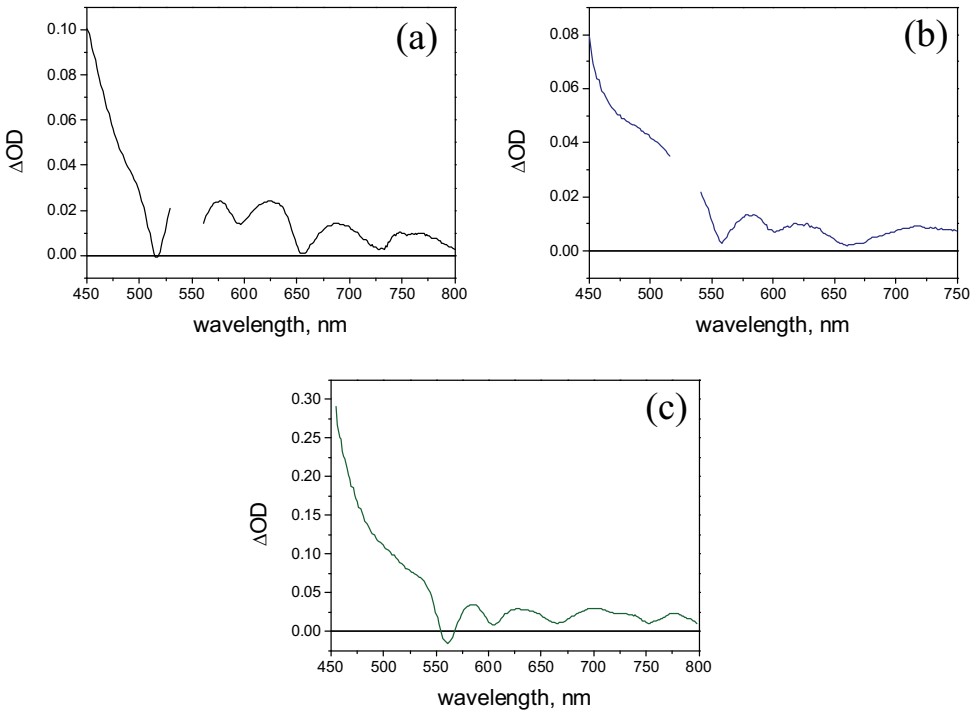

Fig. 6.32. Transient absorption spectra (almost constant along the time window of the experiments, 2000 ps) obtained by ultrafast spectroscopy in THF on (a) **P** (excitation at 550 nm), (b) **ZnP** (excitation at 530 nm), and (c) **AlP** (excitation at 550 nm).

The singlet excited state difference absorption spectra of the model compounds **P**, **ZnP**, **AlP** (Figure 6.32) are characterized by broad and strong absorption around 450-500 nm, Q-band bleach, and broad absorption at longer wavelengths, with superimposed stimulated emission (apparent bleach at 650 and 700 nm for **P**, and at 600 and 650 nm for both **ZnP** and **AlP**). These spectra remain practically constant for **P** and **AlP**, undergoing only a partial decay for **ZnP**, over the whole time-window of the experiment (2000 ps), in agreement with the lifetimes measured by time-correlated single photon counting technique (see above). As to dyads **P-Co**, **ZnP-Co**, **AlP-Co**, in all cases simple monophasic spectral variations are observed indicating rapid decay of the singlet excited state to the ground state. The monoexponential fittings of the kinetic traces yield the time constants of such processes: 290 ps for **P-Co**, 35 ps for **ZnP-Co**, and 65 ps for **AlP-Co**, corresponding to rate constant values of 3.4×10^9, 2.9×10^{10}, and 1.5×10^{10} s^{-1}, respectively. As it can be observed from the data of Figure 6.31, the spectral profiles of the excited singlet state remains unchanged during the whole decay, with no evidence for any other products, besides the ground state, being

permanently or transiently formed. These results clearly rule out heavy-atom effects as possible quenching mechanism, since enhanced intersystem crossing would lead to the formation of the long-lived triplet state of the porphyrin. They are qualitatively compatible, however, with both energy and electron transfer mechanisms, provided that the transient products of these processes, Co(III) complex excited states and charge-separated states, respectively, fail to accumulate to a measurable extent for kinetic reasons (disappearance faster than formation). In fact, ligand field excited states of 3d metal complexes are known to be exceedingly short-lived,[142] undergoing ultrafast non-radiative deactivations. On the other hand, considering the high reorganization energy reported for cobaloxime analogues (between 3-4 eV)[118b] both the charge separation ($\Delta G°$ of −0.19 eV, −0.48 eV, and −0.47 eV for **P-Co**, **ZnP-Co**, and **AlP-Co**, respectively) and charge recombination processes ($\Delta G°$ values of −1.72 eV, −1.59 eV, and −1.57 eV for **P-Co**, **ZnP-Co**, and **AlP-Co**, respectively) should lie in the normal region of the classical Marcus theory,[26] with the more exergonic charge recombination expected to be faster than charge separation.

On quantitative basis, however, an energy transfer quenching can be definitely ruled out. First, given the very low absorption of cobaloxime displayed at $\lambda \geq 500$ nm ($\varepsilon < 10^2$ $M^{-1}cm^{-1}$, see above), spectral overlap between donor emission and acceptor absorption is very small with the result that energy transfer to the cobalt complex, cannot be as fast as experimentally observed. In fact, an estimation of the feasibility of an energy transfer process (using a PhotochemCAD 2.1 software routine),[143] according to a Förster mechanism,[28] yields slower rates by one order of magnitude than the experimental data ($k = 9.5 \times 10^8$ s^{-1} for **P-Co**, $k = 1.8 \times 10^9$ s^{-1} for **ZnP-Co** and **AlP-Co** are obtained with the following parameters: $n = 1.4$; $\kappa^2 = 0.66$, $R_{DA} = 9.5$ Å). On the other hand, the rate constants are in a usual range for photoinduced electron transfer in side-to-face systems of this type.[126,144] More importantly, the observed rates are slower for the free-base case **P-Co** and faster for the metallo-porphyrin cases **ZnP-Co** and **AlP-Co**, well correlating with the driving force for charge separation. Finally, solvent effects on rates are also consistent with an electron transfer mechanism. For instance, in the case of dyad **ZnP-Co** (Figure 6.33), an acceleration of the quenching process (*i.e.*, a decrease in excited-state lifetime) is observed upon increasing the solvent polarity in the order toluene (50 ps), THF (35 ps), DMF (10 ps). In this latter solvent, however, partial dissociation of the cobaloxime from the porphyrin is observed (longer component in the decay of the excited state with a time constant consistent with the **ZnP** excited state lifetime), given the more coordinating character of DMF which competes with the pyridyl ligand to the coordination of the cobalt. This notwithstanding, this is the trend expected, considering the stabilization of the

redox products (and thus the increased driving force for the charge separation process) taking place in more polar solvents. The effect on rates is relatively modest, however, because of the compensating effect, in the Marcus normal region, of the concomitant increase in reorganization energy.

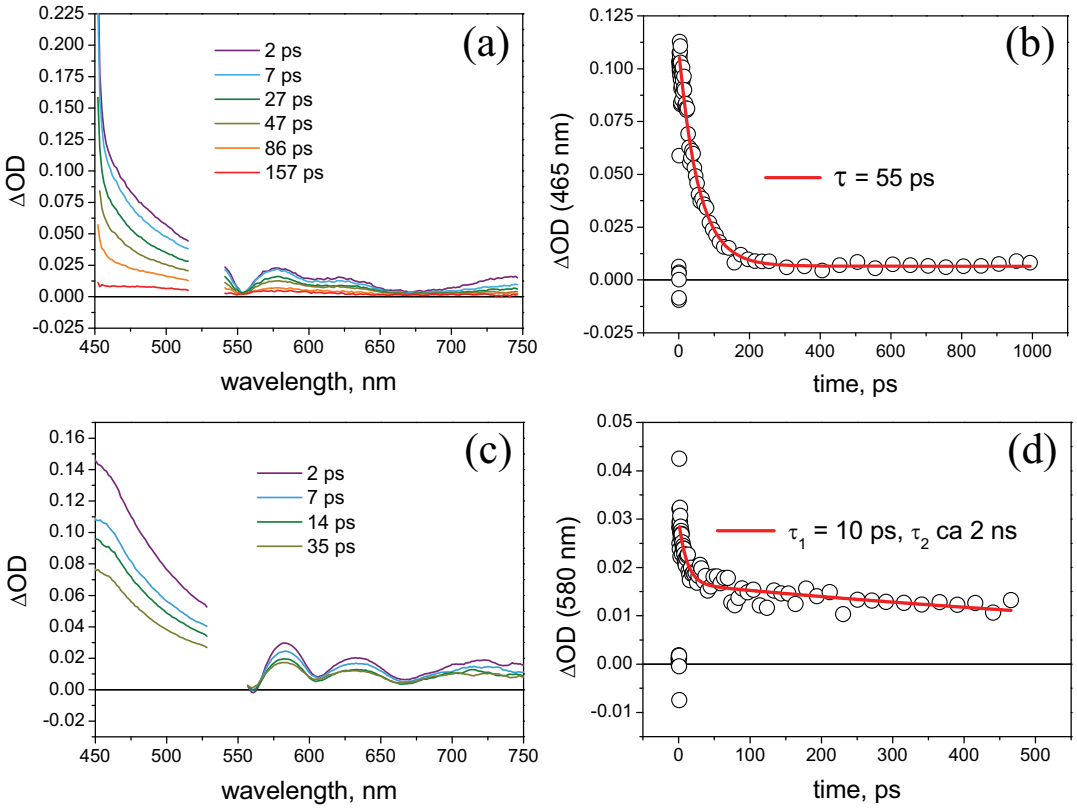

Fig. 6.33. Ultrafast spectroscopy of **ZnP-Co** in: toluene (a) transient absorption spectra (excitation at 530 nm) and (b) kinetic analysis at 465 nm, and DMF (c) transient absorption spectra (excitation at 530 nm) and (b) kinetic analysis at 580 nm.

Overall, these results are relevant to the use of such porphyrin-cobaloxime systems for photocatalytic hydrogen generation. In principle, two pathways are available for photoreduction of the catalyst in the presence of a sacrificial electron donor: (i) reductive quenching of the sensitizer by the donor, followed by electron transfer to the catalyst; (ii) oxidative quenching of the sensitizer by the catalyst, followed by hole shift to the donor. In practice, the fast processes observed in these dyads are potentiallly detrimental to both pathways: charge separation by providing a quenching channel competing with the primary process of path (i), charge recombination by preventing the secondary process of path (ii).

6.5 Conclusions

In this chapter a supramolecular strategy based on the metal-mediated approach has been applied for the construction of porphyrin-cobaloxime dyads suitable for hydrogen production within sacrificial cycles.

In particular, the use of an aluminum(III) pyrydyl porphyrin as photosensitizer unit, beside favoring the complexation of the cobaloxime catalyst *via* the pyridine-cobalt interaction, enables also the attachment of an ascorbate sacrificial donor unit by appropriately exploiting the oxygen-aluminum affinity. This approach enabled the preparation of a self-assembling non-symmetric triad for photocatalytic hydrogen production. The assembling of the cobaloxime and the ascorbate units on the aluminum(III) pyridyl porphyrin platform as well as the occurring photochemical processes have been studied thoroughly. The resulting associated species, however, have been found essentially inactive for hydrogen evolution because of fast unimolecular reversible electron transfer quenching. Rather, the photochemically active species was identified as the fraction of sensitizer present, in the aqueous/organic solvent used for hydrogen evolution, as free species. In fact, its long-lived triplet state reacts bimolecularly with the ascorbate donor, and the reduced sensitizer thus formed subsequently reacts with the cobaloxime catalyst, thereby triggering the hydrogen evolution process. Nevertheless, a good photocatalytic activity has been observed particularly in terms of turnover frequency (TOF = 10.8 min^{-1} or 3.6 min^{-1}, relative to sensitizer or catalyst, respectively) and quantum yield (Φ = 4.6%, *i.e.* 9.2% of maximum possible value). The maximum turnover number found under optimized conditions (TON = 352 or 117, relative to sensitizer or catalyst, respectively) has been shown to be eventually limited by hydrogenation of both sensitizer (chlorin formation) and catalyst.

A detail investigation of the primary photochemical process within a class of porphyrin-cobaloxime dyads was also accomplished by means of stationary and time-resolved spectroscopic techniques. The results still confirm that association is detrimental for hydrogen production because of fast quenching processes of the porphyrin singlet excited state with faster charge recombination. This situation limits irreversible processes required for the storage of the redox gradient into molecular hydrogen.

Chapter 7

A Cationic Cobalt Porphyrin Hydrogen Evolving Catalyst

This chapter is the result of a collaboration with the group of Dr. Elisabetta Iengo at the Department of Chemical and Pharmaceutical Sciences of the University of Trieste. Parts of this chapter can be found in the literature.[145]

7.1 Introduction

In the research field of photochemical water splitting the development of hydrogen evolving catalysts represents a goal of increasing interest. Starting from several pioneering work of the last century,[111,146] macrocyclic cobalt complexes have been extensively used as molecular catalyst for hydrogen evolution,[139,147] with cobaloximes playing by far the main role in the field (see Chapter 6).[105,106,111-124]

Surprisingly, cobalt porphyrins have received very little attention from this viewpoint. Electrocatalytic activity towards hydrogen generation by cobalt porphyrins was indeed investigated on a Hg-pool electrode in 0.1 M trifluoroacetic acid upon application of −0.95 V *vs.* SCE with faradaic efficiency up to 90%.[148] Tentatively, the same authors tried to incorporate the cobalt porphyrin electrocatalyst into a Nafion film on a glassy carbon electrode, obtaining a turnover number (TON) for hydrogen generation of 26 after 90 min electrolysis.[149] More recently, in a study of photocatalytic CO_2 reduction with triethylamine and cobalt tetraphenylporphyrin in polar organic solvents, hydrogen evolution was observed as a side reaction.[150] Afterwards, electrochemical hydrogen production from organic acids catalyzed by a "hangman" cobalt porphyrin in acetonitrile was reported, with the presence of the hanging acid-base function bringing about a decrease in the overpotential for hydrogen generation.[151] Although in this report the catalysis performance was not of interest, the overall results obtained from the cyclic voltammetric analysis uncovered essential mechanistic details of the hydrogen evolving reaction catalyzed by cobalt porphyrins and more generally by cobalt macrocycles.

In this chapter a tetracationic cobalt(II) porphyrin (Figure 7.1) has been studied as hydrogen evolving catalyst in purely aqueous solutions with particular attention to light-activated conditions involving $Ru(bpy)_3^{2+}$ as photosensitizer and ascorbic acid as sacrificial electron donor. As such, this system represents one of the few cobalt-based photocatalytic one working in such an aqueous environment.[108b,c,d,115] A detailed investigation has been also addressed in order to unveil the complex photochemical processes and the kinetic aspects behind the whole photocatalytic cycle.

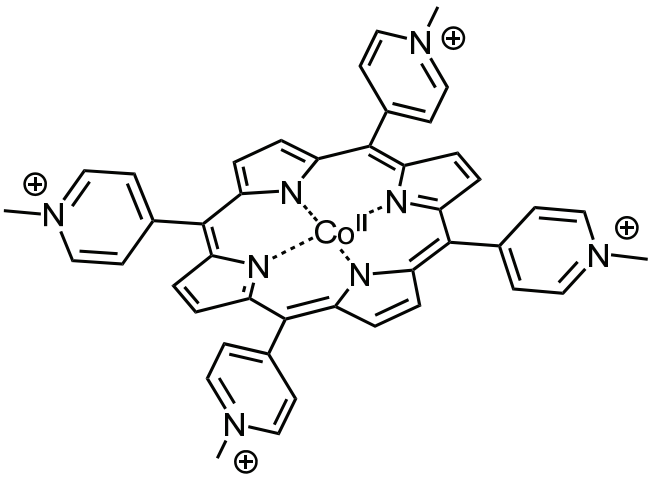

Fig. 7.1. Tetracationic cobalt(II) porphyrin **CoP** used as molecular hydrogen evolving catalyst in this chapter.

As briefly inferred in Chapter 6, in homogeneous photochemical cycles for hydrogen production involving a catalyst, a sensitizer, and a sacrificial electron donor two mechanism are actually available to the excited state of the photosensitizer for the reduction of the catalyst required for hydrogen production: (i) a reductive quenching pathway, involving first photoinduced electron transfer from the donor to the excited sensitizer and subsequent electron transfer to the catalyst (Figure 7.2a), or (ii) an oxidative quenching pathway, where photoinduced electron transfer from the excited sensitizer to the catalyst is followed by hole shift to the donor (Figure 7.2b). It is thus clear that the relative rates of the two quenching (oxidative and reductive) pathways play a crucial role in the whole photocatalytic mechanism.

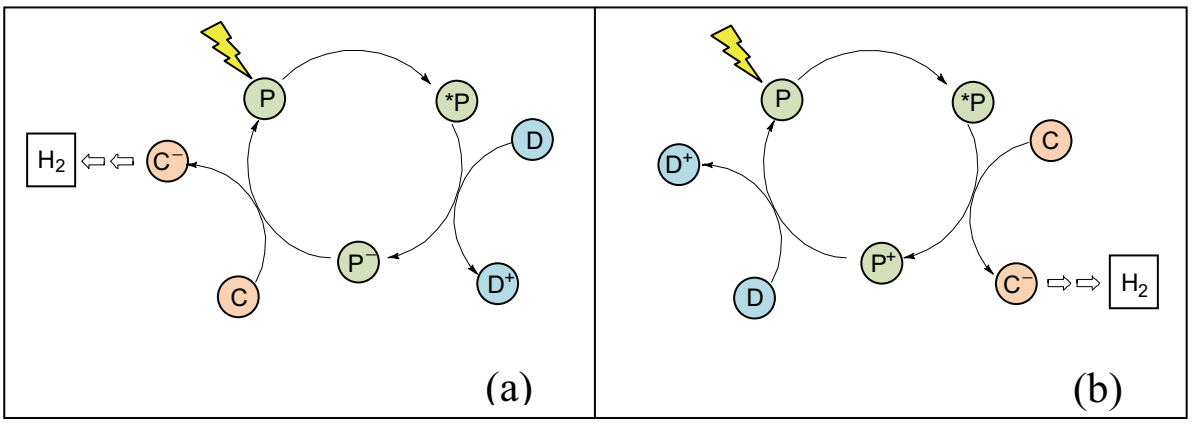

Fig. 7.2. Schematic representation of the two possible photochemical pathways for catalyst reduction and hydrogen generation: (a) reductive quenching pathway and (b) oxidative quenching pathway.

7.2 Experimental section

7.2.1 Synthesis

The synthesis of **CoP**, as a tetraiodide salt, was performed by Alessandra Luisa at the Department of Chemical and Pharmaceutical Sciences of the University of Trieste following slightly adapted literature procedures.[152,153] The synthesis of **CoP** was obtained by a two-step procedure involving (i) insertion of the cobalt(II) within a free-base tetrapyridyl porphyrin (TPyP) and (ii) methylation of the obtained CoTPyP.

(i) 5,10,15,20-tetrakis (4'-pyridyl) porphyrin (TPyP purchased from Sigma-Aldrich, 53.7 mg, 0.087 mmol) was dissolved in chloroform (30 mL) and stirred for 16 hours with an excess of $Co(CH_3COO)_2 \cdot 4H_2O$ (54.0 mg, 0.22 mmol) dissolved in a minimum amount of methanol. The reaction was quenched by addition of deionized water (30 mL). A purple product precipitated after cooling the mixture. The precipitated was filtered, washed thoroughly with methanol and dried under vacuum. Yield: 44.8 mg (76.3%). ESI-MS m/z calcd. for $C_{40}H_{24}N_8Co$ ($[M]^+$) 675.1, found 675.2.

(ii) The obtained 5,10,15,20-tetrakis (4'-pyridyl) cobalt(II) porphyrin (Co(II)TPyP, 30.4 mg, 0.045 mmol) was treated in DMF (5 mL) with a large excess of methyl iodide (0.140 mL, 2.25 mmol) for 2 hours at refluxing temperature. After addition of diethyl ether, a purple solid precipitated and the unreacted CH_3I stayed in the diethyl ether phase. The product was filtered, washed with cold diethyl ether, recrystallized with a water/ethanol mixture and dried under vacuum. Yield: 27.6 mg (83.4%). ESI-MS m/z calcd. for $C_{44}H_{36}N_8Co^{4+}$ ($[M-4I]^+$) 183.8, found 183.7.

7.2.2 Apparatus and procedures

All the reagents were used as received. Acetonitrile was of spectroscopic grade, ultrapure milli-Q water and related buffers were used. See Chapter 2 for experimental details on the electrochemical and spectroscopic techniques.

7.3 Results and discussion

7.3.1 Absorption spectrum and photophysical properties

The electronic absorption spectrum of **CoP** in water (Figure 7.3, red trace) is dominated by the typical features of metalated porphyrins, *i.e.*, Soret (λ_{max} = 433 nm, ε = 59,500 $M^{-1}cm^{-1}$) and Q bands (λ_{max} = 544 nm, ε = 6,000 $M^{-1}cm^{-1}$), corresponding to the $S_0 \rightarrow S_2$ and the $S_0 \rightarrow S_1$ $\pi-\pi^*$ transitions, respectively. On the other hand, cobalt-centered d-d transitions, given their forbidden nature, display negligible absorptions. The intense absorption in the 400-500 nm region is relevant to the use of **CoP** for hydrogen production within sacrificial cycle involving $Ru(bpy)_3^{2+}$ as photosensitizer (see below), due to the partial overlap with the MLCT band of the ruthenium complex (Figure 7.3).

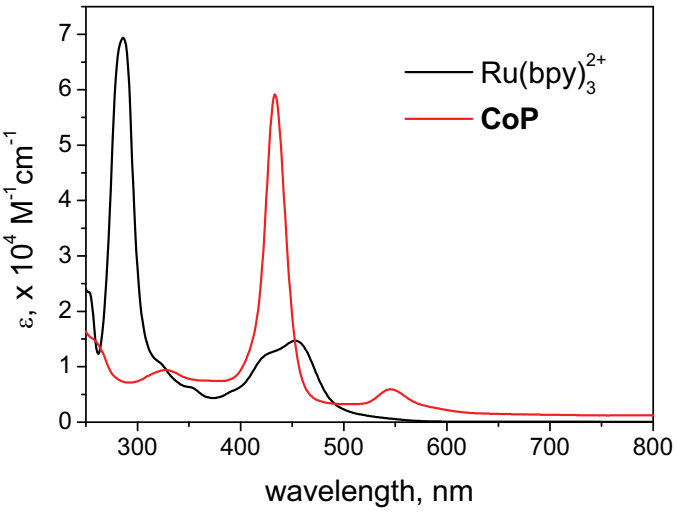

Fig. 7.3. Comparison of the absorption spectra of $Ru(bpy)_3^{2+}$ and **CoP** in water.

Conversely to other metallo-porphyrins (*e.g.*, those studied in Chapter 6), **CoP** is practically non-fluorescent. It is indeed known that the $\pi-\pi^*$ excited state undergoes very fast thermal deactivation through the low lying cobalt d-d states.[78]

7.3.2 Electrochemical characterization

Electrochemical characterization of **CoP** in acetonitrile by cyclic voltammetry (CV) shows the presence of several cathodic processes, occurring in the potential window between 0 and −2.0 V *vs.* SCE (Figure 7.4a). Metal-centered, poorly reversible processes[151] can be identified

at −0.67 V and −1.47 V *vs.* SCE, ascribable to one-electron reductions from Co(II) to Co(I) and from Co(I) to Co(0), respectively. The remaining reversible processes, with half-wave potentials of −1.04 V and −1.10 V, can be attributed to reductions occurring at the porphyrin level, most likely involving the methylpyridinium moieties. As regarding the two one-electron cobalt-centered processes, however, the peak current intensities are clearly not comparable. Differential pulsed voltammetry (DPV) measurements (Figure 7.4b) allow to establish that the first reduction wave observed in the CV is actually a superposition of two cathodic processes: as a matter of fact, it can be noticed that the reduction of dioxygen (inevitably present as residual traces in our working conditions) shows up as a distinguishable peak, very close to the first **CoP** reduction, in the DPV measurements.

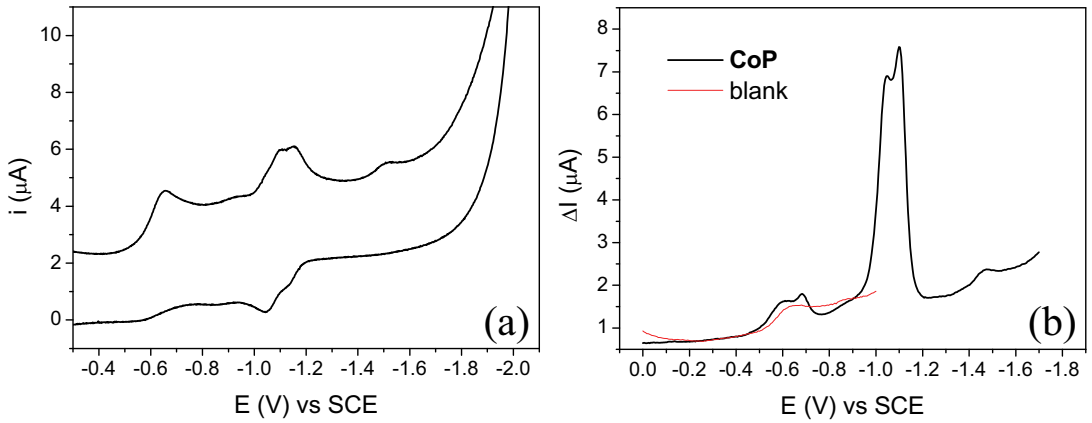

Fig. 7.4. (a) Cyclic voltammetry of 0.1 mM **CoP** solution in acetonitrile (0.1 M $LiClO_4$, scan rate 100 mV/s, room temperature) and (b) differential pulsed voltammetry of 0.1 mM **CoP** solution in acetonitrile (0.1 M $LiClO_4$, ΔE = 20 mV, room temperature) compared with blank.

Upon addition of benzoic acid (Figure 7.5) the Co(II)/Co(I) redox process remains practically unaffected, while the onset of a new irreversible cathodic wave is observed at ca. −1.2 V with peak current intensities proportional to the amount of proton donor present in solution. This behavior is consistent with the assignment of such cathodic wave to catalytic proton reduction.

Important mechanistic information can be obtained from these cyclic voltammetry experiments (eq 31-34). In particular, the fact that the catalytic wave starts at more negative potentials than those of the Co(II)/Co(I) process (eq 31) implies that catalytic hydrogen formation only occurs upon reduction of Co(I) to Co(0) and protonation (*i.e.*, formation of a Co(II)-hydride intermediate).[151] Moreover, this latter process is most likely a proton-coupled electron-transfer (PCET) since the onset of the catalytic wave occurs at less negative potentials with respect to the Co(I)/Co(0) redox couple in the absence of acid (eq 32).[154] As

far as hydrogen evolution from the Co(II)-hydride is concerned, two mechanisms are actually available, a heterolythic pathway (eq 33) and a homolythic one (eq 34).

$$Co(II) + e^- \rightarrow Co(I) \quad (31)$$

$$Co(I) + e^- + H^+ \rightarrow Co(II)\text{-}H \quad (32)$$

$$Co(II)\text{-}H + H^+ \rightarrow H_2 + Co(II) \quad (33)$$

$$2\ Co(II)\text{-}H \rightarrow H_2 + 2\ Co(I) \quad (34)$$

The experiments in Figure 7.5, however, do not allow any attribution of the actual mechanism, since different experimental conditions (for instance different **CoP** concentrations) should be explored to get a more detailed overview. This investigation is, however, out of the scope of this work.

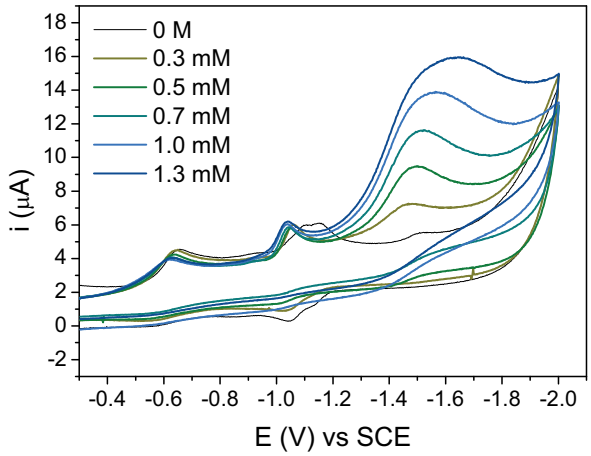

Fig. 7.5. Cyclic voltammetry of 0.1 mM **CoP** solution in acetonitrile (0.1 M $LiClO_4$, scan rate 100 mV/s, room temperature) upon addition of different amount of benzoic acid (0-1.3 mM).

More importantly, similar behavior is also observed in 1 M aqueous phosphate buffer at pH 7 (Figure 7.6), as the catalytic proton discharge starts at ca. −1.2 V, *i.e.*, at a more negative potential than the Co(II)/Co(I) couple. This confirms that reduction/protonation of a Co(I) species is the key step for hydrogen evolution catalyzed by **CoP**. The overpotential η for the hydrogen evolution reaction (taken at a current value of 50 μA), relative to the thermodynamic potential at pH 7, is ca. 700 mV.

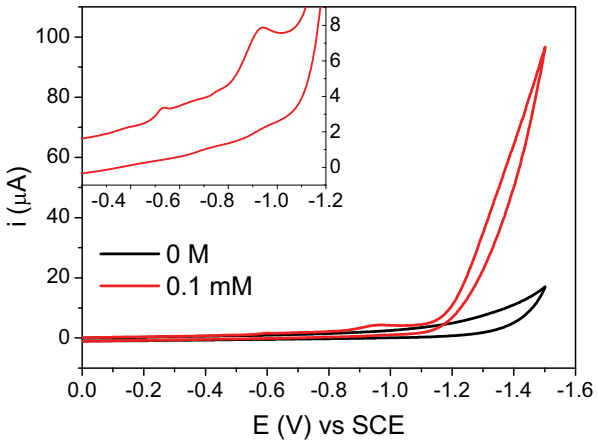

Fig. 7.5. Cyclic voltammetry of 0.1 mM **CoP** solution in 1 M phosphate buffer at pH 7 (0.1 M $LiClO_4$, scan rate 100 mV/s, room temperature) compared with the blank; (inset) detail between −0.3/−1.2 V.

7.3.3 Hydrogen evolution experiments

Hydrogen evolving activity of **CoP** was studied in light-activated experiments, upon continuous irradiation with visible light (175 W Xenon arc lamp, cut-off at 400 nm) of argon purged aqueous solutions containing $Ru(bpy)_3^{2+}$ and ascorbic acid and monitoring the gas-phase of the reactor by gas chromatography. **CoP** was found to generate hydrogen efficiently in solution containing 1 mM $Ru(bpy)_3^{2+}$ and 0.1 M ascorbic acid in 1 M phosphate buffer at pH 7. In such conditions the photocatalytic activity was seen to be strongly dependent on **CoP** concentration (Figures 7.6 and 7.7, Table 7.1).

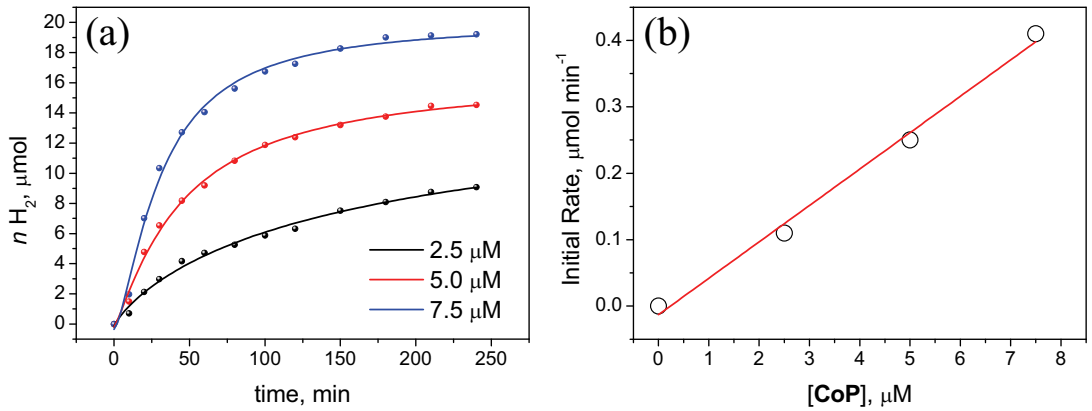

Fig. 7.6. (a) Kinetics of photoinduced hydrogen evolution in 1 M phosphate buffer (pH 7) solutions containing 1 mM $Ru(bpy)_3Cl_2$, 0.1 M ascorbic acid, and 2.5-7.5 μM **CoP**; (b) plot of the initial rate (calculated in the linear part of the kinetic) *vs.* catalyst concentration.

Table 7.1. Photocatalytic hydrogen evolution data.[a]

[CoP], μM	TON	Rate,[b] μmol min^{-1}	TOF,[b] min^{-1}
2.5	725	0.11	8.8
5.0	581	0.25	10.0
7.5	512	0.41	10.9
10	422	0.45	9.0
20	338	0.54	5.4
30	269	0.43	2.9

[a] Obtained upon continuous visible irradiation (175 W Xe arc lamp, cut-off at 400 nm) in the presence of 1 mM $Ru(bpy)_3^{2+}$ and 0.1 M ascorbic acid in 1 M phosphate buffer at pH 7; [b] calculated from the slope of the linear part of the kinetics after the induction period.

In particular, at low catalyst loading (2.5-7.5 μM, Figure 7.6a) the initial rate of hydrogen production follows a linear correlation with **CoP** concentration (Figure 7.6b). As in similar cases (*e.g.*, with cobaloxime catalysts, Chapter 6) this linear relationship can be taken as an indication that hydrogen production occurs *via* a heterolythic pathway involving protonation of the cobalt-hydride intermediate (eq 33).

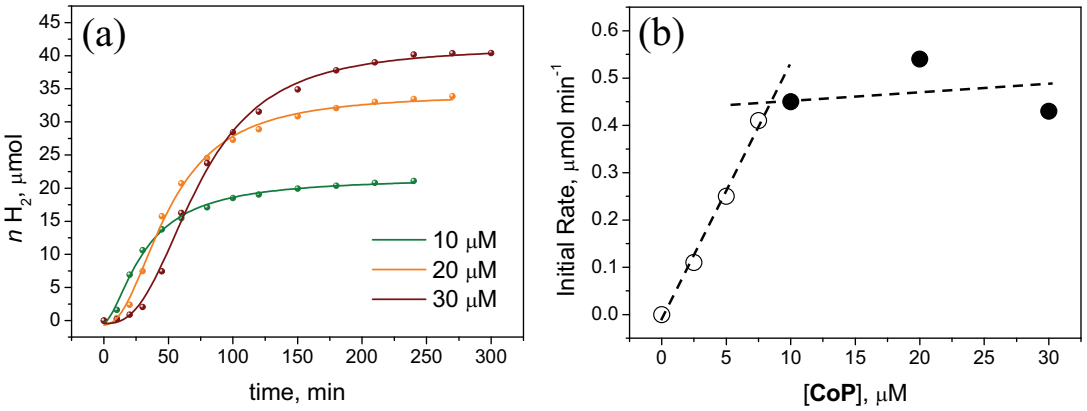

Fig. 7.7. (a) Kinetics of photoinduced hydrogen evolution in 1 M phosphate buffer (pH 7) solutions containing 1 mM $Ru(bpy)_3Cl_2$, 0.1 M ascorbic acid, and 10-30 μM **CoP**; (b) plot of the initial rate (calculated in the linear part of the kinetic) *vs.* catalyst concentration.

On the other hand, when the amount of catalyst in solution increases up to 10-30 μM (Figure 7.7a), two main differences can be observed: (i) the rate of hydrogen production, calculated in the linear part of the kinetics, becomes almost constant reaching its maximum value (Figure 7.7b) and (ii) a more pronounced induction period is revealed as the **CoP** concentration is raised. This latter evidence can be ascribed to both the competition in light

absorption by **CoP** (which becomes important for concentrations of the order of 10 μM or higher, Figure 7.3) and to the extension in the lag-time required for an appreciable fraction of the catalytically active **CoP** species to accumulate at stationary state.

The hydrogen evolving activity ceased after about 4-5 hours of irradiation achieving turnover numbers (TONs) dependent on catalyst concentration (Table 7.1), with the highest value of 725 recorded at 2.5 μM **CoP**. In these conditions the photocatalytic activity seems to be mainly limited by depletion of the catalyst as suggested from the comparison of the absorption spectra before/after photolysis (Figure 7.8). As a matter of fact, for **CoP** concentrations between 10-30 μM, where an appreciable contribution of the porphyrin in the absorption spectrum of the photolyzing mixture is detected (see in Figure 7.8 the difference with respect to solutions in the absence of **CoP**), complete disappearence of the Soret band of **CoP** is actually observed after 4-5 hours of irradiation, whilst the MLCT band of the $Ru(bpy)_3^{2+}$ sensitizer undergoes only minor changes. These latters are qualitatively similar to the spectral variations observed for other photocatalytic systems using the $Ru(bpy)_3^{2+}$/ ascorbate couple,[47c,d] and can be likely ascribed to unproductive routes involving the photogenerated reduced sensitizer and competing with electron transfer to **CoP**.

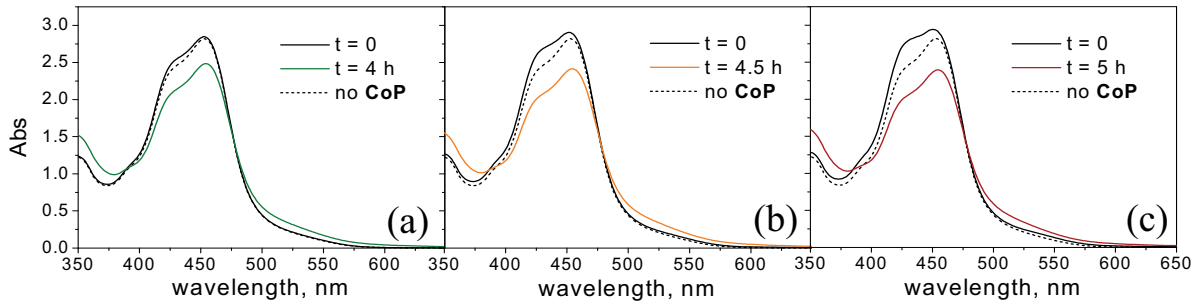

Fig. 7.8. Comparison of absorption spectra before/after the photolysis of 1 M phosphate buffer (pH 7) solutions containing 1 mM $Ru(bpy)_3^{2+}$, 0.1 M ascorbic acid, and (a) 10 μM **CoP**, (b) 20 μM **CoP**, or (c) 30 μM **CoP**.

Hydrogen evolving performance of **CoP** in phosphate buffer was also found to be strongly dependent on pH (Figure 7.9), with results in terms of turnover numbers (TON) and frequency (TOF) peaking at the value of 7. This bell-shaped profile is likely to arise from a balance between several factors playing together towards hydrogen generation: (i) the decreasing stability of the sensitizer under irradiation with decreasing pH, likely related to protonation of its reduced form (Figure 7.10), (ii) the deprotonation of ascorbic acid at higher pH to lower the oxidation potential for faster reductive quenching of the photosensitizer (although reductive quenching of $Ru(bpy)_3^{2+}$ by ascorbic acid was found to be almost pH

independent),[108d] (iii) the thermodynamic driving-force for water reduction (lower at basic pH than at acidic one), and (iv) the formation of the cobalt-hydride catalytic intermediate which is much more favored at acidic pH.

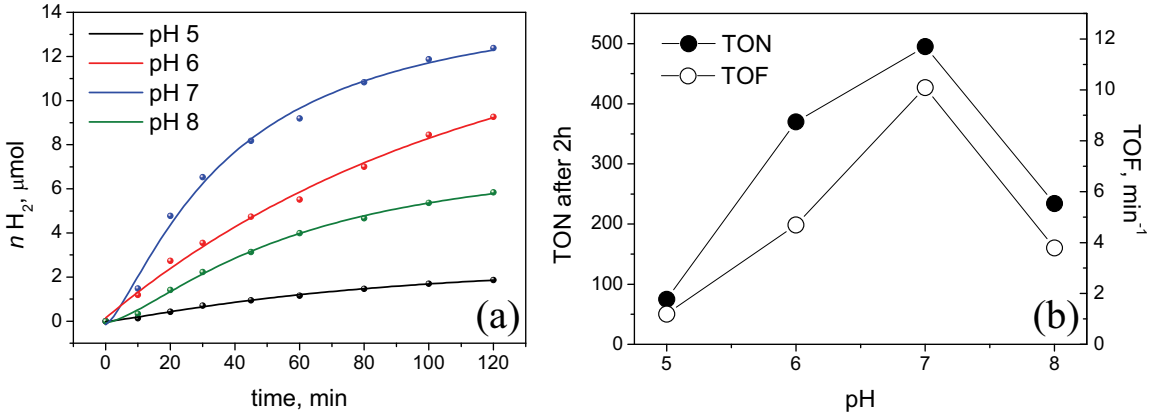

Fig. 7.9. Effect of pH on hydrogen evolving activity of **CoP**: (a) kinetic of hydrogen evolution in 1 M phosphate buffer solutions at different pH containing 5 µM **CoP**, 1 mM $Ru(bpy)_3^{2+}$, and 0.1 M ascorbic acid; (b) plot of TON and TOF *vs.* pH.

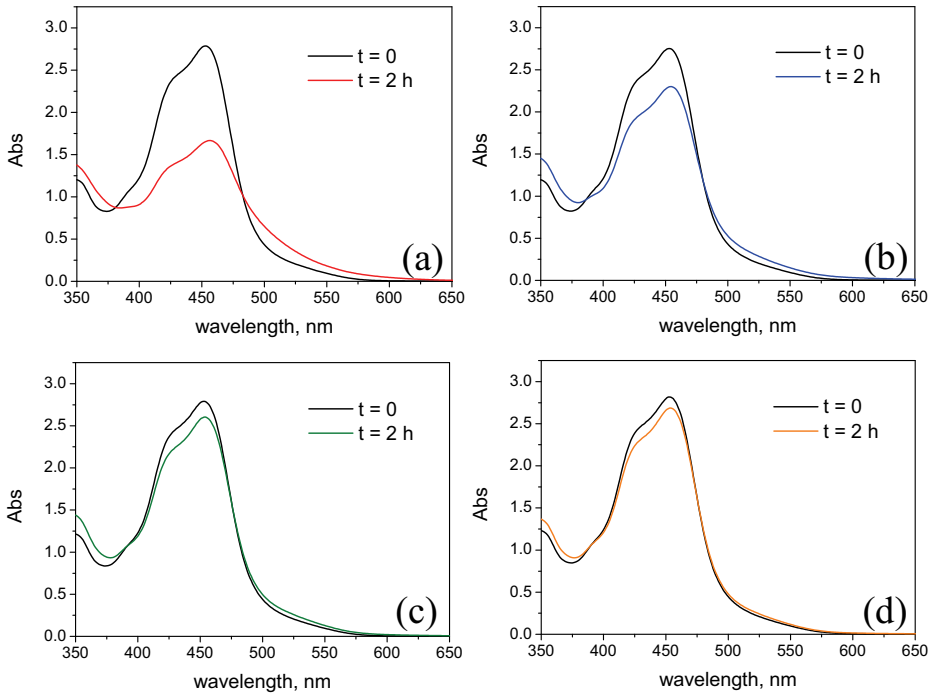

Fig. 7.10. Comparison of absorption spectra before/after the photolysis of solutions containing 5 µM **CoP**, 1 mM $Ru(bpy)_3^{2+}$, and 0.1 M ascorbic acid in 1 M phosphate buffer at (a) pH 5, (b) pH 6, (c) pH 7, and (d) pH 8.

Comparison with the well-known cobaloxime catalyst $(Co(dmgH)_2ClEtPy)$[105,106,110-123] (see also previous Chapter 6) under the experimental conditions used herein shows the superior

activity of **CoP**. In fact, at 5 μM concentration (Figure 7.11a), cobaloxime was found to produce negligible amount of hydrogen (ca. 0.5 μmol after 4 hours of irradiation) compared to **CoP** (14.5 μmol, Figure 7.6a), corresponding to a turnover number (TON) ca. 30-fold lower (17 and 581 for cobaloxime and **CoP**, respectively). Moreover, in order to obtain the same final volume of hydrogen as produced by a 2.5 μM **CoP** solution (ca. 9 μmol, Figure 7.11b), 100 μM $Co(dmgH)_2ClEtPy$ was required (Figure 7.11b). Even though in this latter conditions a similar amount of hydrogen is produced, a substantial difference in terms of turnover numbers (18 and 725 for cobaloxime and **CoP**, respectively), *i.e.*, the number of overall cycles the catalyst is capable of performing, is observed.

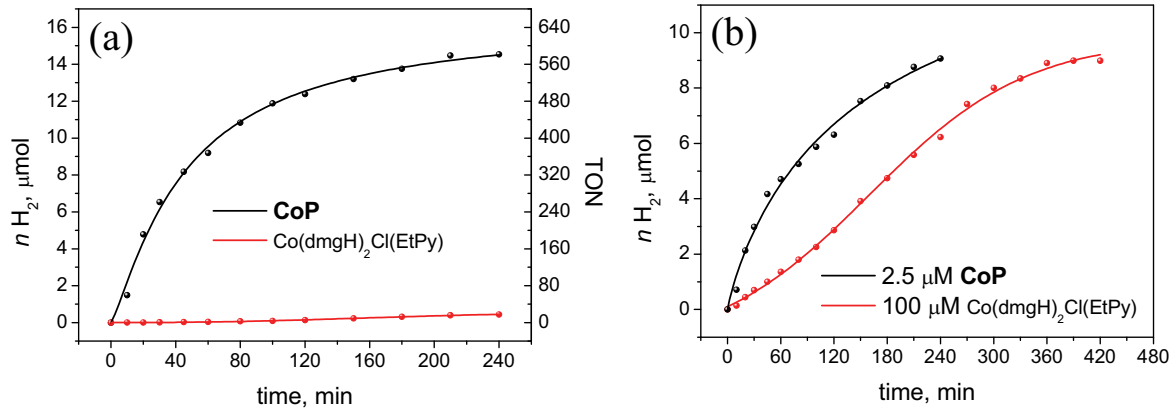

Fig. 7.11. Kinetic of hydrogen evolution upon irradiation of 1 M phosphate buffer (pH 7) solutions containing 1 mM $Ru(bpy)_3^{2+}$, 0.1 M **AscH**, and (a) 5 μM **CoP** or 5 μM cobaloxime, and (b) 2.5 μM **CoP** or 100 μM cobaloxime.

7.3.4 Hydrogen evolution mechanism

As previously mentioned in Section 7.1, the reduction of the catalyst may occur either by (i) oxidative quenching by the catalyst followed by hole shift to the donor (Figure 7.2b) or (ii) reductive quenching by the sacrificial agent followed by electron transfer to the catalyst (Figure 7.2a). To check for these possibilities, the relative kinetics for oxidative quenching by **CoP** and reductive quenching by ascorbic acid have been studied. Given the high ionic strength of the solvent medium (1 M phosphate buffer), specific interactions (*e.g.*, electrostatic ones) between $Ru(bpy)_3^{2+}$, **CoP**, and ascorbic acid can be considered negligible. Therefore all these reactions are bimolecular in nature and their kinetics can be investigated by means of Stern-Volmer type calculations (eqs 35,36).

$$\frac{I^o}{I} = \frac{\tau^o}{\tau} = 1 + k_{SV}[Q] \tag{35}$$

$$k_{SV} = k_Q \, \tau^\circ \tag{36}$$

where I° and I are the emission intensities in the absence and in the presence of the quencher, respectively, τ° and τ are the emission lifetimes in the absence and in the presence of the quencher, respectively, $[Q]$ is the concentration of the quencher and k_Q is the bimolecular rate constant for the quenching process.

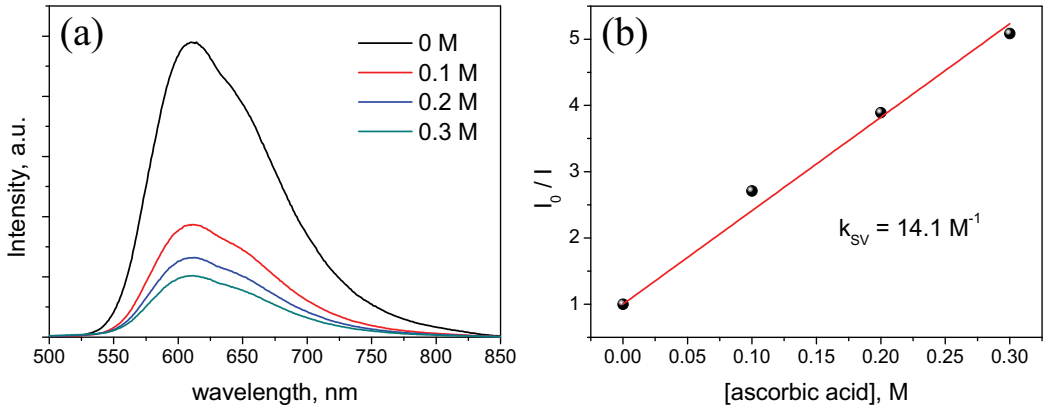

Fig. 7.12. (a) Photoluminescence spectra (excitation at 450 nm) of solution containing 50 μM $Ru(bpy)_3^{2+}$ in 1 M phosphate buffer at pH 7 after addition of different aliquots of ascorbic acid (0-0.3 M); (b) Stern-Volmer plot of quenching by ascorbic acid.

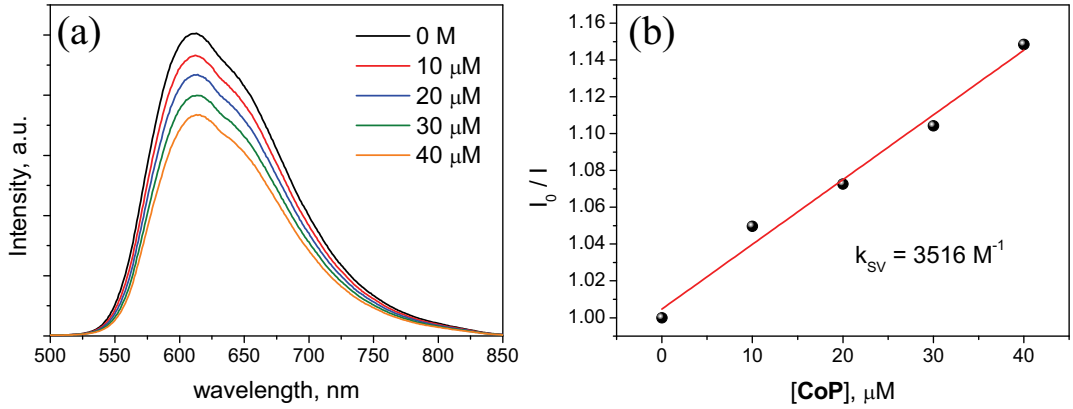

Fig. 7.13. (a) Photoluminescence spectra (excitation at 470 nm) of solution containing 50 μM $Ru(bpy)_3^{2+}$ in 1 M phosphate buffer at pH 7 after addition of different aliquots of **CoP** (0-40 μM); (b) Stern-Volmer plot of quenching by **CoP** (inner filter correction applied).

It was indeed found that ascorbic acid in 1 M phosphate buffer at pH 7 quenches reductively the $Ru(bpy)_3^{2+}$ excited state following a Stern-Volmer behavior with a $k_Q = 3.1 \times 10^7$ $M^{-1}s^{-1}$ (Figure 7.12), whereas **CoP** also quenches ^{3}*$Ru(bpy)_3^{2+}$ following a Stern-Volmer kinetic, but with a higher rate constant $k_Q = 7.8 \times 10^9$ $M^{-1}s^{-1}$ (Figure 7.13). In the working conditions, however, the concentration of ascorbic acid (0.1 M) is much greater than that of **CoP** (2.5-30 μM), with the consequence that reductive quenching by ascorbate (with an effective pseudo-first-order rate of 3.1×10^6 s^{-1}) dominates over oxidative quenching by **CoP** (with a rate between 0.2-2.3 $\times 10^5$ s^{-1}). Therefore, given this difference in rate of about one order of magnitude, the first photochemical event is reductive quenching by ascorbic acid (Figure 7.2a), followed by electron transfer to the **CoP** catalyst, which upon further reduction/protonation is capable of reducing protons to molecular hydrogen. This notwithstanding, negligible amount of hydrogen was produced by lowering ascorbic acid concentration down to 1 mM in order to favor the oxidative quenching by **CoP** (30 μM) over the reductive one by the donor, suggesting that either the oxidative pathway does not work at all in the **CoP**/$Ru(bpy)_3^{2+}$/ascorbic acid three-component system or the quenching by **CoP** is not strictly due to an electron transfer process, but rather to an energy transfer one.

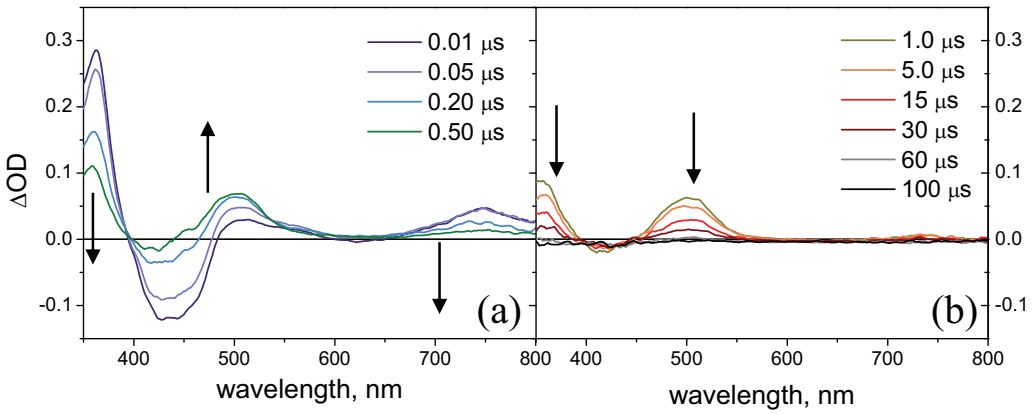

Fig. 7.14. Transient absorption spectra obtained by laser flash photolysis (excitation at 355 nm) on a 1 M phosphate buffer solution (pH 7) containing 0.1 mM $Ru(bpy)_3^{2+}$ and 0.1 M ascorbic acid at different time-delays: (a) 0.01-0.50 μs and (b) 1-100 μs.

According to this scenario, one of the key processes triggering the photocatalytic hydrogen production is the electron transfer from the reduced sensitizer to the catalyst. This process can be conveniently monitored by appropriate laser flash photolysis experiments.[105,108d] Excitation of $Ru(bpy)_3^{2+}$ at 355 nm in 1 M phosphate buffer at pH 7 containing 0.1 M ascorbic acid is followed by electron transfer from the donor with formation of the reduced sensitizer $Ru(bpy)_3^{+}$ (Figure 7.14a). This process, occurring in few hundred ns, can be easily followed

as $Ru(bpy)_3^{+}$ displays a very peculiar absorption around 510 nm.[101,108d] In the absence of **CoP**, this transient decays through recombination with the oxidized donor (ascorbate radical) with a second-order kinetic (Figure 7.14b, estimated τ_{CR} = ca. 37 μs).

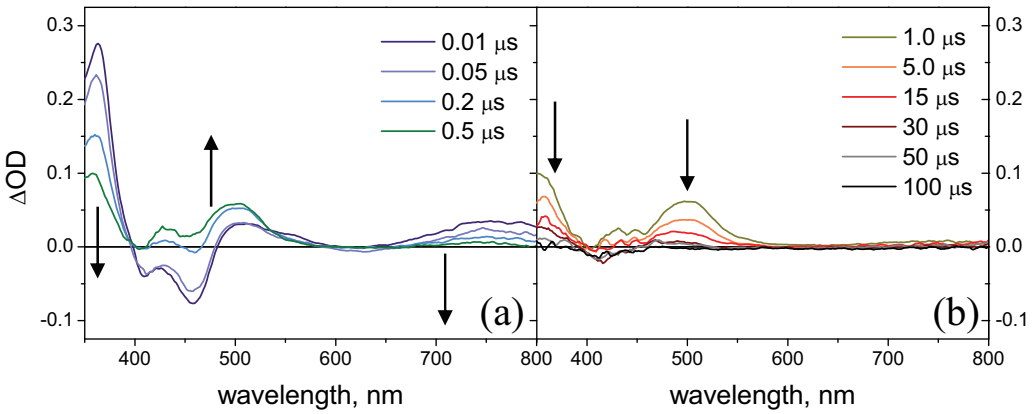

Fig. 7.15. Transient absorption spectra obtained by laser flash photolysis (excitation at 355 nm) on a 1 M phosphate buffer solution (pH 7) containing 0.1 mM $Ru(bpy)_3^{2+}$, 0.1 M ascorbic acid, and 25 μM **CoP** at different time-delays: (a) 0.01-0.50 μs and (b) 1-100 μs.

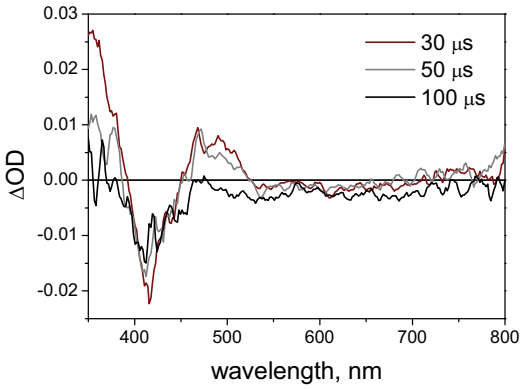

Fig. 7.16. Detailed view of the transient absorption spectra at 30, 50, and 100 μs time-delays of Figure 7.15b.

When 25 μM **CoP** is introduced in solution, reaction of $Ru(bpy)_3^{+}$ with **CoP** can be monitored and time-resolved (Figure 7.15): formation of the reduced sensitizer, with its maximum at 510 nm, is still observed by reaction of ^{3}*$Ru(bpy)_3^{2+}$ with ascorbic acid (Figure 7.15a). However, $Ru(bpy)_3^{+}$ is seen to decay (Figure 7.15b) yielding a different transient (detected at 30, 50, and 100 μs time-delays, Figure 7.16) with spectral features compatible with the formation of the reduced porphyrin species **CoP**$^{-}$,[134] *i.e.*, Soret-band bleach at 420-430 nm and new absorption maximum at 470 nm. This transient is subsequently seen to fade down to the baseline in ca. 90-100 μs (see tails in the kinetics of Figure 7.17a). Importantly,

from the kinetic analysis at 510 nm (Figure 7.17a) the $Ru(bpy)_3^{+}$ transient is observed to decay with appreciably first order dependence on **CoP** concentration. The bimolecular rate constant for this electron transfer process can be calculated under pseudo-first order kinetic conditions (perfectly matched in this study as the concentration of photogenerated reductant can be estimated by means of eq 15 as 1.2 μM considering $\Delta\varepsilon$ = 9,000 $M^{-1}cm^{-1}$ at 510 nm[101] and the instrumental correction parameter 0.74), according to eqs 37-39, with the concentration of $Ru(bpy)_3^{+}$ followed from the transient absorption at 510 nm.

$$v = k\,[Ru(bpy)_3^{+}][\mathbf{CoP}] = k_{obs}\,[Ru(bpy)_3^{+}] \qquad (37)$$

$$[Ru(bpy)_3^{+}] = [Ru(bpy)_3^{+}]_0 \exp -(k_{obs}\,t) \qquad (38)$$

$$k_{obs} = k\,[\mathbf{CoP}] \qquad (39)$$

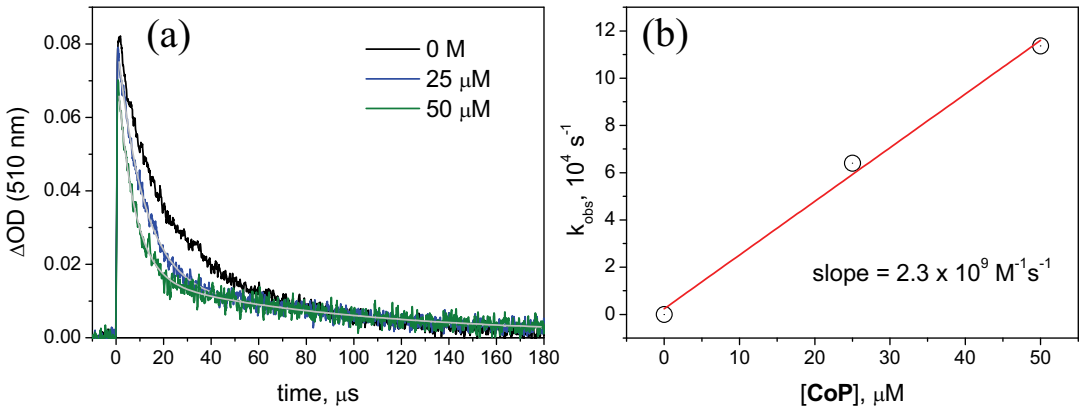

Fig. 7.17. (a) Kinetic analysis at 510 nm obtained by laser flash photolysis (excitation at 355 nm) on a 1 M phosphate buffer solution (pH 7) containing 0.1 mM $Ru(bpy)_3^{2+}$, 0.1 M ascorbic acid, and 0-50 μM **CoP**; (b) plot of the observed rate *vs.* **CoP** concentration for the calculation of the bimolecular rate constant.

When cosidering the decay of $Ru(bpy)_3^{+}$ for the calculation of k_{obs} (eq 37), however, due to the similar time domain of the processes, competition with charge recombination with the radical ascorbate must be taken into account. Therefore the k_{obs} values used in eq 38 are slighly corrected k'_{obs} (eq 40).

$$k'_{obs} = k_{obs} - \frac{1}{\tau_{CR}} \qquad (40)$$

These estimates yield a quite high value (2.3×10^9 $M^{-1}s^{-1}$), which is close to the diffusion limit and as such may likely explain the very high efficiency for hydrogen generation catalyzed by **CoP** at low concentrations.

As a final remark, even though the electrochemistry of **CoP** suggests that the first reduction process involves the cobalt center, the transient signal observed upon reduction by $Ru(bpy)_3^+$ (Figure 7.16), resembling those of π-centered radical species, and the very fast electron transfer rate (Figure 7.17), quite unexpected considering the high reorganization energy of the Co(II)/Co(I) redox couple, are most likely related to the fact that the LUMO of **CoP** (where reduction takes place) displays a significant electron density on the aromatic ring.[151] This evidence has profound effects on a mechanistic viewpoint. A positive effect is indeed that this situation ensures high electron transfer rates enabling **CoP** to operate catalytically at very low concentrations. On the contrary, a negative effect is related to the durability of the system under turnover conditions, in fact the observed decomposition of the catalyst may likely originate from further undesired reduction or disproportionation and protonation of the $\mathbf{CoP}^-$ species involving the aromatic ring.

7.4 Conclusions

The tetracationic cobalt(II) porphyrin **CoP** is a competent catalyst for hydrogen generation from purely aqueous solutions under continuous visible irradiation in the presence of $Ru(bpy)_3^{2+}$ as photosensitizer and ascorbic acid as sacrificial electron donor, achieving TON up to 725. This systems represents one of the few cobalt-based photocatalytic one working in a purely aqueous environment. The photosynthetic performance is mainly limited by depletion of the catalyst. A complete investigation of the photocatalytic system by stationary and time-resolved spectroscopic techniques has shown that hydrogen evolution takes place after reductive quenching of the sensitizer by the donor followed by electron transfer to **CoP**. The high rate observed for the first electron transfer process to the catalyst (2.3×10^9 $M^{-1}s^{-1}$) enables **CoP** to operate catalytically even at very low concentrations. From this standpoint, by comparison with the other hydrogen evolving catalysts used in pure water, **CoP** is seen to work in comparable conditions with the cobalt complex based on the pentadentate "N,Nbis(2-pyridinylmethyl)-2,2'-bipyridine-6-methanamine" ligand,[108c,d] whereas it is more efficient with respect to the pentapyridine cobalt catalyst based on the pentadentate "2,6-bis(1,1-di(pyridin-2-yl)ethyl)pyridine)" ligand,[108a,b] which is shown to require much higher (×10) concentrations to work catalytically.

Chapter 8

Photoactive Dendrimers for Hydrogen Production

This chapter is the result of a collaboration with the group of Dr. Giacomo Bergamini and Prof. Paola Ceroni (Department of Chemistry "G. Ciamician", University of Bologna) and the group of Dr. Vittorio Morandi (IMM-CNR, Bologna). Parts of this chapter can be found in the literature.[155]

8.1 Introduction

In the quest for photochemical hydrogen generation several approaches have been attempted to suitably assemble sensitizers and catalyst within supramolecular architectures.

Dendrimers[156] are repeatedly branched tree-like macromolecules that exhibit a defined structure and a high degree of order in a restricted space. By using suitable synthetic strategies, selected functional units can be placed in predetermined sites of their structure. Moreover, dendrimers can also perform as nanocontainers and templates for the synthesis of metal nanoparticles. In their internal dynamic cavities they can host metal ions which can be reduced to form nanoparticles under suitable experimental conditions.

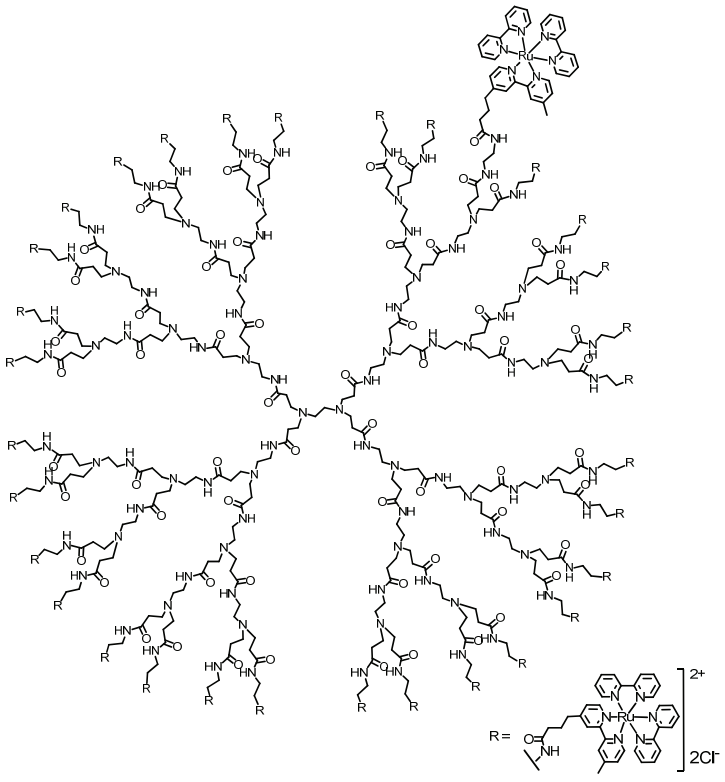

Fig. 8.1. Molecular structure of the functionalized fourth generation polyamidoamine dendrimer **RuPAMAM**.

In this chapter a fourth generation polyamidoamine (PAMAM) dendrimer with 32 $Ru(bpy)_3Cl_2$ metal complexes at the periphery (namely **RuPAMAM**, Figure 8.1)[157] has been used as molecular scaffold for the controlled synthesis of platinum nanoparticles (namely **RuPAMAMPtNps**). Platinum has indeed a low overpotential for hydrogen evolution[158] and as such represents the hydrogen evolving catalyst *par excellence*.

By combining both a photosensitizer and a catalytic moiety, the obtained **RuPAMAMPtNps** system can be used in the presence of a sacrificial electron donor for hydrogen production upon continuous irradiation. As such this system is one of the few dendrimer-based ones reported in literature for photocatalytic hydrogen production[159,160] and the first one where both sensitizer and catalyst are anchored on a dendritic molecular scaffold.

8.2 Experimental section

The **RuPAMAM** dendrimer, as hexafluorophosphate (PF_6^-) salt, was purchased and the counter anions were easily substituted with chloride ones (Cl^-) by ion exchange chromatography. Other reagents were used as received, ultrapure milli-Q water was used. See Chapter 2 for details on the spectroscopic and photolysis apparatus.

Transmission Electron Microscopy (TEM) characterization of the **RuPAMAMPtNps** was carried out at the IMM-CNR in Bologna with a *FEI Tecnai F20* TEM equipped with a Schottky emitter and an Energy Dispersive X-Ray (EDX) spectrometer, operating at 200 keV in both conventional TEM and Scanning Transmission (STEM) mode. Samples were prepared by drop casting an aqueous solution of **RuPAMAMPtNps** on conventional TEM Holey Carbon film copper grid, then heated at 150°C for 10 min to evaporate the solvent.

8.3 Results and discussion

8.3.1 Photophysics of RuPAMAM

The optical properties of the **RuPAMAM** dendrimer were analysed using UV-Vis and fluorescence spectroscopy in water. The absorption spectrum of the dendrimer shows the typical ligand centered (LC) band at 288 nm and the metal-to-ligand charge-transfer (MLCT) band in the visible with a maximum at 455 nm (Figure 8.2). The emission band is identical in

shape and position (maximum at 620 nm) to that of the $Ru(bpy)_3^{2+}$ complex in water, but the emission quantum yield is half (0.014). The quenching is likely due to electron transfer involving the amine moieties present in the skeleton of the dendrimer.

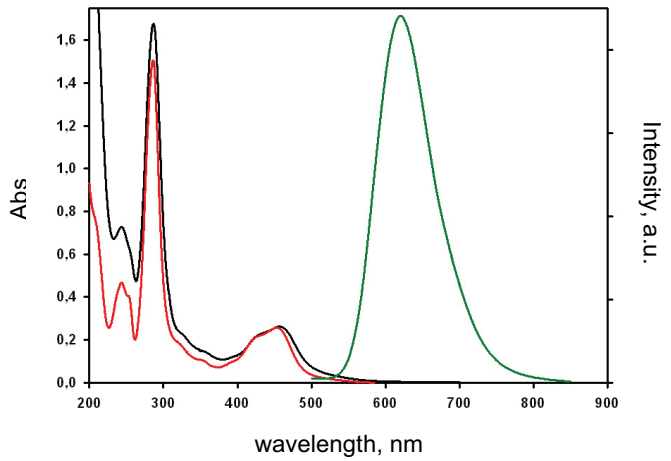

Fig. 8.2. Absorption (black line) and emission (green line) spectra of **RuPAMAM** in water compared to the absorption spectrum of $Ru(bpy)_3^{2+}$.

8.3.2 Preparation of RuPAMAMPtNps

In order to exploit the ability of **RuPAMAM** to template the synthesis of platinum nanoparticles, the coordination of Pt^{2+} ions by the dendrimer was studied.[161] The Pt^{2+} ions can be indeed "hosted" in the dendrimer skeleton by the interaction with the 30 amine units present,[161] even though the precise structure of the metal complexes formed are not well defined, due to the various possibility and the kinetic evolutions of these complexes. Upon titration of a **RuPAMAM** aqueous solution with K_2PtCl_4, small variations in the absorption spectra were observed, namely a decrease of the MLCT band and an increase of a tail below 250 nm (Figure 8.3a). More pronounced changes were observed in the emission spectra upon excitation at an isosbestic point (Figure 8.3b). An 80% decrease of the emission intensity was detected when up to 20 eqs of Pt^{2+} per dendrimer were added to the **RuPAMAM** solution. By still increasing the Pt^{2+}/dendrimer ratio negligible changes in the emission response were then observed. The mechanism of quenching can be very likely ascribed to energy transfer processes from the triplet MLCT excited state of the ruthenium complex to the lower metal centered (MC) states of the Pt^{2+} complex, since the alternative quenching pathways, *i.e.*, photoinduced electron transfer involving formation of either Pt(I) or Pt(III) species, appears very unlikely.

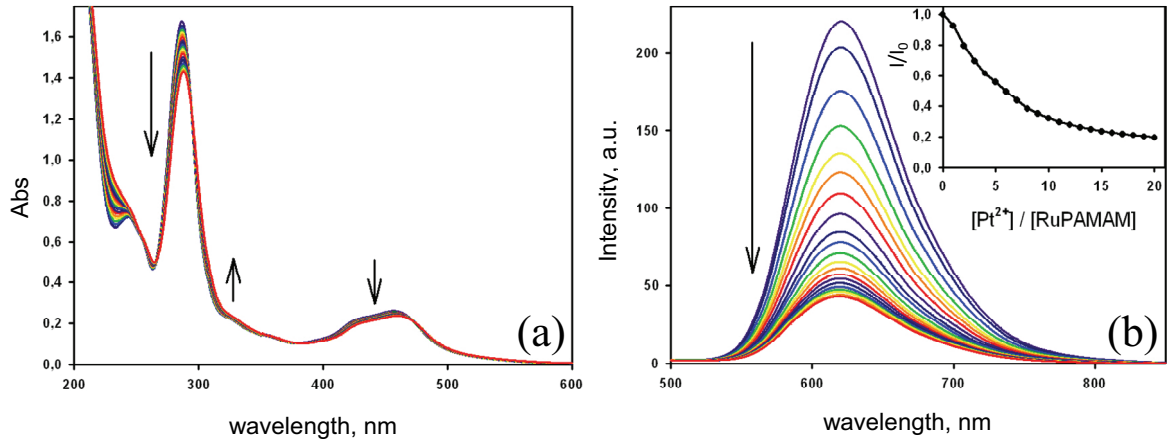

Fig. 8.3. (a) Changes observed in the absorption spectrum of a 1.5 μM **RuPAMAM** in water upon addition of 0-30 μM K_2PtCl_4 and (b) changes of the emission spectrum of **RuPAMAM** in the same conditions (inset, plot of I/I_0 vs. $[Pt^{2+}]$).

After the complexation, the reduction of the platinum metal ions with sodium borohydride ($NaBH_4$) was performed. One equivalent (with respect to Pt^{2+}) of $NaBH_4$ in water was added to a solution of **RuPAMAM** with 20 eqs of Pt^{2+} per dendrimer in order to minimize the amount of platinum ions outside the dendrimers. The solution was stirred for 24 hours and no precipitation was observed confirming that almost all the Pt^{2+} ions were stabilized by the dendrimers. The absorption spectrum obtained after the reduction retained the typical features of the $Ru(bpy)_3^{2+}$ complex (Figure 8.4a) with the growth of a broad band all over the investigated spectral range, as typically observed for nanoparticle formation.[162]

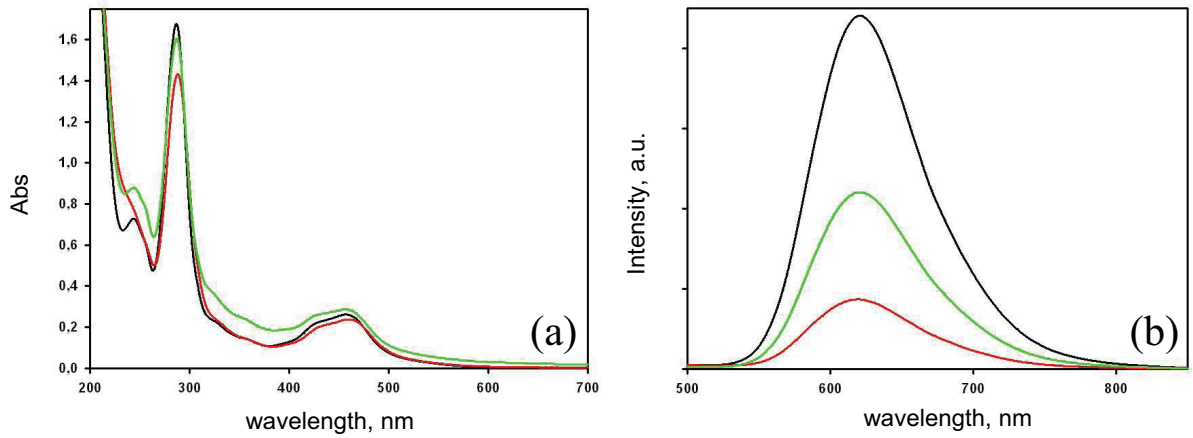

Fig. 8.4. Changes observed in the (a) absorption and (b) emission spectra of a 1.5 μM **RuPAMAM** in water with 30 μM K_2PtCl_4 after reduction with 30 μM $NaBH_4$.

In addition, the emission intensity (Figure 8.4b) increases up to 50% of the initial value (emission before addition of Pt^{2+}). Since Pt^{2+} complexes can quench the ruthenium emission but the platinum nanoparticles cannot,[56a,163] from these emission data we can estimate that the sodium borohydride was capable of reducing ca. 40% of the amount of Pt^{2+} ions coordinated by the dendrimers.

8.3.3 Structural analysis of RuPAMAMPtNps

A low magnification STEM image is reported in Figure 8.5a, in which the contrast is proportional to the atomic number of the elements present. The Pt nanoparticles are clearly visible, represented by the bright white dots, while the dendrimers by the lighter halo surrounding the nanoparticles. Figure 8.5c shows a conventional High Resolution TEM image of a single nanoparticle, confirming at the same time the crystallinity of the nanoclusters and their composition: the interplanar distances of 0.19 nm and 0.22 nm (Figure 8.5d) correspond to the ones of crystalline Pt in (1,0,1) direction. Moreover, the particle size distribution, obtained from the analysis of more than two hundred particles shows an average diameter of 1.3 ± 0.3 nm (Figure 8.5b).

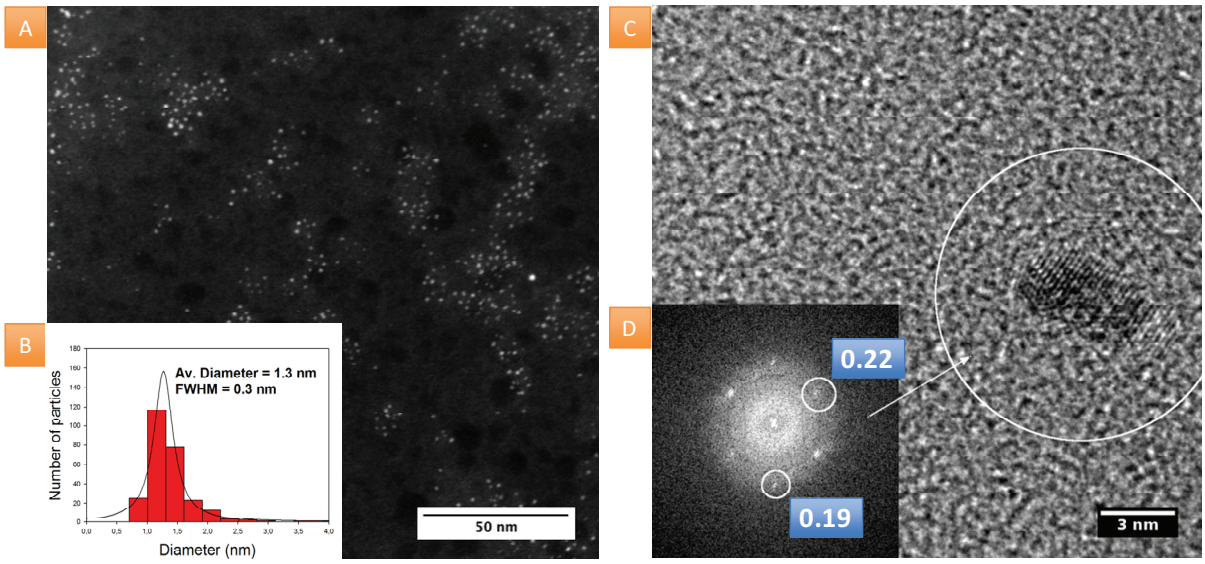

Fig. 8.5. (a) STEM image of **RuPAMAMPtNps** on Holey Carbon film copper grid; (b) histograms showing the PtNps size distribution; (c) HR-TEM image and (d) Fast Fourier Transform of a single nanoparticle.

From these data, an estimate of the number of atoms per nanoparticles *N* can be performed as follows, according to eq 41-43, where *V* (eq 41,42) is the average volume of the Pt

nanoparticle, calculated considering an average radius r of 0.65 nm, d and AW (eq 42) are the density and the atomic weigth of platinum, respectively, n (eq 42) is the number of moles, and N_A (eq 43) is the Avogadro's number.

$$V = \frac{4}{3}\pi\ r^3 = 1.15\times10^{-21} cm^3 \tag{41}$$

$$n = \frac{V \cdot d}{AW} = 1.26\times10^{-22} mol \tag{42}$$

$$N = n\ \cdot N_A = 76 \tag{43}$$

This result suggests that the particle formation involves at least the cooperation of three different dendrimers, not much for the dimension but for average number of platinum per nanoparticle.

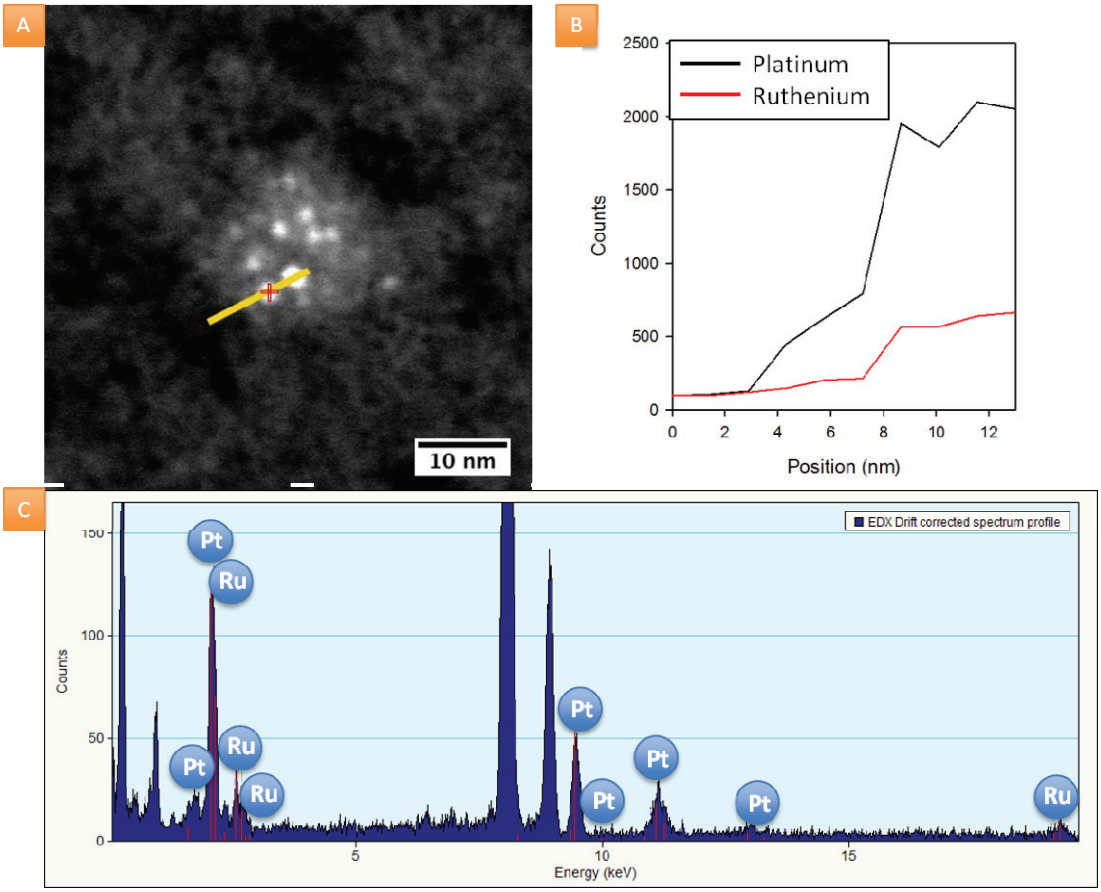

Fig. 8.6. (a) STEM micrograph of a dendrimer aggregate including several Pt nanoparticles; (b) EDX profile taken along the yellow line reported in (a); (c) EDX spectrum relative to the platinum nanoparticle highlighted with the red cross in (a), corresponding to the first peak of Pt profile (black line) in (b).

This is also confirmed by the EDX spectrum profile reported in Figure 8.6. The Pt and Ru EDX profiles (Figure 8.6b) acquired along the yellow line highlighted in Figure 8.6a clearly show the increase of Pt and Ru signals inside the dendrimer as well as the Pt composition of the nanoparticles. This is confirmed by the EDX spectrum (Figure 8.6c) acquired on the nanoparticle marked with the red cross in Figure 8.6a.

8.3.4 Hydrogen evolution experiments

Photocatalytic hydrogen evolution was studied upon continuous irradiation with visible light of an argon purged 1.6 μM aqueous solution of **RuPAMAMPtNPs** at pH 5 in the presence of 0.1 M ascorbic acid and monitoring the gas-phase of the reactor by GC. The pH value of 5 was chosen on the basis of previous investigations[40b] and for the following reasons: (i) lower pH values may protonate the PAMAM dendrimer thus determining release of the Pt nanoparticles from the core; (ii) too basic pH, on the contrary, increases the thermodynamic requirement for the hydrogen evolving reaction, (iii) pH 5 is high enough for almost complete deprotonation of ascorbic acid (pK_a = 4.17 at 298 K) to favor reductive quenching of the ruthenium(II) sensitizer.

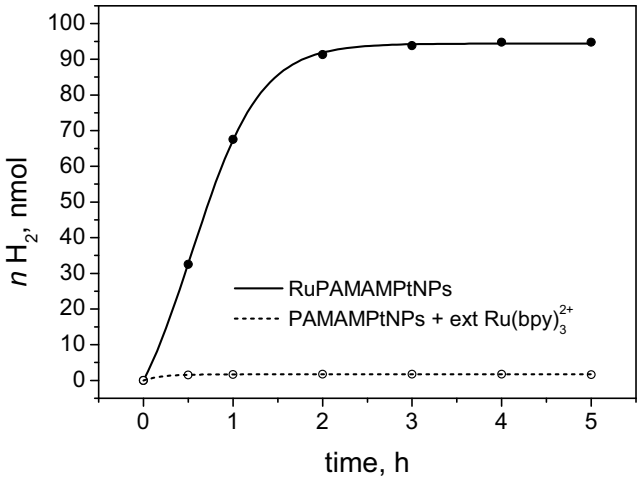

Fig. 8.7. Hydrogen evolution kinetics obtained upon continuous visible irradiation of a pH 5 water solution containing 1.6 μM **RuPAMAMPtNps** and 0.1 M ascorbic acid (solid circles, solid line), and 34 μM $Ru(bpy)_3Cl_2$, 2.1 μM **PAMAMPtNps** and 0.1 M ascorbic acid (open circles, dashed line).

As shown in Figure 8.7, hydrogen evolution was observed. Photocatalytic activity ceased after about 4-5 hours of irradiation achieving up to 95 nmol of hydrogen. According to the

calculation reported above, a 1.6 μM **RuPAMAMPtNps** concentration corresponds to an average value of 1.51 nmol of Pt nanoparticles, so that the turnover number (TON) is 63 per Pt nanoparticle. The maximum rate of hydrogen production, calculated in the linear part of the kinetic, is 67.2 nmol h^{-1}, corresponding to a turnover frequency (TOF) of 44.5 h^{-1} per Pt nanoparticle.

As regarding the mechanism, hydrogen production is likely to take place by first bimolecular reductive quenching of the sensitizer moieties by the ascorbic acid donor, followed by intramolecular electron transfer to the Pt nanoparticle catalyst. The confined Pt nanoparticles are indeed not capable of quenching the triplet MLCT excited state of the sensitizer (as observed by the recovery of the ruthenium-based emission after reduction of the dendritic precursor with $NaBH_4$, see paragraph 8.3.2), whereas ascorbic acid is known to quench reductively the excited state of $Ru(bpy)_3^{2+}$ with a bimolecular rate constant of ca. 10^7 $M^{-1}s^{-1}$.[108d] Comparison of the absorption spectra before/after photolysis (Figure 8.8) suggests that partial decomposition of the sensitizer occurs. According to the mechanism envisioned, this may be related to unproductive routes involving the photogenerated reduced form of the sensitizer and competing with electron transfer to the Pt nanoparticles.[47c,d,145]

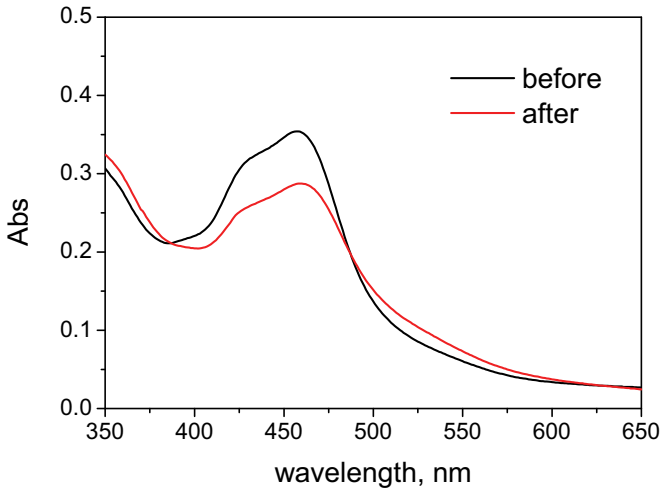

Fig. 8.8. Comparison of absorption spectra before/after 5 hours of continuous visible irradiation of a pH 5 water solution containing 1.6 μM **RuPAMAMPtNps** and 0.1 M ascorbic acid.

Control experiments in which the sensitizer was added externally as $Ru(bpy)_3Cl_2 \cdot 6H_2O$ salt (34 μM in order to have the same sensitizer concentration of the previous experiment) to a water solution (pH 5) of **PAMAMPtNps** (2.1 μM) in the presence of 0.1 M ascorbic acid showed negligible amount of hydrogen produced (Figure 8.7). This evidence seems to suggest that an intimate contact between the sensitizer and the catalyst is required for efficient

hydrogen generation. In particular, the dendrimer scaffold seems to act as a shield for the Pt nanoparticles, likely preventing or at least limiting bimolecular electron transfer to occur. Therefore, only when the ruthenium(II) sensitizer is directly connected to the catalytic site in the dendrimer supramolecule, electron transfer from the photogenerated reduced sensitizer can take place as an intramolecular process thus contributing to hydrogen production.

8.4 Conclusions

In conclusion a fourth generation PAMAM dendrimer decorated with 32 ruthenium(II) polypyridine sensitizers has been used as template for the controlled synthesis of platinum nanoparticles for potential application in photocatlytic hydrogen evolution studies in the presence of a sacrificial electron donor.

Preparation of the hybrid material was achieved after treatment of the **RuPAMAM** dendrimer with 20 eqs of K_2PtCl_4 and subsequent reduction with $NaBH_4$. TEM characterization of a dropcasted water solution of **RuPAMAMPtNPs** showed the presence of monodisperse Pt nanoparticles with an average diameter of 1.3 nm involving the cooperation of at least three dendrimer molecules.

Hydrogen evolution occurs upon continuous visible irradiation of a pH 5 water solution in the presence of 0.1 M ascorbic acid as sacrificial electron donor with estimated TON of 63 and TOF of 44.5 h^{-1} per Pt nanoparticle. The presence of both sensitizer and catalyst onto the same dendrimer scaffold has been recognized as a main requirement for efficient hydrogen evolution, as negligible amount of hydrogen is produced when the $Ru(bpy)_3^{2+}$ sensitizer is added externally to a **PAMAMPtNPs** solution under the same reaction conditions.

This study provides a novel approach in the development of artificial photosynthetic systems by using photoactive dendrimers with the possibility to easily change (i) the catalyst hosted within the supramolecular structure or (ii) the photoactive moieties at the dendrimer periphery for potential applications in both hydrogen production and water oxidation.

Chapter 9

A Ferrocene-(Zinc Porphyrin)-Naphthalenediimide Triad for Photoinduced Charge Separation

This chapter is the result of a collaboration with the group of Prof. Fabrice Odobel at the CEISAM center of the University of Nantes. Parts of this chapter can be found in the literature.[164]

9.1 Introduction

Photoinduced charge separation is the key process triggering the conversion of light into chemical energy in natural photosynthesis, as well as in most conceivable artificial photosynthetic devices.[14,24a,32] Thus, considerable efforts have been devoted to the synthesis and characterization of supramolecular systems ideally suited to produce, following visible light absorption, charge separated states with high energy content, high quantum yield, and long lifetime.[32] Among many supramolecular systems for charge separation, those involving a metal porphyrin as photoexcitable donor and a 1,4,5,8-naphthalenediimide (NDI) as acceptor have received considerable attention.[126,165,166,167,168,169]

The use of porphyrin-type chromophores is obviously suggested by the central role played by this type of molecules in the natural photosynthetic systems. Among metallo-porphyrins with closed shell metal ions, zinc porphyrins (ZnP) are extensively used because of their ease of preparation.[78] They can be easily substituted at the periphery, particularly in the *meso* positions, allowing them to be connected to other units in multi-component devices. The excited state energies and redox potentials are such that zinc porphyrins generally behave as potent excited-state electron donors (reductants).

NDI is a strong electron acceptor, which can be easily connected to other units *via* the nitrogen atoms.[166g] The presence of nodes in the frontier molecular orbitals at these positions along the molecular axis ensures effective electronic decoupling of NDI from attached units.[170] It is transparent in the visible range, facilitating selective excitation of other chromophoric units.

Two main classes of ZnP-NDI dyads have been investigated to date, differing essentially in the binding mode of the NDI acceptor to the ZnP chromophoric donor, *via* a peripheral linkage at a *meso* phenyl group of the ZnP[166b,c] or by axial coordination to the zinc metal center.[166a,f,h] The results obtained on these systems by various authors are quite diverse, as far as charge separation *vs.* charge recombination and lifetime of the charge separated state are concerned.

In this chapter the study of two new covalently linked systems containing the ZnP and NDI as molecular components, namely, dyad **1** and triad **2** with ferrocene as a synthetically

convenient electron donor unit (Figure 9.1), will be undertaken. Molecular components are linked by means of triazole bridges which can be easily constructed by the copper-catalyzed azide-alkyne cycloaddition (CuAAC) "click-chemistry" reaction.[171] Despite their synthetic convenience, relatively little use has been made of 1,2,3 triazole bridges in the construction of dyads, triads, etc. for photoinduced charge separation.[172,173] In this context, their efficiency as electron transfer mediators has been variously evaluated, being classified by different authors as "excellent bridges for rapid and efficient photoinduced electron transfer"[173b] or "poor conduits for electrons".[172a]

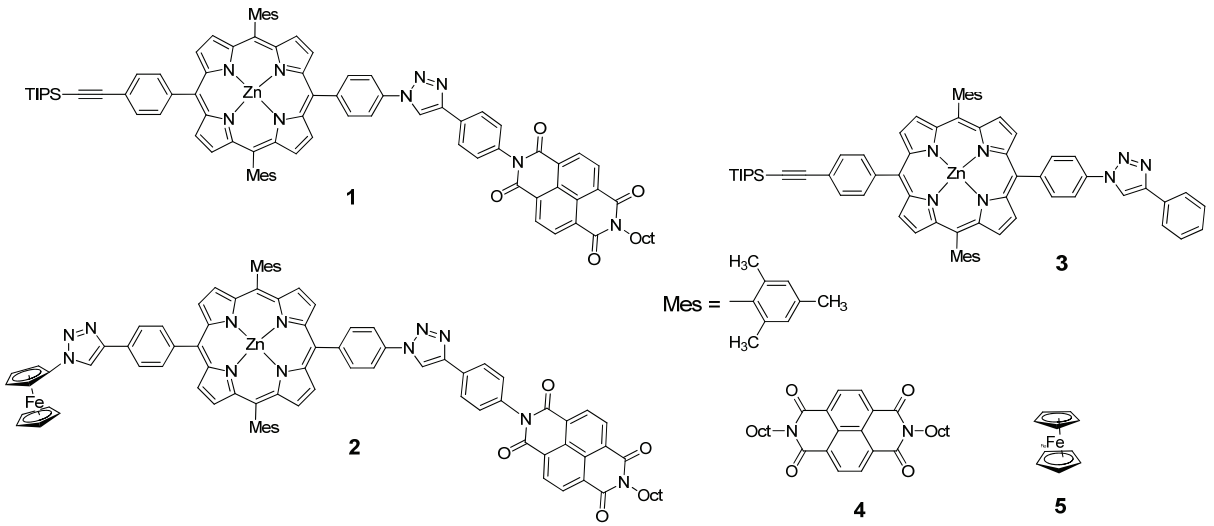

Fig. 9.1. Molecular dyad **1**, triad **2**, and models **3-5** studied in this chapter.

The photophysical behavior of dyad **1** and triad **2** has been studied by stationary and time-resolved techniques, upon excitation not only, as usual, of the ZnP donor chromophore, but also of the NDI acceptor unit. To better understand the photophysics of the more complex dyad/triad systems, model compounds **3**, **4**, and **5** of the three isolated molecular units (zinc porphyrin, naphthalenediimide, and ferrocene respectively) have been studied (Figure 9.1). DFT calculations have also been applied to a bridge-acceptor fragment in order to obtain information about the relative energy level ordering, of interest to the behavior of the bridge in electron and hole transfer processes.

9.2 Experimental section

9.2.1 Synthesis

The synthesis of all the compounds studied in this chapter was performed by Dr. Julien Boixel at the CEISAM center of the University of Nantes. A summary of the procedure will be described herein.

The synthesis of the three porphyrins, namely model **3**, dyad **1**, and triad **2**, is based on the copper-catalyzed azide-alkyne 1,3-cycloaddition Huisgen reaction (CuAAC commonly referred as click chemistry) using the *trans* azidophenyl trisisopropylsilylethynylphenyl zinc porphyrin **6**, which enables to graft, in a stepwise and controlled manner, two different moieties on each side of the porphyrin. Starting with a terminal alkyne substituted moiety, the porphyrin **6** can be first functionalized *via* the azidophenyl side. Then, after deprotection of the triisopropylsilyl group, the second moiety can be introduced *via* an azido substituted unit (Figure 9.2).

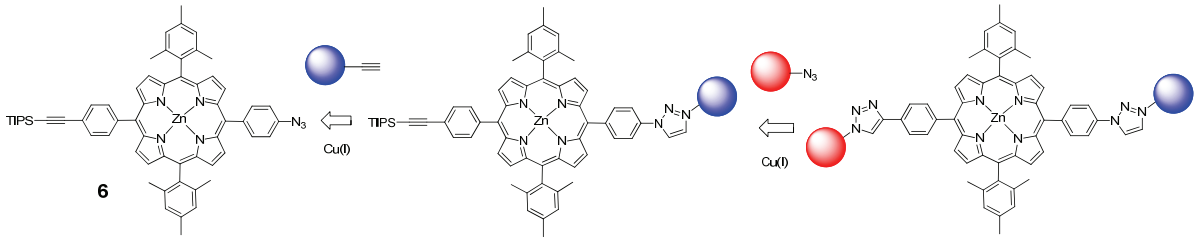

Fig. 9.2. Retrosynthetic scheme for the preparation of triads from *trans* azidophenyl trisisopropylsilylethynylphenyl porphyrin **6**.

The preparation of triad **2** calls for three key building blocks, namely the *trans* azidophenyl trisisopropylsilylethynylphenyl porphyrin **6**, the N-octyl-N'-(4'-ethynylphenyl)naphthalene-tetracarboxylic acid diimide **7** and the azido-ferrocene **8** whose synthesis was previously reported.[174,175] The synthesis of porphyrin **6** is based on the statistical condensation of 5-mesityl-dipyrrylmethane with *para*-nitrobenzaldehyde and *para*-trisisopropylsilylethynyl benzaldehyde using the mild Lindsey conditions at room temperature with BF_3-OEt_2 as catalyst (Figure 9.3).[176] The mesityl substituents give solubility to the porphyrin, prevent aggregation, and finally limit the scrambling reaction during the above porphyrin formation reaction. This reaction naturally led to the formation of three different porphyrins, but they were cleanly separated on silica gel column chromatography. The desired porphyrin **11** was obtained in 20% yield after purification.

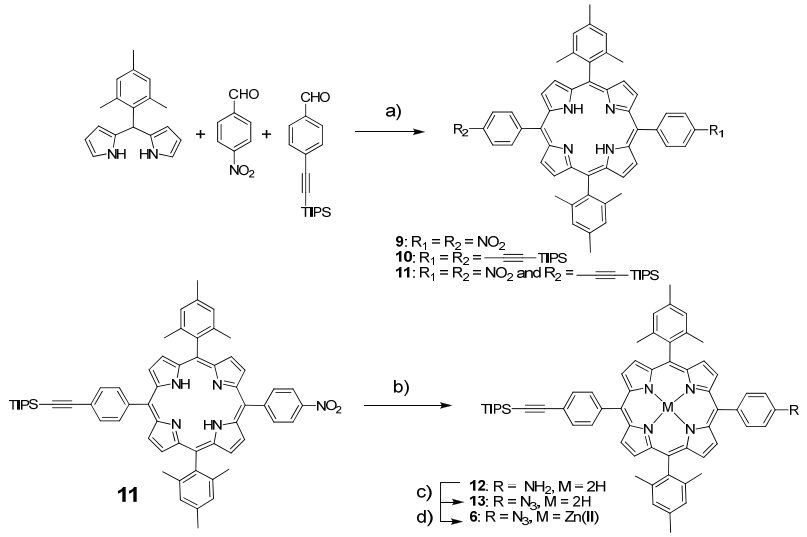

Fig. 9.3. Synthetic route for the preparation of the azidophenyl trisisopropylsilylethynylphenyl porphyrin **6**. Reagents and conditions: a) BF_3-OEt_2, CH_2Cl_2, RT for 12 hours then DDQ for 1 hour; b) $SnCl_2$, 2 H_2O, $CHCl_3$, AcOH, HCl, 70°C; c) $NaNO_2$, TFA, NaN_3 in TFA, 0°C, 1 hour; $Zn(OAc)_2$, $2H_2O$, MeOH, CH_2Cl_2, RT, 1 hour.

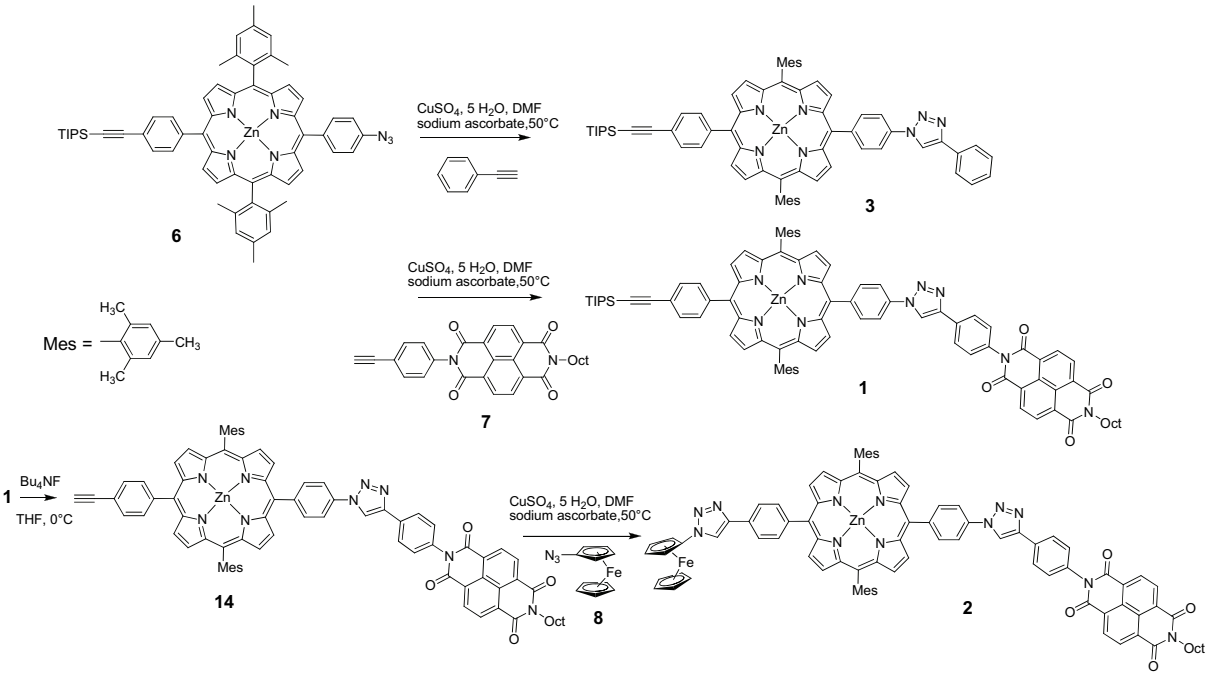

Fig. 9.4. Synthetic route for the preparation of the porphyrins **1**-**3**.

The rest of the synthesis is largely inspired from a previous works on azidophenyl porphyrins,[177] the nitro group of **11** was reduced with tin chloride in acid conditions with a 39% yield. Finally, the amino was transformed into azido group by diazotation with $NaNO_2$ in TFA followed by reaction with NaN_3 to afford porphyrin **13** in a 69% yield. The metallation

of the free porphyrin **13** by zinc(II) (obtaining porphyrin **6**) was necessary to avoid insertion of copper during the subsequent steps of copper catalyzed Huisgen reaction.

Finally, the porphyrins **1-3** were prepared by copper catalyzed Huisgen reaction (Figure 9.4) using the classical conditions ($CuSO_4 \cdot 5\ H_2O$, sodium ascorbate in DMF). The reference porphyrin **3** was synthesized by reaction of porphyrin **6** with ethynyl-benzene in 95% yield. The dyad **1** was obtained in 80% yield by reaction of porphyrin **6** with phenylethynyl-naphthalene diimide **7**. The triad **2** was prepared from the dyad **1** after deprotection of the trisisopropylsilyl group with fluoride followed by click reaction with azido-ferrocene **8** in 40% overall yield.

9.2.2 Apparatus and procedures

All the reagents used were of reagent grade quality and used as received. Solvents for spectroscopy measurements were of spectroscopic grade. See Chapter 2 for details on the experimental techniques.

9.3 Results and discussion

9.3.1 Electrochemical characterization

In order to get information on the energy of the various electron transfer states potentially involved in the photophysical behavior, electrochemical investigation by cyclic voltammetry (Table 9.1) was performed on molecular dyad **1** and triad **2** as well as on the molecular models **3-5**.

Table 9.1. Electrochemical data of model compounds **3**, **4**, **5**, dyad **1** and triad **2**.[a]

	Reduction (V *vs.* SCE)		**Oxidation (V *vs.* SCE)**	
	ZnP/ZnP^-	NDI/NDI^-	Fc/Fc^+	ZnP/ZnP^+
1		− 0.59		0.79
2	− 1.37	− 0.59	0.69	0.79
3	− 1.37			0.81
4		− 0.65		
5			0.46	

[a] Obtained by cyclic voltammetry (CV) in CH_2Cl_2 at 298 K, 0.15 M TBA(PF_6) as supporting electrolyte, SCE as reference electrode, Pt wire as working and counter electrode, scan rate 100 mV/s.

The main significant shift observed is for ferrocene, which is more difficult to oxidize (by ca. 200 mV) in the triad than as a free molecule. This is as expected, because of the electron withdrawing effect of the triazole directly bound to the cyclopentadienyl ring.[178]

Assuming charge separation distances of 20 Å (ZnP-NDI), 15 Å (ZnP-Fc), and 35 Å (Fc-NDI) for the calculation of the electrostatic effects, the following energies for the charge transfer states in the triad can be calculated by means of the Rehm-Weller equation (eq 30):[130] Fc-ZnP^{+}-NDI^{-}, 1.30 eV; Fc^{+}-ZnP^{-}-NDI, 1.96 eV; Fc^{+}-ZnP-NDI^{-}, 1.23 eV.

9.3.2 Photophysics of molecular models

Model ZnP (3). The zinc porphyrin model compound **3** in dichloromethane displays the typical features[179,180] of metallo porphyrins (Figure 9.5, black trace): strong absorption in the visible due to Soret (maximum at 421 nm) and Q-bands (maxima at 550 and 590 nm) and an intense fluorescence ($\Phi = 0.04$)[78] with maxima at 599 and 648 nm and a lifetime of 2.1 ns.

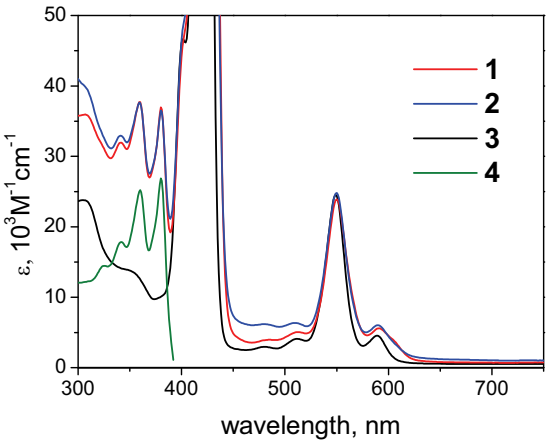

Fig. 9.5. Absorption spectra of dyad **1**, triad **2**, and model compounds **3** and **4.**

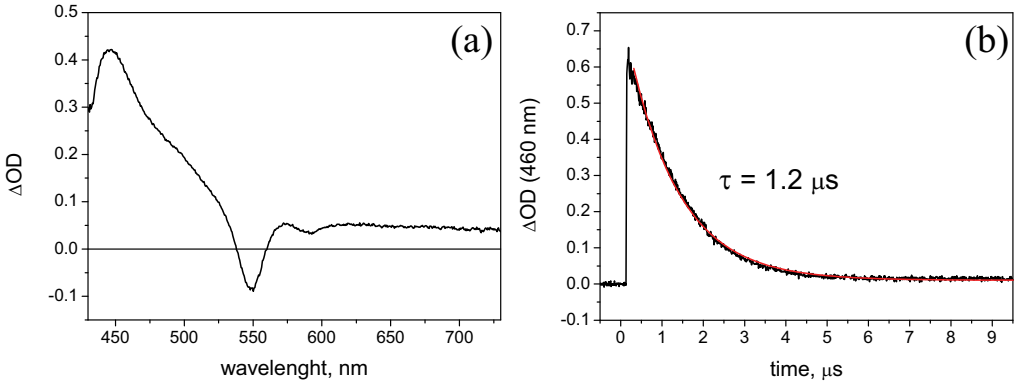

Fig. 9.6. (a) Transient absorption spectrum of the triplet excited state of model compounds **3** in CH_2Cl_2 and (b) kinetic analysis at 460 nm obtained by laser flash photolysis (excitation at 532 nm)**.**

The excited state difference absorption spectrum obtained by nanosecond laser flash photolysis (Figure 9.6) shows a strong and broad absorption with maximum at 445 nm and the Q-band bleach characteristic of the lowest triplet excited state (formation yield, 0.88;[78] energy, 1.58 eV).[179] The lifetime is 1.2 μs in aerated dichloromethane.

Model NDI (4). Model compound **4** in dichloromethane displays a structured absorption spectrum in the UV region with maxima at 343, 360, and 380 nm (Figure 9.5, green trace) and a weak structured fluorescence (maxima at 390, 407, and 431 nm) with lifetime shorter than 250 ps (time resolution of the time-correlated single photon counting technique). The singlet excited state can be monitored, however, by ultrafast spectroscopy (excitation at 266 nm, Figure 9.7): the strong absorption around 600 nm ascribable to the singlet excited state decays in 15 ps giving rise to a sharp peak at 490 nm that remains almost constant over the whole time window of the experiment (2000 ps). The 490-nm peak is the typical absorption of the NDI triplet (energy, 2.05 eV from phosphorescence),[181] decaying in the microsecond time scale, as can be monitored by laser flash photolysis (excitation at 355 nm, Figure 9.8).

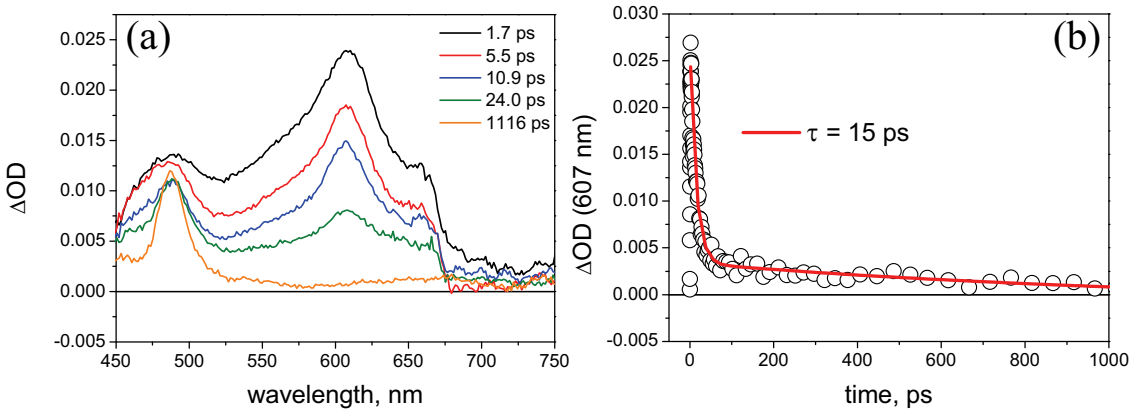

Fig. 9.7. (a) Transient absorption spectra obtained by UFS (excitation at 266 nm) on model compounds **4** in CH_2Cl_2 and (b) kinetic analysis at 607 nm.

Thus, in the NDI model compound **4**, thanks to the relevant spin-orbit coupling,[181,182] a very fast intersystem crossing process rapidly converts the excited singlet state to the triplet. It should be noticed that while model **4** has two alkyl substituents at the imide positions, the NDI component in dyad **1** bears one alkyl and one aryl group. Zuilhof et al.[183] reported that in such a case the deactivation of the singlet state to the triplet takes place, rather than by direct intersystem crossing, in two consecutive steps: fast population (< 1 ps) of a phenyl-to-NDI charge transfer state, followed by fast charge recombination (ca. 30 ps) to the NDI triplet.

Regardless of the detailed mechanism, fast population (15-30 ps) of the triplet state is expected upon excitation of the NDI moiety.

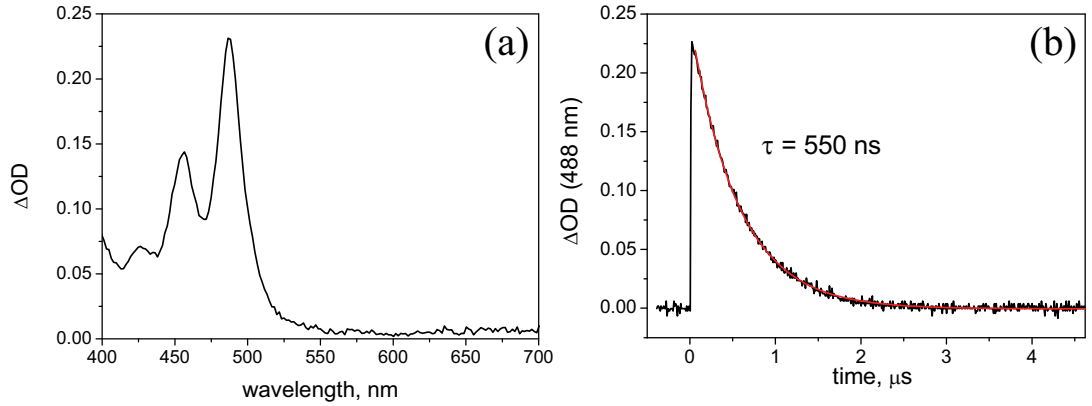

Fig. 9.8. (a) Transient absorption spectrum of the triplet excited state of model compounds **4** in CH_2Cl_2 and (b) kinetic analysis at 488 nm obtained by laser flash photolysis (excitation at 355 nm)**.**

9.3.3 Spectroelectrochemistry of molecular models

In order to obtain informations on the photophysics of dyad and triad systems it is first important to know the spectral features of the transient species possibly generated after excitation. To this aim spectroelectrochemistry is a very useful technique. In Figure 9.9 the differential absorption spectra of the zinc porphyrin radical cation and of the NDI radical anion are reported, compared to the spectrum of the zinc porphyrin triplet excited state.

Spectroelectrochemistry of model compound **3** has been obtained upon application of a potential of ca. 0.90 V (measured with respect to the Ag wire quasi-reference electrode), the differential spectrum displays a strong absorption in the 450-520 nm range with a maximum at 465 nm, the typical Q-band bleach, and a minor absorption at longer wavelength with a relative maximum at 630 nm. Spectroelectrochemistry of model compound **4** has been obtained upon application of a cathodic potential of ca. −0.70 V (measured with respect to the Ag wire quasi-reference electrode), the differential spectrum features two main absorptions in the visible with maximum at 480 and 610 nm respectively, representing nice fingerprints for charge separated states involving the NDI radical anion.

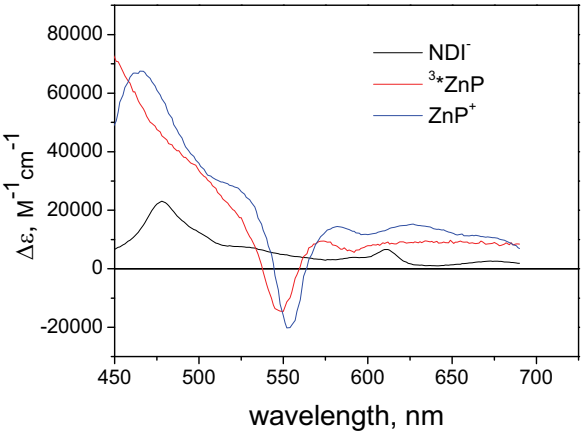

Fig. 9.9. Differential absorption spectra of ZnP radical cation (blue trace), NDI radical anion (black trace) in CH_2Cl_2 (0.1 M $TBAPF_6$) obtained by spectroelectrochemistry of **3** and **4** respectively compared to the transient absorption spectrum of the triplet excited state of model compounds **3** (red trace) obtained by laser flash photolysis (excitation at 532 nm)**.**

9.3.4 Photophysics of molecular dyad and triad systems

ZnP-NDI dyad (1). The absorption spectrum of **1** is compared in Figure 9.5 (red trace) to those of model compounds **3** and **4**. The spectrum of the dyad exhibits, with good additivity, the absorption features of both the zinc porphyrin and NDI units. Selective excitation of the zinc porphyrin is easily achieved in the visible spectral region, while partial excitation of the NDI unit can be obtained in the UV region (*e.g.*, ca. 60% at 355 nm).

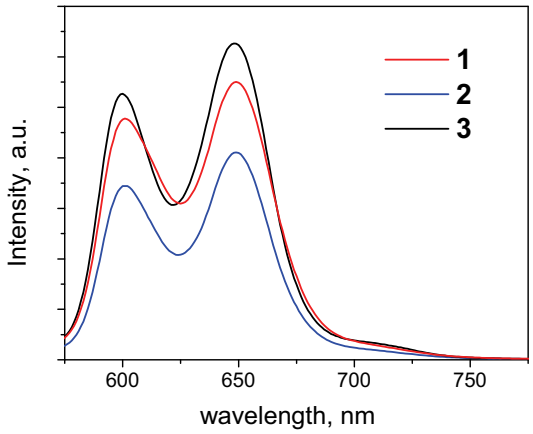

Fig. 9.10. Comparison of emission spectra of model **3**, dyad **1**, and triad **2** in CH_2Cl_2 (excitation at 550 nm, optically matched solutions).

Upon visible excitation, **1** shows the typical zinc porphyrin fluorescence (Figure 9.10), with a slightly lower intensity (ca. 85%) relative to model **3** (optically matched solutions at

the excitation wavelength). A proportional decrease is observed in the emission lifetime (1.7 ns). According to eq 44, where τ_1 and τ° are the lifetimes of the ZnP fluorescence in **1** and **3** respectively, a rate constant $k_1 = 1.1 \times 10^8$ s^{-1} is obtained for this quenching process.

$$k_1 = \frac{1}{\tau_1} - \frac{1}{\tau^\circ} \tag{44}$$

This process takes place very likely along the only additional deactivation path available to the zinc porphyrin singlet excited state in the dyad, namely photoinduced electron transfer to the NDI unit. In fact, in laser flash photolysis experiments upon excitation at 532 nm (Figure 9.11) the only product observed is the zinc porphyrin triplet, with the same transient spectrum and decay kinetics (single exponential, lifetime ca. 1 μs in aerated solution) as model molecule **3**.

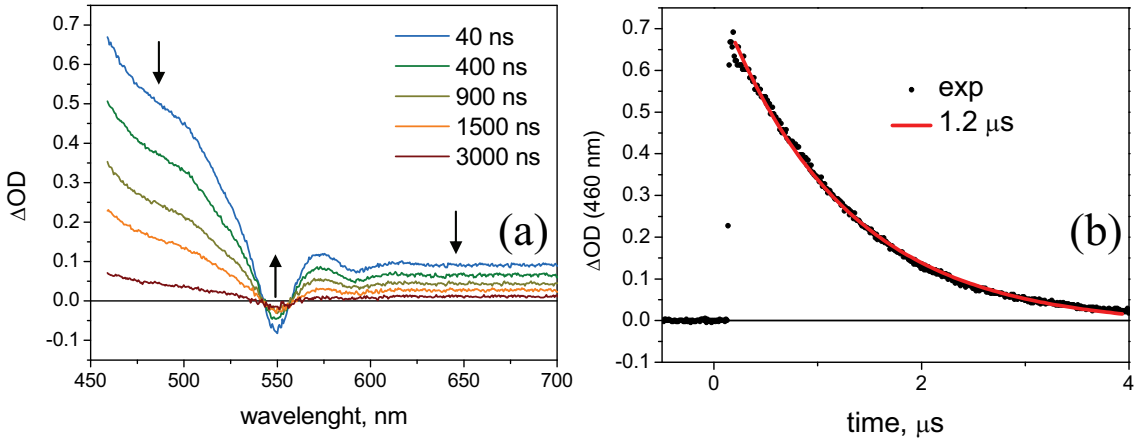

Fig. 9.11. (a) Transient absorption spectra obtained by laser flash photolysis on **1** in CH_2Cl_2 (excitation at 532 nm); (b) kinetic analysis at 460 nm with related fitting.

This is not unexpected as, aside from intrinsic difficulties of spectral detection (see below), the ZnP^+-NDI^- charge separated state is formed with low efficiency (15%). Moreover, it is also expected from classical Marcus theory (eqs 45,46) that in this system charge recombination is much faster than charge separation, leading to negligible accumulation of the transient.

$$k_{et} = k_{et}(0)\exp\left(-\frac{\Delta G^*}{RT}\right) = \frac{2\pi}{\hbar} H_{AB}{}^2 (4\pi\lambda RT)^{-1/2} \exp\left(-\frac{\Delta G^*}{RT}\right) \tag{45}$$

$$\Delta G^* = \frac{(\Delta G^0 + \lambda)^2}{4\lambda} \qquad (46)$$

As reported in the literature,[166b] this donor-acceptor pair is characterized by a very high reorganization energy (1.4 eV in THF). Therefore, the charge separation process (with ΔG = −0.8 eV) lies in the Marcus normal region, with a substantial activation energy, and is thus slow (1.1×10^8 s^{-1}), while charge recombination (with ΔG = −1.3 eV) is close to the activationless regime and expected to be very fast (3.5×10^9 s^{-1}, according to eqs 45,46, assuming the same λ and $k_{et}(0)$ as for charge separation).

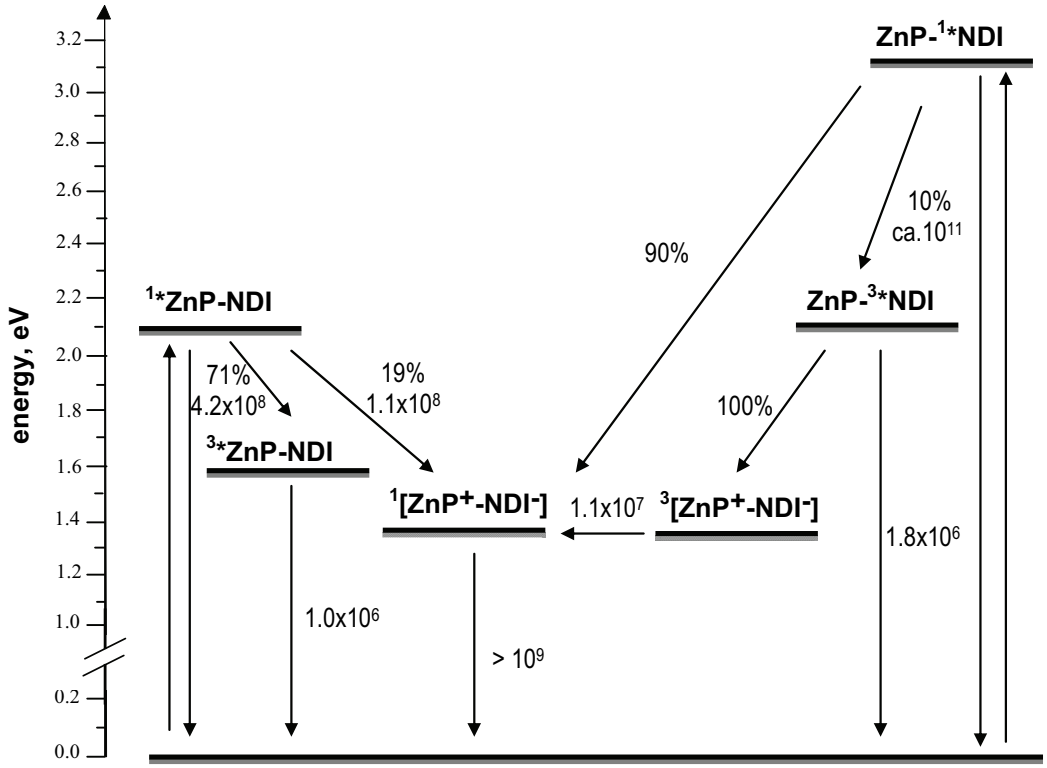

Fig. 9.12. Energy level diagram and photophysical processes of dyad **1**. Rate constants (s^{-1}) and efficiencies of individual processes indicated, where known.

In conclusion, following excitation of the zinc porphyrin unit, dyad **1** undergoes slow, poorly efficient charge separation from the singlet excited state and fast charge recombination (Figure 9.12). The fact that the triplet state of the zinc porphyrin is not quenched indicates that a triplet pathway to charge separation, though thermodynamically allowed (Figure 9.12), is inefficient. This is not surprising in view of the small driving force, ca. −0.2 eV, of this process. With the same λ and $k_{et}(0)$ parameters in eqs 45,46, the smaller driving force is

expected to slow down triplet charge separation relative to the singlet one by almost three orders of magnitude, making it too slow to compete with the zinc porphyrin triplet lifetime.

As far as excitation of the NDI unit is concerned, a relevant observation is that excitation spectrum of the zinc porphyrin fluorescence in dyad **1** (Figure 9.13) matches perfectly that of model **3**, completely lacking the NDI features in the UV region. This means that no energy transfer to the porphyrin unit takes place from the NDI singlet excited state. Since such energy transfer is predicted by Förster theory[28] to have a time constant of ca. 1 ps (calculated using a PhotochemCAD 2.1 software routine[143] with the following parameters: n = 1.424; $\Phi_D/\tau_D = 10^9\ s^{-1}$; $\kappa^2 = 0.66$, $R_{DA} = 20$ Å), this implies that this state in the dyad has a very short lifetime. Whether this comes from ultrafast intersystem crossing within the NDI component or from some ultrafast intercomponent quenching process in the dyad is an open question (see below). Unfortunately, investigation of this issue by ultrafast spectroscopy is prevented by the unavailability (with our setup) of an appropriate wavelength for excitation of the NDI component in the dyad.

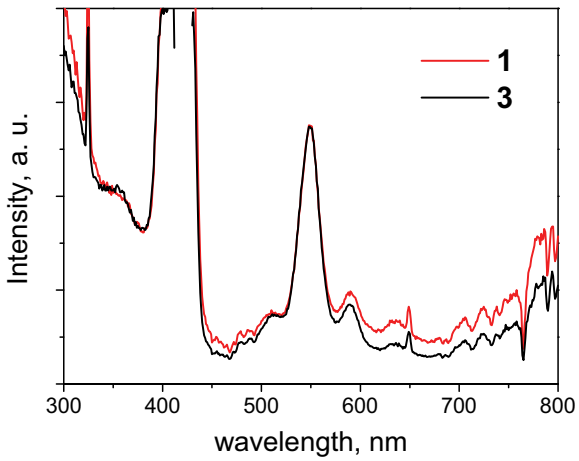

Fig. 9.13. Excitation spectra (recorded emission at 650 nm) of model **3** and dyad **1** in CH_2Cl_2.

Relatively efficient (60%) excitation of the NDI component of dyad **1** can be achieved, on the other hand, by nanosecond laser spectroscopy with 355-nm pulses. The transient spectra obtained although broadly similar, are different in detail from those obtained by 532-nm excitation and suggest that the behavior obtained by 355-nm excitation is more complex than a simple clean decay of the zinc porphyrin triplet state. In fact, the transient behavior (Figure 9.14) is clearly biphasic, with two spectrally and kinetically distinct components of 90 ns and 0.88 μs lifetime. The long-living transient (Figure 9.14b) is consistent in spectral shape, lifetime, and oxygen dependence with the zinc porphyrin triplet. Its amount is as expected assuming exclusive generation by light absorbed by the zinc porphyrin component, since a

value of 0.3 is observed from the ratio of the intensity of the triplet signal in the 355-nm flash photolysis of **1** and that of an iso-absorbing solution of model **3** (expected theorethical value 0.34 cosidering that in **1** the 355-nm light leads to 40% excitation of the zinc porphyrin unit and the triplet yield is 15% lower with respect to **3**). The short-lived transient can be assigned to the ZnP^{+}-NDI^{-} charge separated state for the following reasons. In the spectrum expected for such a state (Figure 9.15b, calculated from the combination of the differential absorption spectra obtained by spectroelectrochemistry in Figure 9.9) the main peak of the NDI radical anion at 480 nm is largely masked by the intense absorption of the zinc porphyrin radical cation. However, the maximum at 480 nm and the sharp feature at 610 nm make the spectrum of the ZnP^{+}-NDI^{-} charge separated state clearly different from that of the zinc porphyrin triplet.

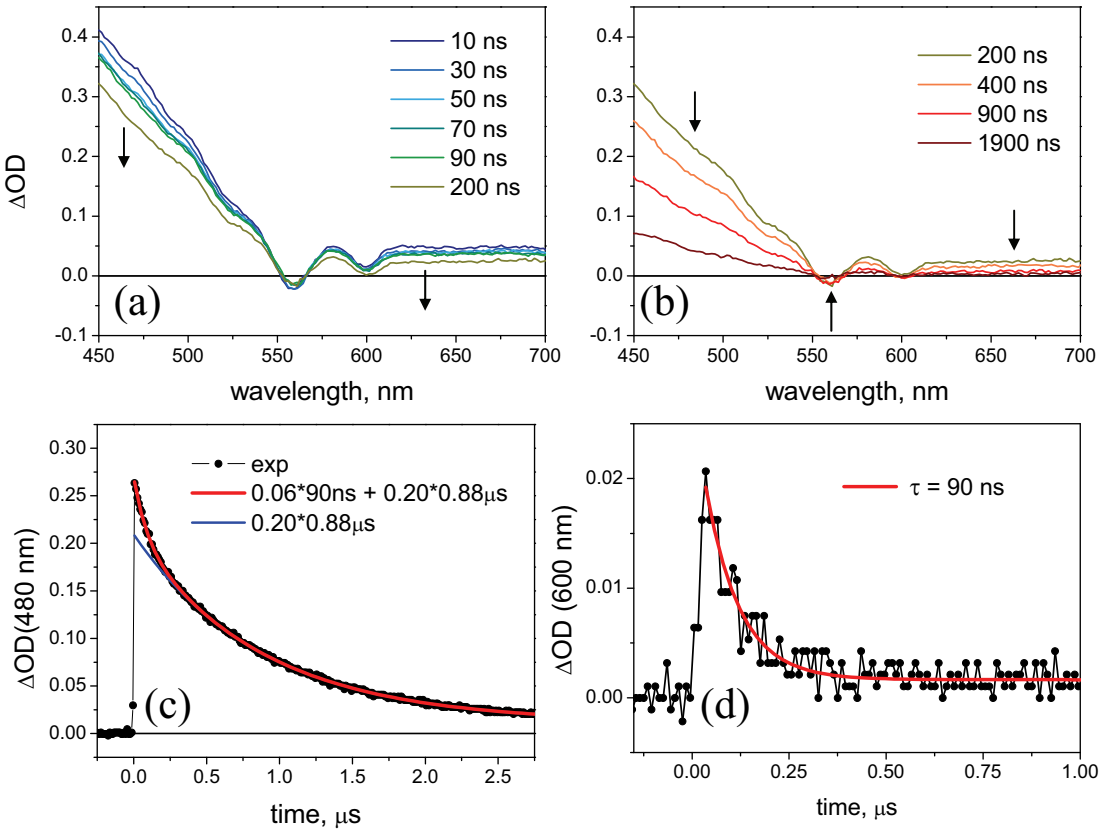

Fig. 9.14. Biphasic spectral changes in the 355-nm flash photolysis of dyad **1** in CH_2Cl_2: (a) transient spectral changes in the 10-200 ns time window; (b) spectral changes in the 200-1900 ns spectral window; (c) decay kinetics measured at 480 nm; (d) decay kinetics measured at 600 nm.

As a proof of the assignment made: (i) the spectrum of the fast decaying transient, obtained by subtracting the 200-ns spectrum from the earlier spectra, matches well the spectrum of the ZnP^{+}-NDI^{-} charge separated state (Figure 9.15a); (ii) the initial transient spectrum of Figure

9.14b can be well reproduced (Figure 9.15c) as a combination of charge separated state and zinc porphyrin triplet, in the concentration ratio 15% to 85%, obtained from the ratio of pre-exponential factors in the biphasic decay kinetics and the relative molar absorptivities of the two transients. The efficiency of formation of the charge separated state following light absorption by the NDI unit can be calculated from this concentration ratio, knowing the partitioning of the incident 355-nm light between the zinc porphyrin and the NDI units (40% and 60%, respectively) and the efficiency of formation of the triplet following light absorption by the zinc porphyrin (85%). Such a calculation shows that light absorption by the NDI unit generates the charge separated state observed in the nanosecond laser flash photolysis experiments with ca. 10% efficiency.

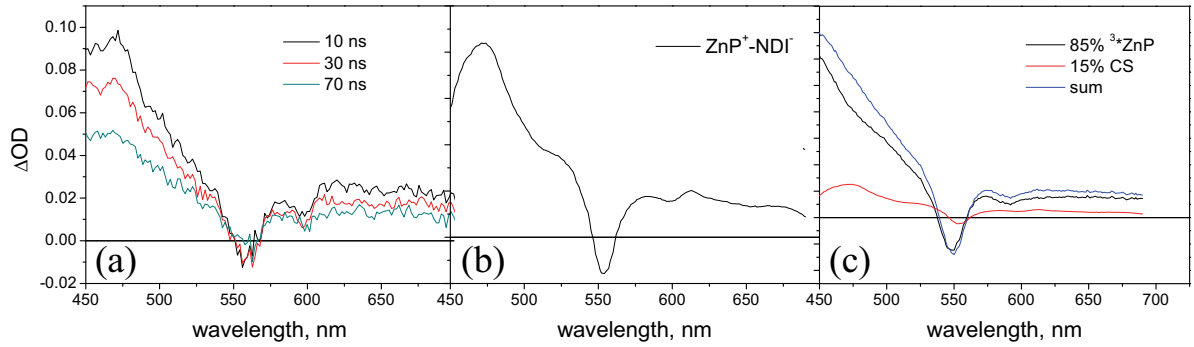

Fig. 9.15. (a) Spectral changes in Figure 9.14a, plotted using the 200-ns spectrum as baseline: 10 ns – 200 ns (black), 30 ns – 200 ns (red), and 70 ns – 200 ns (green); (b) spectrum of the charge separated state obtained by combination of spectroelectrochemical data; (c) simulation of the initial transient spectrum of Figure 9.14a, as the sum of zinc porphyrin triplet and ZnP^{+}-NDI^{-} charge separated in a 85% to 15% proportion.

The main observation from the 355-nm laser photolysis experiments on dyad **1** is that, contrary to what happens upon 532-nm excitation, products of charge separation are detected. In this regard, two facts are mechanistically relevant: (i) the charge separated state recombines relatively slowly (90 ns); (ii) the charge separated state is formed with less than unity efficiency (10%) by NDI light absorption. Point (i) clearly shows that this charge separated state is different from that responsible for the quenching of the zinc porphyrin singlet state (with sub-nanosecond lifetime). As discussed above, in the isolated NDI component the main excited-state deactivation path is *via* very fast intersystem crossing to the long-lived triplet state. Thus, it is quite plausible that in dyad **1** a triplet pathway is followed upon excitation of the NDI component, leading to the formation of a charge separated state with triplet spin multiplicity (Figure 9.12). The failure to observe any NDI triplet in the 355-nm laser

photolysis experiment is consistent with the hypothesis of fast electron transfer quenching of this state. Once the charge separated triplet state is formed, the spin-forbidden nature of the charge recombination easily accounts for the observed slowness of this process. The observed time constant (90 ns) likely reflects the rate of conversion of the triplet charge separated state to the singlet one, which then undergoes fast (< ns) spin-allowed charge recombination.[184] In this scheme, it is not obvious where the less-than-unity efficiency of formation of the charge separated state, point (ii) above, comes from. At the NDI triplet level, the only deactivation channel possibly competing with charge separation could be energy transfer to the zinc porphyrin, but this process is experimentally ruled out as all the observed porphyrin triplet is accounted for by direct zinc porphyrin light absorption (see above). Therefore any sources of inefficiency should be looked for at the singlet level. Since energy transfer to the zinc porphyrin singlet state is ruled out by excitation spectra (Figure 9.13), one is left with the hypothesis that ca. 90% of the NDI excited states populated by light absorption decay by ultrafast electron transfer quenching (Figure 9.12). The singlet charge separated state reached by this route, as already discussed, is expected to recombine too rapidly for observation in nanosecond laser flash photolysis. The picture emerging from the photophysical investigation of dyad **1** is summarized in Figure 9.12.

Fc-ZnP-NDI Triad (2). The absorption spectrum of triad **2** (Figure 9.5, blue trace) is virtually identical to that of the dyad, as absorption by the ferrocene unit is negligible at $\lambda >$ 300 nm. The zinc porphyrin fluorescence in the triad (Figure 9.10) is quenched by ca. 40% relative to model **3**, and thus is somewhat weaker than in dyad **1**. This indicates that the presence of the ferrocene unit provides an additional deactivation path to the excited state of the zinc porphyrin. From the fluorescence lifetime of 1.4 ns, a rate constant $k_2 = 1.3 \times 10^8$ s^{-1} is obtained for the new quenching channel, according to eq 47 where τ_2 and τ° are the lifetimes of the ZnP fluorescence in **2** and **3** respectively and k_1 is the rate of the oxidative quenching by NDI (see above, eq 44).

$$k_2 = \frac{1}{\tau_2} - \frac{1}{\tau^\circ} - k_1 \qquad (47)$$

Nanosecond laser flash photolysis (Figure 9.16) can give some information on this point. In the long time scale (t > 40 ns after the excitation pulse, Figure 9.16b) the spectrum is, as expected, that of the triplet state of the zinc porphyrin unit decaying to the ground state (with oxygen dependent kinetic) in the microsecond time scale (Figure 9.16c,d). In the early time

scale, however, the formation of the triplet state is preceded by evident spectral changes in the 450-525 nm region (Figure 9.16a), decaying with a time constant of 14 ns.

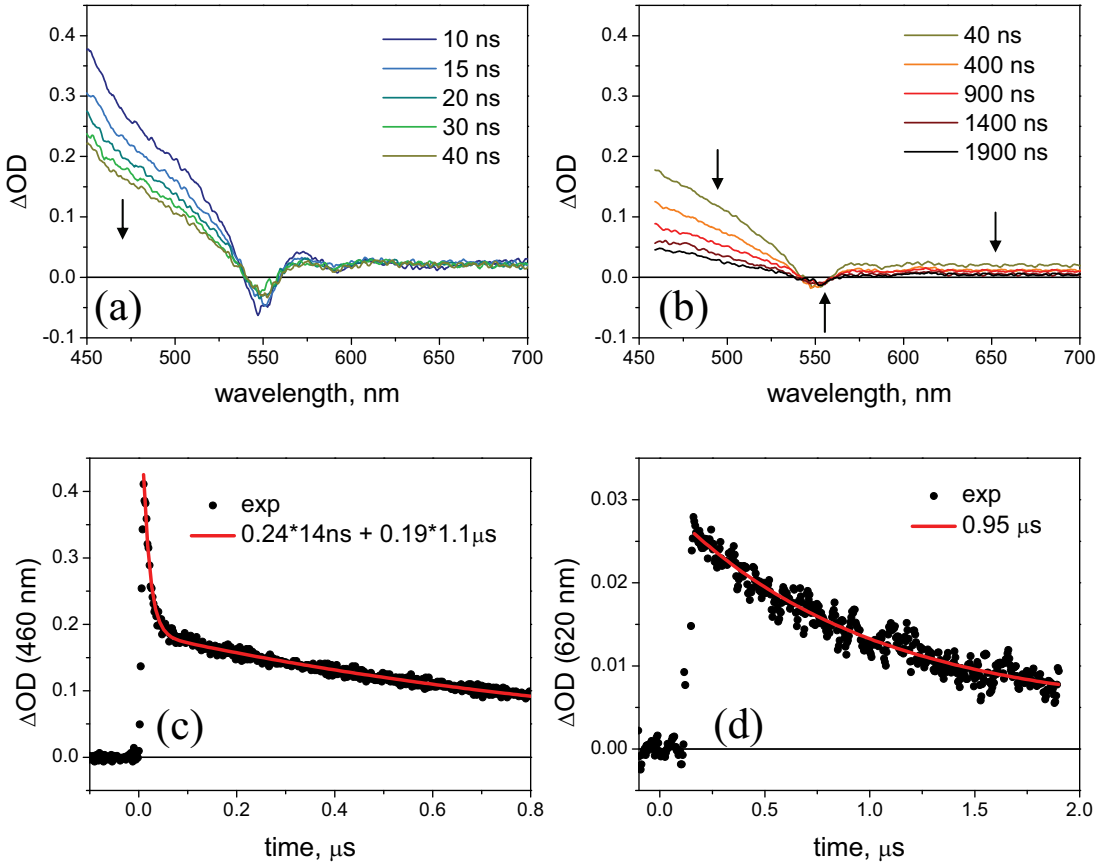

Fig. 9.16. Laser flash photolysis (excitation pulse at 532 nm) on **2** in CH_2Cl_2: (a) detail of early time scale (3-20 ns); (b) transient absorption spectra in the longer time scale (20-1900 ns); (c) kinetic analysis at 460 nm; (d) kinetic analysis at 620 nm.

Since the excited states of ferrocene have negligible molar extinction coefficients in this spectral range,[185] whereas the zinc porphyrin radical anion is known to have a red-shifted intense Soret band in this spectral region,[134] the laser flash photolysis results indicate that the process responsible for the observed quenching of the zinc porphyrin fluorescence is reductive electron transfer (Figure 9.17). The product state Fc^+-ZnP^--NDI decays in about 14 ns, probably by charge recombination to the ground state as, besides the zinc porphyrin triplet, no other transient product is detected.

When triad **2** is excited at 355 nm, *i.e.*, with light substantially (60%) absorbed by the NDI component, the formation of the radical anion of NDI is made evident by prominent maxima at 480 nm and 610 nm (Figure 9.18). The obvious assignment of this long-lived transient is to a long-range charge separated state Fc^+-ZnP-NDI^-, reached by secondary hole shift from zinc porphyrin to ferrocene (Figure 9.17).

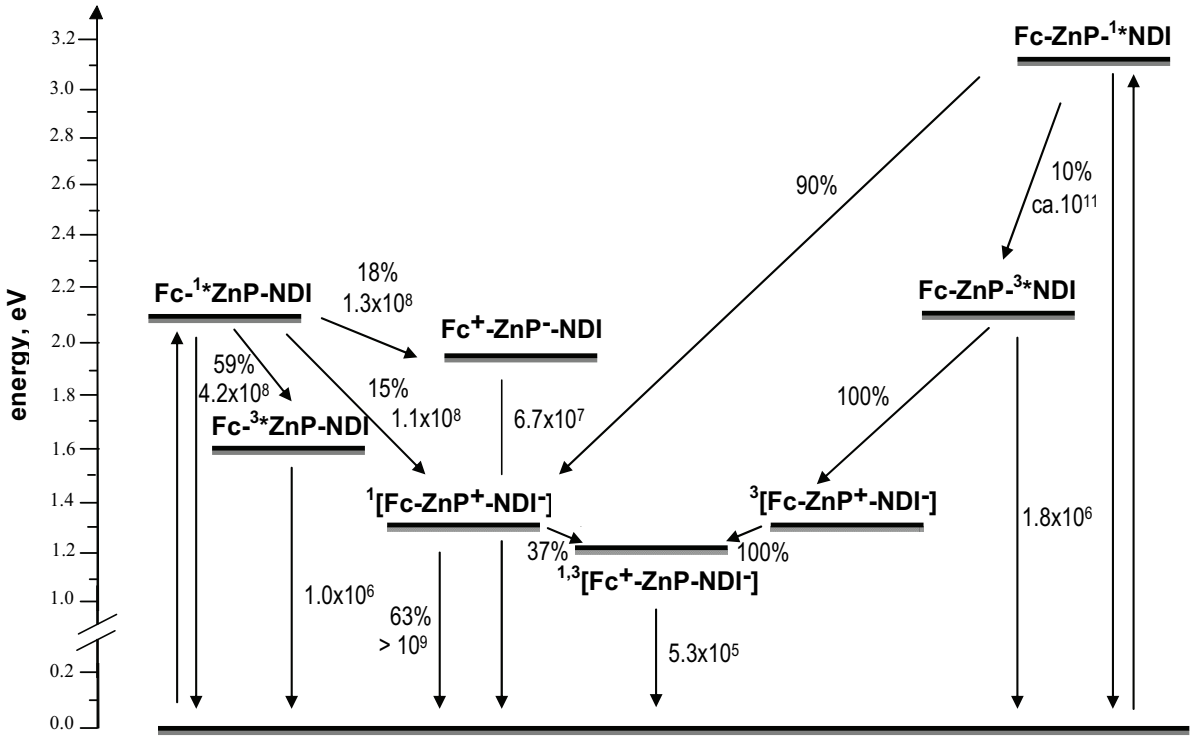

Fig. 9.17. Energy level diagram and photophysical processes of triad **2**. Rate constants (s^{-1}) and efficiencies of individual processes are indicated, where known.

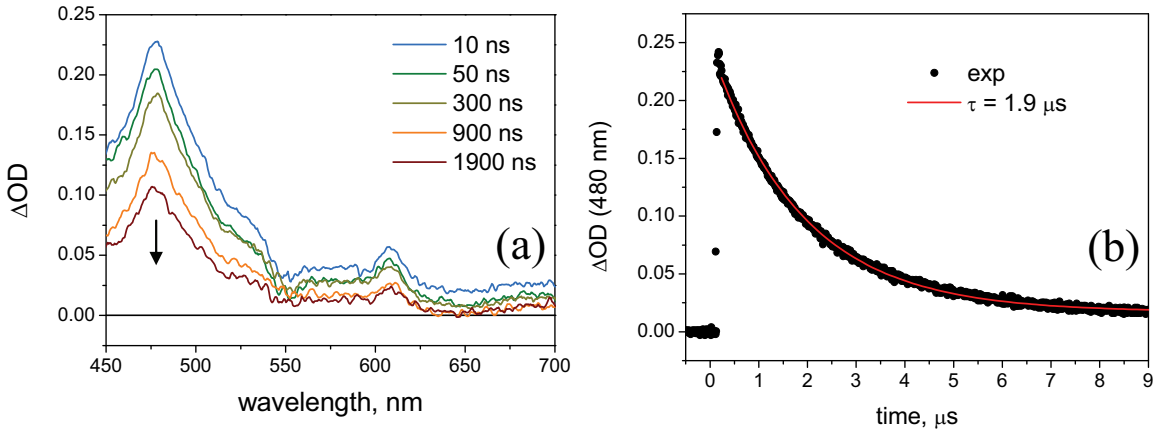

Fig. 9.18. (a) Transient absorption spectra at different time delays and (b) kinetic analysis at 480 nm for **2** obtained by laser flash photolysis (excitation pulse at 355 nm, FWHM 8 ns) in CH_2Cl_2.

With respect to the results obtained with dyad **1** (Figure 9.14), the NDI^{-} absorption peaks (480 and 610 nm) are much more evident here because of the absence of the overlaying absorption of the zinc porphyrin radical cation. Indeed, the initial transient spectrum of Figure 9.18a can be well reproduced (Figure 9.19) with that of the Fc^{+}-ZnP-NDI^{-} charge separated state, taken to be equal to that of the NDI radical anion (as the absorption of Fc^{+} in this

spectral range is negligible, ε_{max} = 1480 $M^{-1}cm^{-1}$ at 502 nm),[185] plus some (ca. 17%) zinc porphyrin triplet.

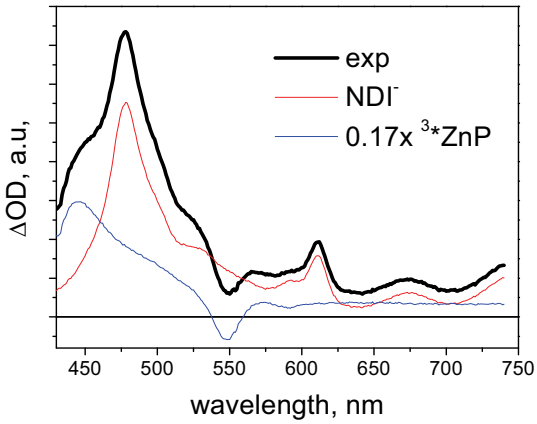

Fig. 9.19. Simulation of the transient spectrum of Figure 9.18, as the sum of zinc porphyrin triplet and Fc^{+}-ZnP-NDI^{-} charge separated (CS) state in a 85% to 15% proportion.

Given the small relative contribution (and similar lifetime) of the underlying zinc porphyrin triplet absorption, the transient decay (Figure 9.18b) shows appreciably single exponential behavior. The lifetime, 1.9 μs, can be taken as the approximate lifetime of the long-range charge separated state Fc^{+}-ZnP-NDI^{-}. The elongation of charge separation lifetime obtained in going from the dyad (90 ns) to the triad is evident. In the triad, the long-range charge separated state Fc^{+}-ZnP-NDI^{-} is supposed to form from the primary charge separated state Fc-ZnP^{+}-NDI^{-} by hole shift from the zinc porphyrin to the ferrocene unit. As previously inferred for the dyad, the primary charge separated state is expected to form following NDI excitation ca. 90% in a singlet and ca. 10% in a triplet spin state (Figure 9.17). These two types of state have very different intrinsic lifetimes (subnanoseconds for the singlet, 90 ns for the triplet). Therefore, depending on how fast the competing hole shift process is, long-range charge separation could either take place exclusively *via* the triplet or *via* both the triplet and singlet pathways. The actual quantum yield of formation of the long-range charge separated state following 355-nm excitation, calculated using $Ru(bpy)_3Cl_2$ as actinometer (considering a ca. 20% contribution by the ZnP triplet to absorption at 355 nm and the appropriate molar extinction coefficients, $\Delta\varepsilon_{480nm}$ = 23,000 $M^{-1}cm^{-1}$ for the NDI radical anion[186] and $\Delta\varepsilon_{450nm}$ = 10,600 $M^{-1}cm^{-1}$ for $*Ru(bpy)_3^{2+}$ excited state),[187] is 0.26. Considering that only 60% of the 355-nm light is absorbed by the NDI component and that, as shown by the 532-nm experiments, excitation of the zinc porphyrin yields negligible amounts of primary charge separation, this quantum yield translates into a 43% efficiency of conversion from the NDI singlet excited state to long-range charge separated state. This efficiency is definitely higher

than that of the triplet primary charge separation (10%), implying a substantial contribution (33%) of the singlet pathway to the formation of the long range charge separated state. This means that hole shift is sufficiently fast so as to compete efficiently (37%) with the subnanosecond lifetime of the singlet primary charge recombination. The photophysical processes taking place in triad **2** are summarized in the energy level diagram of Figure 9.17. In this diagram, no distinction is made between long-range charge separated states Fc^{+}-ZnP-NDI^{-} of singlet and triplet character which, regardless of their yields of formation, are supposed to be in fast equilibrium and thus expected to behave as single entity in the slow recombination to the ground state.[184] Thus, spin memory is largely lost in the long-range charge separated state of triad **2**, whose long lifetime comes essentially from the poor electronic coupling associated to the large charge separation distance.

9.3.5 Kinetic role of the triazole bridges

A point of some general interest is the role of the triazole bridges in mediating photoinduced electron transfer in these dyad and triad systems. In the present case, calculating the activation free energy with Marcus theory (with a driving force value of −0.8 eV and a reorganization energy of 1.4 eV)[166b] a pre-exponential factor of 1.3×10^{9} s^{-1} is required to match the experimental rate constant ($k_1 = 1.1 \times 10^{8}$ s^{-1}). This figure is relatively similar to the rate constant of 3.9×10^{9} s^{-1} obtained on a dyad involving zinc porphyrin as donor, a triazole bridge, and fullerene as acceptor.[173b] In that case, the driving force was very close to the reorganization energy, so that the experimental rate constant is expected to be close to the pre-exponential factor. Interestingly, if the triazole is substituted by an amido bridge, the rate constant increased to 2.2×10^{10} s^{-1}.[188]

The results on the present systems show that the electron transfer quenching of the excited singlet state of the zinc porphyrin chromophore by the NDI acceptor is quite inefficient, with a remarkably low value of rate constant, 1.1×10^{8} s^{-1}. On the other hand, the indirect evidence reported above for the occurrence of a singlet charge separation upon NDI excitation points towards a very fast electron transfer process ($k \geq 7 \times 10^{10}$ s^{-1}) taking place from the singlet excited state of NDI. This difference in rate between processes originating from zinc porphyrin and NDI components can be at least in part ascribed to the high reorganization energy expected for processes involving NDI (λ = ca. 1.4 eV).[166b] Thus, the more exergonic ZnP-^{1}*NDI $\rightarrow$ ZnP^{+}-NDI^{-} process ($\Delta G = -1.8$ eV) is expected to be favored relative to the less exergonic ^{1}*ZnP-NDI $\rightarrow$ ZnP^{+}-NDI^{-} one ($\Delta G = -0.8$ eV). From classical Marcus theory

(eqs 45,46), however, the free-energy difference as such, could only account for a ca. 4-fold difference in rates, suggesting that a substantial part of the observed difference in rate constants (> 700-fold) may originate from pre-exponential factor in the rate constant expression. In fact, application of eqs 45,46 with the above mentioned reorganization energy and driving force parameters would yield $k_{et}(0)$ values of 1.3×10^{9} s^{-1} for ^{1}*ZnP-NDI $\rightarrow$ ZnP^{+}-NDI^{-} and $> 2 \times 10^{11}$ s^{-1} for ZnP-^{1}*NDI $\rightarrow$ ZnP^{+}-NDI^{-}.

In order to discuss possible reasons for such a difference in pre-exponential factors, it is important to realize that photoinduced electron transfer, depending on whether excitation takes place at the donor or at the acceptor unit, follows different one-electron pathways and involves different superexchange interactions (Figure 9.20).[32i,l]

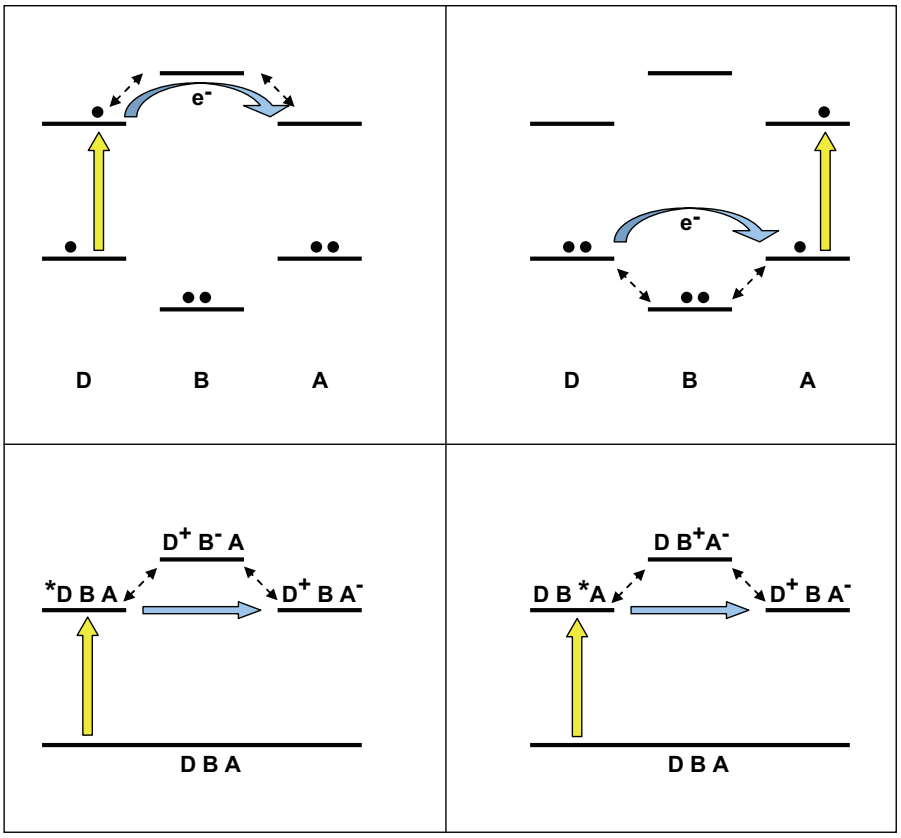

Fig. 9.20. Superexchange pathways for photoinduced electron transfer in a donor-bridge-acceptor (D-B-A) system following excitation of the donor (left panels) or the acceptor (right panels). Upper panels: orbital representation. Lower panels: state representation.

In particular, following donor excitation electron transfer from donor to acceptor takes place at the LUMO level, with indirect orbital mixing involving high unoccupied levels of the bridge.[189,190,191] Upon excitation of the acceptor, on the other hand, electron transfer takes place at the HOMO level from donor to acceptor (equivalent to “hole transfer” from acceptor

to donor), with indirect orbital mixing involving low-lying occupied levels of the bridge.[192,193] In a state representation, the virtual states responsible for the superexchange interactions in the two cases are different, with an additional electron or hole on the bridge (Figure 9.20). It is clear that the photoinduced electron transfer rates will critically depend on the energy gaps between the relevant orbitals (LUMO for donor excitation, HOMO for acceptor excitation) of the donor/acceptor units and of the bridge, *i.e.*, on the energy of the bridge-localized electron- (for donor excitation) or hole- (for acceptor excitation) transfer virtual states. In particular, in order to have a very high rate for photoinduced electron transfer upon excitation of the acceptor, bridge-localized occupied orbitals should lie at relatively high energy, close to the HOMO orbitals of donor and acceptor.

In order to have some insight on this point, DFT calculations, using the B3LYP hybrid functional[194] and the 6-31G* basis set, have been performed on a fragment comprising the NDI acceptor and the diphenyltriazole bridge (Figure 9.21a). The geometry optimization (Figure 9.21b) shows that (i) the diphenyl triazole bridge is almost planar, with small dihedral angles between the triazole unit and the phenyl groups and (ii) the diphenyltriazole bridge and the planar NDI unit are almost perpendicular. This suggests that the two units are substantially electronically decoupled, with relevant molecular orbitals expected, and found, to be largely bridge- or NDI-localized. Some of the relevant molecular orbitals are shown in Figure 9.22.

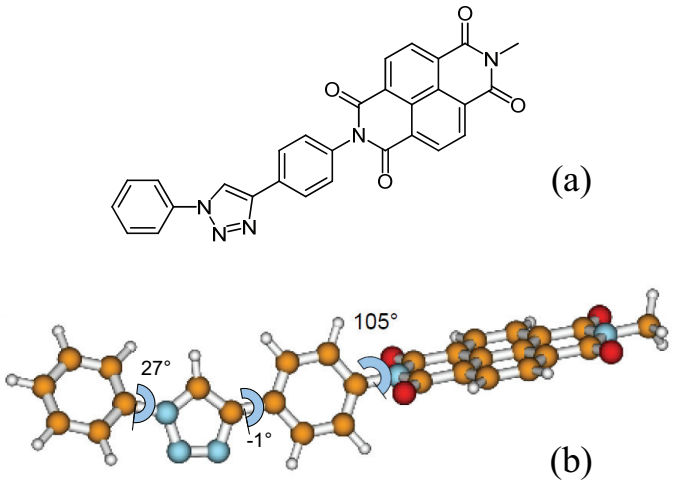

Fig. 9.21. (a) Molecular structure of the fragment investigated by computational techniques; (b) optimized ground-state geometry of the fragment from DFT calculations at the B3LYP level.

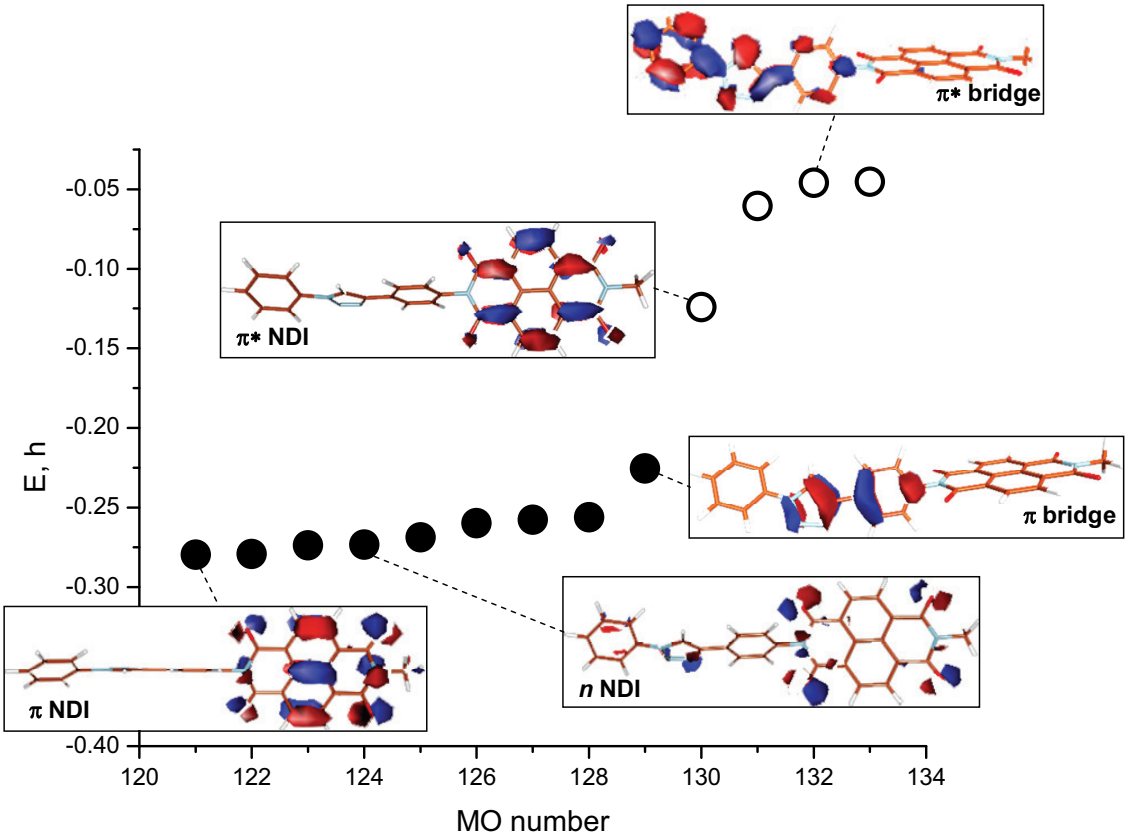

Fig. 9.22. Molecular Orbitals of the bridge-NDI fragment (●, filled; ○, unoccupied) emphasizing the bridge-localized nature of the HOMO and the NDI-localized nature of the LUMO. Also shown are the first NDI-localized filled or unoccupied orbitals encountered in going to lower or higher energy.

As expected, in this bridge-acceptor fragment the LUMO is localized on the NDI unit, while the first unoccupied orbital localized on the bridge lies at high energies (LUMO +2). The striking observation is, however, that the HOMO of the fragment is definitely bridge-localized, whereas occupied levels localized on the NDI unit (an oxygen localized n-type orbital, HOMO -5, and a π bonding one, HOMO -8) can only be found at lower energies. This means that the energy level diagram in our donor-bridge-acceptor dyad is likely to be very different from the standard one depicted in Figure 9.20, having in fact the highest occupied orbital of the bridge higher in energy than that of the NDI unit and presumably lower than that of the zinc porphyrin unit (where the first electrochemical oxidation process takes place, Table 9.1). This implies that the bridge-to-acceptor charge transfer state, instead of being as usual a high-energy virtual state, is here thermodynamically accessible from the acceptor excited state. This situation (Figure 9.23) favors much faster photoinduced electron transfer following excitation of the acceptor (downhill donor-to-acceptor electron cascade through the

bridge at the HOMO level) than following excitation of the donor (usual superexchange pathway at the LUMO level).

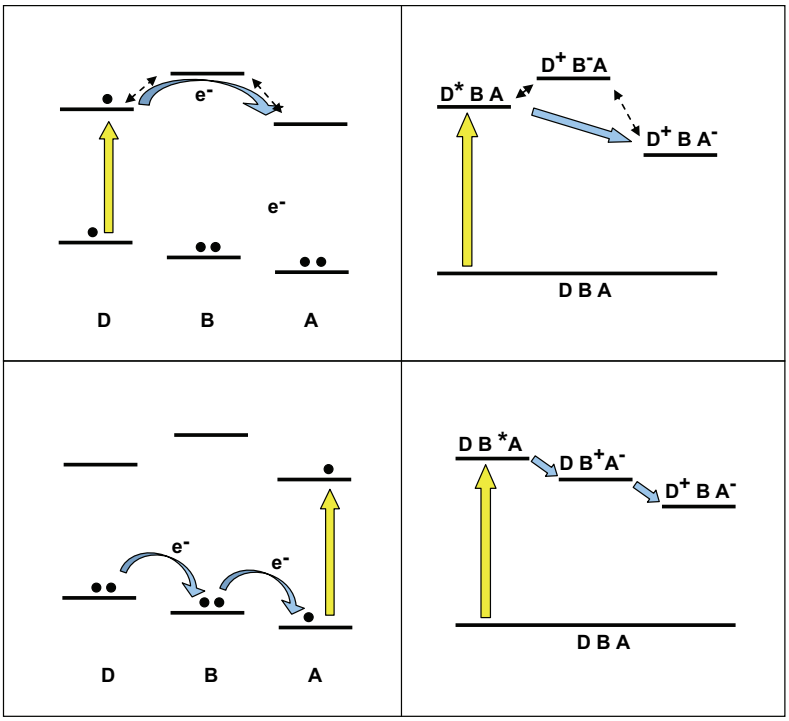

Fig. 9.23. Qualitative energy level diagram for the ZnP-NDI dyad **1**. In this situation, different photoinduced electron transfer mechanisms are expected depending on the unit being excited: superexchange upon excitation of the donor (upper panels), electron cascade through the bridge upon excitation of the acceptor (lower panels). Left panels: orbital representation. Right panels: state representation.

In the light of this energy situation, the presence of an ultrafast singlet charge separation pathway upon NDI excitation, experimentally inferred from formation yield arguments, looks very plausible. The above discussed MO arguments suggest for the triazole bridge a strongly asymmetric nature with respect to photoinduced electron transfer, greatly favoring in a dyad excitation of the acceptor (hole-transfer pathway) over excitation of the donor (electron-transfer pathway).

9.4 Conclusions

In this chapter a new dyad and triad systems based on a zinc porphyrin (ZnP), a naphthalenediimide (NDI), and a ferrocene (Fc) as molecular components, linked by 1,2,3-triazole bridges, ZnP-NDI (**1**) and Fc-ZnP-NDI (**2**), have been investigated by both visible

excitation of the ZnP chromophore and UV excitation of the NDI unit. Upon visible excitation of the ZnP, relatively inefficient quenching of the singlet excited state is observed in both dyad **1** and triad **2**, with slow charge separation processes also followed by faster charge recombination. Excitation of the NDI chromophore, on the other hand, leads to efficient charge separation by both singlet and triplet quenching pathways. In the triad system **2** the primary formation of Fc-ZnP^{+}-NDI^{-} charge separated state is followed by a secondary hole shift process from ZnP to Fc. The product of the stepwise charge-separation, Fc^{+}-ZnP-NDI^{-}, undergoes recombination to the ground state in 1.9 μs.

Although driving force effects may partially account for this difference in efficiency, electronic factors seem to play the major role. In fact, DFT calculations on a bridge-acceptor fragment show that the triazole bridge, displaying a high lying HOMO, much favors photoinduced electron transfer *via* a hole transfer mechanism (most likely in a donor-to-bridge-to-acceptor electron cascade) triggered by excitation of the acceptor (NDI) rather than *via* an electron transfer pathway promoted by excitation of the donor (ZnP).

Dyad **1** and triad **2** represent one of the few cases reported in the literature where charge separation and recombination can be obtained by excitation of both donor and acceptor with completely different efficiencies. As such this study gives fundamental hints for the development of efficient charge separation devices featuring fast charge separation and long-living charge separated states.

Chapter 10

Non-destructive Photoluminescence Read-out by Intramolecular Electron Transfer in a Perylene Bisimide-Diarylethene Dyad

This chapter will describe a side-project on a perylenebisimide-diarylethene dyad system used as fluorescent photoswitch. The results comes from a collaboration with the group of Prof. Frank Würthner (Institut für Organische Chemie and Center for Nanosystems Chemistryof the University of Würzburg, Germany). Parts of this chapter are published in the literature.[195]

10.1 Introduction

The demand for advanced data storage methods has been increased dramatically during the last decade. The development of computer technologies and memory systems with large data storage capacity and fast read-write efficiencies is in a footrace with the increasing need for technologies such as high-resolution photography, high-definition film techniques and the miniaturization for laptops, tablet PCs, and smartphones. An emerging data storage method that has potential for high bit density is based on single organic molecules that are photoswitchable between two thermally stable isomers. This molecular property is known as photochromism.

Several photochromic compounds, such as azobenzenes,[196] fulgides,[197] spiropyrans,[198] and diarylethenes,[199] are reported in the literature and studied. While most of these systems exhibit equilibrating thermal back reactions, diarylethene (DAE) derivatives offer highly desirable thermal bistability in both ring-open (denoted as DAE_O) and ring-closed (denoted as DAE_C) forms, making them unique among photochromic molecular systems. DAEs are generally composed of two aromatic rings, mainly thiophenes or benzo[*b*]thiophenes that are connected by a carbon-carbon double bond bridge (Figure 10.1), the latter usually being a part of a five-membered ring like perfluorocyclopentene or maleimide.

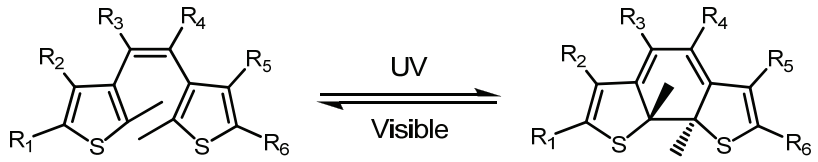

Fig. 10.1. Schematization of the photochromic behavior of diarylethenes.

While the open form of a diarylethene exhibits two rotamers, the so called parallel and anti-parallel rotamers, only the anti-parallel one may undergo the orbital-controlled six π-electron pericyclic isomerisation upon irradiation to afford the ring-closed form (Figure 10.1).

Since the open form isomer of DAE absorbs predominantly in the short-wave spectral region, its ring closure can be initiated by irradiation with UV light. The ring closure of DAE results in an extension of the π-system and thus the ring-closed isomer possesses absorption bands at longer wavelength. Accordingly, the ring-opening reaction of the closed form can be triggered by irradiation with visible light.

The ease of photoswitching between thermally stable ring-open and ring-closed DAE isomers has resulted in their application in different optoelectronic devices, with particular relevance in high-density data storage on a molecular level.[200] One particularly interesting approach consists of the coupling of the diarylethene photochromic unit to a fluorophore with the possibility of tuning the fluorescence properties of the dye through the light-induced chemical modification of the photochromic moiety. In more detail, emission of the dye unit can be turned on and off repeatedly by isomerization of the photochromic DAE unit upon irradiation with light of two different wavelengths and with an additional third light source of a different wavelength, the respective fluorescent or non-fluorescent state can be obtained as the "read-out" signal, resulting in a binary emissive "1" and non-emissive "0" code.

One of the first attempts towards this direction was made by Irie and coworkers[201] by coupling a photoswitchable DAE unit to an anthracene dye. The emission was quenched by intramolecular Förster resonance energy transfer (FRET) from the excited dye to only one of the photochromic isomers. One detrimental effect of this type of quenching, however, was the concomitant sensitization of the ring-closed form of the photochromic dyad during the read-out process, resulting in an undesirable ring opening. Thus, energy transfer may induce the photochromic back reaction of the ring-closed form to the ring-open one during reading of the fluorescence intensity and such energy-transfer-based memory systems lead to destructive read-out.

Emission quenching by intramolecular photoinduced electron transfer may actually circumvent the problem. A few years ago, nearly simultaneously the groups of Scandola and Würthner[202] and the group of Irie[203] have proposed a concept for fluorescence photoswitching by intramolecular electron transfer based on dyads of photochromic diarylethene (DAE) and fluorescent perylene bisimide (PBI) dye. The basic idea behind this concept is that the ring-open and ring-closed isomers of the photochromic DAE moiety exhibit different redox properties and the electron transfer from fluorescent PBI dye is thermodynamically favorable only to one of the two DAE isomers. Perylene bisimides have been chosen as emitters because this class of dyes possesses excellent photochemical stability, high extinction coefficients, and outstanding fluorescence quantum yields. Moreover their optical and redox

properties can be easily tuned over a wide range by appropriate substitutions at the bay area (Figure 10.2).

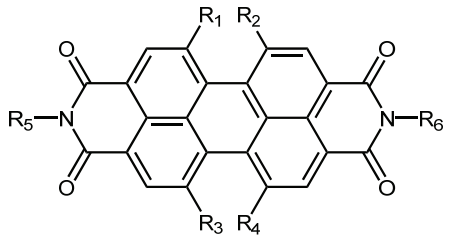

Fig. 10.2. Molecular representation of a perilene bisimide chromophore, R_1, R_2, R_3, and R_4 are the so-called bay-positions where substitution brings about important effects in terms of optical and redox properties.

However, all of the so far reported photoswitching systems based on this concept suffer from certain disadvantages like low fluorescence quantum yield, photocyclization by triplet state population, small driving force for fluorescence-quenching PET, or low photostability. For instance, in one of the PBI-DAE dyads studied,[202] the low fluorescence quantum yield (14% in dichloromethane) and the low photostability of the 1,7-dipyrrolidino-substituted PBI were found as the main drawbacks of the florescence-based photoswitch.

In this chapter, a novel and highly stable PBI-DAE photochromic dyads **1o/1c** (Figure 10.3) will be presented containing two benzo[*b*]thiophene 1,1-dioxide subunits substituted DAE photoswitch, where ring-closed isomer is considerably better electron acceptor than the ring-open isomer, and a highly fluorescent tetraaryloxy-substituted PBI chromophore with a matched oxidation potential to facilitate electron transfer to ring-closed DAE.

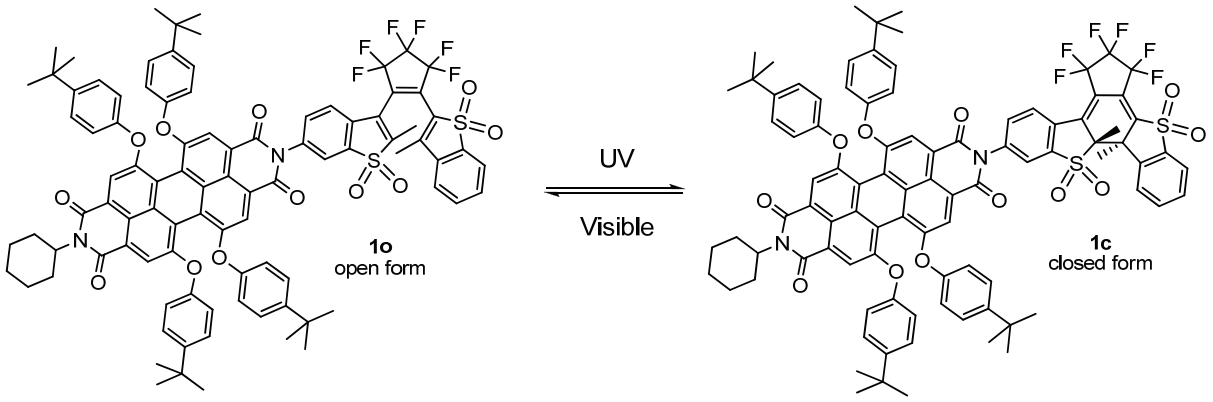

Fig. 10.3. Photoswitchable PBI-DAE dyads **1c/1o** studied in this chapter.

10.2 Experimental section

10.2.1 Synthesis

In order to perform a thorough investigation on the photochromic behavior of dyads **1o/1c** molecular models of both the diarylethene (**2o**) and the perylenebisimide (**3**) units (Figure 10.4) have also been studied.

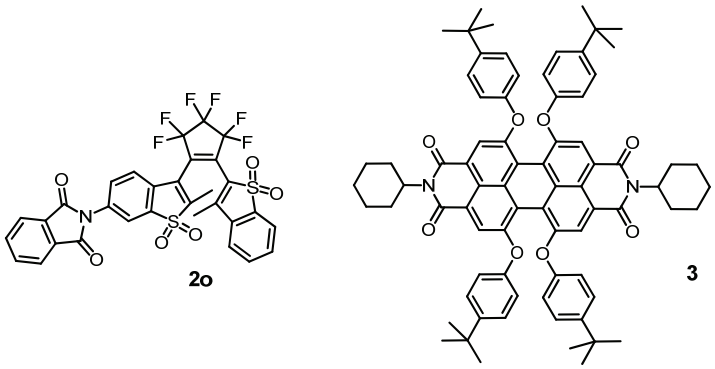

Fig. 10.4. Molecular models of the diarylethene (**2o**) and perylenebisimide (**3**) units.

The synthesis of the photochromic dyad **1o/1c** as well as that of molecular models has been performed by Dr. Martin Berberich and Peter Spenst at the Institut für Organische Chemie and Center for Nanosystems Chemistry of the University of Würzburg (Germany).

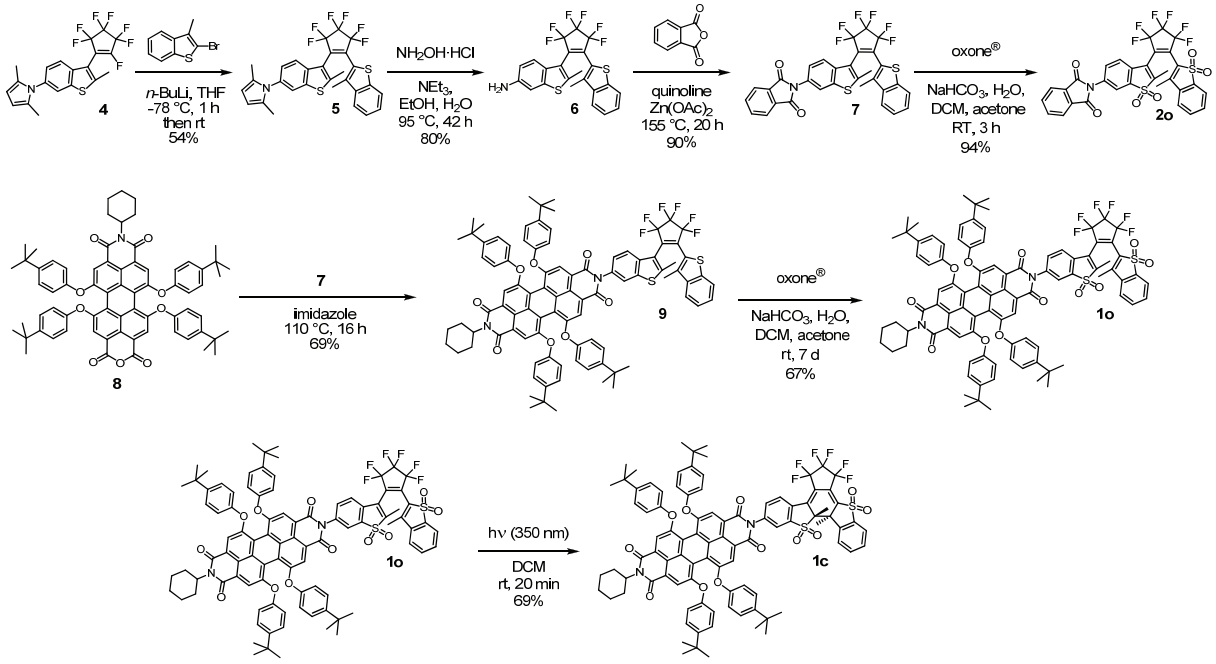

Fig. 10.5. Synthetic route for the preparation of dyad **1o/1c** and reference diarylethene **2**.

The synthetic strategies, adopted for the preparation of the photochromic dyad **1o/1c** and the molecular model **2**, are illustrated in Figure 10.5. All new compounds, including the target dyads as well as reference **2** were properly characterized by ^{1}H and ^{13}C NMR spectroscopy and high-resolution mass spectrometry.

Importantly, in order to characterize separately the two forms of dyad **1**, namely **1o** and **1c**, continuous UV irradiation (350 nm) of the ring-open isomer **1o** in dichloromethane was performed. The closed form **1c** could be easily separated from the remaining open form by column chromatography with silica gel under exclusion of light and pure **1c** was obtained in 69% yield, while the remaining open form **1o** was re-isolated.

10.2.2 Apparatus and procedures

All the reagents used were of reagent grade quality. Solvents were all of spectroscopic grade quality. See Chapter 2 for details of the experimental techniques used.

10.3 Results and discussion

10.3.1 UV-vis absorption and fluorescence studies

Absorption spectra of **1o**, **1c**, and reference PBI dye **3** in dichloromethane are reported in Figure 10.6a. The absorption maximum is bathochromically shifted by about 10 nm for both ring-open (**1o**) and ring-closed (**1c**) dyads compared to PBI **3** and the closed form exhibits a noticeable higher extinction. The emission maximum of PBI chromophore (maximum at 604 nm) is likewise bathochromically shifted by 10 nm for **1o** and **1c**.

The closed form **1c** exhibits, by comparison with the open one **1o**, an additional broad absorption band with a maximum at 368 nm that extends into the visible range and can be thus assigned to the diarylethene moiety. In fact, formation of this absorption, though less pronounced, is also observed for model compound **2o** after irradiation in the UV (Figure 10.6b). Notably, the poor conversion of **2o** into its closed form **2c** suggest that the PBI chromophore in **1c/1c** has a different impact on the photochromic behavior of the diarylethene moiety than phthalic imide in the reference system **2o**/**2c**.

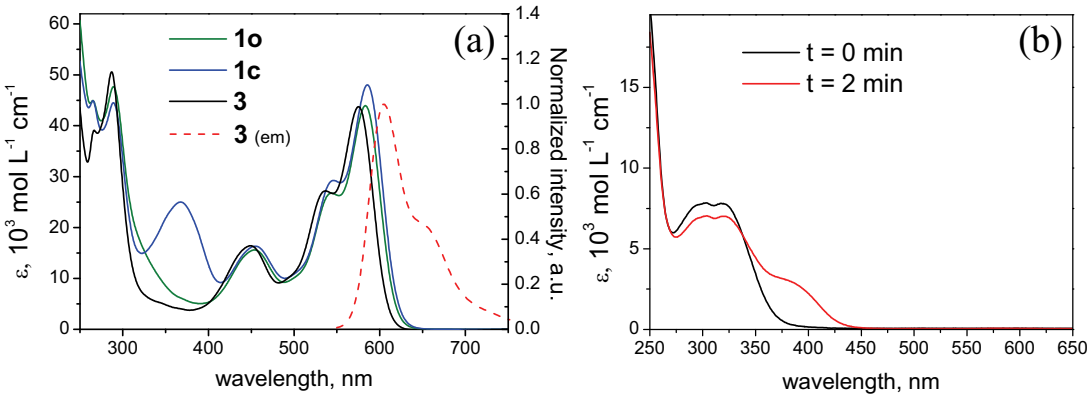

Fig. 10.6. (a) Absorption spectra of dyad **1o/1c** and reference PBI **3**, emission spectrum of reference PBI **3** in dichloromethane (excitation at 530 nm); (b) absorption spectra of model **2o** before and after irradiation with an UV lamp (λ = 254 nm).

Although the open and closed form dyads **1o** and **1c** have similar absorption behavior in the visible region, dichloromethane solutions of these dyads exhibit completely different emission properties. As a matter of fact, the fluorescence quantum yields of open form **1o** (95%) and closed form **1c** (5%) in dichloromethane are strikingly different. The fluorescence quantum yields of **1o** and **1c** were then determined in several solvents of different polarity from tetrachloromethane ($\varepsilon_r = 2.24$) to dimethyl formamide ($\varepsilon_r = 36.71$) and divided by the respective value of reference PBI **3** to explore, whether the fluorescence quenching behavior of these dyads is dependent on the solvent polarity as expected for a PET quenching mechanism. The fluorescence quantum yields of **1o**, **1c**, and PBI **3** in different solvents are listed in Table 10.1.

Table 10.1. Fluorescence quantum yields of **1o**, **1c**, and **3** in different solvents.

		Φ_{fl} (%)		
solvent	ε_r [a]	**1o**	**1c**	**3**
tetrachloromethane	2.24	95 ± 0.8	99 ± 1.8	96 ± 2.5
di-*n*-butyl ether	3.08	95 ± 2.1	91 ± 1.5	95 ± 2.7
chloroform	4.89	97 ± 2.5	11 ± 0.3	96 [b]
dichloromethane	8.93	95 ± 1.1	5 ± 0.3	96 ± 1.1
1,2-dichloroethane	10.36	89 ± 1.5	4 ± 0.1	96 ± 1.2
acetone	20.56	74 ± 1.7	2 ± 0.1	88 ± 4.0
DMF	36.71	67 ± 2.9	3 ± 0.3	87 ± 2.9

[a] solvent polarity values are taken from the literature;[204] [b] taken from the literature.[205]

The open form dyad **1o** shows an almost unitary fluorescence quantum yield in solvents of low or intermediate polarity such as tetrachloromethane and dichloromethane. With increasing solvent polarity, the quantum yield is decreased ultimately to 67% in dimethyl-formamide. Notably, the quantum yield of reference dye **3** is decreased as well from nearly unity in non-polar environments to 87% in dimethyl formamide. For similar PBI dyes this behavior has been attributed to charge transfer from the aryloxy-substituents to the electron-poor PBI.[206] As far as the closed isomer **1c** is concerned, the emission quantum yield is almost unitary in tetrachloromethane, whilst it is seen to drop down sensitively as the solvent polarity is increased (11% in chloroform). In still more polar solvent (acetone, DMF for instance) the emission becomes practically negligible. The trend observed for the luminescence efficiency of **1c** with the solvent polarity is that expected considering a PET mechanism of quenching, since a FRET one should not be affected at all by the change of the solvent.

10.3.2 Photochromic behavior

In view of the application of **1** as a photoswitching memory two main features must be taken into consideration: (i) the possibility of switching repeatedly between two differently emissive states and (ii) the non-destructive read-out capability.

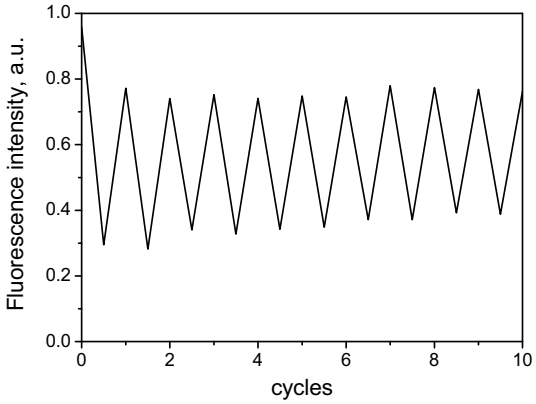

Fig. 10.7. Switching cycles of **1o** in dichloromethane upon alternating irradiation with UV light (320 nm; ±10 nm FWHM; xenon arc lamp 150 W) and visible light (cut-off filter at 395 nm; xenon arc lamp 175 W) followed by the fluorescence intensity at 650 nm.

As far as point (i) is concerned, upon UV excitation in dichloromethane **1o** is progressively converted into its closed isomer **1c** until a photostationary state is reached. At the same time the fluorescence of the PBI unit undergoes a strong decrease in intensity from 95% down to

30% (Figure 10.7). Then, upon excitation in the visible ($\lambda > 395$ nm), the emission intensity increases up to 78%, meaning that **1c** is converted back to **1o** until a new photostationary state is reached. This demonstrates that the emission intensity can be switched between a high emissive state (around 80% open form and 20% closed form) and a less emissive state (around 25% open form and 75% closed form). These ring opening/closure procedures can be performed repeatedly (verified up to 10 opening/closure cycles) without any alteration of the photophysical response and/or decomposition of the system (Figure 10.7).

As regarding point (ii), the non-destructive read-out capability was demonstrated by enduring excitation of the fluorophore unit of **1o** and **1c** at 600 nm in dichloromethane (Figure 10.8). In fact, upon continuous irradiation of the PBI unit negligible changes in the fluorescence response are observed for both **1o** and **1c**, meaning that neither the opening reaction nor the closure one can be sensitized at the reading wavelength.

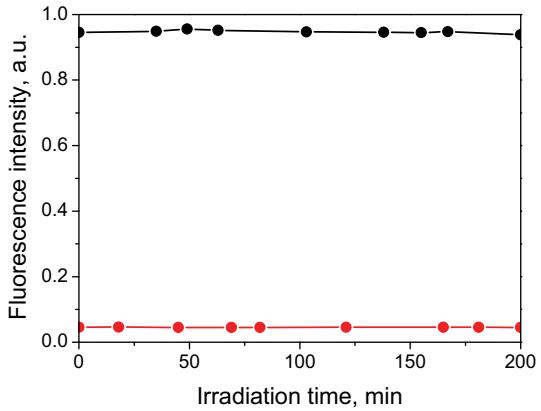

Fig. 10.8. Fluorescence intensity at 650 nm of **1o** (black dots) and **1c** (red dots) in dichloromethane upon continuing excitation with monochromatic light at 600 nm (±10 nm FWHM; xenon short arc lamp 75 W; 6.9 mW/cm^2).

10.3.3 Electrochemistry

In order to calculate the driving force for PET process of dyad **1o**/**1c**, the first oxidation potential of the electron donor in dyad **1**, namely PBI unit, and the first reduction potential of the electron acceptor, namely the diarylethene moiety, are required. Thus, the redox potentials of the open and closed form of dyads **1o** and **1c** as well as of reference compounds **2o** and **3** were measured by cyclic voltammetry. The electrochemical data are collected in Table 10.2. The reduction potentials of the DAE acceptor units in open and closed form are –1.37 V and –0.97 V, respectively, while the oxidation potentials of the PBI unit in both forms are 0.84 V and 0.89 V. The excited state energy was calculated from the average value of the measured

absorption maximum at 585 nm and emission maximum at 614 nm of the PBI moiety in dyad **1**, resulting in a value of 2.07 eV for both open and closed forms. From the optimized structures of **1o** and **1c** at force field level MM3* (MacroModel 9.8) center to center distances R_{CC} between donor and acceptor units of **1o** and **1c** are estimated as 12.7 Å, respectively.

Table 10.2. Electrochemical data of **1o**, **1c**, **2o**, and **3**. [a]

	Reduction (V *vs.* SCE)				Oxidation (V *vs.* SCE)
1o	− 1.83 [c]	− 1.41 [d]	− 1.24 [b]		0.84 [b]
1c	− 1.76 [c]	− 1.32 [b]	− 1.17 [b]	− 0.97 [c]	0.89 [b]
2o	− 1.92 [c,e]	− 1.62 [c,e]	− 1.37 [c,e]		
3		− 1.41 [b]	− 1.27 [b]		0.78 [b]

[a] Obtained by cyclic voltammetry (CV) in dichloromethane (0.1 M $TBAPF_6$) using Fc/Fc^+ as internal standard, scan rate of 100 mV/s; [b] process attributed to the PBI unit; [c] process attributed to the DAE unit; [d] overlapping waves; [e] irreversible process.

According to eq 30, by applying a Rehm-Weller type calculation[130] the driving force for the electron transfer can be estimated as +0.01 eV for the open **1o** and –0.34 eV for the closed form **1c**. This means that in dichloromethane and more generally in solvents with similar polarity photoinduced electron transfer is thermodynamically allowed for the closed form of the dyad only, whereas it is unfeasible in the case of the open form. Moreover, considering the destabilization of the charge separated state in going to less polar solvents like tetrachloromethane, the formation of a charge-transfer state is expected to be energetically uphill for both open and closed forms, as experimentally observed (Table 10.1). In contrast, highly polar solvents like dimethylformamide should stabilize the charge-transfer states and thus fluorescence quenching is expected even for the open form, as observed from the slow decrease of the fluorescence quantum yield in **1o** (Table 10.1).

10.3.4 Photophysical study

To get insight into the fluorescence quenching process of photoswitch **1**, the fluorescence lifetimes of the open-ring (**1o**) and closed-ring (**1c**) isomers as well as reference fluorophore PBI **3** were determined in dichloromethane and acetone by time-correlated single-photon counting (TC-SPC) technique. The obtained results are summarized in Table 10.3.

As the data in Table 10.3 reveal, the lifetime of **1o** is almost identical to that of the reference PBI **3** in dichloromethane, while a small (ca. 20%) decrease compared to the value for **3** is observed in acetone. This behavior, paralleled by the fluorescence quantum yield data

shown in Table 10.1, can be explained by considering that photoinduced electron transfer, with no driving force in dichloromethane may become slightly exergonic in more polar solvent such as acetone, providing a slow (time constant, ca. 20 ns) deactivation process for the PBI excited state of **1o**. Overall, the similar behavior of **1o** and **3** indicates the absence of any major quenching of the PBI excited state by the appended open form of the photochromic DAE unit. By contrast, the lifetime of closed form **1c** is drastically decreased in both solvents compared to those of **1o** and PBI **3**, revealing that the excited state of PBI unit is efficiently quenched in the closed form. These lifetime results are in good agreement with fluorescence quantum yields (Table 10.1), which decrease dramatically in both dichloromethane and acetone for **1c** compared to those for **1o**. Moreover, in both solvents the lifetime of the closed form **1c** is too short (< 0.25 ns) for an accurate determination by single-photon counting technique.

Table 10.3. Fluorescence lifetimes of **1o**, **1c**, and **3** measured by TC-SPC. [a]

		τ (ns)		
solvent	ε_r	**3**	**1o**	**1c**
dichloromethane	8.93	6.6 ± 0.03	6.5 ± 0.03	< 0.25 [b]
acetone	20.56	6.9 ± 0.03	5.3 ± 0.03	< 0.25 [b]

[a] Excitation wavelength: 600 nm, analysis wavelength: 610 nm; [b] Lifetime below instrumental resolution.

To access the shorter timescale and to explore the mechanism responsible for fluorescence quenching of **1c**, ultrafast transient absorption spectroscopy was performed on **1c** and, for comparison, on **1o** and reference PBI **3**. Upon excitation at 550 nm, the transient behavior observed for the open form **1o** in dichloromethane (Figure 10.10) is very similar to that exhibited by the reference dye **3** (Figure 10.9). In both cases, the initial transient spectrum, characteristic of the singlet excited state of the PBI unit, exhibits a ground-state bleaching (mirroring the absorption spectrum of PBI dye) at wavelengths shorter than 610 nm, an apparent bleach between 610 and 680 nm arising from stimulated emission (mirroring the emission spectrum of PBI dye) and a positive signal at wavelengths longer than 680 nm due to excited-state absorption. The observed spectral changes for reference PBI **3** and dyad **1o** consist of a fast process (time constant of 1.7 ps for **3** and 3.8 ps for **1o**) involving a small decrease in ground-state absorption bleach and a red-shift of the stimulated emission (Figure 9.9a and 9.10a). Such fast process can be very likely attributed to vibrational relaxation in the excited state.

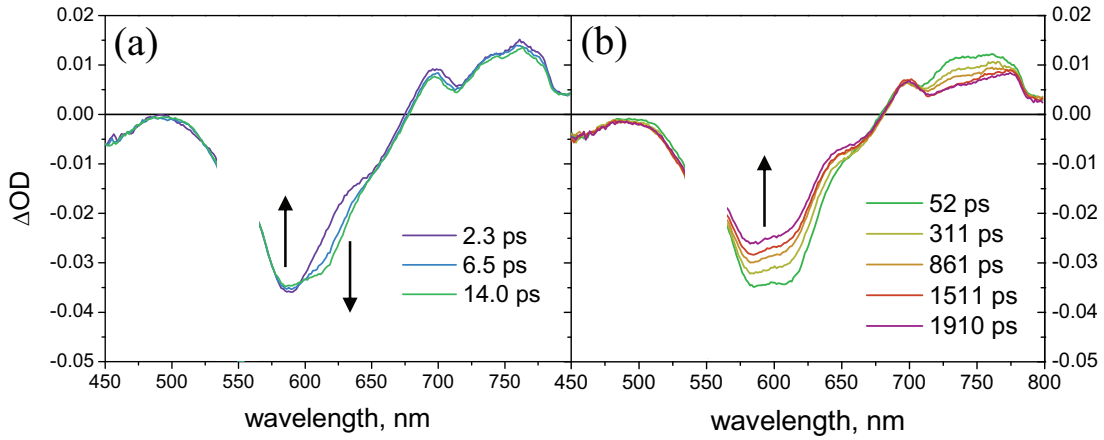

Fig. 10.9. Transient absorption spectra obtained by UFS on model **3** in dichloromethane (excitation at 550 nm): (a) 2.3-14.0 ps and (b) 52-1910 ps time-delays.

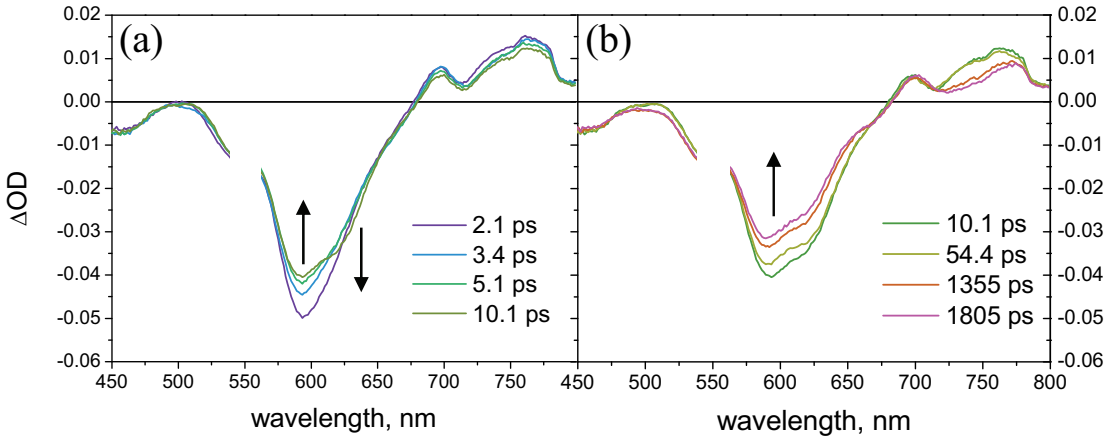

Fig. 10.10. Transient absorption spectra obtained by UFS on dyad **1o** in dichloromethane (excitation at 550 nm): (a) 2.1-10.1 ps and (b) 10.1-1805 ps time-delays.

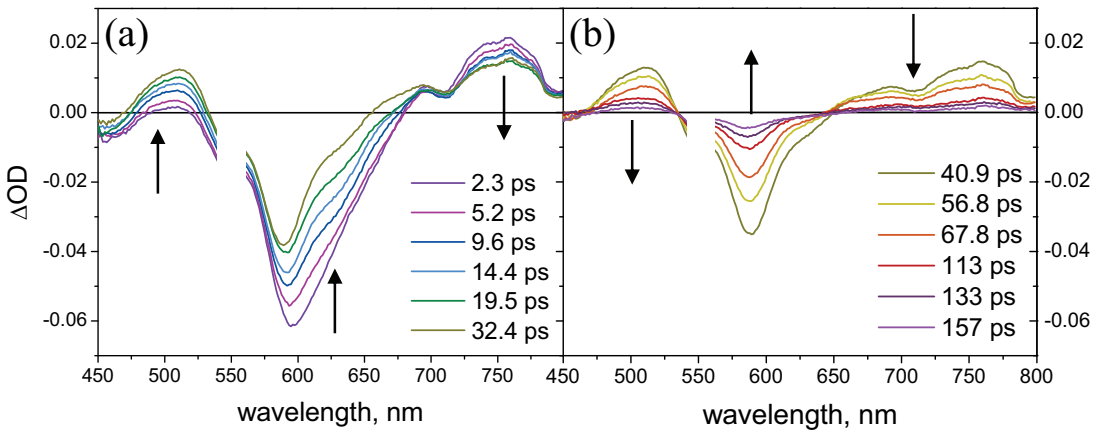

Fig. 10.11. Transient absorption spectra obtained by UFS on dyad **1c** in dichloromethane (excitation at 550 nm): (a) 2.3-32.4 ps and (b) 40.9-157 ps time-delays.

The subsequent, slow decay of the whole transient spectrum, consistent with the long emission lifetimes (shown in Table 10.3), can be assigned to the decay of the PBI excited state (Figure 10.9b and 10.10b). The very similar transient spectral behavior of dyad **1o** and reference PBI **3** confirms the conclusion inferred from the emission measurements that little, if any, intercomponent quenching of the fluorophoric unit takes place in the open form **1o** of the photochromic dyad.

The transient spectral changes of the closed form **1c** in dichloromethane (Figure 10.11), on the other hand, exhibit a biphasic spectral behavior entirely different from that observed for the open form **1o** and reference **3**. In the early time window (ca. 1-35 ps, Figure 10.11a) a complex decay of the features associated to the PBI excited state (ground-state bleach centered at 590 nm, stimulated emission in the 520-680 nm range, excited-state absorption at longer wavelength) is accompanied by the evident formation of a positive absorption centered at 510 nm. In the subsequent time window (ca. 35-160 ps, Figure 10.11b) the transient spectrum undergoes a clean decay to the baseline, with isosbestic points at $\Delta OD = 0$, and 535 and 645 nm. As regarding the mechanism, the first spectral variations can be assigned to a photoinduced electron transfer from the PBI unit to the DAE involving the formation of PBI^{+}-DAE^{-} charge separated state (oxidative quenching), whereas the subsequent spectral changes are consistent with charge recombination to the ground state. This assignment is supported by the spectroelectrochemical data of reference PBI **3** (Figure 10.12), showing that one-electron oxidation of this chromophore is accompanied by bleach in the region of the absorption maximum at 576 nm and by positive absorbance changes at both lower (characteristic maximum at 486 nm) and higher wavelengths.

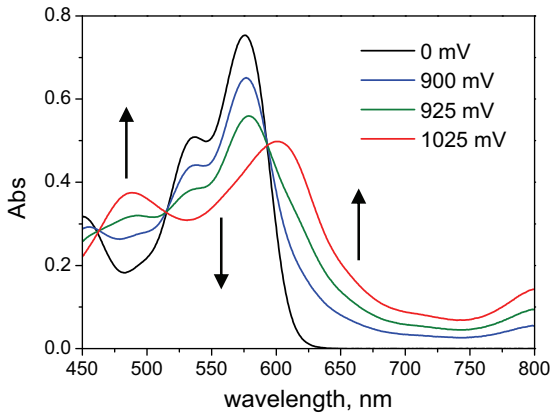

Fig. 10.12. Absorption spectra of model **3** in dichloromethane at different applyed voltage; the red spectrum reasonably resembles the spectrum of the PBI radical cation.

These spectroelectrochemical studies permit an easy interpretation of the transient spectral changes in Figure 10.11: the formation of the charge-separated state from the PBI excited state (Figure 10.11a) is signaled by (i) an asymmetric depletion of the bleach in ground-state maximum and (ii) the build-up of the absorption maximum at 510 nm (formation of oxidized PBI). The decay of the charge-separated state by charge recombination (Figure 10.11b) nicely mirrors the spectral changes observed in the spectroelectrochemical oxidation of reference PBI **3**.

Ultrafast spectroscopy measurements performed in acetone showed for the PBI model **3**, the open form **1o**, and closed form **1c** similar qualitative behavior as in dichloromethane. As regarding **1c**, similar biphasic spectral variations are observed, though with a different time evolution. The kinetics of charge separation and recombination for **1c** can be conveniently monitored at the wavelengths of PBI^{+} absorption maximum at around 500 nm (Figure 10.13). In dichloromethane (Figure 10.13a), the kinetic analysis revealed values of 34 ps and 36 ps for the time constants of charge separation and recombination, respectively. In the more polar acetone the values are 8.6 ps for charge separation and 27 ps for recombination (Figure 10.13b). The acceleration of the photoinduced electron transfer in the more polar solvent are consistent with a process occurring in the Marcus normal region, whilst the contemporaneous slight acceleration of the charge recombination points at a process in the Marcus inverted region. The observed solvent effect on quenching rate is in accordance with the strong fluorescence quenching of **1c** in polar solvents (Table 10.1).

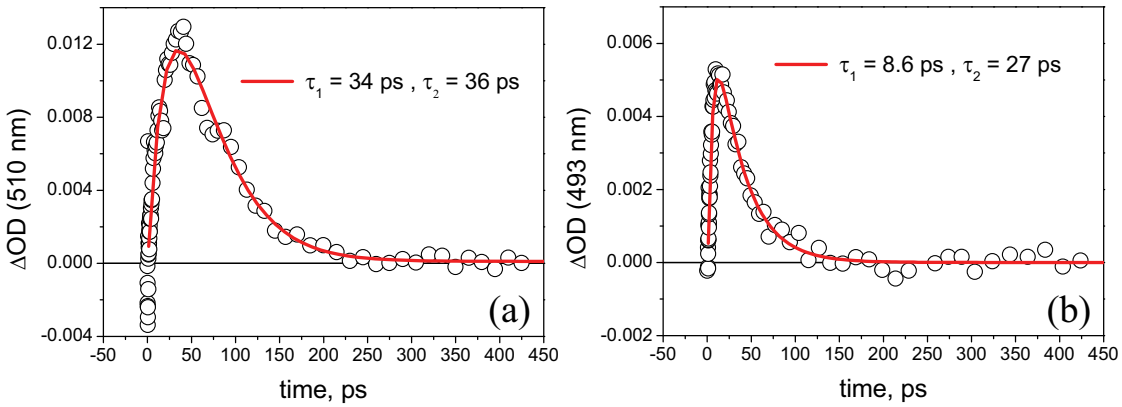

Fig. 10.13. Kinetics of formation and decay of the charge separated state observed by UFS on **1c** (a) in dichloromethane and (b) in acetone.

For the purpose of comparison, ultrafast spectroscopy experiments were also performed with the closed dyad **1c** by excitation at 400 nm. At this wavelength light is absorbed by both molecular components of the dyad in the following proportion: ca. 30% PBI unit and ca. 70%

ring-closed DAE (Figure 10.6). The transient spectral behavior (Figure 10.14) is practically the same as observed upon excitation at 550 nm, with clear evidence for photoinduced charge separation and recombination. The intensity of the transient signals, however, is definitely much larger than expected from the fraction of light absorbed by the PBI unit, as determined by a comparison of iso-absorbing **1c** and **3** solutions. Thus, a sizeable fraction of the light absorbed by the ring-closed DAE unit apparently contributes to the photophysical response from PBI unit. This suggests the occurrence of excitation energy transfer from the closed DAE unit to the PBI moiety.

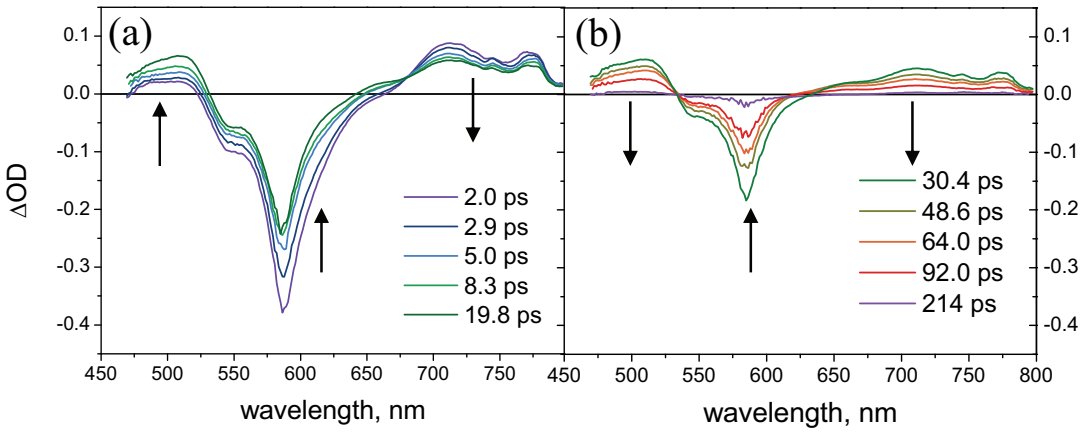

Fig. 10.14. Transient absorption spectra obtained by UFS on dyad **1c** in dichloromethane (excitation at 400 nm): (a) 2.0-19.8 ps and (b) 30.4-214 ps time-delays.

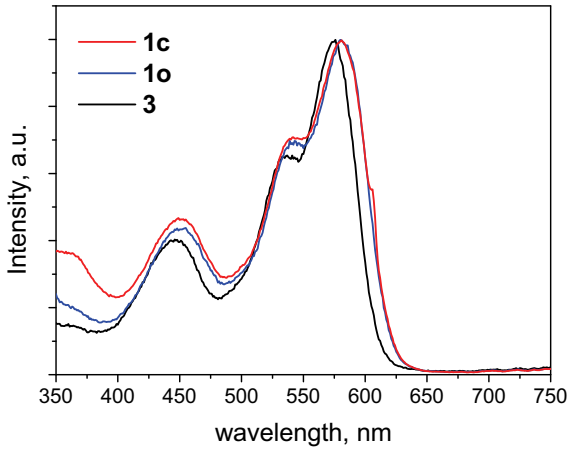

Fig. 10.15. Excitation spectra of the PBI emission (recorded at 610 nm) of **1c**, **1o**, and **3** in dichloromethane.

This hypothesis has been checked by measuring the excitation spectrum of the weak PBI emission of **1c** (Figure 10.15). As a matter of fact, besides the two PBI bands at 590 and 450 nm, a clear feature is observed at 365 nm, where the closed form of the DAE unit has its

absorption maximum. The lower intensity of this feature in the excitation (Figure 10.15) relative to the absorption spectrum (Figure 10.6) indicates that energy transfer is only partially (ca. 50%) efficient, implying a competition between the energy-transfer process and the ring-opening reaction taking place in the excited state of the ring-closed DAE unit.

In the early time window of the 400 nm ultrafast experiment (Figure 10.16), the formation of the PBI excited state (as monitored by the bleach of the ground-state absorption), takes place promptly (within the excitation pulse width) for reference **3** but has clearly a delayed component for dyad **1c**. Within the accuracy limits of the experiment, the time constant of the energy transfer process from ring-closed DAE to PBI (and likewise for the competing ring-opening reaction) can be estimated as ca. 1 ps. The observed energy transfer process, competing in the excited state with ring opening, is relevant for the efficiency of the photochemical ring opening reaction of **1c**.

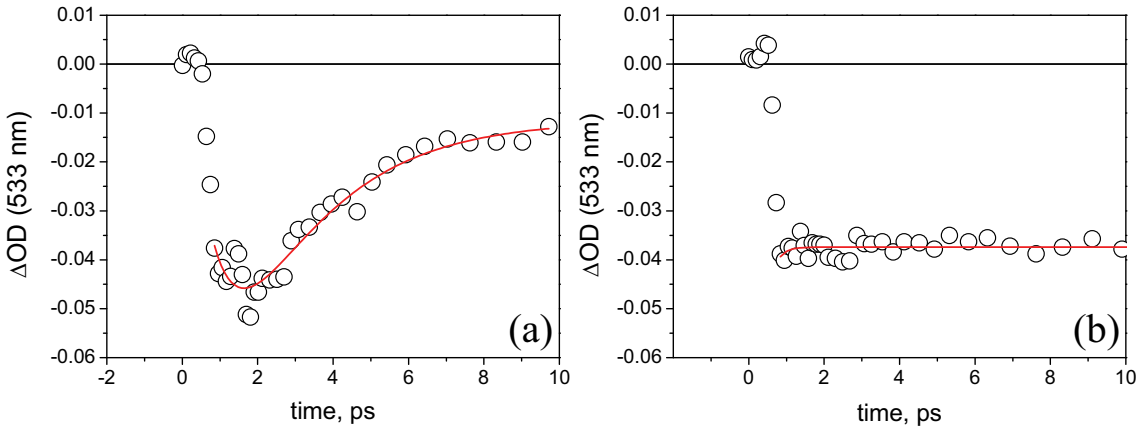

Fig. 10.16. Comparison of the formation kinetics of the PBI excited state (as monitored by the bleach of ground-state absorption) following 400-nm excitation of (a) dyad **1c** and (b) reference **3** in dichloromethane.

The photophysical/photochemical behavior of the **1c** dyad discussed above is summarized in the energy level diagram of Figure 10.17. The triplet state of the DAE unit is not considered to be involved in the photophysical behavior. In this diagram, the energy-transfer process has been assumed to take place *via* FRET to the second singlet excited state of the PBI unit (maximum absorption at 445 nm), which is expected to give a better spectral overlap than the lower energy one. At the same time an energy transfer process from the singlet excited state of the open-form **1o** has been introduced, as suggested, albeit less directly as for **1c**, by the excitation spectrum (Figure 10.15). As such, this energy transfer pathway, competing with the ring closure reaction, is relevant to the efficiency of the photochromic behavior.

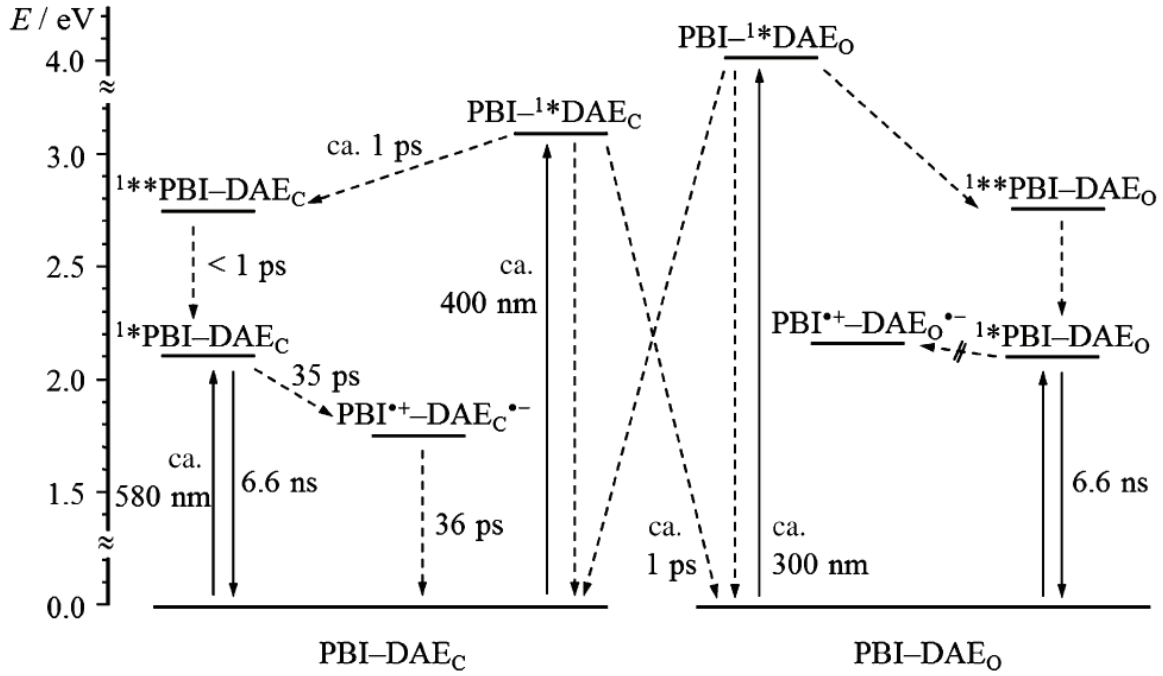

Fig. 10.17. Energy level diagram and photophysical/photochemical processes of PBI-DAE system **1**.

10.4 Conclusions

A novel, highly stable photochromic dyad **1** based on a perylene bisimide (PBI) fluorophore and a diarylethene (DAE) photochrome was synthesized and its optical and photophysical properties were studied in detail by steady-state and time-resolved ultrafast spectroscopy. This photochromic dyad can be switched reversibly by UV light irradiation of its ring-open form **1o** leading to the ring-closed form **1c** and back reaction of **1c** to **1o** by irradiation with visible light. Solvent-dependent fluorescence studies revealed that the emission of ring-closed form **1c** is drastically quenched in solvents of medium (*e.g.*, chloroform) to high (*e.g.*, acetone) polarities. This quenching process is attributed to photoinduced electron transfer from the PBI excited state to the DAE unit which is thermodynamically feasible only for the closed isomer of dyad **1**. The electron transfer mechanism has been fully demonstrated by ultrafast spectroscopy: while the open form **1o** displays spectral variations very similar to the reference PBI **3**, dyad **1c** shows a biphasic behavior featuring distinguishable charge separation and charge recombination processes.

Chapter 11

Conclusions and Perspectives

Artificial photosynthesis, namely conversion of solar energy into chemical fuels, represents a viable way within the global energy crisis with potential zero impact on the environment. One of the most challenging photosynthetic reaction schemes is water splitting with production of hydrogen as a clean and renewable fuel. Being a multielectronic process, water splitting is a complex reaction requiring appropriate catalyst units at both the cathodic (reduction of protons with formation of hydrogen) and the anodic side (oxidation of water to dioxygen). Moreover, in order to drive this reaction with the use of light, these catalysts must be suitably interfaced with photosensitizer units capable of light harvesting and subsequently generating strong reducing (for water reduction) or oxidizing (for water oxidation) species by photoreaction with an electron donor or acceptor, respectively. The interconnection between all these units plays a crucial role on the efficiency of the charge separation and charge collection processes. The control of the kinetics of all the photochemical and thermal steps is thus a strict requirement towards the design and optimization of a system in the view of water splitting. In this thesis several points regarding both the photoinduced oxidation and reduction of water as well as charge separation devices have been considered and studied in detail.

In Chapter 3 two water oxidation catalysts, namely a tetraruthenium and a tetracobalt polyoxotungstate, have been studied within sacrificial cycles involving tris(bipyridine) ruthenium(II) as photosensitizer and persulfate as sacrificial electron donor. Since their oxygen evolving activity was already known, attention has been paid to the investigation of the catalyst/sensitizer interactions in solution and the kinetics of hole transfer from the photogenerated oxidant to the catalyst. Importantly, while for the tetraruthenium catalyst these studies enable a thorough characterization of the photoinduced dynamics within the three-component catalyst/sensitizer/acceptor system, in the case of the tetracobalt polyoxotungstate the hole scavenging experiments demonstrated that in water oxidation involving $Ru(bpy)_3^{3+}$ as the oxidant the competent catalyst is not the tetracobalt cluster its-self, but rather a product of its decomposition upon aging.

In Chapter 4 a new class of tetrametallic catalysts has been introduced, namely tetracobalt cubanes, comprising a tetracobalt cluster stabilized by pyridine and acetate ligands. The water oxidation activity has been investigated in both dark conditions and light-activated experiments in purely aqueous buffer solutions involving $Ru(bpy)_3^{2+}$ and persulfate, reporting good quantum efficiency for oxygen evolution but low chemical yield. This has been attributed to the low driving force dictating the hole transfer processes to the catalyst which affects the stability of the sensitizer (undergoing decomposition from its oxidized form). An improvement of the system has been obtained by changing the solvent to a mixture of buffer/acetonitrile. Suitable functionalization of the *para*-position of the pyridine ligands with

both electron-donating and electron-withdrawing groups has been then attempted in order to tune the photocatalytic activity. Interestingly, a linear correlation was obtained between the hole transfer rate from the photogenerated oxidant to the catalyst and the electronic effect of the substituent. Moreover an outstanding quantum efficiency (80%) in the mixed solvent has been observed for the methoxy-substituted cubane.

In Chapter 5 a single-site cobalt(II) salophen complex has been used as water oxidation catalyst and studied within the typical sacrificial cycles involving $Ru(bpy)_3^{2+}$ and persulfate as sensitizer and sacrificial acceptor, respectively. Low overpotential for the oxygen-evolving reaction, fast hole-scavenging rates from the photogenerated oxidant, and great stability under turnover conditions have been found as the main virtues of the catalyst. The cobalt(II) salophen complex has been also studied in a sensitizer/catalyst covalent dyad with $Ru(bpy)_2(phen)^{2+}$ as the sensitizer moiety. Photocatalytic activity is still retained in the dyad upon continuous irradiation. The photophysical characterization in the phosphate buffer used for the photocatalytic experiments, however, points towards a partial decomposition of the compound with likely release of cobalt(II) ions, which may behave as the actual catalysts.

In Chapter 6 a self-assembling triad for photocatalytic water reduction has been studied, based on an aluminum(III) pyridylporphyrin as sensitizer central unit, an ascorbate sacrificial electron donor, and a cobaloxime as hydrogen evolving catalyst. The self-assembling is triggered by the bifunctional nature of the aluminum(III) pyridyl porphyrin chromophore featuring two different binding sites, namely a Lewis basic site, the pyridyl function, enabling coordination to transition metals such as cobalt and a Lewis acid site, the aluminum center, preferring coordination to oxygen-based ligands like ascorbate. The self-assembling in tetrahydrofuran of the three-component system as well as the photocatalytic activity have been studied thoroughly. Spectroscopic investigation of the system under the best hydrogen evolving conditions, however, suggests that the associated fraction of aluminum porphyrin in not useful for hydrogen production because of largely reversible quenching processes, whereas only the non-associated fraction of sensitizer works for hydrogen production bimolecularly and at the triplet level.

In Chapter 7 a tetracationic cobalt(II) porphyrin has been studied as hydrogen evolving catalyst in sacrificial cycles involving $Ru(bpy)_3^{2+}$ and ascorbic acid as photosensitizer and sacrificial donor, respectively. Efficient hydrogen production from purely aqueous buffer at neutral pH takes place upon visible light irradiation achieving turnover numbers up to 725, mainly limited by decomposition of the catalyst. A remarkable high rate has been measured for the first electron transfer from the photogenerated $Ru(bpy)_3^{+}$ reductant to the catalyst

which explains why efficient hydrogen production is observed even at low catalyst concentration, *i.e.*, with micromolar concentration of cobalt(II) porphyrin.

In Chapter 8 a fourth generation PAMAM dendrimer decorated with 32 ruthenium(II) polypyridine chromophores has been used as molecular scaffold where the synthesis of monodisperse platinum nanoparticles (average diameter of ca. 1.3 nm) has been accomplished. By combining both a sensitizer moiety and a catalytic unit this system has been demonstrated to produce hydrogen from a pH 5 water solution in the presence of ascorbic acid as sacrificial electron donor. Hydrogen evolution occurs *via* reductive quenching of the sensitizer moieties by ascorbic acid and subsequent intramolecular electron transfer to the platinum nanoparticles.

In Chapter 9 a triad system for photoinduced charge separation has been described, based on a naphthalene bisimide electron acceptor, a zinc porphyrin electron donor, and a ferrocene as secondary electron donor, connected *via* 1,2,3-triazole bridges. The triad system and the related dyad without the ferrocene display a particular behavior as far as charge separation efficiency and charge recombination rate are concerned. In fact, upon excitation of the zinc porphyrin unit the charge separated state involving the naphthalene bisimide moiety is obtained with very low efficiency (15%) and the charge recombination takes place in a sub-ns time scale. Conversely, upon excitation of the acceptor unit charge separation takes place efficiently at both singlet and triplet level and the long-range charge separated state involving the ferrocene has a quite long lifetime of 1.9 μs. This differences have been justified in terms of the asymmetric behavior of the phenyl-triazole bridges displaying, as confirmed by DFT calculations, a high lying HOMO which seems to favor photoinduced electron transfer through a hole transfer pathway upon excitation of the acceptor over an electron transfer pathway following excitation of the donor.

Finally, in Chapter 10 as a side-project of my Ph.D., a new photochromic dyad based on a perylene bisimide fluorophore and a diarylethene photochromic unit, suitable for application as optical memory element, has been characterized. Emission of the perylene bisimide unit can be turned off and on repeatedly by isomerization of the photochromic diarylethene upon irradiation in the UV (ring closure) or in the visible (ring opening), resulting in a binary emissive “1” and non-emissive “0” code. The mechanism responsible for the quenching of the fluorescence has been observed directly by ultrafast spectroscopy and attributed to a photoinduced electron transfer from the perylene bisimide excited state to the diarylethene moiety which is thermodynamically feasible only for the closed isomer. This quenching mechanism ensures the “non-destructive” read-out properties of the perylene bisimide-diarylethene dyad because the respective fluorescent or non-fluorescent state can be read upon

excitation at a wavelength which does not interfere with the photochemistry of the diarylethene.

In summary this thesis describes several fundamental aspects of an artificial photosynthetic scheme by dealing with different functional units such as charge separation, water oxidation and reduction. It is clear that the integration of these different functional units within a single device for artificial photosynthesis is the main goal of the future research. In particular, the use of sacrificial electron acceptors (for water oxidation) or electron donors (for water reduction) should be replaced by electrode surfaces made of nanostructured semiconductors (photoanodes or photocathodes) with formation of a regenerative photoelectrocatalytic water splitting cell where at the same time oxygen formation and hydrogen evolution take place at the anodic and cathodic side, respectively.

However, the complete understanding of the interplay between the catalytic and photosensitizing moieties, which is important for the development of a working device, clearly requires fundamental studies which can be reached only under appropriate experimental conditions. As such this thesis provides an approach to the water splitting issue based on the study of systems in solution with particular emphasis on the spectroscopic investigation of single electron transfer processes which, overall, are the basic, fundamental steps of the complex water splitting reaction.

List of Publications

1) "Light-driven Water Oxidation with a Molecular Tetra-Cobalt(III) Cubane Cluster"

Giuseppina La Ganga, Fausto Puntoriero, Sebastiano Campagna, Irene Bazzan, Serena Berardi, Marcella Bonchio, Andrea Sartorel, Mirco Natali, Franco Scandola

Faraday Discuss., **2012**, *155*, 177-190
DOI: 10.1039/c1fd00093d

2) "Non-destructive Photoluminescence Read-out by Intramolecular Electron Transfer in a Perylene Bisimide-Diarylethene Dyad"

Martin Berberich, Mirco Natali, Peter Spenst, Claudio Chiorboli, Franco Scandola, Frank Würthner

Chem. Eur. J., **2012**, *18*, 13651-13664
DOI: 10.1002/chem.201201484

3) "Photoinduced Water Oxidation by a Tetraruthenium Polyoxometalate Catalyst: Ion-pairing and Primary Processes with $Ru(bpy)_3^{2+}$ Photosensitizer"

Mirco Natali, Michele Orlandi, Serena Berardi, Sebastiano Campagna, Marcella Bonchio, Andrea Sartorel, Franco Scandola

Inorg. Chem., **2012**, *51*, 7324-7331
DOI: 10.1021/ic300703f

4) "Photocatalytic Water Oxidation: Tuning Light-Induced Electron Transfer by Molecular Co_4O_4 Cores"

Serena Berardi, Giuseppina La Ganga, Mirco Natali, Irene Bazzan, Fausto Puntoriero, Andrea Sartorel, Franco Scandola, Sebastiano Campagna, Marcella Bonchio

J. Am. Chem. Soc., **2012**, *134*, 11104-11107
DOI: 10.1021/ja303951z

5) "Is $[Co_4(H_2O)_2(\alpha\text{-}PW_9O_{34})_2]^{10-}$ a Genuine Molecular Catalyst in Photochemical Water Oxidation? Answers from Time-Resolved Hole Scavenging Experiments"

Mirco Natali, Serena Berardi, Andrea Sartorel, Marcella Bonchio, Sebastiano Campagna, Franco Scandola

Chem. Commun., **2012**, *48*, 8808-8810
DOI: 10.1039/c2cc34804g

6) "Photocatalytic Hydrogen Evolution with a Self-Assembling Reductant-Sensitizer-Catalyst System."

Mirco Natali, Roberto Argazzi, Claudio Chiorboli, Elisabetta Iengo, Franco Scandola

Chem. Eur. J., **2013**, *19*, 9261-9271
DOI: 10.1002/chem.201300133

7) "Porphyrin-Cobaloxime Dyads for Photoinduced Hydrogen Production: Investigation of the Primary Photochemical Process."

Mirco Natali, Michele Orlandi, Claudio Chiorboli, Elisabetta Iengo, Valerio Bertolasi, Franco Scandola

Photochem. Photobiol. Sci., **2013**, *12*, 1749-1753
DOI: 10.1039/c3pp50184a

8) "Long Range Charge Separation in a Ferrocene-(Zinc-Porphyrin)-Naphtalenediimide Triad. Asymmetric Role of 1,2,3-Triazole Linkers."

Mirco Natali, Marcella Ravaglia, Franco Scandola, Julien Boixel, Yann Pellegrin, Errol Blart, Fabrice Odobel

J. Phys. Chem. C, **2013**, *117*, 19334-19345
DOI: 10.1021/jp406405k

9) "Light Driven Water Oxidation by a Single Site Cobalt Salophen Catalyst."

Erica Pizzolato, Mirco Natali, Bianca Posocco, Alejandro Montellano López, Irene Bazzan, Marilena Di Valentin, Pierluca Galloni, Valeria Conte, Marcella Bonchio, Franco Scandola, Andrea Sartorel

Chem. Commun., **2013**, *49*, 9941-9943
DOI: 10.1039/c3cc45457f

10) "On the Effect of the Nature of the Bridge on Oxidative or Reductive Photoinduced Electron Transfer in Donor-Bridge-Acceptor Systems."

Antonino Arrigo, Antonio Santoro, Maria Teresa Indelli, Mirco Natali, Franco Scandola, Sebastiano Campagna.

Phys. Chem. Chem. Phys., **2014**, *16*, 818-826
DOI: 10.1039/c3cp53992j

11) "Fullerene-Driven Efficient Encapsulation of a Luminescent Eu(III) Complex Inside Carbon Nanotubes."

Laura Maggini, Melinda-Emese Füstös, Thomas William Chamberlain, Cristina Cebrián Ávila, Mirco Natali, Marek Pietraszkiewicz, Oksana Pietraszkiewicz, Mircea-Vasile Diudea, Edit Székely, Katalin Kamarás, Luisa De Cola, Andrei Nicolaevich Khlobystov, Davide Bonifazi

Nanoscale, **2014**, *6*, 2887-2894
DOI: 10.1039/c3nr05876j

12) "Efficient Photocatalytic Hydrogen Generation from Water by a Cationic Cobalt(II) Porphyrin."

Mirco Natali, Alessandra Luisa, Elisabetta Iengo, Franco Scandola

Chem. Commun., **2014**, *50*, 1842-1844
DOI: 10.1039/c3cc48882a

13) "Photoinduced Electron Transfer Across Molecular Bridges. Electron- and Hole-Transfer Superexchange Pathways."

Mirco Natali, Sebastiano Campagna, Franco Scandola

Chem. Soc. Rev, **2014**, in press
DOI: 10.1039/c3cs60463b

14) "Photoactive Dendrimer for Water Photoreduction: A Scaffold to Combine Sensitizers and Catalysts."

Luca Ravotto, Raffaello Mazzaro, Mirco Natali, Luca Ortolani, Vittorio Morandi, Paola Ceroni, Giacomo Bergamini

J. Phys. Chem. Lett., **2014**, 5, 798-803
DOI: 10.1021/jz500160w

Acknowledgements

First of all, I would like to thank my advisor Prof. Franco Scandola for giving me the opportunity to work in his group in Ferrara and in particular for driving me from the top of his experience in all the topics investigated during these years.

I would like also to thank all the people who take part in the several projects described in the present thesis and in particular to Dr. Andrea Sartorel and his coworkers in Padova, Dr. Elisabetta Iengo and her coworkers in Trieste, the group of Prof. Sebastiano Campagna in Messina, Dr. Giacomo Bergamini and his coworkers in Bologna, the group of Prof. Fabrice Odobel in Nantes, and the group of Prof. Frank Wurthner in Wurzburg. Being part of collaborations between different teams with different and complementary skills has been a very fruitful opportunity.

Special acknowledgements go to Dr. Claudio Chiorboli for his particular dedication to the ultrafast spectroscopy apparatus and to Dr. Roberto Argazzi for his help with both the laser flash photolysis and GC set-up.

I would like to thank Prof. Luisa De Cola and his group for giving me the possibility to spend two months in her laboratories in Strasbourg.

I am grateful to all the Ph.D. students and post-doctoral researchers of the first floor of the Department of Chemical and Pharmaceutical Sciences of the University of Ferrara for sharing labs, facilities, office, and particularly time. A special thank goes also to Davide Rosestolato and the time spent together along eight years of chemistry.

Finally, I wish to thank all my family for strongly supporting all my decisions and primarily my wife Federica and my son Alessandro: the everyday moments spent together are something that makes a man feel special.

References

1 Energy Information Association; U.S. Department of Energy: Washington DC; www.eia.doe.gov (accessed January 2010).

2 T. R. Cook, D. K. Dogutan, S. Y. Reece, Y. Surendranath, T. S. Teets, D. G. Nocera, *Chem. Rev.*, **2010**, *110*, 6474-6502.

3 N. S. Lewis, D. G. Nocera, *Proc. Natl. Acad. Sci. U.S.A.*, **2006**, *103*, 15729-15725.

4 REN21's Renewables **2013** Global Status Report (GSR).

5 S. Shafiee, E. Topal, *Energy Policy*, **2009**, *37*, 181-189.

6 J. R. Petit, J. Jouzel, D. Raynaud, N. I. Barkov, J.-M. Barnola, I. Basile, M. Bender, J. Chappellaz, M. Davis, G. Delaygue, *Nature*, **1999**, *399*, 429-436.

7 PCC 2007, Summary for Policymakers, in *Climate Change 2007: Impacts, Adaptation and Vulnerability. Contribution of Working Group II to the Fourth Assessment Report of the Intergovernmental Panel on Climate Change,* Cambridge University Press, Cambridge, UK.

8 J. A. Church, N. J. White, *Geophys. Res. Lett.*, **2006**, *33*, L01602.

9 S. Levitus, J. I. Antonov, T. P. Boyer, R. A. Locarnini, H. E. Garcia, A. V. Mishonov, *Geophys. Res. Lett.*, **2009**, *36*, L07608.

10 (a) L. Polyak, R. B. Alley, J. T. Andrews, J. Brigham-Grette, T. M. Cronin, D. A. Darby, A. S. Dyke, J. J. Fitzpatrick, S. Funder, M. Holland, A. E. Jennings, G. H. Miller, M. O'Regan, J. Savelle, M. Serreze, K. St. John, J. W. C. White, E. Wolff, *Quaternary Science Reviews*, **2010**, *29*, 1757-1778; (b) R. Kwok, D. A. Rothrock, *Geophys. Res. Lett.*, **2009**, *36*, L15501.

11 N. Armaroli, V. Balzani, *Angew. Chem., Int. Ed.*, **2007**, *46*, 52-66.

12 C. L. Archer, M. Z. Jacobson, *J. Geophys. Res. Atmos.*, **2005**, *110*, D12110.

13 A. S. Bahaj, *Renew. Sustain. Energy Rev.*, **2011**, *15*, 3399-3416.

14 B. D. Sherman, M. D. Vaughn, J. J. Bergkamp, D. Gust, A. L. Moore, T. A. Moore, *Photosynth. Res.*, **2013**, DOI 10.1007/s11120-013-9795-4.

15 B. S. Sorensen, *Renewable energy, fourth edition: physics, engineering, environmental impacts, economics & planning*. **2010**, Academic Press, Oxford.

16 United Nations Development Program (**2003**) World Energy Assessment Report: *Energy and the Challenge of Sustainability* (United Nations, NewYork).

17 B. O'Regan, M. Grätzel, *Nature*, **1991**, *353*, 737-740.

18 C. A. Bignozzi, R. Argazzi, C. J. Kleverlaan, *Chem. Soc. Rev.*, **2000**, *29*, 87-96.

19 A. Hagfeldt, G. Boschloo, L. Sun, L. Kloo, H. Pettersson, *Chem. Rev.*, **2010**, *110*, 6595-6663.

20 F. Odobel, L. Le Pleux, Y. Pellegrin, E. Blart, *Acc. Chem. Res.*, **2010**, *43*, 1063-1071.

21 S. Günes, H. Neugebauer, N. S. Sariciftci, *Chem. Rev.*, **2007,** *107*, 1324-1338.

22 T. M. Clarke, J. R. Durrant, *Chem. Rev.*, **2010,** *110,* 6736-6767

23 B. Ke, *Photosynthesis: Photobiochemistry and Photobiophysics*; **2001**; Vol. 10. Kluwer Academic.

24 (a) J. Barber, *Chem. Soc. Rev.*, **2009**, *38*, 185-196; (b) Y. Umena, K. Kawakami, J.-R. Shen, N. Kamiya, *Nature*, **2011**, *4*, 55-60; (c) A. Grundmeier, H. Dau, *Biophys. Biochim. Acta*, **2012**, *1817*, 88-105.

25 B. Loll, J. Kern, W. Saenger, A. Zouni, J. Biesiadka, *Nature*, **2005**, *438*, 1040-1044.

26 (a) R. A. Marcus, *Ann. Rev. Phys. Chem.*, **1964**, *15*, 155-196; (b) P. Siders, R. A. Marcus, *J. Am. Chem. Soc.*, **1981**, *103*, 741-748; (c) N. Sutin, *Prog.Inorg. Chem.*, **1983**, *30*, 441-498; (d) R. A. Marcus, N. Sutin, *Biochim. Biophys. Acta*, **1985**, *811*, 265-322.

27 B. Kok, B. Forbush, M. McGloin, *Photochem. Photobiol.*, **1970**, 11, 457-475.

28 (a) T. Förster, *Ann. Phys.*, **1948**, *2*, 55-75; (b) T. Förster, *Discuss. Faraday Soc.*, **1959**, *27*, 7-17.

29 (a) D. L. Dexter, *J. Chem. Phys.*, **1953**, *21*, 836-850; (b) D. L. Dexter, J. H. Schulman, *J. Chem. Phys.*, **1954**, *22*, 1063-1070.

30 G. D. Scholes, *Annu. Rev. Phys. Chem.*, **2003**, 54, 57-87.

31 P. D. Frischmann, K. Mahata, F. Wurthner, *Chem. Soc. Rev.*, **2013**, *42*, 1847-1870.

32 (a) M. D. Newton, *Chem. Rev.*, **1991**, *91*, 767-792; (b) M. R. Wasielewski, *Chem. Rev.*, **1992**, *92*, 435-461; (c) K. D. Jordan, M. N. Paddon-Row, *Chem. Rev.*, **1992**, 92, 395-410; (d) P. F. Barbara, T. J. Meyer, M. A. Ratner, *J. Phys. Chem.*, **1996,** *100,* 13148-13168; (e) D. Gust, T. A. Moore, A. L. Moore, *Acc. Chem. Res.*, **2001**, *34*, 40-48; (f) S. Fukuzumi, *Bull. Chem. Soc. Jpn.* **2006**, *79*, 177-195; (g) B. Albinsson, J. Mårtensson, *J. Photochem. Photobiol. C*, **2008**, *9*, 138-155. (h) S. Wenger, *Acc. Chem. Res.*, **2011**, *44*, 22-35; (i) A. Arrigo, A. Santoro, M. T. Indelli, M. Natali, F. Scandola, S. Campagna, *Phys. Chem. Chem. Phys.*, **2014**, *16*, 818-826; (l) M. Natali, S. Campagna, F. Scandola, *Chem. Soc. Rev.*, **2014**, DOI:10.1039/c3cs60463b.

33 A. Sartorel, M. Bonchio, S. Campagna, F. Scandola, *Chem. Soc. Rev.*, **2013**, *42*, 2262-2280.

34 (a) J. L. Fillol, Z. Codolá, I. Garcia-Bosch, L. Gòmez, J. J. Pla, M. Costas, *Nat. Chem.*, **2011**, *3*, 807-813; (b) Z. Codolà, I. Garcia-Bosch, F. Acuna-Parés, I. Prat, J. M. Luis, M. Costas, J. L. Fillol, *Chem. Eur. J.*, **2013**, *19*, 8042-8047.

35 (a) M. T. Zhang, Z. Chen, P. Kang, T. J. Meyer, *J. Am. Chem. Soc.*, **2013**, *135*, 2048-2051; (b) Z. Chen, T. J. Meyer, *Angew. Chem., Int. Ed.*, **2013**, *52*, 700-703; (c) T. Zhang, C. Wang, S. Liu, J.-L. Wang, T. Liu, *J. Am. Chem. Soc.*, **2014**, *136*, 273-281.

36 (a) L. Duan, Y. Xu, M. Gorlov, L. Tong, S. Andersson, L. Sun, *Chem. Eur. J.*, **2010**, *16*, 4659-4668; (b) L. Wang, L. Duan, B. Stewart, M. Pu, J. Liu, T. Privalov, L. Sun, *J. Am. Chem. Soc.*, **2012**, *134*, 18868-18880; (c) L. Duan, F. Bozoglian, S. Mandal, B. Stewart, T. Privalov, A. Llobet, L. Sun, *Nat. Chem.*, **2012**, *4*, 418-423; (d) Y. Gao, Y. Ding, J. Liu, L. Wang, Z. Lu, L. Li, L. Sun, *J. Am. Chem. Soc.*, **2013**, *135*, 4219-4222.

37 (a) S. W. Gersten, G. J. Samuels, T. J. Meyer, *J. Am. Chem. Soc.*, **1982**, *104*, 4029-4030; (b) T. J. Meyer, M. H. V. Huynh, H. H. Thorp, *Angew. Chem. Int. Ed.*, **2007**, *46*, 5284-5304; (c) F. Liu, J. J. Concepcion, J. W. Jurss, T. Cardolaccia, J. L. Templeton, T. J. Meyer, *Inorg. Chem.*, **2008**, *47*, 1727-1752; (d) J. W. Jurss, J. J. Concepcion, M. R. Norris, J. L. Templeton, T. J. Meyer, *Inorg. Chem.*, **2010**, *49*, 3980-3982; (e) W. Song, C. R. K. Glasson, H. Luo, K. Hanson, M. K. Brennaman, J. J. Concepcion, T. J. Meyer, *J. Phys. Chem. Lett.*, **2011**, *2*, 1808-1813; (f) M. R. Norris, J. J. Concepcion, Z. Fang, G. L. Templeton, T. J. Meyer, *Angew. Chem., Int. Ed.*, **2013**, *52*, 13580-13583.

38 (a) N. D. McDaniel, M. J. Coughlin, L. L. Tinker, S. Bernhard, *J. Am. Chem. Soc.*, **2008**, *130*, 210-217; (b) W. C. Ellis, N. D. McDaniel, S. Bernhard, T. J. Collins, *J. Am. Chem. Soc.*, **2010**, *132*, 10990-19991.

39 D. J. Wasylenko, R. D. Palmer, C. P. Berlinguette, *Chem. Commun.*, **2013**, *49*, 218-227.

40 (a) X. Li, M. Wang, S. Zhang, J. Pan, Y. Na, J. Liu, B. Åkermark, L. Sun, *J. Phys. Chem. B*, **2008**, *112*, 8198-8202; (b) D. Streich, Y. Astuti, M. Orlandi, L. Schwartz, R. Lomoth, L. Hammarström, S. Ott, *Chem. Eur. J.*, **2010**, *16*, 60-63; (c) A. P. S. Samuel, D. T. Co, C. L. Stern, M. R. Wasielewski, *J. Am. Chem. Soc.*, **2010**, *132*, 8813-8815; (d) T. Yu, Y. Zeng, J. Chen, Y.-Y. Li, G. Yang, Y. Li, *Angew. Chem., Int. Ed.*, **2013**, *52*, 5631-5635; (e) F. Wang, W. J. Liang, J. X. Jian, C. B. Li, B. Chen, C. H. Tung, L. Z. Wu, *Angew. Chem., Int. Ed.*, **2013**, *52*, 8134-8138.

41 W. T. Eckenhoff, W. R. McNamara, P. Du, R. Eisenberg, *Biochim. Biophys. Acta*, **2013**, *1827*, 958-973.

42 (a) M. L. Helm, M. P. Stewart, R. M. Bullock, M. R. DuBois, D. L. DuBois, *Science*, **2011**, *333*, 863-866; (b) M. P. McLaughlin, T. M. McCormick, R. Esienberg, P. L. Holland, *Chem. Commun.*, **2011**, *47*, 7989-7991; (c) M. Gross, A. Reynal, J. R. Durrant, E. Reisner, *J. Am. Chem. Soc.*, **2014**, *136*, 356-366.

43 (a) Z. Han, W. R. McNamara, M.-S. Eum, P. L. Holland, R. Eisenberg, *Angew. Chem., Int. Ed.*, **2012**, *51*, 1667-1670; (b) Z. Han, L. Shen, W. W. Brennessel, P. L. Holland, R. Eisenberg, *J. Am. Chem. Soc.*, **2013**, *135*, 14659-14669.

44 (a) H. I. Karunadasa, C. J. Chang, J. R. Long, *Nature*, **2010**, *464*, 1329-1333; (b) H. I. Karunadasa, E. Montalvo, Y. Sun, M. Majda, J. R. Long, C. J. Chang, *Science*, **2012**, *335*, 698-702.

45 (a) H. Ozawa, M. Haga, K. Sakai, *J. Am. Chem. Soc.*, **2006**, *128*, 4926-4927; (b) H. Ozawa, K. Sakai, *Chem. Commun.*, **2011**, *47*, 2227-2242.

46 S. Rau, B. Schäfer, D. Gleich, E. Anders, M. Rudolph, M. Friedrich, H. Görls, W. Henry, J. G. Vos, *Angew. Chem., Int. Ed.*, **2006**, *45*, 6215-6218.

47 (a) A. F. Heyduk, D. G. Nocera, *Science*, **2001**, *293*, 1639-1641; (b) E. D. Cline, S. E. Adamson, S. Bernhard, *Inorg. Chem.*, **2008**, *47*, 10378-10388; (c) T. Stoll, M. Gennari, I. Serrano, J. Fortage, J. Chauvin, F. Odobel, M. Rebarz, O. Poizat, M. Sliwa, A. Deronzier, M.-N. Collomb, *Chem. Eur. J.*, **2013**, *19*, 782-792; (d) T. Stoll, M. Gennari, J. Fortage, C. E. Castillo, M. Rebarz, M. Sliwa, O. Poizat, F. Odobel, A. Deronzier, M.-N. Collomb, *Angew. Chem., Int. Ed.*, **2014**, *53*, 1654-1658.

48 J.-M. Lehn, *Supramolecular Chemistry*, **1995**, Wiley-VCH.

49 V. Balzani, F. Scandola, *Supramolecular Photochemistry*, **1991**, Ellis Horwood.

50 J. R. Lakowicz, *Principles of Fluorescence Spectroscopy*, **2006**, Springer.

51 C. Chiorboli, M. A. J. Rodgers, F. Scandola, *J. Am. Chem. Soc.*, **2003**, *125*, 483-491.

52 M. Natali, M. Orlandi, S. Berardi, S. Campagna, M. Bonchio, A. Sartorel, F. Scandola, *Inorg. Chem.*, **2012**, *51*, 7324-7331.

53 M. Natali, S. Berardi, A. Sartorel, M. Bonchio, S. Campagna, F. Scandola, *Chem. Commun.*, **2012**, *48*, 8808-8810.

54 (a) R. Eisenberg, H. B. Gray, *Inorg. Chem*., **2008**, *47*, 1697-1699; (b) C. Herrero, B. Lassalle-Kaisea, W. Leibl, A. W. Rutherford, A. Aukauloo, *Coord. Chem. Rev*., **2008**, *252*, 456-468; (c) X. Sala, I. Romero, M. Rodriguez, L. Escriche, A. Llobet, *Angew. Chem. Int. Ed*., **2009**, *48*, 2-13; (d) W. J. Youngblood, S.-H. A. Lee, K. Maeda, T. E. Mallouk, *Acc. Chem. Res*., **2009**, *42*, 1966-1973.

55 (a) J. P. McEvoy, G. W. Brudvig, *Chem. Rev.*, **2006**, *106*, 4455-4483; (b) M. H. V. Huynh, T. J. Meyer, *Chem. Rev.*, **2007**, *107*, 5004-5064; (c) D. Gust, T. A. Moore, A. L. Moore, *Acc. Chem. Res.*, **2009**, *42*, 1890-1898.

56 (a) J.-M Lehn, J.-P. Sauvage, *Nouv. J. Chem.*, **1977**, *1*, 449-451; (b) J.-M. Lehn, J.-P. Sauvage, R. Ziessel, *Nouv. J. Chem.*, **1979**, *3*, 423-427; (c) J. Kiwi, M. Graetzel, *Angew.*

Chem., Int. Ed. Engl., **1978**, *17*, 860-861; (d) A. Harriman, G. Porter, P. Walters, *J. Chem. Soc. Faraday Trans. 2*, **1981**, *77*, 2373-2383.

57 (a) F. Jiao, H. Frei, *Energy Environ. Sci.*, **2010**, *3*, 1018-1027; (b) Y. Gorlin, T. F. Jamarillo, *J. Am. Chem. Soc.*, **2010**, *132*, 13612-13614.

58 A. Harriman, M. Richoux, P. A. Christensen, S. Moseri, P. Neta, *J. Chem. Soc. Faraday Trans. 1*, **1987**, *83*, 3001-3014.

59 (a) M. Hara, C. C. Waraksa, J. T. Lean, B. A. Lewis, T. E. Mallouk, *J. Phys. Chem. A*, **2000**, *104*, 5275-5280; (b) N. D. Morris, M. Suzuki, T. E. Mallouk, *J. Phys. Chem. A*, **2004**, *108*, 9115-9119; (c) P. G. Hoertz, Y. I. Kim, W. J. Youngblood, T. E. Mallouk, *J. Phys. Chem. B* **2007**, *111*, 6845-6856; (d) W. J. Youngblood, S.-H. A. Lee, Y. Bobayashi, E. A. Hernandez-Pagan, P. G. Hoertz, T. A. Moore, A. L. Moore, D. Gust, T. E. Mallouk, *J. Am. Chem. Soc.*, **2009**, *131*, 926-929; (e) Y. Zhao, J. R. Swierk, J. D. Megiatto Jr, B. Sherman, W. J. Youngblood, D. Qin, D. M. Lentz, A. L. Moore, T. A. Moore, D. Gust, T. E. Mallouk, *Proc. Nat. Acad. Sci. U.S.A.*, **2012**, *109*, 15612-15616.

60 D. Hong, Y. Yamada, T. Nagatomi, Y. Takai, S. Fukuzumi, *J. Am. Chem. Soc.*, **2012**, *134*, 19572-19575.

61 (a) M. W. Kanan, D. G. Nocera, *Science*, **2008**, *321*, 1072-1075; (b) Y. Surendranath, M. Dinca, D. G. Nocera, *J. Am. Chem. Soc.*, **2009**, *131*, 2615-2620; (c) M. Dinca, Y. Surendranath, D. G. Nocera, *Proc. Natl. Acad. Sci. U.S.A.*, **2010**, *107*, 10337-10341.

62 G. Zhu, E. N. Glass, C. Zhao, H. Lv, J. W. Vickers, Y. V. Geletii, D. G. Musaev, J. Song, C. L. Hill, *Dalton Trans.*, **2012**, *41*, 13043-13049.

63 (a) A. Sartorel, M. Carraro, G. Scorrano, R. De Zorzi, S. Geremia, N. D. McDaniel, S. Bernhard, M. Bonchio, *J. Am. Chem. Soc.*, **2008**, *130*, 5006-5007; (b) A. Sartorel, P. Mirò, E. Salvadori, S. Romain, M. Carraro, G. Scorrano, M. Di Valentin, A. Llobet, C. Bo, M. Bonchio, *J. Am. Chem. Soc.*, **2009**, *131*, 16051-16053.

64 (a) Y. V. Geletii, B. Botar, P. Köegerler, D. A. Hillesheim, D. G. Musaev, C. L. Hill, *Angew. Chem. Int. Ed.*, **2008**, *47*, 3896-3899; (b) Y. V. Geletii, Z. Huang, Y. Hou, D. G. Musaev, T. Lian, C. L. Hill, *J. Am. Chem. Soc.*, **2009**, 131, 7522-7523; (c) Y. V. Geletii, C. Besson, Y. Hou, Q. Yin, D. G. Musaev, D. Quiñonero, R. Cao, K. I. Hardcastle, A. Proust, P. Kögerler, C. L. Hill, *J. Am. Chem. Soc.*, **2009**, *131*, 17360-17370.

65 (a) G. La Ganga, F. Puntoriero, S. Campagna, I. Bazzan, S. Berardi, M. Bonchio, A. Sartorel, M. Natali, F. Scandola, *Faraday Discuss.*, **2012**, *155*, 177-190; (b) N. S. McCool, D. M. Robinson, J. E. Sheats, G. C. Dismukes, *J. Am. Chem. Soc.*, **2011**, *133*, 11446-11449; (c) S. Berardi, G. La Ganga, M. Natali, I. Bazzan, F. Puntoriero, A.

Sartorel, F. Scandola, S. Campagna, M. Bonchio, *J. Am. Chem. Soc.*, **2012**, *134*, 11104-11107.

66 (a) Q. Yin, J. M. Tan, C. Besson, Y. V. Geletii, D. G. Musaev, A. E. Kuznetsov, Z. Luo, K. I. Hardcastle, C. L. Hill, *Science*, **2010**, *328*, 342-345; (b) Z. Huang, Z. Luo, Y. V. Geletii, J. W. Vickers, Q. Yin, D. Wu, Y. Hou, Y. Ding, J. Song, D. G. Musaev, C. L. Hill, T. Lian, *J. Am. Chem. Soc.*, **2011**, *133*, 2068-2071; (c) J. W. Vickers, H. Lv, G. M. Sumliner, G. Zhu, Z. Luo, D. G. Musaev, Y. V. Geletii, C. L. Hill, *J. Am. Chem. Soc.*, **2013**, *135*, 14110-14118.

67 (a) G. C. Dismukes, R. Brimblecombe, G. A. N. Felton, R. S. Pryadun, J. E. Sheats, L. Spiccia, G. F. Swiegers, *Acc. Chem. Res.*, **2009**, *42*, 1935-1943; (b) R. Brimblecombe, A. Koo, G. C. Dismukes, G. F. Swiegers, L. Spiccia, *J. Am. Chem. Soc.*, **2010**, *132*, 2892-2894.

68 T. J. R. Weakley, H. T. Evans, J. S. Showell, G. F. Tourné, C. M. Tourné, *J. Chem. Soc., Chem. Commun.*, **1973**, 139-140.

69 (a) F. Puntoriero, G. La Ganga, A. Sartorel, M. Carraro, G. Scorrano, M. Bonchio, S. Campagna, *Chem. Commun.*, **2010**, *46*, 4725-4727; (b) F. Puntoriero, A. Sartorel, M. Orlandi, G. La Ganga, S. Serroni, M. Bonchio, F. Scandola, S. Campagna, *Coord. Chem. Rev.*, **2011**, *255*, 2594-2601; (c) M. Carraro, A. Sartorel, F. M. Toma, F. Puntoriero, F. Scandola, S. Campagna, M. Prato, M. Bonchio, *Top. Curr. Chem.*, **2011**, *303*, 120-151.

70 M. Orlandi, R. Argazzi, A. Sartorel, M. Carraro, G. Scorrano, M. Bonchio, F. Scandola, *Chem. Commun.*, **2010**, *46*, 3152-3154.

71 P. K. Ghosh, B. S. Brunschwig, M. H. Chou, C. Creutz, N. Sutin, *J. Am. Chem. Soc.*, **1984**, *106*, 4772-4783.

72 F. M. Toma, A. Sartorel, M. Iurlo, M. Carraro, P. Parisse, C. Maccato, S. Rapino, B. Rodriguez Gonzalez, H. Amenitsch, T. Da Ros, L. Casalis, A. Goldoni, M. Marcaccio, G. Scorrano, G. Scoles, F. Paolucci, M. Prato, M. Bonchio, *Nat. Chem.*, **2010**, *2*, 826-831.

73 F. M. Toma, A. Sartorel, M. Iurlo, M. Carraro, S. Rapino, L. Hoober-Burkhardt, T. Da Ros, M. Marcaccio, G. Scorrano, F. Paolucci, M. Bonchio, M. Prato, *ChemSusChem*, **2011**, *4*, 1447-1451.

74 A. Sartorel, M. Truccolo, S. Berardi, M. Gardan, M. Carraro, F. M. Toma, G. Scorrano, M. Prato, M. Bonchio, *Chem. Commun.*, **2011**, *47*, 1716-1718.

75 M. Quintana, A. Montellano Lòpez, S. Rapino, F. M. Toma, M. Iurlo, M. Carraro, A. Sartorel, C. Maccato, X. Ke, C. Bittencourt, T. Da Ros, G. Van Tendeloo, M. Marcaccio, F. Paolucci, M. Prato, M. Bonchio, *ACS Nano*, **2013**, *7*, 811-817.

76 J. Zhang, S. Guo, Y. Liu. C. Lee, A. M. Bond, Y. Geletii, C. L. Hill, *Energy Environ. Sci.*, **2013**, *6*, 2654-2663.

77 X. Xiang, J. Fielden, W. Rodríguez-Córdoba, Z. Huang, N. Zhang, Z. Luo, D. G. Musaev, T. Lian, C. L. Hill, *J. Phys. Chem. C*, **2013**, *117*, 918-926.

78 K. Kalyanasundaram, *Photochemistry and Photophysics of Polypyridine and Porphyrin Complexes*, Academic Press, London, UK, **1996.**

79 C. Besson, Z. Huang, Y. V. Geletii, S. Lense, K. I. Hardcastle, D. G. Musaev, T. Lian, A. Proust, C. L. Hill, *Chem. Commun.*, **2010**, *46*, 2784-2786.

80 F. Bolletta, A. Juris, M. Maestri, D. Sandrini, *Inorg. Chim. Acta*, **1980**, *44*, L175-L176.

81 J. J. Stracke, R.G. Finke, *J. Am. Chem. Soc*., **2011**, *133*, 14872-14875.

82 R. G. Finke, M. Droege, J. R. Hutchinson, O. Gansow, *J. Am. Chem. Soc.*, **1981**, *103*, 1587-1589.

83 (a) S. Y. Reece, J. A. Hamel, K. Sung, T. D. Jarvi, A. J. Esswein, J. J. H. Pijpers, D. G. Nocera, *Science*, **2011**, *334*, 645-648; (b) D. G. Nocera, *Acc. Chem. Res.*, **2012**, *45*, 767-776.

84 R. Chakrabarty, S. J. Bora, B. K. Das, *Inorg. Chem.*, **2007**, *46*, 9450-9462.

85 J. G. McAlpin, T. A. Stich, C. A. Ohlin, Y. Surendranath, D. G. Nocera, W. H. Casey, R. D. Britt, *J. Am. Chem. Soc.*, **2011**, *133*, 15444-15452.

86 T. A. Stich, J. Krzystek, B. Q. Mercado, J. G. McAlpin, C. A. Ohlin, M. M. Olmstead, W. H. Casey, R. D. Britt, *Polyhedron*, **2013**, *64*, 304-307.

87 (a) V. Y. Shafirovich, N. K. Khannanov, V. V. Strelets, *Nouv. J. Chim.*, **1980**, *4*, 81-84; (b) B. S. Brunschwig, M. H. Chou, C. Creutz, P. K. Ghosh, N. Sutin, *J. Am. Chem. Soc.*, **1983**, *105*, 4832-4833.

88 E. Pizzolato, M. Natali, B. Posocco, A. Montellano Lòpez, I. Bazzan, M. Di Valentin, P. Galloni, V. Conte, M. Bonchio, F. Scandola, A. Sartorel, *Chem.Commun.*, **2013**, *49*, 9941-9943.

89 D. K. Dogutan, R. McGuire Jr., D. G. Nocera, *J. Am. Chem. Soc.*, **2011**, *133*, 9178-9180.

90 (a) D. J. Wasylenko, C. Ganesamoorthy, J. Borau-Garcia, C. P. Berlinguette, *Chem. Commun.*, **2011**, *47*, 4249-4251; (b) D. J. Wasylenko, R. D. Palmer, E. Schott, C. P. Berlinguette, *Chem. Commun.*, **2012**, *48*, 2107-2109; (c) D. J. Wasylenko, H. M.

Tatlock, L. S. Bandhari, J. R. Gardinier, C. P. Berlinguette, *Chem. Sci.*, **2013**, *4*, 734-738.

91 D. Wang, J. T. Groves, *Proc. Natl. Acad. Sci. U.S.A.*, **2013**, *110*, 15579-15584.

92 T. Nakazono, A. R. Parent, K. Sakai, *Chem. Commun.*, **2013**, *49*, 6325-6327.

93 J. J. Concepcion, J. W. Jurss, J. L. Templeton, T. J. Meyer, *J. Am. Chem. Soc.*, **2008**, *130*, 16462-16463.

94 D.A. Safin, K. Robeyns, Y. Garcia, *RSC Advances*, **2012**, *2*, 11379-11388.

95 R. H. Bailes, M. Calvin, *J. Am. Chem. Soc.*, **1947**, *69*,1886-1893; (b) R. Deiasi, S. L. Holt, B. Post, *Inorg. Chem.*, **1971**, *10*, 1498-1500.

96 (a) Y. Pellegrin, K. E. Berg, G. Blondin, E. Anxolabéhère-Malart, W. Leibl, A. Aukauloo, *Eur. J. Inorg. Chem.*, **2003**, 1900-1910; (b) Y. Pellegrin, A. Quaranta, P. Dorlet, M. F. Charlot, W. Liebl, A. Aukauloo, *Chem. Eur. J.*, **2005**, *11*, 3698-3710.

97 (a) B. Bennett, R. C. Holz, *J. Am. Chem. Soc.*, **1997**, *119*, 1923-1933; (b) E. Vinck, D. M. Murphy, I. A. Fallis, S. Van Doorslaer, *Appl. Magn. Res.*, **2010**, *37*, 289-303.

98 E. Vinck, E. Carter, D. M. Murphy, S. Van Doorslaer, *Inorg. Chem.*, **2012**, *51*, 8014-8024.

99 A. A. Isse, A. Gennaro, E. Vianello, C. Floriani, *J. Mol. Catal.*, **1991**, *70*, 197-208.

100 S. Campagna, F. Puntoriero, F. Nastasi, G. Bergamini, V. Balzani, *Top. Curr. Chem.*, **2007**, *280*, 117-214.

101 L. A. Kelly, M. A. J. Rodgers, *J. Phys. Chem.*, **1994**, *98*, 6377-6385.

102 (a) S. H. Alarcón, D. Pagani, J. Bacigalupo, A. C. Olivieri, *J. Mol. Struct.*, **1999**, *475*, 233-240; (b) P. M. Dominiak, E. Grech, G. Barr, S. Teat, P. Mallinson, K. Woźniak, *Chem. Eur. J.*, **2003**, *9*, 963-970.

103 A. A. Khandar, B. Shaabani, F. Belaj, A. Bakhtiari, *Inorg. Chim. Acta*, **2007**, *360*, 3255-3264.

104 D. Hong, J. Jung, Y. Yamada, T. Suenobu, Y.-M Lee, W. Nam, S. Fukuzumi, *Energy Environ. Sci.*, **2012**, *5*, 7606-7616.

105 M. Natali, R. Argazzi, C. Chiorboli, E. Iengo, F. Scandola, *Chem. Eur. J.*, **2013**, *19*, 9261-9271.

106 M. Natali, M. Orlandi, C. Chiorboli, E. Iengo, V. Bertolasi, F. Scandola, *Photochem. Photobio. Sci.*, **2013**, *12*, 1749-1753.

107 (a) W. R. McNamara, Z. Han, P. J. Alperin, W. W. Brennessel, P. L. Holland, R. Eisenberg, *J. Am. Chem. Soc.*, **2011**, *133*, 15368-15371; (b) W. R. McNamara, Z. Han,

C.-J. Yin, W. W. Brennessel, P. L. Holland, R. Eisenberg, *Proc. Natl. Acad. Sci. U.S.A.*, **2012**, *109*, 15594-15600.

108 (a) Y. Sun, J. P. Bigi, N. A. Piro, M. L. Tang, J. R. Long, C. J. Chang, *J. Am. Chem. Soc.*, **2011**, *133*, 9212-9215; (b) Y. Sun, J. Sun, J. R. Long, P. Yang, C. J. Chang, *Chem. Sci.*, **2013**, *4*, 118-125; (c) W. M. Singh, T. Baine, S. Kudo, S. Tian, X. A. N. Ma, H. Zhou, N. J. DeYonker, T. C. Pham, J. C. Bollinger, D. L. Baker, B. Yan, C. E. Webster and X. Zhao, *Angew. Chem., Int. Ed.*, **2012**, *51*, 5941-5944; (d) B. Shan, T. Baine, X. A. N. Ma, X. Zhao, R. H. Schmehl, *Inorg. Chem.*, **2013**, *52*, 4853-4859.

109 (a) F. Gärtner, B. Sundararaju, A. E. Surkus, A. Boddien, B. Loges, H. Junge, P. H. Dixneuf, M. Beller, *Angew. Chem. Int. Ed.*, **2009**, *48*, 9962-9965; (b) F. Gärtner, D. Cozzula, S. Losse, A. Boddien, G. Anilkumar, H. Junge, T. Schulz, N. Marquet, A. Spannenberg, S. Gladiali, M. Beller, *Chem. Eur. J.*, **2011**, *17*, 6998-7006; (c) S.-P. Luo, E. Mejìa, A. Friedrich, A. Pazidis, H. Junge, A. E. Surkus, R. Jackstell, S. Denurra, S. Gladiali, S. Lochbrunner, M. Beller, *Angew. Chem., Int. Ed.*, **2013**, *52*, 419-423.

110 (a) M. Razavet, V. Artero, M. Fontecave, *Inorg. Chem.*, **2005**, *44*, 4786-4795; (b) C. Baffert, V. Artero, M. Fontecave, *Inorg. Chem.*, **2007**, *46*, 1817-1824; (c) X. Hu, B. S. Brunschwig, J. C. Peters, *J. Am. Chem. Soc.*, **2007**, *129*, 8988-8998.

111 J. Hawecker, J.-M. Lehn, R. Ziessel, *Nouv. J. Chim.*, **1983**, *7*, 271-277.

112 P. Du, K. Knowles, R. Eisenberg, *J. Am. Chem. Soc.*, **2008**, *130*, 12576-12577.

113 X. Wang, S. Goeb, Z. Ji, N. A. Pogulaichenko, F. N. Castellano, *Inorg. Chem.*, **2011**, *50*, 705-707.

114 (a) B. Probst, C. Kolano, P. Hamm, R. Alberto, *Inorg. Chem.*, **2009**, *48*, 1836-1843; (b) B. Probst, A. Rodenberg, M. Guttentag, P. Hamm, R. Alberto, *Inorg. Chem.*, **2010**, *49*, 6453-6460; (c) B. Probst, M. Guttentag, A. Rodenberg, P. Hamm, R. Alberto, *Inorg. Chem.*, **2011**, *50*, 3404-3412; (d) M. Guttentag, A. Rodenberg, R. Kopelent, B. Probst, C. Buchwalder, M. Brandstätter, P. Hamm, R. Alberto, *Eur. J. Inorg. Chem.*, **2012**, 59-64.

115 (a) F. Lakadamyali, E. Reisner, *Chem. Commun.*, **2011**, *47*, 11695-1697; (b) F. Lakadamyali, A. Reynal, M. Kato, J. R. Durrant, E. Reisner, *Chem. Eur. J.*, **2012**, *18*, 15464-15475; (c) F. Lakadamyali, M. Kato, N. M. Muresan, E. Reisner, *Angew. Chem., Int. Ed.*, **2012**, *124*, 9515-9518.

116 (a) T. Lazarides, T. McCormick, P. Du, G. Luo, B. Lindley, R. Eisenberg, *J. Am. Chem. Soc.*, **2009**, *131*, 9192-9194; (b) T. McCormick, B. D. Calitree, A. Orchard, N. D. Kraut, F. V. Bright, M. R. Detty, R. Eisenberg, *J. Am. Chem. Soc.*, **2010**, *132*,

15480-15483; (c) T. McCormick, Z. Han, D. J. Weinberg, W. W. Brennessel, P. L. Holland, R. Eisenberg, *Inorg. Chem.*, **2011**, *50*, 10660-10666.

117 P. Zhang, M. Wang, J. Dong, X. Li, F. Wang, L. Wu, L. Sun, *J. Phys. Chem. C*, **2010**, *114*, 15868-15874.

118 (a) J. L. Dempsey, B. S. Brunschwig, J. R. Winkler, H. B. Gray, *Acc. Chem. Res.*, **2009**, *42*, 1995-2004; (b) J. L. Dempsey, J. R. Winkler, H. B. Gray, *J. Am. Chem. Soc.*, **2010**, *132*, 1060-1065; (c) J. L. Dempsey, J. R. Winkler, H. B. Gray, *J. Am. Chem. Soc.*, **2010**, *132*, 16774-16776; (d) C. N. Valdez, J. L. Dempsey, B. S. Brunschwig, J. R. Winkler, H. B. Gray, *Proc. Natl. Acad. Sci. U.S.A.*, **2012**, 109, 15589-15593.

119 (a) A. Fihri, V. Artero, M. Razavet, C. Baffert, W. Leibl, M. Fontecave, *Angew. Chem., Int. Ed.*, **2008**, *47*, 564-567; (b) A. Fihri, V. Artero, A. Pereira, M. Fontecave, *Dalton Trans.*, **2008**, 5567-5569.

120 C. Li, M. Wang, J. Pang, P. Zhang, R. Zhang, L. Sun, *J. Organomet. Chem.*, **2009**, *694*, 2814-2819.

121 (a) P. Zhang, M. Wang, C. Li, X. Li, J. Dong, L. Sun, *Chem. Commun.*, **2010**, *46*, 8806-8808; (b) P. Zhang, M. Wang, X. Q. Li, H. G. Cui, J. F. Dong, L. Sun, *Sci. China: Chem.*, **2012**, *55*, 1274-1282.

122 K. Peutinger, T. Lazarides, D. Dafnomili, G. Charalambidis, G. Landrou, A. Kahnt, R. P. Sabatini, D. W. McCamant, D. T. Gryko, A. G. Coutsolelos, D. M. Guldi, *J. Phys. Chem. C*, **2013**, *117*, 1647-1655.

123 K. L. Mulfort, D. M. Tiede, *J. Phys. Chem. B*, **2010**, *114*, 14572-14581.

124 J. Bartelmess, W. W. Weare, R. D. Sommer, *Dalton Trans.*, **2013**, *42*, 14883-14891.

125 (a) G. J. E. Davidson, L. H. Tong, P. R. Raithby, J. K. M. Sanders, *Chem. Commun.*, **2006**, 3087-3089; (b) G. A. Metselaar, J. K. M. Sanders, J. de Mendoza, *Dalton Trans.*, **2008**, 588-590; (c) G. J. E. Davidson, L. A. Lane, P. R. Raithby, J. E. Warren, C. V. Robinson, J. K. M. Sanders, *Inorg. Chem.*, **2008**, *47*, 8721-8726.

126 E. Iengo, D. G. Pantos, J. K. M. Sanders, M. Orlandi, C. Chiorboli, S. Fracasso, F. Scandola, *Chem. Sci.*, **2011**, *2*, 676-685.

127 E. B. Fleischer, A. M. Shacter, *Inorg. Chem.*, **1991**, *30*, 3763-3769.

128 G. N. Schrauzer, *Inorg. Synth.*, **1968**, *11*, 61-70.

129 N. G. Connelly, W. E. Geiger, *Chem. Rev.*, **1996**, *96*, 877-910.

130 (a) D. Rehm, A. Weller, *Ber. Bunsen-Ges. Phys. Chem.*, **1969**, *73*, 834-839; (b) A. Weller, *Z. Phys. Chem.*, **1982**, *133*, 93-98.

131 S. P. Perone, W. J. Kretlow, *Anal. Chem.*, **1966**, *38*, 1760-1763.

132 (a) Y. Harel, J. Manassen, *J. Am. Chem. Soc.*, **1977**, *99*, 5817-5818; (b) C. D. Windle, M. V. Câmpian, A.-K. Duhme-Klair, E. A. Gibson, R. N. Perutz, J. Schneider, *Chem. Commun.*, **2012**, *48*, 8189-8191.

133 G. L. Closs, E. L. Closs, *J. Am. Chem. Soc.*, **1963**, *85*, 818-819.

134 J. Pawlik, L. Gherghel, S. Karabunarliev, M. Baumgarten, *Chem. Phys*., **1997**, *221*, 121-133.

135 O. Pantani, E. Anxolabéhère-Mallart, A. Aukauloo, P. Millet, *Electrochem. Commun.*, **2007**, *9*, 54-58.

136 H. Ma, C. Wan, A. H. Zewail, *Proc. Natl. Acad. Sci. U.S.A.*, **2008**, *105*, 12754-12757.

137 B. H. J. Bielski, D. A. Comstock, R. A. Bowen, *J. Am. Chem. Soc.*, **1971**, *93*, 5624-5629.

138 C. Creutz, N. Sutin, B. S. Brunschwig, *J. Am. Chem. Soc.*, **1979**, *101*, 1298-1300.

139 P. Du, R. Eisenberg, *Energy Environ. Sci.*, **2012**, *5*, 6012-6021.

140 J. Manono, P. A. Marzilli, F. R. Fronczek, L. G. Marzilli, *Inorg. Chem.*, **2009**, *48*, 5626-5635.

141 E. G. Azenha, A. C. Serra, M. Pineiro, M. M. Pereira, J. S. de Melo, L. G. Arnaut, S. J. Formosinho, A.M.d'A. Rocha Gonsalves, *Chem. Phys.*, **2002**, *208*, 177-190.

142 E. A. Juban, A. L. Smeigh, J. E. Monat, J. K. McCusker, *Coord. Chem. Rev.*, **2006**, *250*, 1783-1791.

143 J. M. Dixon, M. Taniguchi, J. S. Lindsey, *Photochem. Photobiol.*, **2005**, *81*, 212-213.

144 (a) M. T. Indelli, C. Chiorboli, M. Ghirotti, M. Orlandi, F. Scandola, H. J. Kim, H.-J. Kim, *J. Phys. Chem. B*, **2010**, *114*, 14273-14282; (b) M. T. Indelli, C. Chiorboli, F. Scandola, E. Iengo, P. Osswald, F. Würthner, *J. Phys. Chem. B*, **2010**, *114*, 14495-14504.

145 M. Natali, A. Luisa, E. Iengo, F. Scandola, *Chem. Commun.*, **2014**, *50*, 1842-1844.

146 G. M. Brown, B. S. Brunschwig, C. Creutz, J. F. Endicott, N. Sutin, *J. Am. Chem. Soc.*, **1979**, *101*, 1298-1300.

147 (a) S. Losse, J. G. Vos, S. Rau, *Coord. Chem. Rev*., **2010**, *254*, 2492-2504; (b) V. Artero, M. Chavarot-Kerlidou, M. Fontecave, *Angew. Chem., Int. Ed.*, **2011**, *50*, 7238-7266.

148 R.M. Kellett, T.G. Spiro, *Inorg. Chem.*, **1985**, *24*, 2373-2377.

149 R.M. Kellett, T.G. Spiro, *Inorg. Chem.*, **1985**, *24*, 2378-2382.

150 T. Dhanasekaran, J. Grodkowski, P. Neta, P. Hambright, E. Fujita, *J. Phys. Chem. A*, **1999**, *103*, 7742-7748.

151 C. H. Lee, D. K. Dogutan, D. G. Nocera, *J. Am. Chem. Soc*., **2011**, *133*, 8775-8777.

152 M. Perrée-Fauvet, C. Verchère-Béaur, E. Tarnaud, G. Anneheim- Herbelin, N. Bône, A. Gaudemer, *Tetrahedron*, **1996**, *52*, 13569-13588.

153 B. Steiger, C. Shi, F. C. Anson, *Inorg. Chem.*, **1993**, *32*, 2107-2113.

154 J. T. Muckerman, E. Fujita, *Chem. Commun.*, **2011**, *47*, 12456-12458.

155 L. Ravotto, R. Mazzaro, M. Natali, L. Ortolani, V. Morandi, P. Ceroni, G. Bergamini, *J. Phys. Chem. Lett.*, **2014**, *5*, 798-803.

156 S. Campagna, P. Ceroni, F. Puntoriero, *Designing Dendrimers*, ed. John Wiley & Sons: Hoboken, USA, **2012**.

157 (a) G. D. Storrier, K. Takada, H. D. Abruña, *Langmuir*, **1999**, *15*, 872-884; (b) S. Glazier, J. A. Barron, P. L. Houston, H. D. Abruña, *J. Phys. Chem. B*, **2002**, *106*, 9993-10003.

158 N. M. Markovic, B. N. Grgur, P. N. Ross, *J. Phys. Chem. B*, **1997**, *101*, 5405-5413.

159 T. Yu, W. Wang, J. Chen, Y. Zeng, Y. Li, G. Yang, Y. Li, *J. Phys. Chem. C*, **2012**, *116*, 10516-10521.

160 T. Yu, Y. Zeng, J. Chen, Y.-Y. Li, G. Yang, Y. Li, *Angew. Chem., Int. Ed.*, **2013**, *52*, 5631-5635.

161 L. M. Bronstein, Z. B. Shifrina, *Chem. Rev*., **2011**, *111*, 5301-5344.

162 R. M. Crooks, M. Zhao, L. Sun, V. Chechik, L. K. Yeung, *Acc. Chem Res.*, **2001**, *34*, 181-190.

163 P.-A. Brugger, P. Cuendet, M. Grätzel, *J. Am. Chem. Soc.*, **1981**, *103*, 2923-2927.

164 M. Natali, M. Ravaglia, F. Scandola, J. Boixel, Y. Pellegrin, E. Blart, F. Odobel, *J. Phys. Chem. C*, **2013**, *117*, 19334-19345.

165 (a) A. Osuka, R. P. Zhang, K. Maruyama, T. Ohno, K. Nozaki, *Bull. Chem. Soc. Jpn*., **1993**, *66*, 3773-3782; (b) H. Shiratori, T. Ohno, K. Nozaki, I. Yamazaki, Y. Nishimura, A. Osuka, *J. Org. Chem*., **2000**, *65*, 8747-8757.

166 (a) Y. Mori, Y. Sakaguchi, H. Hayashi, *J. Phys. Chem. A*, **2002,** *106*, 4453-4467; (b) H. Imahori, H. Yamada, D. M. Guldi, Y. Endo, A. Shimomura, S. Kundu, K. Yamada, T. Okada, Y. Sakata, S. Fukuzumi, *Angew. Chem., Int. Ed*., **2002**, *41*, 2344-2347; (c) K. Okamoto, Y. Mori, H. Yamada, H. Imahori, S. Fukuzumi, *Chem. Eur. J*., **2004**, *10*, 474-483; (d) K. Saito, Y. Kashiwagi, K. Ohkubo, S. Fukuzumi, *J. Porphyrins Phthalocyanines*, **2006**, *10*, 1371-1379; (e) S. J. Langford, M. J. Latter, C. P.

Woodward, *Photochem. Photobiol*., **2006**, *82*, 1530-1540; (f) K. P. Ghiggino, J. A. Hutchison, S. J. Langford, M. J. Latter, M. A.-P. Lee, M. Takezaki, *Aust. J. Chem*., **2006**, *59*, 179-185; (g) S. V. Bhosale, C. H. Jani, S. J. Langford, *Chem. Soc. Rev.*, **2008**, *37*, 331-342; (h) A. G. Moiseev, P. K. Poddutoori, A. Van der Est, *Appl. Magn. Reson*., **2012**, *42*, 41-55.

167 P. K. Poddutoori, N. Zarrabi, A. G. Moiseev, R. Gumbau-Brisa, S. Vassiliev, A. Van der Est, *Chem. Eur. J.*, **2013**, *19*, 3148-3161.

168 R. T. Hayes, M. R. Wasielewski, D. Gosztola, *J. Am. Chem. Soc.*, **2000,** *122*, 5563-5567.

169 N. P. Redmore, I. V. Rubtsov, M. J. Therien, *J. Am. Chem. Soc*., **2003**, *125*, 8769-8778.

170 F. Wurthner, S. Ahmed, C. Thalacker, T. Debaerdemaeker, *Chem. Eur. J*., **2002**, *8*, 4742-4750.

171 (a) V. V. Rostovtsev, L. G. Green, V. V. Fokin, K. B. Sharpless, *Angew. Chem., Int. Ed*., **2002**, *41*, 2596-2599; (b) C. W. Tornøe, C. Christensen, M. Meldal, *J. Org. Chem*., **2002**, *67*, 3057-3064.

172 (a) A. Harriman, K. J. Elliott, M. A. Alamiry, L. Le Pleux, M. Séerac, Y. Pellegrin, E. Blart, C. Fosse, C. Cannizzo, C. R. Mayer, F. Odobel, *J. Phys. Chem. C*, **2009**, *113*, 5834-5842 ; (b) F. Odobel, M. Séverac, Y. Pellegrin, E. Blart, C. Fosse, C. Cannizzo, C. R. Mayer, K. J. Elliott, A. Harriman, *Chem. Eur. J*., **2009**, *15*, 3130-3138; (c) L. Le Pleux, Y. Pellegrin, E. Blart, F. Odobel, A. Harriman, *J. Phys. Chem. A*, **2011**, *115*, 5069-5080.

173 (a) M. A. Fazio, O. P. Lee, D. I. Schuster, *Org. Lett.*, **2008***, 10*, 4979-4982; (b) G. De Miguel, M. Wielopolski, D. I. Schuster, M. A. Fazio, O. P. Lee, C. K. Haley, A. L. Ortiz, L. Echegoyen, T. Clark, D. M. Guldi, *J. Am. Chem. Soc*., **2011**, *133*, 13036-13054.

174 F. Chaignon, M. Falkenström, S. Karlsson, E. Blart, F. Odobel, L. Hammarström, *Chem. Commun.*, **2007**, 64-66.

175 D. Plażuk, B. Rychlik, A. Błauż, S. Domagała, *J. Organomet. Chem.*, **2012**, *715*, 102-112.

176 B. J. Littler, Y. Ciringh, J. S. Lindsey, *J. Org. Chem.*, **1999,** *64*, 2864-2872.

177 M. Séverac, L. L. Pleux, A. Scarpaci, E. Blart, F. Odobel, *Tetrahedron Lett.*, **2007,** *48*, 6518-6522.

178 S. D. Köster, J. Dittrich, G. Gasser, N. Hüsken, I. C. Henao Castañeda, J. L. Jios, C. O. Della Védova, N. Metzler-Nolte, *Organometallics*, **2008**, *27*, 6326-6332.

179 A. Prodi, M. T. Indelli, C. J. Kleverlaan, F. Scandola, E. Alessio, T. Gianferrara, L. G. Marzilli, *Chem. Eur. J.*, **1999**, *5*, 2668-2679.

180 D. Gust, T. A. Moore, A. L. Moore, *The Porphyrin Handbook*, vol. 8, Electron Transfer (eds. K. M. Kadish, K. M. Smith and R. Guillard), Academic Press: San Diego, **2000**.

181 S. Green, M. A. Fox, *J. Phys. Chem.*, **1995**, *99*, 14752-14757.

182 V. Wintgens, P. Valat, J. Kossanyi, L. Biczòk, A. Demeter, T. Bèrces, *J. Chem. Soc., Faraday Trans.*, **1994**, *90*, 411-422.

183 P. Ganesan, J. Baggerman, H. Zhang, E. J. R. Sudhollter, H. Zuilhof, *J. Phys. Chem. A*, **2007**, *111,* 6151-6156.

184 J. W. Verhoeven, *J. Photochem. Photobiol. C*, **2006**, *7*, 40-60.

185 (a) T.-Y. Dong, S.-H. Lee, *J. Organomet. Chem.*, **1995**, *487*, 77-88; (b) A. N. Amin, M. E. El-Khouly, N. K. Subbaiyan, M. E. Zandler, M. Supur, S. Fukuzumi, F. D'Souza, *J. Phys. Chem. A*, **2011**, *115*, 9810-9819.

186 O. Johansson, M. Borgström, R. Lomoth, M. Palmblad, J. Bergquist, L. Hammarström, L. Sun, B. Åkermark, *Inorg. Chem.*, **2003**, *42*, 2908-2918.

187 C. Creutz, M. Chou, T. L. Netzel, M. Okumura, N. Sutin, *J. Am. Chem. Soc*., **1980**, *102*, 1309-1319.

188 H. Imahori, K. Tamaki, H. Yamada, K. Yamada, Y. Sakata, Y. Nishimura, I. Yamazaki, M. Fujitsuka, O. Ito, *Carbon*, **2000**, *38*, 1599-1605.

189 W. B. Davis, W. A. Svec, M. A. Ratner, M. R. Wasielewski, *Nature*, **1998**, *396*, 60-63.

190 J. Wiberg, L. Guo, K. Pettersson, D. Nilsson, T. Ljungdahl, J. Mårtensson, B. Albinsson, *J. Am. Chem. Soc.*, **2007**, *129*, 155-163.

191 M. T. Indelli, M. Orlandi, C. Chiorboli, M. Ravaglia, F. Scandola, F. Lafolet, S. Welter, L. De Cola, *J. Phys. Chem. A*, **2012**, *116*, 119-131.

192 E. A. Weiss, M. J. Ahrens, L. E. Sinks, A. V. Gusev, M. A. Ratner, M. R. Wasielewski, *J. Am. Chem. Soc.*, **2004**, *126*, 5577-5584.

193 D. Hanss, M. E. Walther, O. S. Wenger, *Coord. Chem. Rev*., **2010**, *254*, 2584-2592.

194 (a) A. D. Becke, *J. Chem. Phys.*, **1993**, *98*, 5648-5652; (b) P. J. Hay, *J. Phys. Chem. A*, **2002**, *106*, 1634-1641; (c) C. T. Lee, W. T. Yang, R. G. Parr, *Phys. Rev. B*, **1988**, 37, 785-789.

195 M. Berberich, M. Natali, P. Spenst, C. Chiorboli, F. Scandola, F. Würthner, *Chem. Eur. J.*, **2012**, *18*, 13651-13664.

196 A. A. Beharry, G. A. Woolley, *Chem. Soc. Rev.*, **2011**, *40*, 4422-4437.

197 Y. Yokoyama, *Chem. Rev.*, **2000**, *100*, 1717-1740.

198 G. Berkovic, V. Krongauz, V. Weiss, *Chem. Rev.*, **2000**, *100*, 1741-1754

199 (a) M. Irie, *Chem. Rev.*, **2000**, *100*, 1685-1716; (b) H. Tian, S. Yang, *Chem. Soc. Rev.*, **2004**, *33*, 85-97.

200 (a) T. Fukaminato, T. Umemoto, Y. Iwata, S. Yokojima, M. Yoneyama, S. Nakamura, M. Irie, *J. Am. Chem. Soc.*, **2007**, *129*, 5932-5938; (b) J. Kärnbratt, M. Hammarson, S. Li, H. L. Anderson, B. Albinsson, J. Andréasson, *Angew. Chem., Int. Ed.*, **2010**, *49*, 1854-1857.

201 (a) M. Irie, T. Fukaminato, T. Sasaki, N. Tamai, T. Kawai, *Nature*, **2002**, *420*, 759-760; (b) T. Fukaminato, T. Sasaki, T. Kawai, N. Tamai, M. Irie, *J. Am. Chem. Soc.*, **2004**, *126*, 14843-14849.

202 M. Berberich, A.-M. Krause, M. Orlandi, F. Scandola, F. Würthner, *Angew. Chem., Int. Ed.*, **2008**, *47*, 6616-6619.

203 Y. Odo, T. Fukaminato, M. Irie, *Chem. Lett.*, **2007**, *36*, 240-241.

204 C. Reichardt, *Solvents and Solvent Effects in Organic Chemistry*; 3 ed.; Wiley-VCH: Weinheim, **2003**.

205 R. Gvishi, R. Reisfeld, Z. Burshstein, *Chem. Phys. Lett.*, **1993**, *213*, 338-344.

206 E. Fron, G. Schweitzer, P. Osswald, F. Würthner, P. Marsal, D. Beljonne, K. Müllen, F. C. De Schryver, M. Van der Auweraer, *Photochem. Photobiol. Sci.*, **2008**, *7*, 1509-1521.